Analysis of Glomerular Permselectivity in the Rat Using Theoretical Models of Hindered Transport

by

James Douglas Oliver III

S.B., Massachusetts Institute of Technology (1981)
S.M., Massachusetts Institute of Technology (1986)

Submitted to the Harvard-MIT Division of Health Sciences and Technology
in partial fulfillment of the requirements for the degree of

Doctor of Philosophy

at the

MASSACHUSETTS INSTITUTE OF TECHNOLOGY

October 1992

Author .....
Harvard-MIT Division of Health Sciences and Technology
October 19, 1992

Certified by .....
William M. Deen
Professor of Chemical Engineering
Thesis Supervisor

Accepted by .....
Roger G. Mark
Chairman, Departmental Committee on Graduate Students

Analysis of Glomerular Permselectivity in the Rat Using Theoretical Models of Hindered Transport

by

James Douglas Oliver III

Submitted to the Harvard-MIT Division of Health Sciences and Technology
on October 19, 1992, in partial fulfillment of the
requirements for the degree of
Doctor of Philosophy

Abstract

Changes in glomerular permselectivity are the physiological basis for proteinuria, which typically accompanies chronic kidney disease. Traditionally, changes in the size-restrictive properties of the glomerular barrier have been quantified by measuring the fractional clearance (Θ) of exogenous infused dextrans and interpreting the results using the hindered transport theory for uncharged, solid spheres in cylindrical pores. The observed values of Θ for dextran in normal rats and healthy humans are unexpectedly large, however, given the normal absence of proteinuria. Recent *in vitro* diffusion studies show that dextran's hindered transport behavior is better represented by a random coil with attractive pore/solute interactions, while Ficoll follows the predictions for a neutral solid sphere. Thus, Ficoll sieving data should provide a better indication of the size-selective properties of the glomerular capillary wall. In one of the studies for this thesis, healthy Munich-Wistar rats were infused with either ^{3}H-dextran or ^{3}H-Ficoll. Plasma and urine samples were fractionated on gel chromatography columns which had been calibrated with narrowly-sized dextran and Ficoll standards. While values of Θ for Ficoll were similar to those measured for nearly-neutral proteins, dextran values were significantly higher at all molecular sizes. On this basis, the glomerular capillary wall is shown to be considerably more size-restrictive than had been previously determined. The random coil model was applied to the dextran data, and the attractive energy required to explain the dextran/Ficoll discrepancies *in vivo* was nearly the same as that required *in vitro*. Thus it appears that dextran's enhanced transport is nearly independent of the medium through which it travels.

The implications of the more size-restrictive barrier were examined in a second experimental protocol, in which ^{3}H-Ficoll was infused into four groups of fawn-hooded (FH) rats: a two-kidney (2K) control group, a uninephrectomized (UNX) group, a UNX group treated with the angiotensin converting enzyme inhibitor enalapril (ENA), and a UNX group treated with the nitrous oxide inhibitor NAME. The UNX and NAME groups had significantly higher glomerular filtration pressures ($\overline{\Delta P}$) and more proteinuria than the 2K and ENA groups, but the membrane pore size parameters of the four groups were essentially the same. The extent of albuminuria correlated strongly with $\overline{\Delta P}$, while the total rate of excretion of non-albumin proteins did not. Because albumin is negatively charged, these findings imply that albuminuria in FH rats results from a specific defect in glomerular charge-, rather than size-, selectivity, induced by chronic glomerular hypertension. Finally, to examine the potential for using fractional clearances to estimate filtration pressures in the clinical setting, the mathematical model was modified to make $\overline{\Delta P}$ an adjustable parameter, and fitted values were compared with those actually measured in the FH rats. The fitted and measured $\overline{\Delta P}$ did not show significant correlation, suggesting that Θ may not be sufficiently sensitive to $\overline{\Delta P}$ to allow such estimations.

Thesis Supervisor: William M. Deen
Title: Professor of Chemical Engineering

Acknowledgments

- My advisor, Bill Deen, for his continued advice, wisdom, patience, and understanding.
- My thesis committee, Prof. Alan Grodzinsky, Prof. Roger Kamm, and Dr. Sharon Anderson, for being a source of encouragement. Additional thanks are due to Sharon for her indispensable contributions in performing the Munich-Wistar rat experiments.
- The support of Dr. Barry Brenner and the Laboratory of Kidney and Electrolyte Physiology at Brigham and Women's Hospital. The work of Drs. Jacob Simons and Abraham Provoost of Erasumus University were essential in the fawn-hooded rat experiments. Special gratitude to Julia Troy, who knows everything there is to know and does everything that needs doing.
- Drs. K. Granath and K. H. Ebert kindly supplied dextran and Ficoll standards for GPC calibration. Prof. Robert Langer provided the scintillation counter and QLS equipment. The Radiation Protection/Safety Offices at MIT and Brigham and Women's, especially Judi Reilly and Milton Poirier, for their assistance with transferring samples.
- National Medical Fellowships, for a Commonwealth Fund Fellowship, and the NIH, for a predoctoral grant (5F 31 DK 08720-02).
- My past and present labmates, for putting up with me: Marc Davidson, Ron Phillips, Nelson Lin, Jennifer Smith, Nikola Juhasz, Claudia Drumond, Erin Malley, Randy Lewis, and Aurelie Jacquand. Come to think of it, it was actually I who put up with Nikola, but now is not a time to quibble.
- The Nerds, Kathy Donahue and Minerva (Shirley) Garcia, for their expert envelope-stuffing skills. Also to the other members of the MEMP program, who will now have to find a new shortstop.
- "Da Boyz"—Derrick Cameron, Kirk Gilpin, Steve Isabelle, Vince McNeil, Damon Phillips, Darryll Pines, Bobby Satcher, Collin Stultz. All the best to you guys, but I hope none of you ever get nominated to the Supreme Court.
- D'Juanna White, for being right all of the time.
- Innumerable friends at MIT and Harvard Medical School, and to Jamela Franklin-Kenea for finally following through on the dinner she promised.
- Unlike my friends, my family—Mom, Dad, Jeanne, June—really had no choice in the matter, but have somehow managed to keep their complaints to a minimum over the last thirty-odd years. In return, they get another book for the coffee table and an answer to the question, "What *has* he been doing all this time?".

Contents

List of Figures

List of Tables

Chapter 1

Introduction

1.1 Clinical Relevance of Glomerular Function

The spectrum of glomerular diseases includes both primary entities such as the glomerulonephrites, whose principal involvement is with the kidney, and systemic diseases such as diabetes and essential hypertension, where the renal involvement is a secondary outgrowth. Leaf and Cotran[163] classify the mechanisms for the pathogenesis of glomerular injury into three types: those that are immune-mediated, those that result from altered glomerular hemodynamics, and those that are related to loss of glomerular charge-selectivity (which can more generally be extended to a loss of overall permselectivity). This classification scheme is not mutually exclusive, as changes in hemodynamic patterns and permselectivity have been observed in both immune- and non-immune mediated disease. Perhaps a better method of categorization is to divide into those disorders in which there is a primary chemically- or immune-mediated derangement in the glomerular wall and those in which the injury is secondary to hemodynamic changes. Again, however, the distinction is not clear-cut since, as described in the following section, primary disease affecting some glomeruli can lead to altered hemodynamics and secondary disease in other healthy glomeruli.

The two most important clinical manifestations of glomerular disease are a decreased urinary output, a consequence of a reduction in the glomerular filtration rate (GFR), and proteinuria, the loss of serum proteins—predominantly albumin—in the urine, which results from a loss of the ability of the glomerulus to retain large and anionic molecules in the intracapillary space.

Several models of glomerular disease in the rat and other animals have been used to explore the etiologies and pathophysiologies of renal disorders. These models have the advantage over clinical studies in that hemodynamic parameters such as the transmural hydraulic pressure and the ultrafiltration coefficient can be directly measured. In addition, such experiments pioneered the use of exogenous polymers to study the permeability properties of the glomerular capillary wall. An important result of these studies is the hypothesis for the hemodynamically-mediated progression of glomerular disease.

1.2 Hemodynamically-Mediated Damage of the Glomerulus

The role of altered glomerular hemodynamics in the pathogenesis of renal injury is of interest because of the adaptive response of the kidney to reductions in renal mass: an increase in glomerular pressure results in a higher filtration rate plus structural and functional hypertrophy.[128] Surgical ablation of

renal tissue is a common animal model for this process. Total glomerular filtration rate is maintained through hyperfiltration, but at a cost of a progressive sclerotic process which eventually reduces function in the surviving nephrons. Data also suggests losses in the ability of the glomerular capillary wall to discriminate on the basis of both size and charge.[198]

An example of a disease in which this mechanism appears to play an important role is diabetes mellitus.[49,101,180,187,226,242,255] A hallmark of the renal involvement in clinical diabetes is sustained hyperfiltration in the early years followed by a reduction in *GFR* and increased proteinuria. Histologically, characteristic nodular sclerotic lesions develop in the glomerulus. The filtration barrier to large molecules is reduced, and evidence suggests that the charge selectivity is also impaired.[49,101,242] Animal models of streptozotocin- and alloxan-induced diabetes show similar pathological changes and alterations in hemodynamics and size-permselective properties.[129,177,178,205,266] The charge-selectivity of diabetic glomeruli has not been studied extensively, but one study of alloxan-induced diabetes indicates a unique and unexplained enhancement of this property.[178]

A different example of the connection between renal performance and hemodynamics is in patients who are postoperative from cardiac surgery, where impaired cardiac output is sometimes associated with azotemia or renal failure. One report indicates that glomerular hypofiltration is associated with a decrease in the intrinsic ultrafiltration ability of the membrane.[186] There was no apparent change in the permselective properties in this study nor in a study in the rat of decreased perfusion pressure,[253] but the data is too limited to be conclusive.

It is therefore of considerable interest to find a means to ameliorate the damage caused by hyperfiltration. Dietary protein restriction has been shown as one way by which glomerular pressure and filtration rate can be reduced, accompanied by diminished glomerulosclerosis.[38,128,175] The therapeutic use of angiotensin I converting enzyme (ACE) inhibitors in arresting the progression of renal damage has been investigated in models of renal ablation[6,7,175] and diabetes.[266] Three generalizations emerge as a result of this work:

1. Anatomical damage to the glomerular capillary wall and progressive proteinuria can be arrested by normalization of the transmural hydraulic pressure difference, even if the filtration rate *per se* remains high.[6,128]

2. Renal damage is prevented by purely hemodynamic interventions even if an underlying systemic abnormality, such as diabetes, persists.[175,266]

3. Specific normalization of glomerular pressure by angiotensin I converting enzyme inhibitors has a therapeutic advantage over treatment for systemic hypertension.[7]

Thus there is a growing body of evidence which suggests that primary alterations in renal hemodynamics affect the permselective properties of the glomerular capillary wall. Furthermore, the

development of a method for estimating glomerular filtration pressures in humans is strongly motivated for monitoring the efficacy of therapeutic interventions.

1.3 Thesis Summary

The goals of this thesis were to extend the applications of sieving curve analysis, in particular to the study of the interactions between renal hemodynamics, proteinuria, and the progression of renal disease. Chapter 2 summarizes glomerular anatomy and physiology and the relevant mathematical models. The remaining chapters address specific issues related to the thesis goals:

1. Methodological issues of gel chromatography calibration and dispersion and their effects on the accuracy of sieving data were examined (Chapter 3).

2. Dextran and Ficoll tracer studies were performed in Munich-Wistar rats to determine the effect of molecular configuration on glomerular sieving (Chapter 4). The dextran data was then analyzed using recent theoretical developments in the transport of linear chains through pores (Chapter 5).

3. To examine more systematically the interaction between hemodynamics and size-selectivity, Ficoll tracer studies were performed in groups of fawn-hooded rats in varying states of chronic renal disease (Chapter 6).

4. Finally, a computational approach for estimating glomerular transmural hydraulic pressure from sieving data was developed and applied to the data from the fawn-hooded rats (Chapter 7).

Chapter 2

Background

2.1 Overview of Kidney Anatomy and Function

The kidneys are paired retroperitoneal organs lying on opposite sides of the vertebral column, between the twelfth thoracic and third lumbar vertebrae. The primary function of the kidney is to maintain the so-called internal milieu of the body by regulating the volume and composition of the extracellular fluid. The initial mechanism is the filtration of blood through a specialized capillary wall into the renal tubules. Blood constituents that are too large (such as cells) or too highly anionic (such as proteins) to pass through the capillary wall are retained in the blood stream. The rest of the kidney serves to reabsorb the vast majority of the water and important solutes from the tubules, to secrete other solutes at various stages, and ultimately to form a urine concentrated in waste materials.

Each kidney obtains its blood supply from a renal artery which branches into smaller segmental, interlobar, and interlobular arteries, until the level of the *afferent arterioles* is reached. The afferent arteriole feeds into the functional unit of the kidney, the *nephron*. A nephron is responsible for the filtration and downstream processing of the ultrafiltrate from a single afferent arteriole. Each nephron consists of a glomerulus, a tubule, and a collecting duct. Broadly speaking, the glomerulus is the site of filtration, the tubule is the location of water and solute reabsorption and secretion, and the duct is the site of urine concentration. The high level of activity required at each of these three stages is indicated by the volume flow rates: renal blood flow (RBF) in a 70-kg human being is about 1.2 l/min, one-fifth of the resting cardiac output,[36] which translates to a renal plasma flow (RPF) of about 0.54 l/min. The total glomerular filtration rate (GFR) is about 0.13 l/min.[37] Since normal urine output over a 24-hour period is approximately one liter,[163] only 0.5% of the filtered volume is actually excreted.

The animals most commonly studied as models for human kidney function are rats and dogs. A human kidney has around 1.2×10^6 nephrons, while a dog's has approximately 4.3×10^5 and a rat's, about 3.2×10^4.[240] On the basis of total renal blood flow rate per mass of kidney tissue, all three species have comparable values ranging from 3 to 5 ml/min/g.[41]

2.2 The Glomerular Capillary Wall

The glomerulus is the site of the first step in urine formation—the creation of a cell- and protein-free filtrate of the blood. A glomerulus is a tuft of interweaving and interconnecting capillaries

about 200 μm in diameter enclosed by Bowman's capsule, a bi-layer of squamous epithelium over basement membrane (Figure 2-1a). Ultrafiltrate flows from the capillary into the cavity—known as Bowman's space—between the vessel tuft and Bowman's capsule. A glomerulus has four histological components: the mesangial cells, which provide the architectural support, and the three layers of the glomerular capillary wall—the vascular endothelium, glomerular basement membrane, and visceral epithelium. Under normal circumstances, the bulk of filtration occurs through the capillary wall, with a small but undetermined percentage filtering through the mesangium.[176] In some pathological conditions, the amount of mesangial filtration may be increased.[222]

There have been several attempts to pinpoint anatomical sites which demonstrate size or charge selectivity. Permeability studies with electron-dense tracers indicated that the glomerular basement membrane was a primary source of restriction,[97] but as emphasized by Skorecki *et al.*,[231] the numerous interactions between the cellular and acellular components of the capillary wall make it difficult to attribute selective properties to any one particular component. Rather, it appears that the charge and structure of the combined endothelium, basement membrane, and epithelium all contribute to the filtration properties of the glomerulus.

2.2.1 Endothelium

The vascular endothelial cells of the glomerulus, which line the inner lumen of the capillaries, are perforated by small openings, or fenestrae, 500 to 1000 Å wide. These fenestrae are unique in that they allow for direct exposure of the basement membrane to the plasma, in contrast to fenestrated capillaries of endocrine glands and intestine which have diaphragms. Thus it appears that the endothelium provides almost no resistance to the passage of macromolecules.[97] Endothelial cell membranes have sialic acid-containing glycoproteins which are postulated to be important for maintaining the structure of the capillary wall and for some charge-selectivity.

2.2.2 Glomerular Basement Membrane

Histologically, the glomerular basement membrane (GBM) is seen to have three distinct layers. Two lucent layers, the lamina rarae interna and externa, are adjacent to the endothelium and epithelium, respectively. The more opaque lamina densa lies between the two (Figure 2-1b).

The GBM, with a thickness of 3500 Å in humans and 1500 Å in rats,[240] is a sheet of extracellular matrix composed of type IV collagen, proteoglycans (heparan sulfate and chondroitin sulfate), and the glycoproteins laminin and fibronectin.[97] The absolute relative amounts and distribution of the components is a subject of active research, but it appears that collagen makes up the bulk of the lamina densa, while the proteoglycans and glycoproteins are localized to the lamina rarae. Laminin and fibronectin are postulated to be important in the attachment of epithelial and endothelial cells to the extracellular matrix.

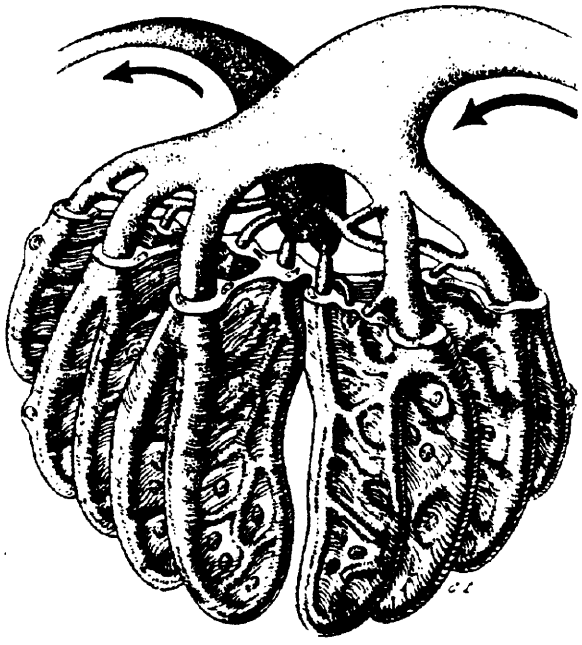

(a) Anatomy of the glomerular capillary network. Arrows indicate direction of blood flow. From Elias *et al.*[95]

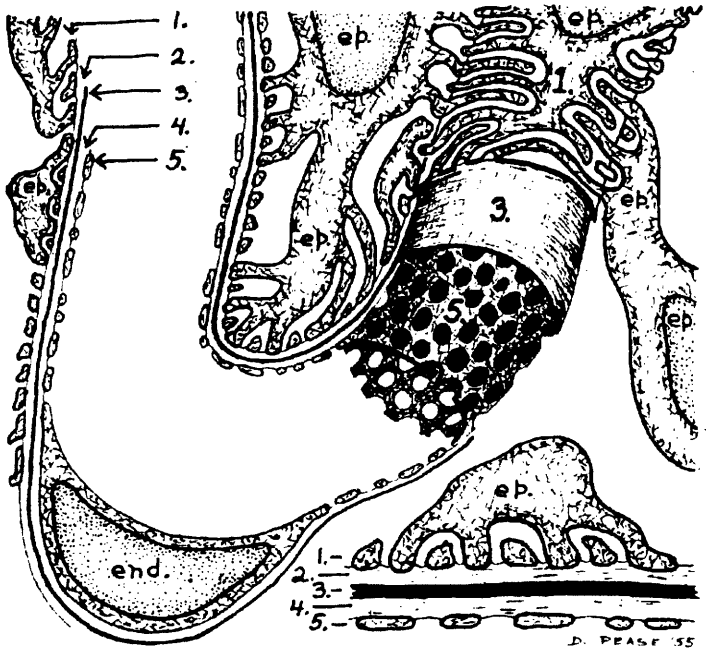

(b) Cross-sectional schematic of the glomerular capillary wall. *end*–endothelial cell, *ep*–epithelial cell. 1–epithelium, 2–lamina rara externa, 3–lamina densa, 4–lamina rara interna, 5–endothelium. From Peace.[203]

Figure 2-1: Glomerular capillary structure.

Anionic glycosaminoglycans in the lamina rara interna and externa have been proposed as the principal determinants of charge selectivity, *i.e.*, the hindered transport of negatively-charged molecules such as proteins and the facilitated transport of cationic molecules.[141] Cationic staining studies of the basement membrane by Kanwar and Farquhar[140] resulted in staining of clumps of anionic sites within both lamina rarae, spaced about 600 Å apart, indicating that charge distribution may not be homogeneous in the GBM.

2.2.3 Epithelium

The visceral epithelial cells, or podocytes, are distinguished by their arrangement of interdigitating "foot processes" which rest on the lamina rara externa (Figure 2-1b). The spaces between the foot processes, which are 250-600 Å wide, are known as *filtration slits* and are covered by a thin diaphragm. Like the endothelial cells, the epithelial membranes are coated with anionic glycoprotein.

In several nephrotic pathological conditions, the foot processes of the epithelial cells are replaced by a continuous rim of cytoplasm with variable degrees of vacuolization, a phenomenon often referred to as "fusion" of the foot process, although there is no true fusion of the cells.[8] This histological pattern can be mimicked in rat kidneys by the infusion of polycations such as protamine sulfate,[223] and thus has been suggested to result from a loss of the endothelial fixed charges.[44,50,256]

2.3 Control and Chemical Mediation of Glomerular Ultrafiltration

The details of glomerular filtration have been extensively reviewed by Maddox *et al.*.[169] Conceptually, glomerular ultrafiltration is controlled by the adjustment of three parameters: the afferent and efferent arteriolar resistances R_A and R_E and the ultrafiltration coefficient K_f, where

$$R_A \equiv \frac{P_A - \overline{P}_{GC}}{AABF}, \tag{2.1a}$$

$$R_E \equiv \frac{\overline{P}_{GC} - P_E}{EABF}, \tag{2.1b}$$

$$K_f \equiv \frac{SNGFR}{\overline{P}_{UF}}. \tag{2.1c}$$

The afferent and efferent arteriolar pressures in the above equations are designated by P_A and P_E, respectively, and the afferent and efferent arteriolar blood flow rates are $AABF$and $EABF$. $\overline{P}_{GC}$ is the length-averaged pressure in the glomerular capillary, while $\overline{P}_{UF}$ is the length-averaged ultrafiltration driving pressure, a function of both hydrostatic and osmotic pressure as described in Section 2.5.1. $SNGFR$ is the single nephron glomerular filtration rate. Alterations in vascular tone result in corresponding changes in R_A and R_E, while changes in intrinsic capillary permeability and filtration surface area are manifested in K_f.[132] Afferent renal plasma flow (Q_A) is modulated by the total renal vascular resistance $R_T = R_A + R_E$; $\overline{\Delta P}$ is a function of R_A/R_T; and $SNGFR$ is

Compund	R_A	R_E	R_T	K_f	Q_A	$\overline{\Delta P}$	$SNGFR$
Angiotensin II	0	↑	↑	↓	↓	↑	↓
Norepinephrine	↑	↑	↑		↓	↑	0
ADH	0	0	0	↓	0	↑*	0
Leukotriene LTC_4			↑				
Leukotriene LTD_4	0	↑	↑	↓	↓	↑	↓
High-dos PAF	↑	↑	↑	↓	↓		↓
Endothelin			↑				
Histamine	↓		↓	↓	↑	↑	0
Prostaglandin $E_1^{\#}$				↓	↑	0	0
Prostaglandin $E_2^{\#}$	↑	↑	↑	↓		↑	↓
Prostaglandin $I_2^{\#}$	↑	↑	↑	↓		↑	↓
Bradykinin	↓	↓	↓	↓	↑	0	0
Acetylcholine	↓	↓	↓	↓	↑	↑	0
Glucocorticoids	↓	↓	↓	0	↑	0	↑
cAMP			↓	0	↑	↓	↑
EDRF		↓	↓	↑		↓	0
ANP	↓	↑		0	0	↑	↑
Parathyroid hormone				↓	0	0	↓

Table 2.1: Chemical modulators of glomerular hemodynamics. *Abbreviations:* ADH–anti-diuretic hormone, PAF–platelet activating factor, EDRF–endothelium-derived relaxing factor, ANP–atrial natriuretic peptide. *Caused by reduction in P_T. #Excluding effect on renin synthesis. Information summarized from Maddox *et al.*.[169]

a function of Q_A, K_f, and the transmural hydraulic pressure $\overline{\Delta P}$ ($= \overline{P}_{GC} - P_T$, where P_T is the pressure in the tubule).[36]

Physiologic control of glomerular function involves many complex interactions, the relative importance of which are not yet fully determined. The major chemical mediators of glomerular filtration are summarized in Table 2.1. Two mechanisms have been relatively well-defined: *autoregulation* and *tubuloglomerular feedback*.

2.3.1 Autoregulation

In the absence of any neural or hormonal control, the kidney can respond to variatons in systemic arterial perfusion pressure in such a way as to keep renal plasma flow and $\overline{\Delta P}$, and consequently GFR, relatively constant. This autoregulation of RBF is seen for mean arterial pressures above 80 mm Hg in rats[218] and is an intrinsic response to changes in the tangential wall tension of the arterioles; it is seen in de-ennervated and isolated kidney preparations.[93,100] Physiologically, autoregulation is demonstrated as the kidney's ability, in the face of decreasing arterial pressure, to maintain R_E constant while lowering R_A.[218]

2.3.2 Tubuloglomerular Feedback and the Renin-Angiotensin-Aldosterone System

The macula densa cells of the early proximal tubule and the afferent and efferent arterioles of the glomerulus are located close together. It has been observed that high flow rates past the macula densa cells lead to a reduction in *SNGFR*, apparently signaled by increased chloride uptake.[258] This reduction in *SNGFR* is a result of reduced Q_A and K_f with constant $\overline{\Delta P}$, suggesting an increase in R_A and R_E brought about by a contraction of mesangial cells.[132]

The renin-angiotensin-aldosterone system has been proposed as the effector mechanism of tubuloglomerular feedback, but this has as yet not been proven conclusively. Renin is a proteolytic enzyme stored in the granules of afferent arterioles in the juxtaglomerular appartus. It is secreted in response to increased intracellular levels of cyclic AMP or decreased intracellecular levels of calcium. The factors that regulate renin secretion include (1) sympathetic control (β-adrenergic stimulation, β-antagonistic or α-adrenergic inhibition), (2) baroreceptor control (stimulation by reduced arterial wall tension, inhibited by increased tension), (3) hormonal regulation (histamine, glucagon, and parathyroid hormone stimulation or angiotensin II and vasopressin inhibition), (4) prostaglandin stimulation, and (5) an as-yet-undetermined signal from macula densa cells when the concentration of chloride ion in the proximal tubule fluid increases. Renin cleaves a circulating α_2-globulin, *angiotensinogen*, into the inactive peptide *angiotensin I* (A-I). Angiotensin I is transformed in pulmonary microvessels into *angiotensin II* (A-II) by *angiotensin I converting enzyme* (ACE).

Angiotensin II is a powerful vasoconstrictor which also serves to release the hormone *aldosterone* from the adrenal cortex. Aldosterone stimulates sodium reabsorption in the tubules, leading to an increased intravascular volume. These two substances counteract hypotension and/or decreased perfusion of the kidney.

Studies by Myers *et al.*[185] and Ichikawa *et al.*[136] indicate that the principal glomerular effect of angiotensin II is to specifically increase R_E, leading to an increase in $\overline{\Delta P}$. A secondary rise in R_A is seen in response to the systemic pressor actions of A-II. Angiotensin II has also been shown to lower K_f,[24] apparently through a loss of parenchymal volume in the glomerular tuft which results from contraction of the mesangial cells.[12,121]

Chemical inhibition of A-II effects may be accomplished by two classes of compounds—the *angiotensin receptor antagonists* and the *ACE blockers*—both of which are important in experimental studies of glomerular ultrafiltration. Saralasin is a receptor antagonist frequently used clinically as a tool for establishing a diagnosis of renovascular hypertension. Captopril and enalapril are ACE inhibitors used clinically for systemic hypertension and experimentally for lowering $\overline{\Delta P}$.

2.4 Theoretical Models of Glomerular Function

Theoretical models of glomerular function address the question of to what extent ultrafiltration and permselectivity are modulated by variations in the system hemodynamics—renal plasma flow and glomerular pressure—versus the extent to which they are affected by changes in properties of the glomerular capillary wall—permeability and available surface area for filtration. For example, a reduction in GFR may result from a lowered perfusion, a reduction in the driving force, a decrease in the intrinsic membrane permeability, or a loss of filtration surface area. Similarly, proteinuria could be postulated as a manifestation of an increased bulk filtration or as a loss of the capillary's power to restrict transport. The success of these models has been their ability to explain specific renal pathophysiological processes in terms of such changes.

2.5 Glomerular Ultrafiltration

2.5.1 Determinants of Glomerular Ultrafiltration

The progress in the understanding of the process of glomerular ultrafiltration has come about over the last twenty years primarily from two advances: the development of servo-nulling techniques for pressure measurement and the discovery of a strain of Munich-Wistar rats which have glomeruli located at the surface of the renal cortex, allowing for direct access to the glomerular capillary and Bowman's space. The theoretical approach to ultrafiltration in the glomerulus was developed by Deen *et al.*[81] If each glomerular capillary is idealized as a tube of length L (Figure 2-2), the local transmural flux J_v at a point y along the capillary can be expressed as the product of a permeability and a driving force:

$$J_v(y) = k\left[\Delta P(y) - \Delta\pi(y)\right] \tag{2.2a}$$

$$\approx k\left[\overline{\Delta P} - \pi_{GC}(y)\right], \tag{2.2b}$$

where k is the (empirical) effective hydraulic permeability of the wall, $\Delta P(y) = P_{GC}(y) - P_T$ is the radially-averaged transmural hydraulic pressure difference (often simply referred to as the filtration pressure), and $\Delta\pi(y) = \pi_{GC}(y) - \pi_T$ is the radially-averaged transmural oncotic pressure difference. (The subscripts GC and T represent glomerular capillary and tubule [Bowman's space] values, respectively). The approximation in Eq. 2.2b results from observations that the axial drop in hydraulic pressure over the capillary length is small, on the order of 2 to 3 mm Hg, and the hydraulic pressure in Bowman's space is assumed to be independent of position. Thus the local pressure difference can be replaced by the length-averaged value, $\overline{\Delta P}$.[37,127] Inclusion of the axial pressure drop makes for a more physically realistic model but requires exceptional accuracy in the experimental measurement of the afferent and efferent protein concentrations.[81] The osmotic

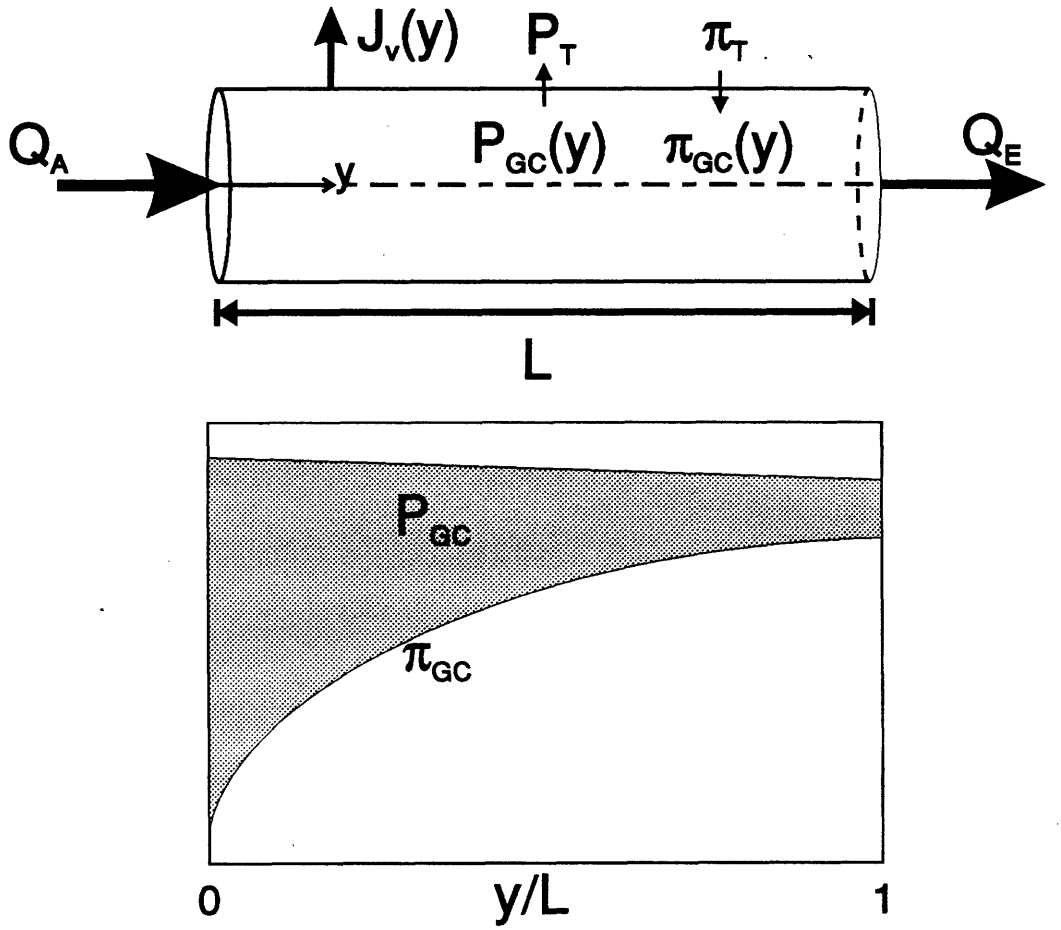

Figure 2-2: Model of glomerular ultrafiltration. *Top*: Afferent (Q_A) and efferent (Q_E) plasma flow is axial in a tube of length L, while solvent flux (J_v) is radial. Hydraulic and osmotic pressures in the capillary (P_{GC}, π_{GC}) vary with position, while those in Bowman's space (P_T, π_T) are constant. Filtration is governed by opposing hydraulic and osmotic pressure differences, resulting in the net flux of solvent (J_v) into Bowman's space. *Bottom*: Hydraulic and osmotic pressure profiles along the length of the glomerular capillary. Hdraulic pressure is nearly constant, while osmotic pressure increases significantly. Shaded area represents the net ultrafiltration driving pressure ($\overline{P}_{UF}$).

pressure difference is assumed to result entirely from the difference in protein concentration, since even in states of heavy proteinuria Bowman's space normally contains a negligible amount of protein compared to plasma[193] (*i.e.*, $\pi_T \approx 0$ and $\Delta\pi(y) \approx \pi_{GC}(y)$). The oncotic pressure is calculated from plasma protein concentration by the relation[81]

$$\pi = 1.629c_p + 0.2935c_p^2, \tag{2.3}$$

where c_p is in units of g/dl (valid over the range 4 to 10 g/dl) and π is in mm Hg.

Near the inlet, the loss of fluid from ultrafiltration with concomitant retention of protein causes the oncotic pressure within the capillary to rise, resulting in a diminishing of the driving force and less filtration toward the outlet. Physiologically, the opposing hydraulic and oncotic pressure come close to balancing at the efferent end (Figure 2-2).

The effective membrane hydraulic permeability k differs from the true hydraulic permeability of the glomerular capillary wall k_0 because the effects of radial protein concentration gradients are not included. Concentration polarization within the capillary lumen results in a higher protein concentration at the wall surface than at the midline axis. The actual $\Delta\pi$, and therefore k_0, is underestimated by approximately 10% when using bulk protein concentrations.[82]

If the total volumetric flow rate of plasma is $Q(y)$ and the total surface area of the capillary is S, then assuming no protein transport across the membrane (a valid approximation for the osmotic pressure difference even with massive proteinuria[193]) we have the following expressions for conservation of mass:

$$\frac{dQ}{d\hat{y}} = -SJ_v(\hat{y}), \tag{2.4a}$$

$$\frac{d(Qc_p)}{d\hat{y}} = 0. \tag{2.4b}$$

where $c_p(y)$ is the plasma protein concentration and $\hat{y} = y/L$ is a normalized length scale.

Eqs. 2.2b, 2.3, and 2.4, plus the afferent plasma flow rate $Q_A = Q(0)$ and afferent protein concentration $c_{p,A} = c_P(0)$ are needed to solve for the complete flux, and osmotic pressure profiles. Of particular interest are the flux and permeability integrated over the capillary length, which can be obtained by substituting Eq. 2.2b in Eq. 2.4:

$$SNGFR = K_f \overline{P}_{UF} \tag{2.5}$$

where

$$SNGFR \equiv \int_0^1 SJ_v(\hat{y})\, d\hat{y} \tag{2.6a}$$

$$\overline{P}_{UF} \equiv \int_0^1 \left[\overline{\Delta P} - \pi_{GC}(y)\right] d\hat{y} \tag{2.6b}$$

$$K_f \equiv S \cdot k \tag{2.6c}$$

Eq. 2.5 is the whole-glomerular analog to Eq. 2.2b. Here it can be seen that K_f is the product of the capillary hydraulic permeability and the surface area, while $\overline{P}_{UF}$ is the difference of the mean hydraulic and mean osmotic pressures, given by the shaded graphical area of Figure 2-2. A closed-form expression for K_f as a function of Q_A, $SNGFR$, $\overline{\Delta P}$, and $c_{p,A}$ is given by Deen *et al.*[81]

Implicit in the derivation of Eq. 2.5 is the assumption that the glomerular capillary network can be represented as a number of identical capillaries in parallel. Anatomical studies of the rat glomerulus in fact suggest that there is significant heterogeneity in both capillary length and radius within a single glomerulus.[157,225] Remuzzi and Deen[211] investigated the theoretical implications of independent distributions in capillary length and radius and found that for a fixed K_f, increasing heterogeneity in either dimension reduced $SNGFR$, but a distribution in length had a more noticeable effect. Based on literature data estimating the length distribution for rat glomeruli, Remuzzi and Deen established that a K_f calculated using identical capillaries underestimates the actual K_f by about 30%.[211]

The situation pictured in Figure 2-2 represents one of *filtration pressure disequilibrium*; that is, the efferent osmotic pressure π_E is smaller than $\overline{\Delta P}$. This is a condition found experimentally in euvolemic animals, where surgical fluid losses are replaced by continuous infusion. Filtration pressure *equilibrium* ($\pi_E = \overline{\Delta P}$) is the physiologic condition commonly found in hydropenic rats, where fluid volume replacement is not performed.[135] It is not possible to calculate a unique value for K_f in this instance, since the exact point along the capillary where equilibrium is reached, and therefore $\overline{P}_{UF}$ is not known. The best that can be done is to establish a minimum value for K_f by assuming that the osmotic and hydraulic pressure balance just at $\hat{y} = 1$.

2.5.2 Theoretical Dependence of Ultrafiltration Coefficient on Parameters

As previously stated, Q_A, $\overline{\Delta P}$, and $SNGFR$ are controlled by the interaction of R_A, R_E, and K_f. According to the model, at filtration pressure equilibrium $SNGFR$ increases directly with Q_A; the single nephron filtration fraction ($SNFF$), defined as

$$SNFF = \frac{SNGFR}{Q_A}, \tag{2.7}$$

is a constant. For conditions of filtration pressure disequilibrium, $SNGFR$ increases proportionally less than the increase in Q_A, and $SNFF$ decreases. These theoretical predictions have been verified experimentally in rats.[40,80,84,135,218] From the basic tenet of filtration pressure equilibrium versus disequilibrium, the effect of specific changes in the other hemodynamic parameters on glomerular

ultrafiltration can be summarized:

- As K_f increases, *SNGFR* and *SNFF* increase until filtration pressure equilibrium is reached, and then they hold constant with further increases. Variations in the ultrafiltration coefficient are not independent of the other hemodynamic parameters, as discussed next. Changes in K_f are important in several pathophysiological states (see Section 2.5.3).

- As afferent osmotic pressure π_A increases, *SNGFR* and *SNFF* decrease until they become zero at $\pi_A = \overline{\Delta P}$. Experimental studies on rats have shown, however, that decreasing π_A leads to a fall in K_f, and thus a smaller increase in *SNGFR* than would be predicted.[17,23,25,244] Multivariate statistical analysis of this association shows a direct dependence which is not a result of an intermediate relationship with Q_A or $\overline{\Delta P}$.[244] The mechanism of this interaction has not been elucidated, but Brenner *et al.*[37] suggest that protein concentration may be a factor in the regulation of K_f by vasoactive hormones.

- As $\overline{\Delta P}$ increases above π_A, *SNGFR* and *SNFF* also rise. This increase is not a linear relationship, because the larger local fluxes ($J_v(y)$) along the capillary lead to higher values for $c_P(y)$ and local osmotic pressures, partially offsetting the hydraulic pressure increase. Experimentally, as for osmotic pressure changes, there is a significant relationship with the ultrafiltration coefficient, but here an inverse correlation.[244] Thus increasing pressure is associated with an offsetting decrease in K_f.

2.5.3 Pathophysiological Behavior of Ultrafiltration Parameters

A reduction in K_f is believed to be an important clinical mechanism in the pathogenesis of acute renal failure[43] and several forms of glomerulonephritis,[231] although it can only be documented in animal models. Animal models of nephrotoxic serum nephritis (NSN, an analogue to human anti-GBM disease) show a change in *SNGFR* that is proportional to the severity of the injury. In response to mild treatment with anti-GBM antibody, the glomeruli maintained a relatively normal *SNGFR* despite a lower K_f by increasing $\overline{\Delta P}$.[168] For major injuries of the same type, *SNGFR* dropped by 50%, principally caused by a reduction in K_f (offset by a larger $\overline{\Delta P}$), although a contributing factor was a rise in R_A and R_E leading to a reduced Q_A.[26]

Studies of Heymann's nephritis, a model resembling human membranous glomerulopathy, have shown an intrarenal heterogeneity in *SNGFR* determined by variances in K_f and Q_A.[134] Values for $\overline{\Delta P}$ and π were found to be constant for all glomeruli regardless of the particular *SNGFR* . Other studies have confirmed that $\overline{\Delta P}$ is not significantly elevated in Heymann's nephritis.[262]

Puromycin aminonucleoside (PAN) nephrosis is a non-immunological model for human minimal change disease. Rats infused with PAN demonstrate a decrease in *SNGFR* which is related to a lowered K_f.[137] As with Heymann's nephritis, $\overline{\Delta P}$ remains normal.[29]

Hemodynamic alterations in adriamycin nephrosis are similar to those observed in severe NSN injury. Q_A decreases as a result of an elevated R_A and R_E, and a $\overline{\Delta P}$ increase is accompanied by a reduced K_f. The net effect is a smaller *SNGFR* while *SNFF* is relatively constant.[192,252]

Studies of renal ablation (surgical infarction of functional renal tissue) in rats indicate that K_f is not altered in response to a purely hemodynamic increase in Q_A and $\overline{\Delta P}$.[80,128] When filtration pressure is normalized, however, either by ACE inhibitors or dietary protein reduction, the ultrafiltration coefficient increases to maintain *SNGFR* relatively constant.[6,7,175]

Hyperfiltration in streptozotocin (STZ)-treated diabetic rats appears to be a function of increased perfusion and filtration pressure resulting from a specific decrease in R_A, as K_f does not differ significantly from normal controls.[129,266] In more severe STZ-induced diabetic conditions, R_A and R_E are high, Q_A and *SNGFR* are markedly reduced, but $\overline{\Delta P}$ is normal. Conversely, the situation in alloxan-induced diabetes seems to be one of hypofiltration or increased R_A, where *SNGFR* and $\overline{\Delta P}$ are slightly reduced from controls, while K_f is unchanged.[177] Insulin therapy of alloxan-infused rats reduces R_A while having no effect on K_f.

2.6 Glomerular Permselectivity

2.6.1 General Aspects

Normally, the glomerular capillary wall serves as a very effective discriminator on the basis of both molecular size and charge. Small uncharged molecules are filtered without measurable restriction, but the resistance to transport increases with larger or more anionic molecules. The concentration of inulin in the glomerular ultrafiltrate equals that in the afferent arteriole, as opposed to albumin, where the ultrafiltrate concentration is less than 0.1% of the afferent arteriole.[195]

Many disease states are characterized by a deficit of these permselective abilities, most seriously manifested as protein loss in the urine. Development of theoretical models of glomerular permselectivity has led to greater understanding of the importance of molecular size, charge, and configuration to the normal ultrafiltration process, and to an understanding of the pathophysiological changes in system hemodynamics and membrane properties in the disease state.

2.6.2 Clearance

The concept of *clearance* allows the relation of measurable solute concentrations in arterial blood and excreted urine to concentrations in Bowman's space, which is not, in general, available for sampling. The clearance of solute i is symbolized by $\dot{C}_i$ and defined as

$$\dot{C}_i \equiv \frac{\dot{U} c_{i,U}}{c_{i,A}}, \tag{2.8}$$

here $\dot{C}_i$ has units of volume/time, $\dot{U}$ is the urinary flow rate in volume/time, $c_{i,U}$ is the concentration of solute in urine, and $c_{i,A}$ is the concentration of solute in the afferent arteriole. The clearance is the hypothetical rate at which blood is completely "cleared" of solute i by the kidney. If the solute is one such as the fructose polymer inulin–which is uncharged, freely filtered through the glomerular capillary wall, and does not undergo reabsorption or any further secretion downstream–then its clearance is equal to *GFR*. The *fractional clearance FRC* is a dimensionless quantity

$$FRC_i \equiv \frac{\dot{C}_i}{GFR}. \tag{2.9}$$

A fractional clearance less than unity indicates that the solute undergoes some combination of restricted filtration or tubular reabsorption. A fractional clearance greater than one indicates that the solute is secreted in the tubules.

The *sieving coefficient* of a solute Θ_i is defined with respect to its concentration in the afferent arteriole $c_{i,A}$ and its average concentration in Bowman's space $\langle c_{i,B} \rangle$:

$$\Theta_i \equiv \frac{\langle c_{i,B} \rangle}{c_{i,A}}. \tag{2.10}$$

For a solute which is neither secreted nor reabsorbed in the tubules, it can be shown that

$$FRC_i = \Theta_i, \tag{2.11}$$

and thus this parameter of theoretical interest can be obtained directly from blood and urine concentrations. If a polydisperse polymeric substance such as dextran (a polymer of D-glucopyranose) is infused as a marker, then the plasma and urine samples can be fractionated by size, and subsequent determination of the sieving coefficients as a function of molecular size leads to the construction of sieving curves. As discussed below, these sieving curves are affected by both hemodynamic changes and alterations in the membrane properties and potentially can be used as tools for the clinical estimation of parameters not directly measurable.

2.6.3 Early Models

In the 1950s, Pappenheimer, Renkin, and Borrero[200,201,214] performed the pioneering theoretical and experimental work which lay the foundation for much of the progress in modeling restricted transport in pores. The results from these early studies are somewhat limited in their application to glomerular filtration in that the blood vessel and extravascular space were each taken to be well-mixed reservoirs. The dependence of transport on afferent plasma flow rate and on the gradients of concentration, flux, and osmotic pressure in the capillary were not considered until the cross-flow filtration models of the 1970's.[62,81] This more complete modeling was coupled with increased

sophistication in the theoretical analysis of the restricted transport of solid spheres in cylindrical pores.[5,42,47]

The pore model originally derived by Chang *et al.*[62] is summarized below. Additional models based on alternative membrane geometries or without the assumption of any particular membrane structure (nonequilibrium thermodynamics) have been proposed,[62,200] but none have had extensive application.

2.6.4 Isoporous Solid-Sphere Model of Permselectivity

In the simplest model, the capillary walls are assumed to be perforated by right cylindrical pores with pore radius $r_p = r_0$ (Figure 2-3). Capillary flow occurs along direction y while filtration is conducted in direction x. The porosity of the membrane (equal to the fractional pore area of the membrane surface) is given by f and the total membrane surface area is S. The plasma and glomerular filtrate are modeled as aqueous continua into which salts, proteins, and various tracer molecules are dissolved. The tracer molecule concentration c_T is small so that it does not contribute to osmotic pressure or to electrostatic interactions within the membrane. Traditionally, all solute molecules are assumed to behave as spheres with a radius equivalent to that of the Stokes-Einstein radius

$$r_s = \frac{k_B T}{6\pi\mu\mathcal{D}_i}, \tag{2.12}$$

where k_B is Boltzmann's constant and T is the absolute temperature at which the solvent viscosity μ and diffusion coefficient $\mathcal{D}_i$ are measured.

The solute flux $J_i(y)$ of a neutral macromolecule through the pores is governed by both diffusional and convective forces and is given by[62]

$$J_i(y) = \frac{J_v(y)c_i(y)W_i}{1 - e^{-Pe(y)}(1 - W_i)}, \tag{2.13}$$

$$Pe(y) = \frac{W_i J_v \ell}{f H_i \mathcal{D}_i} = \frac{W_i(SJ_v)}{(fS/\ell)H_i\mathcal{D}_i}, \tag{2.14}$$

where $c_i(y)$ is the solute concentration in the capillary, ℓ is the thickness of the membrane (the length of the pore), $\mathcal{D}_i$ is the diffusion coefficient of the solute in bulk solution, f is the fractional porosity of the wall, and H_i and W_i are solute pore hindrance factors for diffusion and convection, respectively.

The Peclet number $Pe(y)$ is a dimensionless quantity indicating the relative magnitude of the convective to diffusive forces driving the solute through the pore. The second equality in Eq. 2.14 is written to emphasize that parameters related to the physical dimensions and porosity of the membrane—f, S, and ℓ—are not explicitly known. Only fS/ℓ must be calculated, and for an array

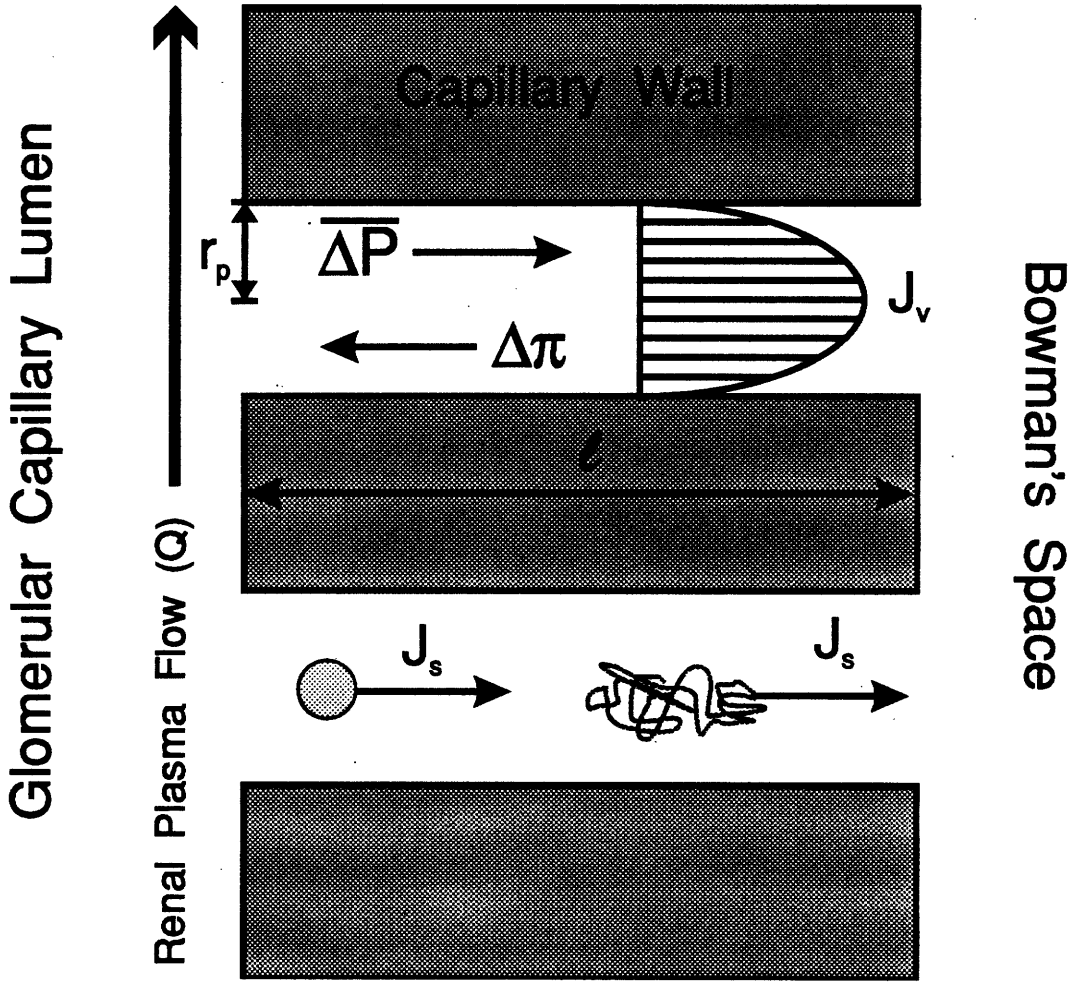

Figure 2-3: Pore model of glomerular permselectivity. Renal plasma flow (Q) is parallel to the inner surface of the glomerular capillary wall. Cross-flow filtration from the capillary is assumed to be conducted through pores of radius r_p and length ℓ in the wall. Filtration is governed by opposing hydraulic ($\overline{\Delta P}$) and osmotic ($\Delta\pi$) pressure differences, resulting in the net flux of both solvent (J_v) and solute (J_s) into Bowman's space. Possible solute configurations include those of a solid sphere (*bottom pore, left*) or a flexible coil (*bottom pore, right*).

of uniform cylindrical pores it can be shown from the Poiseuille equation[62] that

$$\frac{fS}{\ell} = 8K_f\mu/r_0^2 \tag{2.15}$$

where μ is the viscosity of the solvent passing through the pores.

Methods for calculation of the hindrance factors H_i and W_i are reviewed in depth by Deen.[76] They will be summarized here and will be discussed in greater detail in Chapter 5. Briefly, H_i and W_i are functions of the relative molecule-to-pore size dimensions. In the absence of energetic interactions, they equal one for small, freely filtered molecules and equal zero for molecules completely excluded from the pores. Hindrance factors can be approximated as the product of a steric term (the partition coefficient Φ or its convective equivalent Ω), which accounts for the difference between the solute concentration in the capillary lumen and that in the pore, and a hydrodynamic term (the inverse enhanced drag coefficient K^{-1} or the lag coefficient G), a measure of the increased frictional force the molecule experiences in moving through the pore:

$$H_i \approx \Phi K^{-1}, \tag{2.16}$$

$$W_i \approx \Omega G. \tag{2.17}$$

For a solid-sphere in a cylindrical pore, expressions of Bungay and Brenner[47] are most commonly used:

$$H = \frac{6\pi\Phi}{K'_t}, \tag{2.18}$$

$$W = \frac{K'_s\Phi(2-\Phi)}{2K'_t}, \tag{2.19}$$

$$K'_t = \frac{9}{4}\pi^2\sqrt{2}(1-\lambda_s)^{-5/2}\left[1-\frac{73}{60}(1-\lambda_s)+\frac{77,293}{50,400}(1-\lambda_s)^2\right] - 22.5083 - 5.6117\lambda_s - 0.3363\lambda_s^2 - 1.216\lambda_s^3 + 1.647\lambda_s^4, \tag{2.20}$$

$$K'_s = \frac{9}{4}\pi^2\sqrt{2}(1-\lambda_s)^{-5/2}\left[1-\frac{7}{60}(1-\lambda_s)+\frac{2227}{50,400}(1-\lambda_s)^2\right] + 4.0180 - 3.9788\lambda_s - 1.9215\lambda_s^2 - 4.392\lambda_s^3 + 5.006\lambda_s^4, \tag{2.21}$$

where the partition coefficient $\Phi = (1-\lambda_s)^2$.

The sieving coefficient of the solute is calculated by performing mass balances on the total volume flux and protein flux as described in Section 2.5.1, plus an additional balance on solute flux:

$$\frac{d(Qc_i)}{d\hat{y}} = -SJ_i(\hat{y}). \tag{2.22}$$

Eq. 2.22 is numerically integrated along the length of the capillary using Eq. 2.13. The average solute

concentration in Bowman's space, $\langle c_{i,B} \rangle$, and the sieving coefficient, Θ_i, may then be calculated from

$$\langle c_{i,B} \rangle \equiv \frac{Q_A c_{i,A} - Q_E c_{i,E}}{SNGFR} \tag{2.23}$$

$$\Theta_i \equiv \frac{\langle c_{i,B} \rangle}{c_{i,A}} \tag{2.24}$$

where $c_{i,A}$ and $c_{i,E}$ are the solute concentrations in the afferent and efferent arterioles.

The nature of the boundary condition in Bowman's capsule is worth some discussion. If Bowman's space is considered well-mixed, then the appropriate boundary condition would be

$$c_i(\ell, y) = \langle c_{i,B} \rangle = \Theta_i \cdot c_{i,A} \tag{2.25}$$

This was the original assumption employed by Chang *et al.*.[62] Deen *et al.*,[83] using an analysis of characteristic times based on the dimensions of Bowman's space, concluded that the well-mixed assumption was probably not valid and that a preferable condition was spatially-dependent:

$$c_i(\ell, y) = \frac{J_i(y)}{J_v(y)}. \tag{2.26}$$

Du Bois *et al.*,[89] showed that the theoretical sieving coefficients for these two cases are not substantially different when the model assumes no axial pressure drop in the capillary. If, however, such a pressure drop is included, relatively significant differences in predicted sieving coefficients occur for small solutes ($r_s < 30$ Å): Θ_i using Eq. 2.26 was 5-10% lower than for the well-mixed case.

2.6.5 Heteroporous Models

The principal failing of the simple isoporous model is that it predicts a sharp cutoff of Θ at $r_s = r_0$. Typical values for r_0 are 45–50 Å in the rat, yet small but significant filtration of macromolecules with $r_s = 60$ Å or greater occurs. Deen *et al.*[79] addressed this discrepancy by comparing various heteroporous models. Recent work has centered around two approaches: a continuous *lognormal* distribution of pore sizes and the so-called *isoporous + shunt* distribution, which postulates a small number of infinitely-sized pores in parallel with the isoporous membrane. Both of these models require two parameters to describe membrane size-selectivity, as opposed to the one-parameter isoporous membrane. They are discussed in more detail in Section 4.2.5 and Appendix B.

Additional models based on principles of distribution moments[145,146] or on non-equilibrium thermodynamics[62,200] have been proposed, but none have received extensive application in analysis of glomerular sieving.

2.6.6 Pathophysiological Behavior of Permselectivity Parameters

Permselectivity changes in clinical disease states are usually characterized by a loss of both size- and charge-selective properties. The size changes are manifested in the theoretical model as larger values of the pore radius parameters. For neutral dextrans, a characteristic pattern in deviations from normal sieving behavior is seen in almost all cases, both animal and clinical: sieving coefficients of small-to-medium sized molecules are normal or slightly lowered, while Θ for large ($r_s > 50$ Å) molecules are elevated. This pattern is generally consistent with an increased filtration pressure and/or decreased K_f and an increased number of large pores compared to controls. These changes have been observed in NSN,[60] PAN nephrosis,[13,199] adriamycin nephrosis,[252] Heymann's nephritis,[262] renal ablation,[198] clinical diabetes,[49,101,187,242,255] and minimal change disease.[79] One model where it has not yet been documented is for experimental diabetes, where studies of STZ- and alloxan-induced diabetes showed no change in sieving from controls.[177,205] It must be noted, however, that in these two studies the maximum dextran size measured extended only up to around 48 Å, and so it is quite probable that larger sizes must be examined to demonstrate the larger shunt.

2.6.7 Charge Selectivity

To date only limited modeling of the charge-selective properties of the glomerular capillary wall has been performed. Deen *et al.*[83] superimposed a homogeneous charge distribution on the isoporous model and, based on studies of anionic dextran sulfate and cationic DEAE-dextran, calculated a charge density of around -165 mEq/l for the normal capillary wall. Studies of charge permselectivity have also been relatively limited in number. A significant increase in the fractional clearance of dextran sulfate has been shown in both NSN and PAN nephrosis,[20,29] as well as a inhibition of cationic DEAE dextran transport in NSN.[28] These alterations have been correlated to reductions in the fixed membrane charge from -165 mEq/l to -25 and -100 mEq/l for NSN and PAN, respectively.[83] Interpretation of this data is made difficult by recent findings that dextran sulfate binds to albumin *in vivo*.[174] Hence, while the qualitative conclusions of lost charge selectivity are still valid, quantitation based on dextran sulfate data probably is not. A suitable charged test molecule for evaluation of capillary charge selectvity remains to be developed.

Chapter 3

Calibration of Gel Permeation Chromatography Columns with Narrowly-Sized Polymer Standards

3.1 Introduction

If sieving curve analysis is to be used to estimate filtration pressures, great care must be taken to minimize methodological errors in the determination of tracer size and concentration. Two possible sources of error in gel chromatography which have not been previously considered in great detail are the calibration of the chromatography columns and the effect of column dispersion on the elution profiles.

3.2 Theory of Gel Chromatography and Column Calibration

Separation of infused polymers into narrow fractions is performed by gel permeation chromatography (GPC). The sample is eluted through a column packed with a porous material which will allow small molecules access to the interstitial volume while excluding large molecules. Smaller molecules will thus be retained longer in the column. Solute molecules are sized according to K_t, the fraction of the column volume to which they have access, or by K_{av}, a commonly-used approximation for K_t:

$$K_t = \frac{V_e - V_0}{V_t - V_0 - V_s}, \tag{3.1a}$$

$$K_{av} = \frac{V_e - V_0}{V_t - V_0}, \tag{3.1b}$$

where V_e is the elution volume of the solute, V_0 is the void volume (the solvent volume external to the gel beads), V_t is the total column volume, and V_s is the volume of the gel stationary phase. K_{av} is more frequently used because values for V_s are generally not available. A solute completely excluded from the packing interstitium (such as Blue Dextran 200, m.w.$= 2 \times 10^6$ daltons) will have a K_{av} of 0, while solvent or molecules with unrestricted passage into the stationary phase will have a K_{av} near 1, with the difference from unity due to V_s.

Determination of the Stokes-Einstein radius (r_s) of polysaccharide fractions is traditionally done with calibration curves derived from globular protein standards. The assumption is that for polysaccharides $r_s = \tilde{r}_s$, where $\tilde{r}_s$ is the Stokes-Einstein radius of a globular protein with the same K_{av}. Chang *et al.*[63] found that r_s for commercial dextrans T10 and T20 preparations correlated well with a linear calibration plot of K_{av} vs. $\ln \tilde{r}_s$ on Sephadex G-100 columns.

More recently, however, work by Jørgensen and Møller[139] on Sephadex G-200 columns and by

Squire[232] and Frigon *et al.*[102] on silica gel (TSK-SQ) columns indicates that protein calibration is not a suitable method of determining dextran size. In both of these studies, dextran samples were seen to have smaller values for r_s than proteins at equivalent K_{av}. In other words, dextrans on these columns were more excluded from the gel interstitium than proteins and $r_s < \tilde{r}_s$. The magnitude of this difference in silica gels is on the order of 10-20% for mid-sized dextrans (15-40 Å).[102] In contrast, another study by Deen *et al.*[77] employing Sephadex G-100 columns showed discrepancies in the opposite direction ($r_s > \tilde{r}_s$).

Frigon *et al.*[102] corrected for configurational effects using a model of Benoit *et al.*[21] in which an effective hydrodynamic volume v_h is employed as the metric of molecular size. This volume is given by

$$v_h = \frac{M[\eta]}{\nu N_A}, \tag{3.2}$$

where M is the molecular weight of the polymer, $[\eta]$ is the intrinsic viscosity, ν is a shape factor equal to 2.5 for spherical particles, and N_A is Avogadro's number. Values for $[\eta]$ for protein were taken from the literature, while those for dextrans were calculated from an empirical relationship to molecular weight. Thus v_h for spherical particles scales as $[\eta]M$. When $[\eta]M$ was substituted for r_s in the calibration, differences between proteins and dextrans were diminished.

In the study by Frigon *et al.*,[102] the values for dextran r_s were based on measurements by Granath[119] in a diffusion cell. The Frigon study neglected to account for the fact that the dextran fractions used by Granath were not monodisperse, with polydispersity indices (defined as the weight-averaged molecular weight divided by the number-averaged molecular weight) ranging from 1.09 to 1.8, with most around 1.3–1.4. Thus their correlation of molecular weight to r_s may not have been particularly accurate.

More importantly, there is evidence that the Benoit hydrodynamic volume model does not completely explain gel permeation phenomena. Data by Belenkii *et al.*[19] on Sephadex columns indicates that dextran and polyvinylpyrrolidone are less excluded (have higher retention volumes) than polyethylene oxide at equivalent hydrodynamic volumes. Since all three molecules have random-coil configurations, the lack of agreement suggests that additional mechanisms such as solute-gel interactions may be important.

It would seem logical to expect that the behavior of macromolecules in gel exclusion would follow the observed sieving trends in the glomerulus; that is, that dextrans, which experience a more facilitated transport through the glomerulus than neutral globular proteins of equivalent Stokes-Einstein radius,[216] would also be retained to a greater extent in the stationary phase of the gel beads. While this appears to be true for the data of Deen *et al.*[77] and Belenkii *et al.*,[19] the reverse holds for the data of Frigon *et al.*[102] and Jørgensen and Møller.[139] It therefore appears that the degree and manner to which molecular configuration influences retention volume is dependent upon the type of gel matrix in the column. Of particular note, the Belenkii *et al.* results, where dextran and

PVP show similar degrees of transport into the gel and are less restricted than PEO, are consistent with findings in glomerular filtration.[139,246]

The consequences of calibration errors on the analysis of sieving curves are shown in Figure 3-1. The shifting of a sieving curve along the r_s axis by calibration errors will lead to errors in fitted pore parameters and, when performed, to fitted filtration pressures ($\overline{\Delta P}$). The baseline curve, shown by the solid line, was calculated directly from the isoporous solid-sphere model with $r_0 = 50$ Å, $\overline{\Delta P} =$ 35 mm Hg, and the other hemodynamic inputs as described in Figure 3-1. The dotted lines are the same data as the solid line, but shifted 2 and 4 Å to the left, equivalent to a calibration error where $r_s > \tilde{r}_s$. Values of r_0 and $\overline{\Delta P}$ were then fit to the shifted curves using the methods of Section 7.3.1. The error in r_0 is seen to be approximately equal to and in the same direction as the calibration error, while the the fit overestimates $\overline{\Delta P}$ by 8 mm Hg or more. The dashed lines show analogous results for $r_s < \tilde{r}_s$. Again, the r_0 error scales with the calibration error, but the $\overline{\Delta P}$ error is an underestimation on the order of 5 mm Hg.

A possible discrepancy of 5 to 10 Å in r_s is thus seen to be of enough significance to warrant a more accurate way of sizing the polymers. Since it will not be feasible to routinely calibrate with narrowly sized fractions, it is proposed instead to develop simple correction functions from protein calibration curves.

The most direct way to determine correct molecular sizes is to calibrate the GPC columns using narrow molecular weight-range fractions of the polymers of interest. We report in Section 3.6.1 a comparison of calibration results obtained with proteins or with nearly monodisperse dextran or Ficoll standards using Sephadex G-100 and Sephacryl S-300 HR columns. The r_s values of the various dextran and Ficoll samples were measured using quasielastic light scattering, and correlations of r_s versus molecular weight are given for both polymers. We also derive correction factors that may be used in conjunction with protein calibrations of this type of column.

3.3 Effect of Column Dispersion on Sieving Curves

Dispersion causes backmixing as the sample elutes through the column and decreases the resolution of the fractionation. For a monodisperse sample, dispersion leads to broadening of the elution peak; for a polydisperse sample, it causes a "smearing" of the elution profile. The phenomenon is described by a modified diffusion equation:

$$\frac{\partial \bar{c}}{\partial t} = \mathcal{K} \frac{\partial^2 \bar{c}}{\partial z^2}. \tag{3.3}$$

where $\bar{c}$ is the concentration averaged over the column cross-section, t is time, $\mathcal{K}$ is the Taylor dispersion coefficient, and z is axial position in the frame of reference of the moving solute, with $z = 0$ corresponding to the solute peak concentration. The solution for a pulse input at the top of

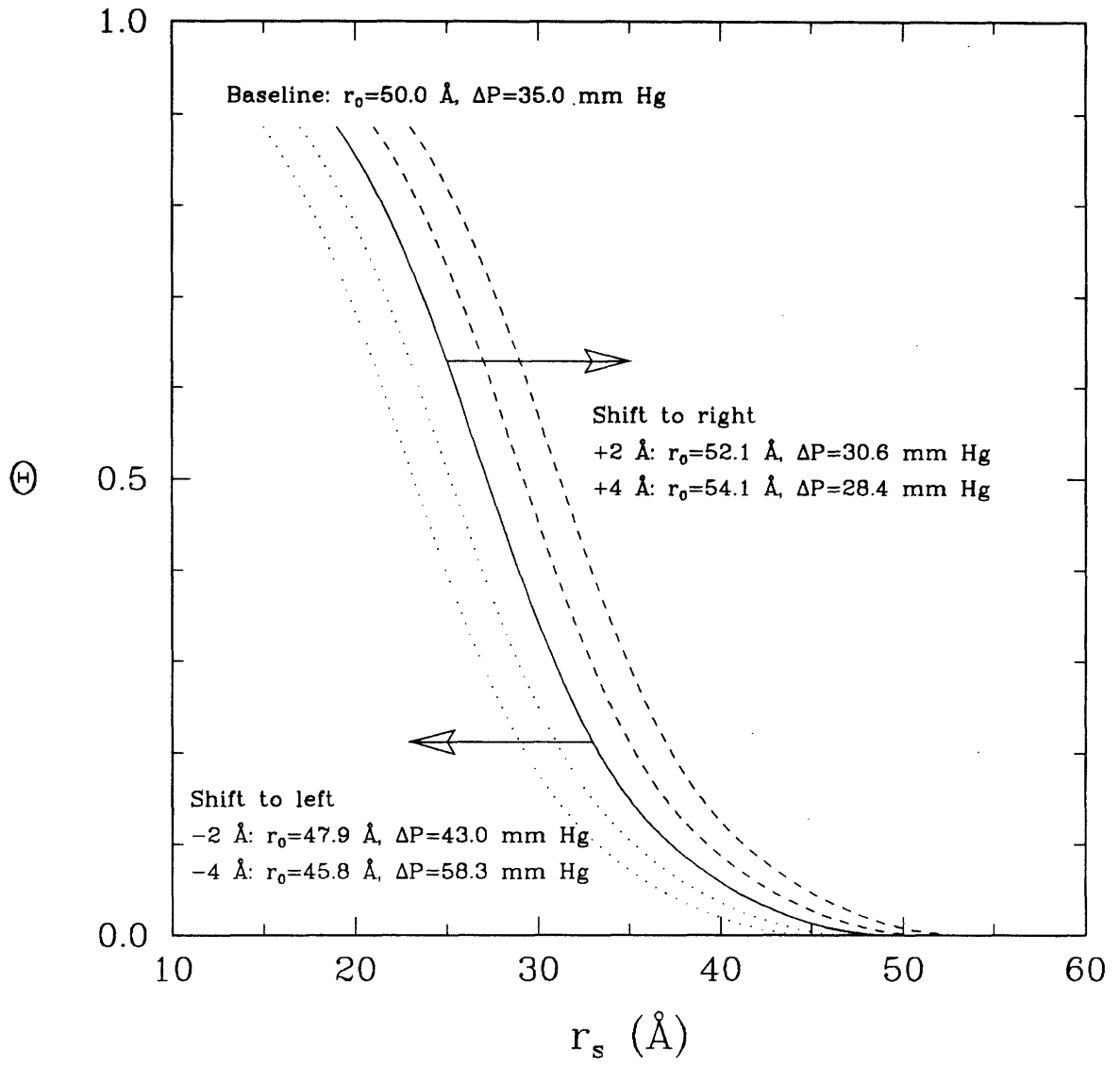

Figure 3-1: Theoretical effect of a shift in sieving curve due to r_s calibration error. The other hemodynamic inputs are Q_A =172 nl/min, $SNGFR$ =49.8 nl/min, $c_{p,A}$ = 5.2 g/dl. The baseline case is shown by the solid line. Dotted lines demonstrate shifts to the left of 2 and 4 Å, dashed lines indicated analogous shifts to the right. New values for r_0 and $\overline{\Delta P}$ were fitted for the shifted curves using the isoporous, solid-sphere model.

the column is[9,238]

$$\bar{c} = \frac{A/\pi R_c^2}{\sqrt{4\pi \mathcal{K} t}} \exp\left[-\frac{z^2}{4\mathcal{K}t}\right], \tag{3.4}$$

where A is the amount of solute in the pulse and R_c is the column radius. For fully developed laminar flow in an open tube, the dispersion coefficient can be shown analytically to be equal to $\mathcal{D} + (UR_c)^2/48\mathcal{D}$, where U is the average fluid velocity in the column.[69] Several theories exist for describing the functional dependence of $\mathcal{K}$ for gel columns,[122,260] but all rely on some degree of empiricism.

The theoretical effect of dispersion on column elution is shown in Figure 3-2. As a first approximation, data from typical plasma and urine elution curves in Sephacryl 300-HR columns were used as the inputs into a theoretical column. (Rigorous analysis would require use of the data as output and calculation of the input by deconvolution.) The quantity of labeled tracer was measured in counts per minute per microliter of sample. Input samples were modeled as a combination of discrete pulses with sizes corresponding to elution volumes 3 ml apart (equal to the volume collected in each tube of the fractionator). With no spreading in the column ($\mathcal{K} = 0$, solid lines) there is perfect separation and the elution curves are exactly the same as the size distribution of the samples. For a dispersion coefficient of 10^{-4} cm^2/s, there is minimal deviation of the elution curves from perfect separation. In the plasma sample, the deviation is -0.6% at 20 Å, -4.8% at 40 Å, and 2.3% at 60 Å. In urine, the respective deviations are 1.6%, 4.2%, and 8.3%. For $\mathcal{K} = 10^{-3}$ cm^2/s, dispersive effects become more noticeable, especially for the urine sample, leading to a "flattening" of the profiles. The deviations in the plasma samples are -0.6%, -18.3%, and 17.8% at 20, 40, and 60 Å, respectively, and for urine the deviations are -10.5%, 47.3%, and 144%, respectively. Because the plasma profile is more nearly constant than the urine profile, it is less affected by dispersion. (Values for Θ were calculated from Eq. 4.1 with the inulin ratio and protein correction factor given in Figure 3-3.) The effect of dispersion on the resultant sieving curve is shown in Figure 3-3. The sieving curve is altered in a manner similar to that of the urine profile, with values lowered at small r_s and raised at large r_s. Again, dispersion coefficients of 10^{-4} are not significant, changing Θ by 2%, 9.4%, and 6% at 20, 40, and 60 Å, respectively, while those of 10^{-3} noticeably affect the sieving curve, changing Θ by -10.1%, 80.5%, and 107%.

3.4 Effect of Elution Volume Errors on Sieving Curves

A final possible source of error is in the measurement of elution volume. If the error is the same for both plasma and urine samples (*i.e.*, V_e is incorrectly measured by the same amount), then the effect is equivalent to that of an r_s calibration error. Alternatively, there may be a relative "tube shift" error (so called because the elution volumes are collected into numbered tubes), where V_e for one sample does not correspond to V_e for the other. This situation is examined in Figure 3-4. The

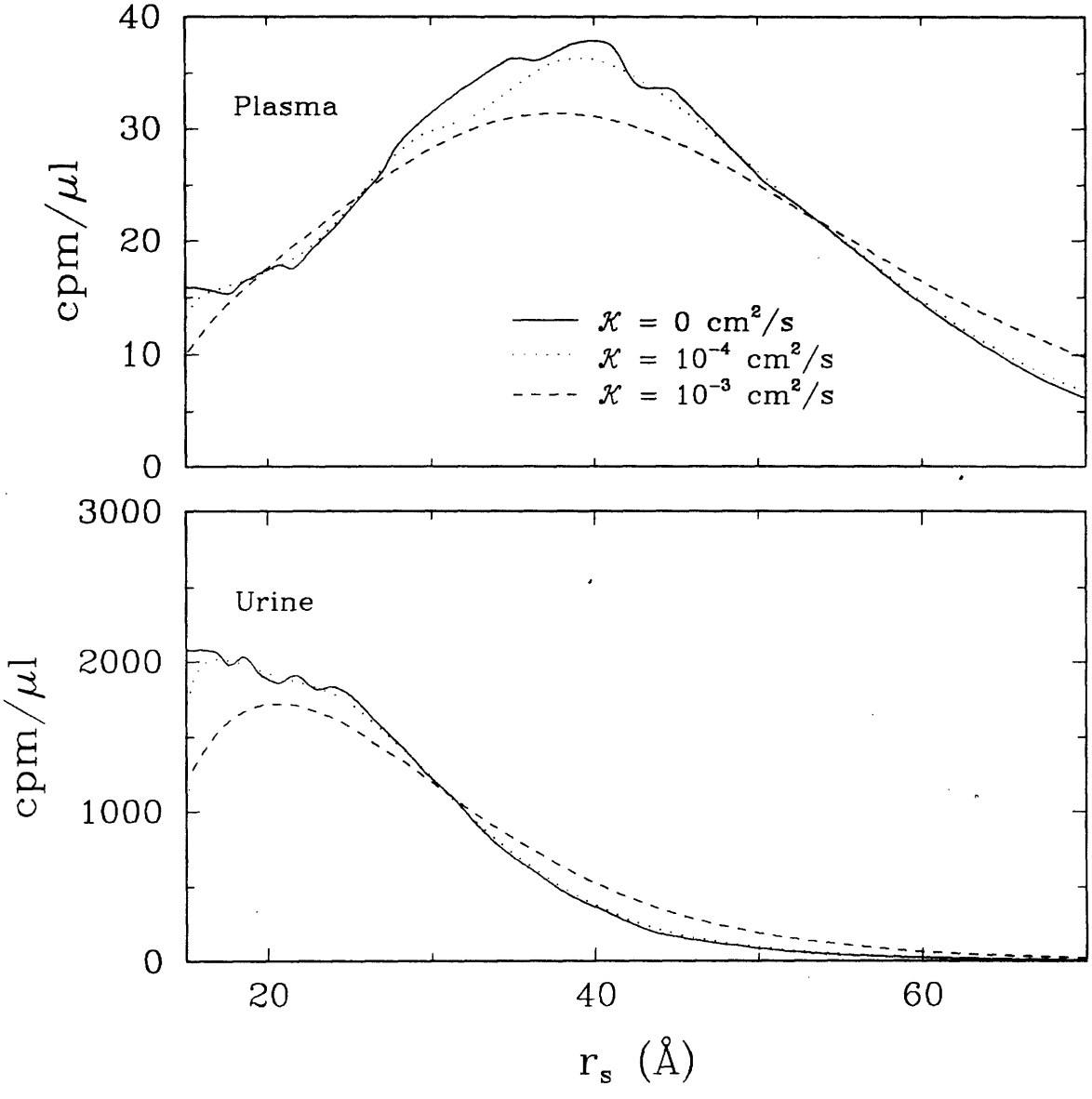

Figure 3-2: Theoretical effects of column dispersion on plasma and urine elution curves. Curves calculated using column height = 56 cm, R_c = 1.3 cm, and solvent velocity = 0.0126 cm/s. The fluctuations in the solid lines represent normal scatter in the data

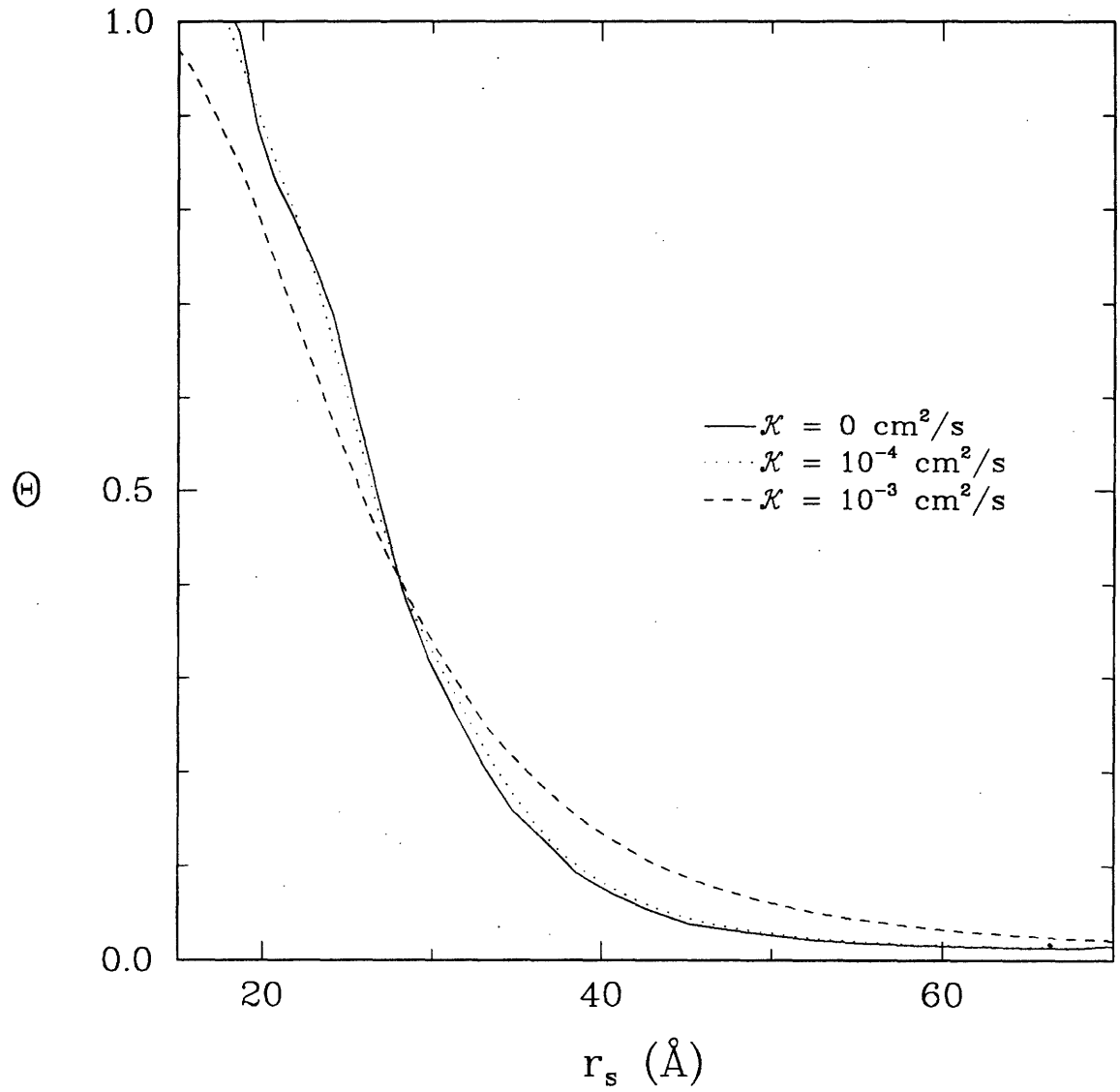

Figure 3-3: Theoretical effects of column dispersion on sieving curves. Sieving coefficients calculated from Eq. 4.1 using plasma and urine elution curves of Figure 3-2 and $(U/P)_{\text{inulin}} = 119.03$, $f' = 0.95$.

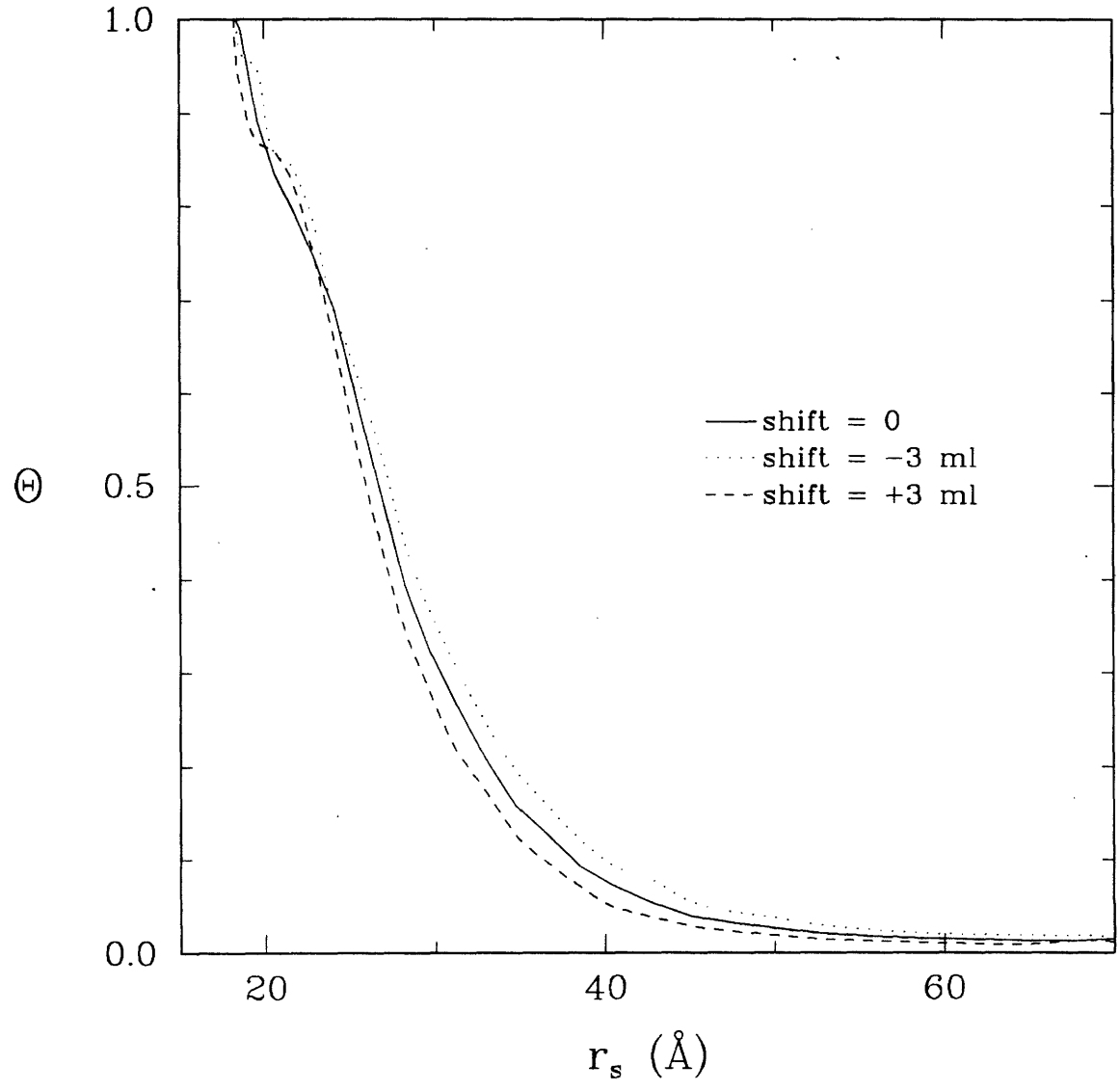

Figure 3-4: Theoretical effects of "tube shift" on sieving curves. Θ calculated as in Figure 3-3. Shift is denoted by a change in urine V_e from the zero shift case. Curve for zero shift is the same as the $\mathcal{K} = 0$ curve of Figure 3-3.

Polymer	Sample ID	M_w	M_n	M_w/M_n	r_s (Å)
Dextran	FDR 7314+403 Fr 4	87,500	76,700	1.14	72
	70 Fr I-1	72,100	62,600	1.15	64
	FDR 7314+403 Fr 8	53,300	48,100	1.11	58
	FDR 7314 Fr 22	41,200	38,000	1.08	52
	RMI T8630 Fr 3	40,400	38,900	1.04	47
	FDR 7314 Fr 32-36	25,600	24,200	1.06	42
	FDR 7314 Fr 32	25,600	24,200	1.06	41
	T5558+7650 Fr 2	10,000	9,200	1.09	26
	PD T5558 Fr 10	9,860	9,430	1.05	26
	T5558+7650 Fr 5	4,300	3,880	1.11	20
Ficoll	T1800 Fr 20	132,000	—	—	69
	T2580-IVB Fr 2	71,800	64,600	1.11	49
	T2580-IVB Fr 4	58,700	53,000	1.11	44
	T2580-IVB Fr 8	37,500	34,500	1.09	35
	T2580-IVB Fr 11	21,800	20,300	1.07	29
	T2580-IVB Fr 12	17,500	16,200	1.08	30

Table 3.1: Polymer standards used for GPC calibration. *Abbreviations*: M_w—weight-averaged molecular weight, M_n—number-averaged molecular weight. Sample ID, M_w, and M_n are those provided by manufacturer. Values of r_s were determined by quasi-elastic light scattering.

$K = 0$ case of Figure 3-3 is used as the baseline case. Shifting the urine elution curves by 3 ml (equivalent to one tube volume for the experiments of this work) in either direction is seen to have a small effect on Θ. The deviation from baseline is around 5% at 20 Å and 30% at 40 and 60 Å. This will be true as long as the tracer distribution in the plasma is relatively uniform, as in Figure 3-2. If the plasma profile has significant gradients, then tube shift effects will be large in the region of the gradients.

3.5 Materials and Methods

3.5.1 Polymer Standards

Ten relatively monodisperse samples of dextran and six of Ficoll were obtained courtesy of Dr. Kirsti Granath of Pharmacia, Uppsala, Sweden. The weight-averaged molecular weights (M_w) and number-averaged molecular weights (M_n), as supplied by Dr. Granath, are given in Table 3.1. The polydispersity index (M_w/M_n) for all samples was ≤ 1.15.

3.5.2 Quasi-elastic Light Scattering

The diffusion coefficients ($\mathcal{D}$) for the dextran and Ficoll standards were measured by quasielastic light scattering. Polymer samples (2 or 5 mg/ml) were prepared by dissolving dextran or Ficoll in high-purity water (MilliQ, Millipore Corporation, Bedford, MA) and filtering the solution five

times through 0.22 μm pore diameter films. (Millex-GV, Millipore). The light scattering apparatus consisted of a 2 W argon-ion laser (Model-95-2 Ion Laser, Lexel, Fremont, CA), goniometer (Model BI-2000 SM, Brookhaven Instruments Corp., Holtsville, NY,), and 136-channel digital correlator (Model BI-2030 AT, Brookhaven Instruments). The sample temperature was maintained at 25 °C by a circulating water bath (System II Liquid/Liquid Recirculator, Neslab, Newington, NH). The wavelength of the measured light was 488 nm, the aperture was 200 nm, and the scattering angle was 135°. Sampling time varied from 01. to 0.5 μs, depending on molecular weight, with a total counting time of one minute. Diffusion coefficients were fitted to the autocorrelation function by a second-order cumulant method.[147]

The Stokes-Einstein radius r_s is related to $\mathcal{D}$ by

$$r_s = \frac{k_B T}{6\pi\mu\mathcal{D}}, \tag{3.5}$$

where k_B is Boltzmann's constant, T is absolute temperature, and μ is the viscosity of water.

3.5.3 Gel Permeation Chromatography

A set of GPC columns of 2.6 cm diameter (Model C 26/100, Pharmacia Fine Chemicals, Piscataway, NJ) was packed with Sephacryl S-200 HR (Pharmacia). The packed column height was 56 cm and a buffer flow rate of 3.8–4.0 ml/min was maintained by a peristaltic pump (2232 Microperpex S, LKB, Bromma, Sweden). The eluent buffer was 0.05 M ammonium acetate at pH 7. The void volume (V_0) of the columns was determined by the elution of blue dextran (Sigma Chemical Co., St. Louis, MO). Continuous dextran and Ficoll elution curves were determined by differential refractometry (Series R-400 Differential Refractometer, Waters Associates, Milford, MA). The elution volumes of colored proteins were measured by collection of 3 ml aliquots in an automatic fraction collector (2070 Ultrorac II, LKB) and reading of light absorbance at 415 nm (DU-50 Spectrophotometer, Beckman Instruments, Fullerton, CA). The proteins used were ferritin (horse spleen), horseradish peroxidase, myoglobin (horse heart), and cytochrome c (horse heart) (Sigma Chemical). Based on published diffusivities,[54,171,219,239] their molecular radii were taken to be 59.4, 30.4, 19.0, and 16.5 Å, respectively.

A second set of columns of 2.5 cm diameter were packed with Sephadex G-100 (Pharmacia) to a column height of 46.5 cm. As a pump could not be used with this packing, elution was performed by a constant pressure head of 90 cm of water. Four ml aliquots of dextran, Ficoll, and protein elutions were collected in the fraction collector. Dextran and Ficoll elution peaks were determined by batch refractometry and protein peaks were determined by absorption.

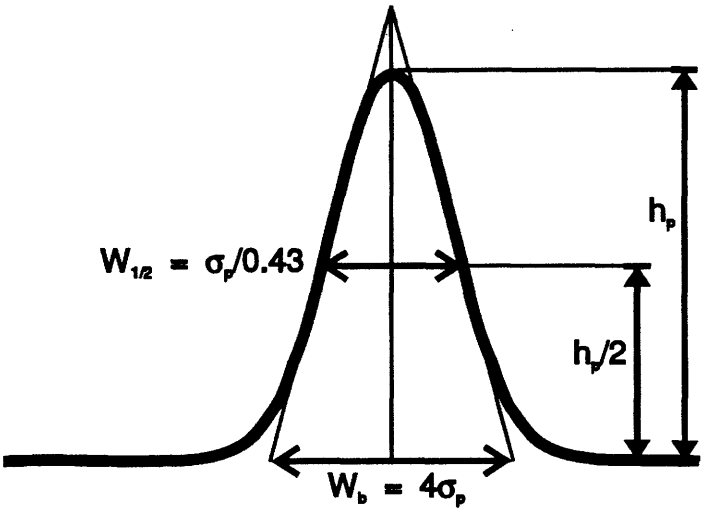

Figure 3-5: Graphical method of calculating peak variance.

3.5.4 Calculation of Dispersion Coefficients

Dispersion coefficients were calculated graphically from the elution peaks. Each peak was assumed to approximate a Gaussian curve, and the variance σ_p for each peak was calculated by measurement of either W_b or $W_{1/2}$ as shown in Figure 3-5.[260] The dispersion coefficient is then given by[10]

$$\mathcal{K} = \frac{\sigma_p^2}{2t_e}. \tag{3.6}$$

This method is strictly true only for a monodisperse pulse. Any polydispersity in the sample will also contribute to widening of the peak, so the values reported are in fact upper limits for $\mathcal{K}$.

3.6 Results and Discussion

3.6.1 Quasi-elastic Light Scattering

The values of r_s obtained by quasielastic light scattering are shown in Table 3.1, and are plotted as a function of M_w in Figure 3-6. The dependence of r_s on M_w is described to within 9% by the correlations

$$r_s = 0.488 M_w^{0.437} \text{for dextran} \tag{3.7a}$$

$$r_s = 0.421 M_w^{0.427} \text{for Ficoll} \tag{3.7b}$$

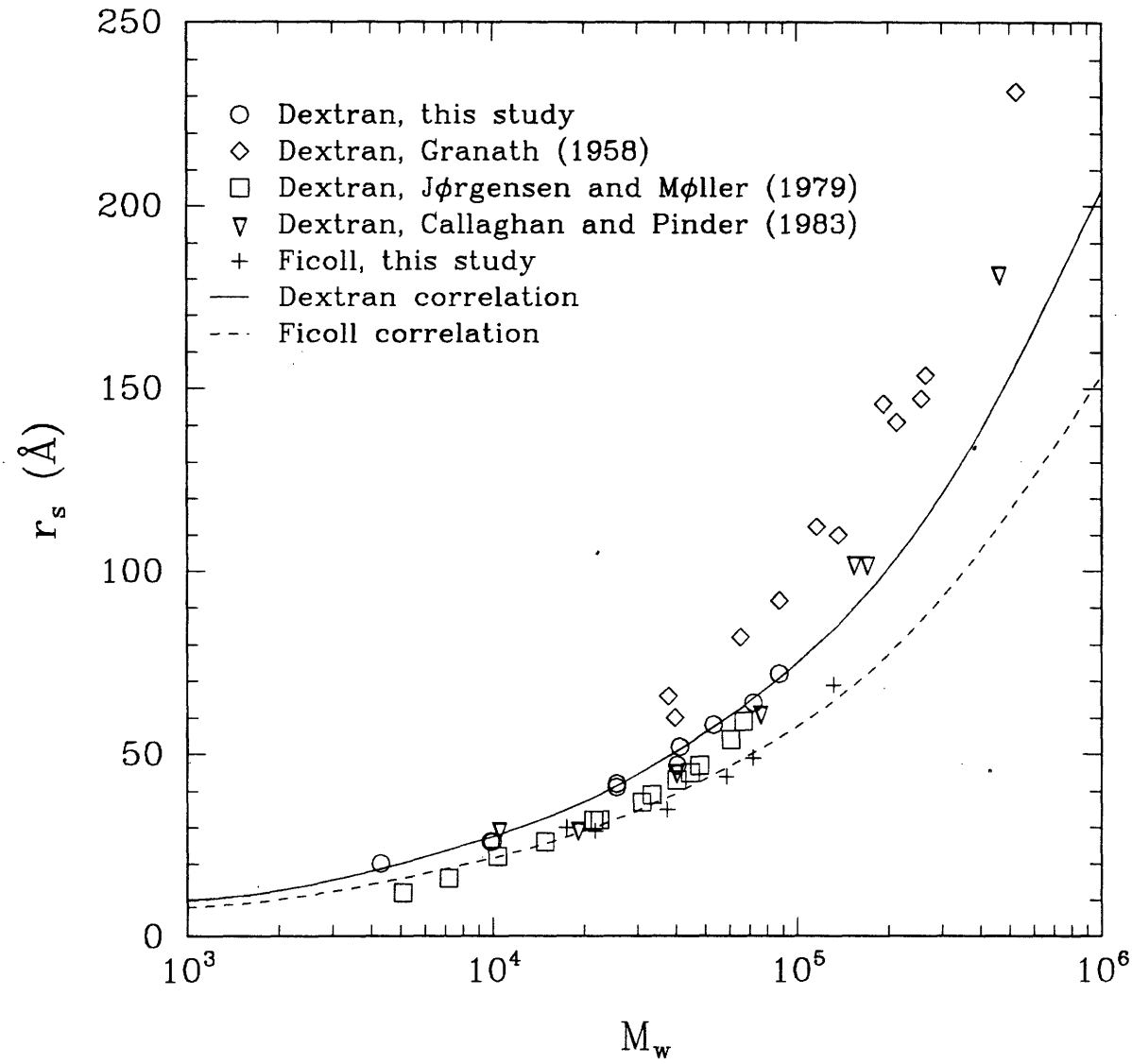

Figure 3-6: Stokes-Einstein radius (r_s) of dextran and Ficoll as a function of weight-average molecular weight (M_w). The present results for dextran are compared with those from the literature.[48,119,139] The curves are correlations given by Eqs. 3.7.

Gel	Polymer	a	b
Sephacryl S-300 HR	Dextran	0.3150	1.522
	Ficoll	0.2924	1.438
	Proteins	0.3048	1.458
Sephadex S-100	Dextran	0.5798	2.277
	Ficoll	0.6330	2.407
	Proteins	0.5543	2.135

Table 3.2: Constants in correlations of K_{av} versus r_s (Eq. 3.8).

where r_s is given in Å.

Also shown in Figure 3-6 are r_s values reported previously for dextran using three different methods. The data of Granath[119] were obtained by measurements in a diffusion cell, Callaghan and Pinder[48] used pulsed field gradient NMR, and Jørgensen and Møller[139] used analytical centrifugation. The first two of these studies used commercial dextran fractions having significant polydispersity ($M_w/M_n > 1.3$), while Jørgensen and Møller used narrow fractions comparable to those employed here. Our results for dextran coincide fairly closely with those of Callaghan and Pinder[48] and Jørgensen and Møller,[139] while the r_s values of Granath[119] are larger at any given value of M_w. For the same M_w the Stokes-Einstein radius of Ficoll tends to be somewhat lower than that for dextran. There appear to be no previously published data for r_s versus M_w for Ficoll.

3.6.2 Gel Permeation Chromatography

The calibration results for the Sephacryl and Sephadex columns are shown in Figure 3-7 as semilog plots of K_{av} versus r_s. Unlike the columns used by Jørgensen and Møller[139] and Frigon *et al.*,[102] the differences between protein and polysaccharide elution volumes on Sephacryl S-300 HR columns are fairly small. The differences are also small for Sephadex G-100 columns, in agreement with the previous measurements by Chang *et al.*[63]

The best-fit lines for the data in Figure 3-7 are of the form

$$K_{av} = -a \ln r_s + b, \tag{3.8}$$

with r_s expressed in Å. The values of the constants a and b for the various polymers and gel materials are given in Table 3.2 These results may be used to derive correction factors for r_s of dextran or Ficoll which compensate for the use of proteins as the calibration standard. These correction factors, defined as $\Delta = r_s - \tilde{r}_s$, are shown in Figure 3-8 for dextran and Ficoll. As shown, Sephacryl S-300 HR columns calibrated with proteins would yield slight underestimates of r_s for both dextran and Ficoll ($\Delta > 0$), while such calibrations on Sephadex G-100 would also underestimate r_s for dextran

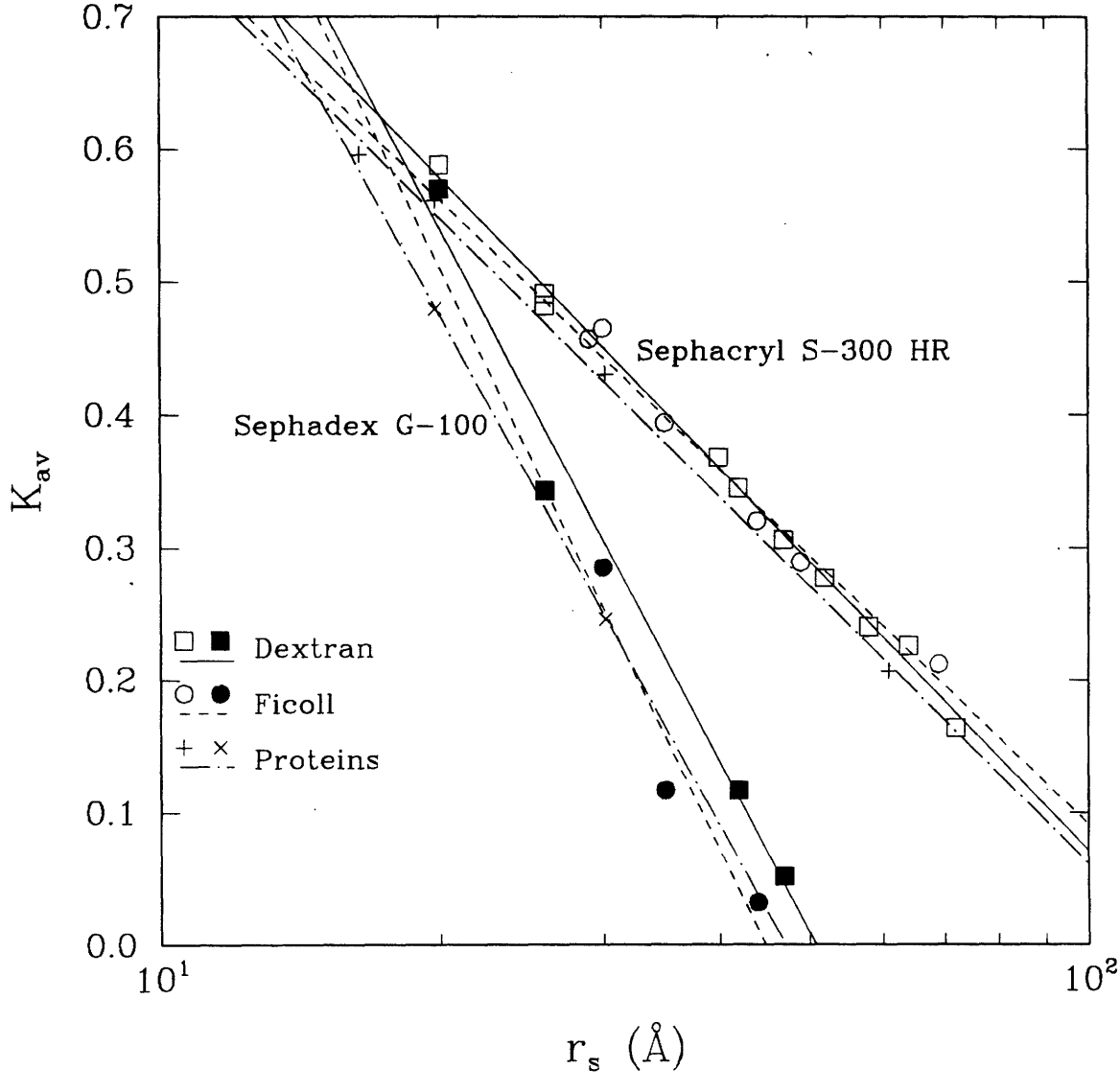

Figure 3-7: Fractional retention volume (K_{av}) as a function of Stokes-Einstein radius (r_s) for dextran, Ficoll, and various globular proteins on Sephacryl S-300 HR columns. The lines represent the correlations given by Eq. 3.8 and Table 3.2.

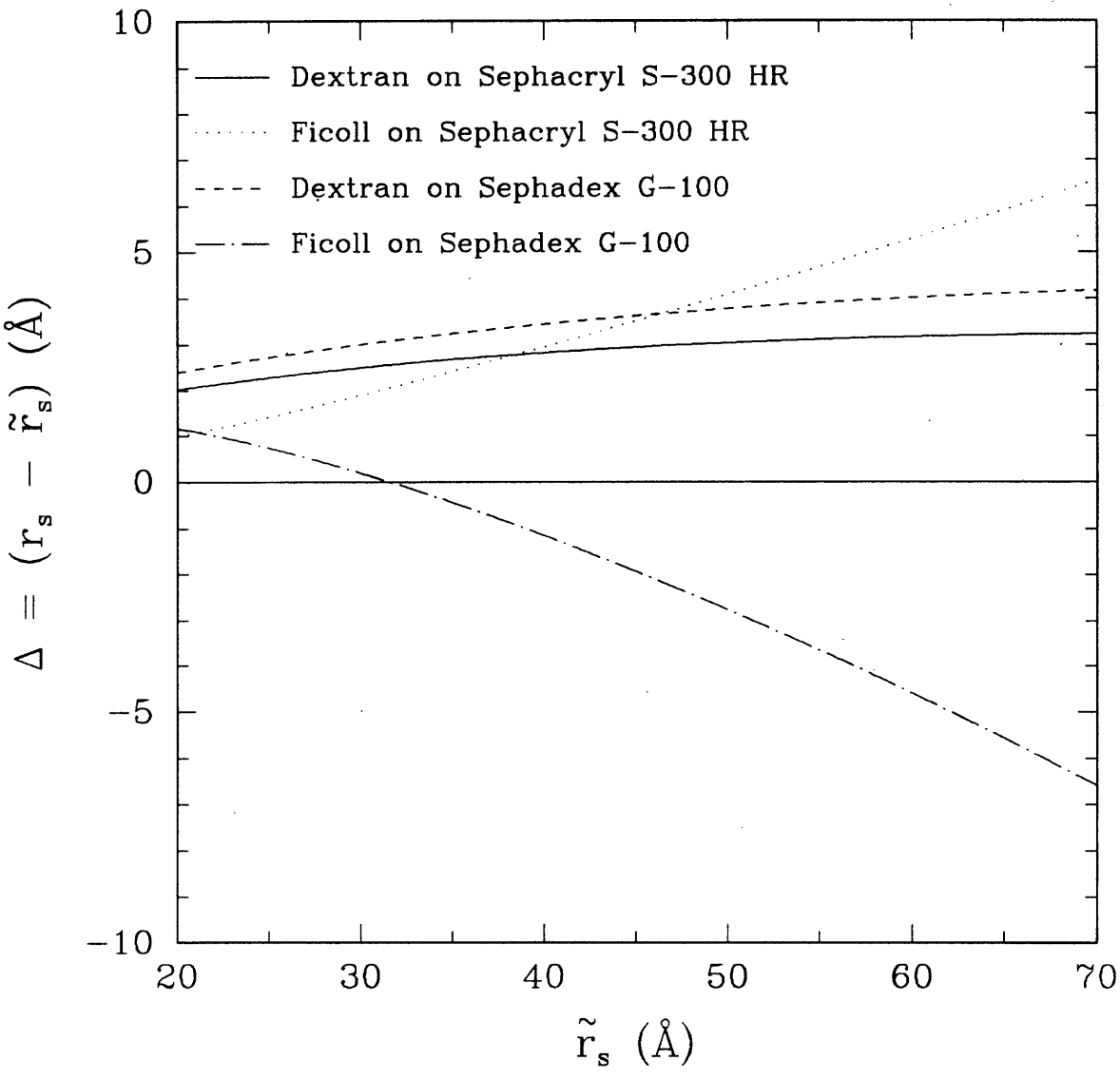

Figure 3-8: Molecular radius correction factors for dextran and Ficoll on Sephacryl S-300 HR and Sephadex S-100 columns.

but overestimate r_s for Ficoll for $\tilde{r}_s > 30$ Å.

3.6.3 Dispersion Coefficients

Figure 3-9 shows the estimated dispersion coefficients for eight dextran and four Ficoll samples for which calculations could be performed. There is no discernible difference between dextran and Ficoll results. A linear dependence of $\mathcal{K}$ on r_s is indicated, supported by theoretical formulations which indicate that $\sigma_p \propto 1/\mathcal{D}$.[126] The dispersion coefficients are on the order of 10^{-3}–10^{-4} cm^2/s, placing them at the border of significantly affecting the elution curves. The actual values of $\mathcal{K}$ are somewhat lower than those shown in Figure 3-9 because of sample polydispersity. Thus sieving coefficients below 40 Å should be only minimally affected by dispersion. For Θ at $r_s > 60$ Å, $\mathcal{K}$ may be more on the order of 10^{-3} cm^2/s, and Figure 3-3 suggests that the error due to dispersion may be as high as a factor of two. However, standard errors for Θ at large r_s are on the order of Θ, and so correcting for dispersion would probably not contribute significantly to the normal analysis of sieving data.

3.7 Summary and Conclusions

In this chapter, we have used monodisperse dextran and Ficoll standards to demonstrate the differences between calibration curves derived from globular proteins and those derived from linear (dextran) and cross-linked (Ficoll) polysaccharides. On the Sephacryl 300-HR columns empolyed by this study, the differences were found to be small, on the order of 5 Å or less. The effect of column dispersion on a polydisperse elution profile was determined by estimation of Taylor dispersion coefficients from the monodisperse elution peaks. For typical plasma and urine samples obtained from sieving analysis, column dispersion was shown to be negligible for small ($r_s < 40$ Å) tracers. While dispersion effects may be theoretically important for larger ($r_s > 60$ Å) molecules, it probably has no practical significance due to the high degree of experimental scatter in measured values of Θ at these sizes.

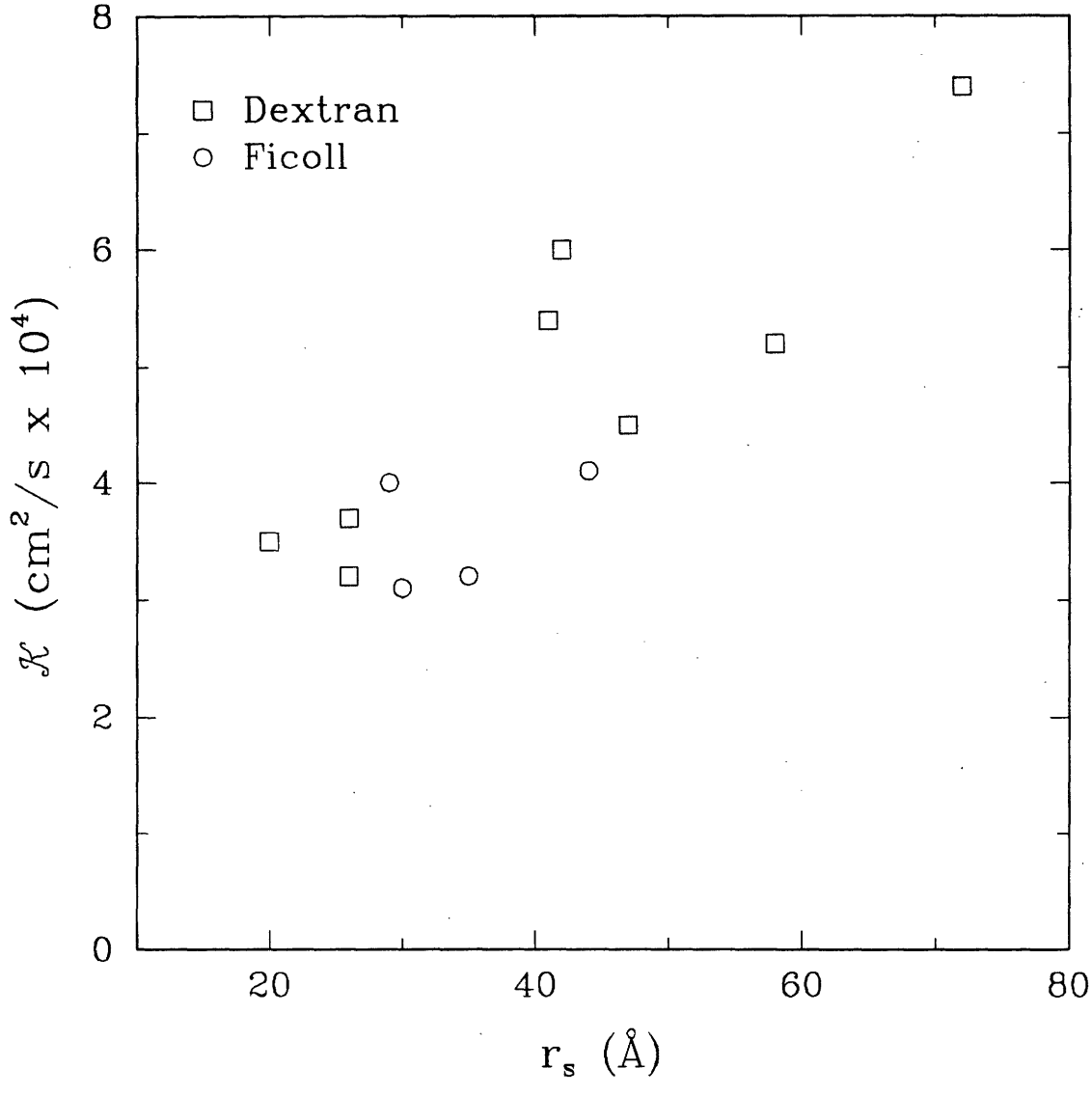

Figure 3-9: Estimated dispersion coefficients for dextran and Ficoll on Sephacryl S-300 HR columns.

Chapter 4

Comparison of Ficoll and Dextran Sieving in the Normal Munich-Wistar Rat

4.1 Introduction

Ideally, the fractional clearance of a neutral tracer at a given molecular size would be independent of the polymer used and identical to that of a neutral endogenous protein of the same size. In practice, using the Stokes-Einstein radius r_s as the metric of molecular size, considerable variation exists in the values of Θ from different macromolecules. In animal studies comparing dextran sieving to that of Ficoll,[31] polyethylene oxide (PEO),[139] polyvinylpyrrolidone (PVP),[246] and horseradish peroxidase (HRP),[198,199,216,252] dextran Θ exceeds those of the other tracers, although only slightly in the case of PVP. In terms of the traditional pore model of glomerular permselectivity—which assumes that all tracers behave as solid spheres of radius r_s—the dextran values correspond to a membrane of comparatively larger pore radius.

Consequently, although the pore-size parameters derived from dextran sieving data for nephrotic humans often account quantitatively for the observed levels of proteinuria, the pore-size parameters in healthy controls fail to explain the absence of appreciable protein excretion.[79,120] Because albumin has a net negative charge under physiological conditions, the presence of at most trace levels of albumin excretion in healthy individuals might be explained largely by the charge-selectivity of the normal glomerular capillary wall.[30,61,215] The charge-selectivity of the filtration barrier does not, however, explain the virtual absence in normal urine of IgG, which is nearly neutral. Protein reabsorption by the tubules certainly contributes to the discrepancy between the urinary clearances of dextran and protein in normal individuals, but the reported values of fractional protein reabsorption of $\approx 90\%$[104,196] would account for only a ten-fold difference between dextran and proteins such as IgG. Therefore, some factor in addition to charge-selectivity and protein reabsorption is needed to explain the differing urinary excretion rates of dextrans and proteins of similar r_s.

The sieving coefficient in normal rats has been measured in the range of 1.9×10^{-4} to 1.1×10^{-3} for albumin[14,22,94,98,104,105,161,164,166,193–195,235,249,264] (r_s = 35.5 Å), at approximately 0.07 for neutral HRP[198,199,216,252] (r_s = 30.4 Å), and at 5.2×10^{-3} for IgG[105] (r_s = 55 Å). In comparison, reported ranges for dextran values at 30, 40, and 50 Å are 0.20–0.86, 0.01–0.49, and 0.002–0.13, respectively.[169] Again, while the difference between dextran and albumin may be explained in part by charge-selectivity, this rationale does not hold for neutral HRP or IgG.

The applicability of theoretical modeling is thus limited in that membrane pore parameters are

specific for a particular tracer and do not provide an absolute measure of the ability of the glomerulus to retain proteins. There is considerable evidence that, in addition to the effects of molecular size and charge, differences in molecular configuration may have an important influence on the relative filtration rates of proteins and various exogenous macromolecules. Dextran, PEO, and PVP are linear, flexible chains of varying degrees of solvation, while Ficoll and proteins are cross-linked and comparatively rigid. Of particular interest is the fact that the relative ranking of filtration rates *in vivo* is mimicked by the diffusion rates of these polymers through synthetic porous membranes; that is, $\Theta_{dextran} \approx \Theta_{PVP} > \Theta_{Ficoll} > \Theta_{PEG}$. Thus, the transport rates of various neutral macromolecules differ appreciably and the relative rates seem more dependent on the type of permeating molecule than on the chemical composition of the barrier.

Especially noteworthy is the fact that in track-etched polycarbonate membranes of known pore size, the measured diffusivity for Ficoll has been found to closely match the theoretical predictions for a neutral, solid sphere, whereas that for dextran is much larger.[32,71] These findings and the aforementioned similarities among transport rates *in vivo* and *in vitro* suggest that Ficoll should provide accurate absolute values of effective glomerular pore size, values which might be extrapolated reliably to proteins. These results also imply that using dextran together with the customary solid sphere theory will lead to systematic overestimates of glomerular pore size. In other words, Ficoll is probably a more accurate marker for filtration of neutral, globular proteins than is dextran. As with dextran, Ficoll is not secreted or reabsorbed by the tubules,[31] and it can be prepared in a broad range of sizes.

There has been only one previous physiological investigation using Ficoll, where Bohrer *et al.*[31] performed sieving measurements in Munich-Wistar rats and found that Ficoll sieving coefficients were considerably lower than those for dextran at r_s= 24 to 44 Å. While the results are significant, the data are inadequate for in-depth analysis for three reasons:

1. It was a two-period study: in a given animal, a ^{3}H-dextran sieving measurement was followed by a ^{3}H-Ficoll sieving measurement, or *vice versa*. The time between polymer infusions was approximately three hours, which may not have been sufficient for complete removal of the first tracer, especially at larger sizes, and so residual activity may have influenced the second set of values.

2. Micropuncture measurements of flow rate and pressures were not performed, so direct calculation of pore parameters cannot be made.

3. The largest size examined was only 44 Å. Advances in separation technology now make it possible to examine Θ at r_s up to 65–70 Å—where the effects of glomerular permselectivity are more important. Additionally, gel chromatographic calibration in the Bohrer study was performed with globular proteins, which as seen in Chapter 3 may lead to errors in the

determination of molecular size.

In the following study, we compared dextran and Ficoll sieving in a manner which addresses the deficiencies above. Separate animals were used for each tracer, micropuncture and whole kidney hemodynamic measurements were performed, and permselectivity data was taken over a wider range of r_s. Several heteroporous membrane models were used to analyze the data. In the following chapter a theoretical model for random coil permselectivity is used to quantitate the effects of molecular configuration and to suggest a possible explanation for dextran/Ficoll sieving differences.

4.2 Materials and Methods

4.2.1 Preparation of Radiolabeled Polymers

Tritiated dextran (#TRA 382, $M_w \approx 70,000$) was obtained from Amersham Corp. (Arlington Heights, IL). Ficoll was tritiated using the following modified version of the protocol of Bohrer *et al.*:[31] One gram of Ficoll 70 (Pharmacia Fine Chemicals, Piscataway, NJ) was dissolved in 5 ml of water and oxidized by adding 0.525 g of $NaIO_4$ and reacting in the dark for 18 h. The solution was desalted by elution through disposable PD-10 gel chromatography columns (Pharmacia LKB Biotechnology AB, Uppsala, Sweden). The pH was adjusted to 8.0 by addition of NH_4OH. One hundred mCi of tritiated sodium borohydride (New England Nuclear, Boston, MA) was added to the oxidized Ficoll in a fume hood. After 4 h, excess (0.2 g) unlabeled $NaBH_4$ was added and the reaction was allowed to proceed for an additional hour. A few drops of acetic acid were added to remove residual borohydride, and then the unreacted label was removed by elution with phosphate-buffered saline (pH 7.0) through disposable PD-10 columns.

The resulting stock ^{3}H-Ficoll solution was approximately 10 ml in volume with a total activity of 11 mCi. Dilutions of this stock were used for infusion in the rats as described in the next section.

4.2.2 Animal Studies

All animal care and preparation, whole kidney measurements, and micropuncture studies were performed by Dr. Sharon Anderson and Julia L. Troy at the Laboratory of Kidney and Electrolyte Physiology at Brigham and Women's Hospital.

4.2.2.1 Animals

Sixteen healthy male Munich-Wistar rats with weights ranging from 240-306 g were used in these studies. All were fed *ad libitum* standard rat chow (Wayne Rodent Blox, Allied Mills, Chicago, IL) containing $\approx$ 24% protein by weight and allowed free access to water. Sieving measurements were performed in each animal using either radiolabeled dextran (7 animals) or Ficoll (9 animals) as the

infused tracer. Micropuncture measurements of single nephron pressures and flows were performed immediately before the sieving studies in eight of the animals (2 with dextran, 6 with Ficoll).

4.2.2.2 Surgical Preparation

The rats were anesthetized with Inactin (100 mg/kg i.p.) and placed on a temperature-regulated table. The left femoral artery (FA) was catheterized with a polyethylene tube (PE-50 Clay Adams, Parsippany, NJ), and a baseline collection of blood was obtained for hematocrit and inulin "blank" measurements. The FA catheter was used for subsequent periodic blood sampling, for the continuous arterial collection of dextran or Ficoll tracer, and for estimation of mean arterial pressure ($\overline{AP}$) via an electronic transducer connected to a recorder. A tracheostomy (PE-240) was performed, and PE-50 catheters were inserted into the left and right jugular veins for infusions of inulin, para-amino hippurate (PAH), plasma, and radiolabeled tracer. The left kidney was exposed and suspended on a lucite holder, and its surface was illuminated and bathed with isotonic saline. The left ureter was catheterized (PE-10 Clay Adams) for urine collections.

Since the rats lose approximately 20% of their plasma volume in surgical preparation,[135] euvolemia was maintained using the following protocol: isoncotic rat plasma was infused at 0.1 ml/min to a volume equal to 1% of the body weight, followed by a sustained infusion rate of 1.6 ml/kg/h for the duration of the experiment. Intravenous infusions of 10% inulin + 0.8% PAH in 0.9% NaCl at 1.2 ml/h were started one hour before measurements and continued through the experiment.

4.2.2.3 Whole Kidney Hemodynamic Measurements

FA blood samples were obtained for determination of hematocrit and plasma concentrations of protein ($c_{p,A}$), inulin, and PAH. Timed urine collections were obtained for determination of flow rate and inulin and PAH concentration. These measurements permitted calculation of GFR (from inulin clearance), RPF (from PAH clearance), and FF ($= GFR/RPF$).

4.2.2.4 Micropuncture Measurements

In the animals subjected to micropuncture, timed samples of tubule fluid were collected from superficial proximal tubules for determination of flow rate and inulin concentration and calculation of $SNGFR$. Blood samples from efferent arterioles were obtained for determination of the efferent protein concentration ($c_{p,E}$). The FA measurements described above were used for glomerular afferent arteriole values. From these, single nephron filtration fraction ($SNFF$) and glomerular plasma flow rate (Q_A) could be calculated.

Time-averaged hydraulic pressures were measured in surface glomerular capillaries ($\overline{P}_{GC}$), proximal tubules (P_T), and efferent arterioles (P_E) with a servo-null micropipette transducer system

(Instrumentation for Physiology & Medicine, San Deigo, CA). The glomerular transcapillary hydraulic pressure difference was calculated as $\overline{\Delta P} = \overline{P}_{GC} - P_T$.

4.2.2.5 Tracer Infusion and Collection

Immediately after the micropuncture measurements had been completed, a 0.4 ml bolus of isotonic saline solution containing either tritiated dextran or Ficoll of broad molecular size distribution (dextran concentration $<$ 100 mg/dl, specific activity $\approx$ 50 μCi/ml; Ficoll concentration $<$ 700 mg/dl (estimated assuming 70% of the original Ficoll was recovered in the labeled stock solution), specific activity $\approx$ 110 μCi/ml) was infused intravenously over 1.5 min, followed immediately by a constant infusion of the same solution at the rate of 1.2 ml/h.

The oncotic pressure due to the tracer can be approximately calculated using the estimated Ficoll concentration of 700 mg/dl (which is a conservative upper bound). Using an average time of an hour for an experiment, the total amount of tracer infused is (700 mg/dl $\times$ 0.4 ml) + (700 mg/dl $\times$ 1.2 ml/h $\times$ 1 h) = 11.2 mg. Assuming the total plasma volume of a 0.265 kg rat is proportional to that of a 70 kg man with a hematocrit of 45 and circulating volume of 6 l, plasma volume = 6 l $\times(1-0.45)\times 0.265/70 = 0.125$ dl. The maximum possible tracer concentration is then 11.2 mg/0.125 dl $\approx$ 0.1 g/dl, which is just low enough to have a negligible effect on total oncotic pressure.

Ten to fifteen minutes after the the priming bolus, a continuous FA blood collection was begun at a rate of 24 μl/min for 15 minutes. These samples were drawn into capillaries containing heparinzed saline. Urine collection were initiated and terminated 1.5 minutes after the arterial blood collections, to allow for transit time from Bowman's space to the tip of the ureteral catheter.

The FA sample was spun at 3000 rpm in a refrigerated centrifuge (Sorvall Model RT6000B, DuPont, Wilmington, DE) to remove cells, yielding a supernatant plasma volume of approximately 150 μl. Duplicate aliquots of 25–75 μl of FA plasma or 50–100 μl of urine were added to 1 ml of 2 mg% blue dextran (Sigma Chemical Co., St. Louis, MO). These samples were then fractionated and counted as described in Section 4.2.3.

4.2.2.6 Analytical Methods

The volume of fluid collected from individual proximal tubules was estimated from the length of the fluid column in a constant bore capillary of known internal diameter. Tubule inulin concentration was measured by the micro-fluorescence method of Vurek and Pegram.[250] Inulin concentrations in plasma and urine were measured using the macro-anthrone method of Führ *et al.*[103] Protein concentrations were determined using the fluorometric method of Viets *et al.*[248] PAH concentrations were measured by the method of Chasis *et al.*[65] Colloid osmotic pressure of plasma entering and leaving glomerular capillaries was estimated from $c_{p,A}$ and $c_{p,E}$ using the equation of Deen *et al.*[84]

4.2.3 Fractionation of Radiolabeled Plasma and Urine Samples

Labeled plasma or urine samples was drawn into a syringe, and the empty vial was rinsed twice with a volume of 0.5 ml distilled water. The rinsings were added to the sample. The total 2-ml volume was fractionated on a Sephacryl S-300 HR column (Pharmacia) which had been calibrated with polymer standards as described in Chapter 3. The eluent buffer was 0.05 M ammonium acetate at pH 7, and the method of operation was as described in Section 3.5.3. The samples were fractionated into 3 ml aliquots, and 2 ml from each aliquot was mixed with 4 ml of scintillation fluid (Ultima Gold, Packard Instrument Co., Inc., Downers Grove, IL). Activity was measured in a scintillation counter (Tri-Carb Model 4530, Packard Instrument Co.). Based on an analysis of the minimum significant activity above background, cpm rates below 120 were rejected (see Appendix C).

4.2.4 Calculation of Sieving Coefficients

It has been shown previously using relatively monodisperse dextran[62] or Ficoll[31] samples that there is close agreement between values of Θ obtained from Bowman's space collections and from urinary fractional clearances in the same animal. Sieving coefficients from plasma and urine activity were calculated from

$$\Theta = \frac{(U/P)_{\text{cpm}}}{(U/P)_{\text{inulin}}} \times f', \tag{4.1}$$

$$f' = -0.007895 c_{p,A} + 0.9916, \tag{4.2}$$

where $(U/P)_{\text{cpm}}$ is the urine-to-plasma ratio of scintillation counts per unit volume of sample, $(U/P)_{\text{inulin}}$ is the urine-to-plasma ratio of inulin concentration, and f' is a plasma volume correction factor which accounts for the fact that the inulin plasma concentrations were measured in protein-free plasma water, while the labeled plasma samples contained protein. A typical value for f' was 0.95. Finally, Θ was calculated at integer values of r, from the raw sieving curve using the interpolation scheme of Akima.[3,4]

4.2.5 Data Analysis

The approximate method of Deen *et al.*[79] was used to fit membrane pore parameters to heteroporous models. Modifications to the numerical method which reduced computation time are discussed in Appendix B.

Several hypothetical pore-size distributions were considered. The *isoporous + shunt* and *lognormal* models[79] are the most frequently employed in the literature. Briefly, the isoporous + shunt model is described by the parameters r_0 and ω_0, where r_0 is the radius of the overwhelming majority of the pores, while ω_0 describes the fraction of the volume flux transported through a tiny number of pore of effectively infinite size ("shunt" pores). The lognormal distribution is described

by parameters u and s, where the pore-size probability distribution $g(r)$ is given by

$$g(r) = \frac{1}{r \ln s \sqrt{2\pi}} \exp\left(-\frac{1}{2}\left[\frac{\ln(r/u)}{\ln s}\right]^2\right). \tag{4.3}$$

Here we introduced two new models, logical extensions of the previous two. The *lognormal + shunt* model assumes a small number of infinitely large pores in conjunction with a lognormal distribution, using parameters u, s, and ω_0.

The *double lognormal* model assumes two populations of pores each distributed lognormally, with a parameter q_2 indicating the fractional number of pores from the second distribution. Then

$$g(r) = \frac{1-q_2}{r \ln s_1 \sqrt{2\pi}} \exp\left(-\frac{1}{2}\left[\frac{\ln(r/u_1)}{\ln s_1}\right]^2\right) + \frac{q_2}{r \ln s_2 \sqrt{2\pi}} \exp\left(-\frac{1}{2}\left[\frac{\ln(r/u_2)}{\ln s_2}\right]^2\right), \tag{4.4}$$

and $g(r)$ is the pore probability distribution function discussed in Chapter 2. Issues pertaining to the use of the approximate model for the lognormal + shunt and double lognormal models are discussed in Appendix B.

(A third new model, an intermediate of the lognormal and double lognormal models, was briefly examined. This model had parameters u, s_1, s_2, and q_2 where

$$g(r) = \frac{1-q_2}{r \ln s_1 \sqrt{2\pi}} \exp\left(-\frac{1}{2}\left[\frac{\ln(r/u)}{\ln s_1}\right]^2\right) + \frac{q_2}{r \ln s_2 \sqrt{2\pi}} \exp\left(-\frac{1}{2}\left[\frac{\ln(r/u)}{\ln s_2}\right]^2\right). \tag{4.5}$$

It was discarded because fitting results were indistinguishable from the lognormal distribution.)

Powell's method[206] was used to fit the pore parameters for a given model by minimizing χ^2, defined as

$$\chi^2 = \sum_{i=1}^{m} \left(\frac{\Theta_{i,\mathrm{exp}} - \Theta_{i,\mathrm{calc}}}{\sigma_{i,\mathrm{exp}}}\right)^2, \tag{4.6}$$

where m is the number of data points, $\Theta_{i,\mathrm{exp}}$ and $\Theta_{i,\mathrm{calc}}$ are the experimental and calculated sieving coefficients, respectively, for molecular size i, and $\sigma_{i,\mathrm{exp}}$ is the standard error of $\Theta_{i,\mathrm{exp}}$.

Standard errors σ_j for each fitted parameter a_j were estimated by[206]

$$\sigma_j = \sqrt{C_{jj}}, \tag{4.7}$$

where C_{jj} are the diagonal elements of the covariance matrix $\mathbf{C}$ of the fit with respect to the parameter vector $\boldsymbol{a}$:

$$\mathbf{C} = \boldsymbol{\alpha}^{-1}, \tag{4.8}$$

$$\alpha_{kl} = \sum_{i=1}^{m} \frac{1}{\sigma_i^2}\left[\frac{\partial \Theta_{i,\mathrm{calc}}}{\partial a_k}\frac{\partial \Theta_{i,\mathrm{calc}}}{\partial a_l}\right]. \tag{4.9}$$

The partial derivatives were calculated numerically using a finite-difference scheme. This method assumes that the model can be approximated linearly near the optimization point, and tends to underestimate the true value of the standard error.

Statistical comparisons between two groups were made using the unpaired two-sample Student's t-test. Comparisons between more than two groups were made by analysis of variance, with Scheffe's test used to determine conservatively if values were significantly different and Tukey's test used to determine conservatively if values were not significantly different. [220, pp. 941–948]

4.3 Results

4.3.1 Hemodynamic Data

The mean values of various systemic and whole kidney quantities are shown in Table 4.1 for the rats given dextran, those given Ficoll, and the two groups combined. There were no statistically significant differences in body weight, hematocrit, GFR, FF, or $c_{p,A}$ between the dextran and Ficoll groups. There were modest differences in RPF (20%) and $\overline{AP}$ (10%) between the two groups which did achieve statistical significance. As will be discussed, a difference in RPF of this magnitude is expected to have little effect on the measured dextran or Ficoll sieving curves.

The single nephron quantities obtained in the 8 rats which underwent micropuncture are summarized in Table 4.2. The value of the single nephron glomerular ultrafiltration coefficient (K_f) computed from the data in the "total" column of Table 4.2 was 4.25 nl/min/mm Hg. All of these values are within typical ranges for normal euvolemic Munich-Wistar rats in this laboratory. Because of this, and the aforementioned similarities in whole kidney hemodynamics quantities, the data in the "total" column of Table 4.2 were taken as representative of the entire group of rats studied (including those which did not undergo micropuncture).

4.3.2 Sieving Data

The sieving coefficients (fractional clearances) measured for dextran and Ficoll are shown in Table 4.3 and Figure 4-1. As the Stokes-Einstein radius (r_s) increased from 19 to 65 Å Θ for dextran decreased from 7.1×10^{-1} to 7.7×10^{-3}; the corresponding range of Θ for Ficoll was 3.3×10^{-1} to 7.1×10^{-4}. At any given value of r_s, Θ for dextran greatly exceeded that for Ficoll, with a nearly constant dextran-to-Ficoll ratio of ≈ 10 for $r_s > 30$ Å. The differences between dextran and Ficoll were highly significant ($p < 0.01$) for all molecular radii examined. The differences in $\log(\Theta)$ between the groups, which is a more valid comparison as $\Theta \rightarrow 0$, are even more significant ($p < 0.0001$).

4.3.3 Pore Size Parameters

The membrane pore parameters derived from the dextran and Ficoll data are shown in Table 4.4.

	Dextran			Ficoll			Combined		
	w/micro. ($n = 2$)	w/o micro. ($n = 5$)	total ($n = 7$)	w/micro. ($n = 6$)	w/o micro. ($n = 3$)	total ($n = 9$)	w/micro. ($n = 8$)	w/o micro. ($n = 8$)	total ($n = 16$)
Body weight (g)	255±6	258±7	257±5	270±10	280±20	273±9	266±9	266±8	266±6
$\overline{AP}$ (mm Hg)	115±5	100±2†	104±3	116±3‡	105±0	112±3*	102±1	116±2†	109±2
Hematocrit	46.4±0.8	45.8±0.7	45.9±0.5	46.6±0.7	48.7±1.4	47.3±3.5	46.9±0.8	46.5±0.5	46.7±0.5
GFR (ml/min)	1.1±0.17	1.1±0.03	1.1±0.04	1.0±0.06	1.1±0.05	1.0±0.04	1.1±0.02	1.0±0.06	1.1±0.03
$RPF^{\#}$ (ml/min)	4.5±0.3	5.0±0.3	4.8±0.2	4.0±0.2*‡		4.0±0.2*	5.0±0.3	4.1±0.2†	4.3±0.2
$FF^{\#}$	0.25±0.06	0.23±0.01	0.24±0.02	0.24±0.01		0.24±0.01	0.23±0.01	0.24±0.01	0.24±0.01
$c_{p,A}$ (g/dl)	5.2±0.2	5.1±0.1	5.1±0.1	5.1±0.1	5.4±0.1	5.2±0.1	5.2±0.1	5.1±0.1	5.1±0.1

Table 4.1: Mean systemic and whole kidney quantities for dextran- and Ficoll-infused normal Munich-Wistar rats. All values shown are mean ± one standard error. $^{*}p < 0.05$, Ficoll vs. dextran; $^{\dagger}p < 0.05$, without micropuncture vs. with micropuncture; $^{\ddagger}p < 0.05$, Ficoll with micropuncture vs. dextran without micropuncture. ($^{\#}$For RPF and FF: $n = 3$ for dextran without micropuncture and combined without micropuncture, $n = 5$ for dextran total, $n = 0$ for Ficoll without micropuncture, $n = 6$ for Ficoll total, and $n = 11$ for combined total.)

	Dextran ($n = 2$)	Ficoll ($n = 7$)	Total ($n = 9$)
$SNGFR$ (nl/min)	58.0±4.0	47.0±3.4	49.8±3.2
Q_A (nl/min)	191±20	166±14	172±12
$SNFF$	0.30±0.01	0.29±0.01	0.29±0.01
$\overline{\Delta P}$ (mm Hg)	37.0±2.9	32.7±1.6	33.8±1.5
$c_{p,A}$ (g/dl)	5.2±0.2	5.2±0.1	5.2±0.1

Table 4.2: Single nephron pressures and flows for dextran- and Ficoll-infused normal Munich-Wistar rats rats. All values shown are mean ± one standard error.

r_s (Å)	Dextran (n=7)	Ficoll (n=9)
19	$7.06\times10^{-1}\pm8.72\times10^{-2}$	$3.28\times10^{-1}\pm3.68\times10^{-2}$
21	$5.74\times10^{-1}\pm7.65\times10^{-2}$	$2.01\times10^{-1}\pm2.66\times10^{-2}$
23	$4.81\times10^{-1}\pm8.02\times10^{-2}$	$1.20\times10^{-1}\pm1.80\times10^{-2}$
25	$3.72\times10^{-1}\pm6.94\times10^{-2}$	$7.39\times10^{-2}\pm1.25\times10^{-1}$
27	$2.84\times10^{-1}\pm5.57\times10^{-2}$	$4.09\times10^{-2}\pm8.09\times10^{-3}$
29	$2.16\times10^{-1}\pm4.26\times10^{-2}$	$2.65\times10^{-2}\pm4.61\times10^{-3}$
31	$1.64\times10^{-1}\pm3.36\times10^{-2}$	$1.65\times10^{-2}\pm3.05\times10^{-3}$
33	$1.35\times10^{-1}\pm3.34\times10^{-2}$	$1.13\times10^{-2}\pm2.19\times10^{-3}$
35	$8.94\times10^{-2}\pm1.89\times10^{-2}$	$8.15\times10^{-3}\pm1.71\times10^{-3}$
37	$6.99\times10^{-2}\pm1.45\times10^{-2}$	$6.04\times10^{-3}\pm1.35\times10^{-3}$
39	$5.26\times10^{-2}\pm1.05\times10^{-2}$	$4.79\times10^{-3}\pm1.10\times10^{-3}$
41	$4.18\times10^{-2}\pm8.11\times10^{-3}$	$3.76\times10^{-3}\pm9.06\times10^{-4}$
43	$3.03\times10^{-2}\pm6.12\times10^{-3}$	$3.32\times10^{-3}\pm8.50\times10^{-4}$
45	$2.34\times10^{-2}\pm4.03\times10^{-3}$	$2.57\times10^{-3}\pm6.79\times10^{-4}$
47	$2.14\times10^{-2}\pm3.56\times10^{-3}$	$2.23\times10^{-3}\pm5.96\times10^{-4}$
49	$1.80\times10^{-2}\pm2.95\times10^{-3}$	$1.94\times10^{-3}\pm5.27\times10^{-4}$
51	$1.55\times10^{-2}\pm2.43\times10^{-3}$	$1.66\times10^{-3}\pm4.53\times10^{-4}$
53	$1.36\times10^{-2}\pm2.06\times10^{-3}$	$1.41\times10^{-3}\pm3.74\times10^{-4}$
55	$1.18\times10^{-2}\pm1.78\times10^{-3}$	$1.23\times10^{-3}\pm3.30\times10^{-4}$
57	$1.05\times10^{-2}\pm1.61\times10^{-3}$	$1.10\times10^{-3}\pm3.11\times10^{-4}$
59	$9.46\times10^{-3}\pm1.54\times10^{-3}$	$9.75\times10^{-4}\pm2.62\times10^{-4}$
61	$9.00\times10^{-3}\pm1.48\times10^{-3}$	$8.68\times10^{-4}\pm2.27\times10^{-4}$
63	$8.34\times10^{-3}\pm1.41\times10^{-3}$	$7.83\times10^{-4}\pm2.01\times10^{-4}$
65	$7.71\times10^{-3}\pm1.33\times10^{-3}$	$7.10\times10^{-4}\pm1.72\times10^{-4}$

Table 4.3: Sieving coefficients for dextran- and Ficoll-infused normal Munich-Wistar rats. All values are given as mean ± standard error.

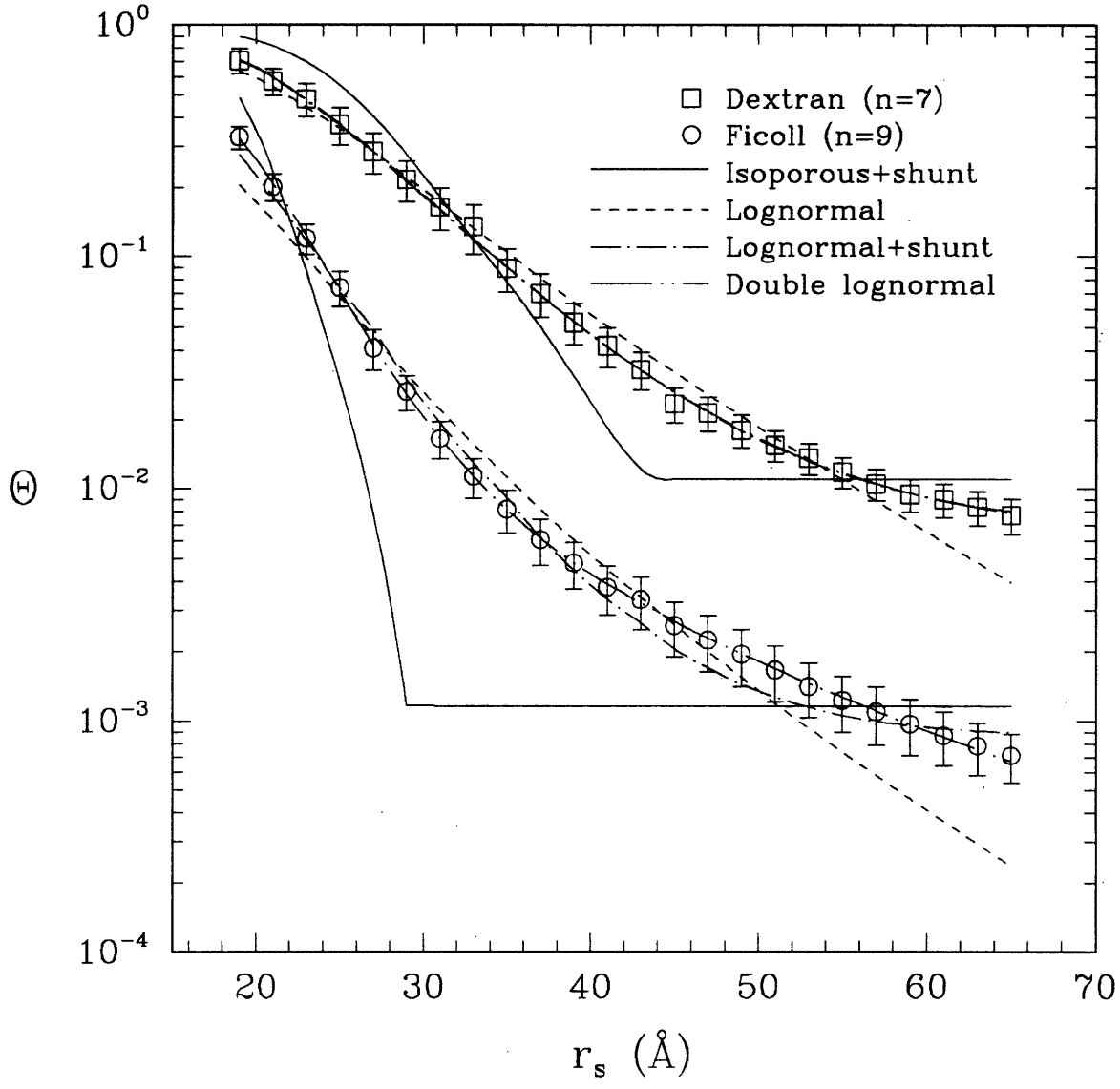

Figure 4-1: Sieving coefficients (Θ) for dextran- and Ficoll-infused normal Munich-Wistar rats as a function of molecular radius (r_s). Error bars denote $\pm$ one standard error of the mean. Curves plotted are fits of various heteroporous distribution models to the data as described in the text.

Model			Dextran	Ficoll
Isoporous +shunt	r_0	(Å)	44.3±1.1	29.1±0.8
	ω_0	$\times 10^{-3}$	5.02±0.55	5.26±0.12
	χ^2		103	208
Lognormal	u	(Å)	15.4±1.7	6.19±1.53
	s		1.52±0.03	1.64±0.06
	$r^*(5\%)$	(Å)	61.7	37.2
	$r^*(1\%)$	(Å)	82.1	52.1
	χ^2		35.4	64.6
Lognormal +shunt	u	(Å)	20.8±0.4	11.4±0.1
	s		1.40±0.01	1.46±0.01
	ω_0	$\times 10^{-3}$	3.04±0.10	0.382±0.035
	$r^*(5\%)$	(Å)	58.0	37.6
	$r^*(1\%)$	(Å)	78.8	49.0
	χ^2		1.05	12.5
Double Lognormal	u_1	(Å)	20.8±0.4	0.46±0.06
	s_1		1.40±0.01	2.31±0.03
	u_2	(Å)	104±72	24.1±1.2
	s_2		1.90±0.79	1.20±0.02
	q_2	$\times 10^{-6}$	1.01±1.04	22.2±9.9
	$r^*(5\%)$	(Å)	56.9	30.4
	$r^*(1\%)$	(Å)	71.5	53.8
	χ^2		1.05	0.37

Table 4.4: Membrane pore parameter fits of dextran vs. Ficoll sieving coefficients to single nephron hemodynamic values. Fitted values are shown ± one standard error.

The calculations used the single nephron quantities given in Table 4.2, as well as the sieving data of Table 4.3. The fits for each model are graphically compared to the data in Figure 4-1. Based on the visual appearance of the curve fits and on the values of χ^2, the isoporous + shunt model provided the poorest fit to either set of data, although it was much better for dextran than for Ficoll. The values of r_0 and ω_0 for Ficoll were much smaller than those for dextran, reflecting the smaller sieving coefficients for Ficoll. The lognormal pore-size distribution, which also contains two parameters, performed better than the isoporous + shunt model in either case. However, the lognormal distribution become noticeably less accurate at large or small r_s than at intermediate r_s (Figure 4-1).

Additional improvements in goodness of fit were obtained with the lognormal +shunt model. Although any lognormal distribution theoretically includes some shunt-like pore of infinite size, for the parameter values in Table 4.4 ($u = 20.8$ Å and $s = 1.40$ for dextran, $u = 11.4$ Å and $s = 1.46$ for Ficoll), the contributions to Θ of pores over 100 Å were calculated to be negligible. Thus, adding a shunt to the lognormal distribution did not lead to any appreciable double counting of very large pores. The values of ω_0 obtained from the lognormal + shunt model were fairly similar to those from the isoporous + shunt case. With either type of shunt model, the value of ω_0 calculated for Ficoll was $\approx 1/10$ that for dextran.

The double lognormal model showed still more improvement in χ^2 over the lognormal + shunt model. For dextran, u_1 and s_1 for the double lognormal model were exactly equal to u and s for the lognormal distribution, indicating that the second lognormal distribution was the functional equivalent of a shunt. χ^2 did not improve for dextran, indicating that the double lognormal model afforded no advantage over the lognormal + shunt model. For Ficoll, the improvement was substantial. The Ficoll double lognormal parameters also indicated a predominate number of pores of one distribution ($q_2 \ll 1$) but there was little resemblance to the lognormal or lognormal + shunt results. A double lognormal fit of the Ficoll data fixing u_1 and s_1 at the lognormal fit values (11.4 and 1.46) gave $u_2 = 102$, $s_2 = 1.64$, $q_2 = 2.52 \times 10^{-7}$, and $\chi^2 = 9.3$.

Because of the difficulty in relating u and s in terms of the net number of large pores, Remuzzi *et al.*[210] developed the concept of an $r^*(V)$ value, where V is defined as the fraction of volume filtrate passing through pores of $r > r^*$:

$$V = \frac{\int_{r^*}^{\infty} r^4 g(r) dr}{\int_0^{\infty} r^4 g(r) dr}. \tag{4.10}$$

For the lognormal + shunt model, V is defined as

$$V = \frac{\int_{r^*}^{\infty} r^4 g(r) dr}{\int_0^{\infty} r^4 g(r) dr} \cdot (1 - \langle \omega \rangle) + \langle \omega \rangle, \tag{4.11}$$

where $\langle \omega \rangle$ is the fraction of the filtrate that passes through the shunt. Typically, $r^*(5\%)$ and $r^*(1\%)$ values are reported. As expected, r^* values were considerably smaller for Ficoll than for dextran

Enhanced model:Simpler model	Dextran p-value	Ficoll p-value
Lognormal+shunt:Lognormal	3×10^{-17}	1×10^{-8}
Double lognormal:Lognormal+shunt	N.S.	6×10^{-15}

Table 4.5: F-test comparisons of heteroporous model fits to dextran vs. Ficoll data. p values are those for the significance of the χ^2 reduction by the "enhanced" model over the "simple" one. N.S.= not significant.

(Table 4.4).

The performance of the various heteroporous models was compared objectively by an F-test, which weighs the trade-off between lowering χ^2 and increasing the number of parameters.[184] The F-test results, given in Table 4.5, indicate that the improvement of the lognormal + shunt model over the lognormal distribution is significant in both cases, but that the improvement provided by the double lognormal model is significant only for Ficoll.

Pore-number probability densities for $g(r)$ and the integral volume flux $1 - V$ are plotted for the different distributions in Figures 4-2 and 4-3. In all cases, the number of pores of the shunt or second distribution are so small that they contribute little to $g(r)$ or to volume flux.

4.3.4 Sensitivity of Calculations to Hemodynamic Inputs

To determine the sensitivity of the pore-size parameters to the hemodynamic inputs used in the calculations, we employed four different sets of inputs. The single nephron values shown in Table 4.2, which were used to obtained the parameter values in Table 4.4 and the theoretical curves in Figure 4-1, are denoted as Case 1. Cases 2–4 were based on various choices for the pertinent whole kidney quantities (GFR, RPF, and $c_{p,A}$). Case 2 used the whole kidney data averaged for all animals studies (right-hand column of Table 4.1). Cases 3 and 4 differed from Case 2 only in the assumed value value of RPF. The average RPF for the dextran group (4.8 ml/min) was used in Case 3, while the average RPF for the Ficoll group (4.0 ml/min) was used in Case 4. In each case the value of $\overline{\Delta P}$ employed was that obtained from micropuncture.

The range of each membrane-pore parameter obtained from the four cases is shown in Table 4.6. In general, changing the hemodynamic inputs results in only minor variations in the computed pore-size parameters. The similarity of the results for Case 1 to those for Cases 2–4 indicates that the choice of single nephron vs. whole kidney hemodynamic inputs does not affect the trends observed in the pore-size parameters. Likewise, the similarity between Cases 3 and 4 demonstrates that the measured difference in RPF between the dextran and Ficoll groups also has a negligible effect on the computed pore sizes.

The possible significance of the measured difference in RPF between the dextran and Ficoll

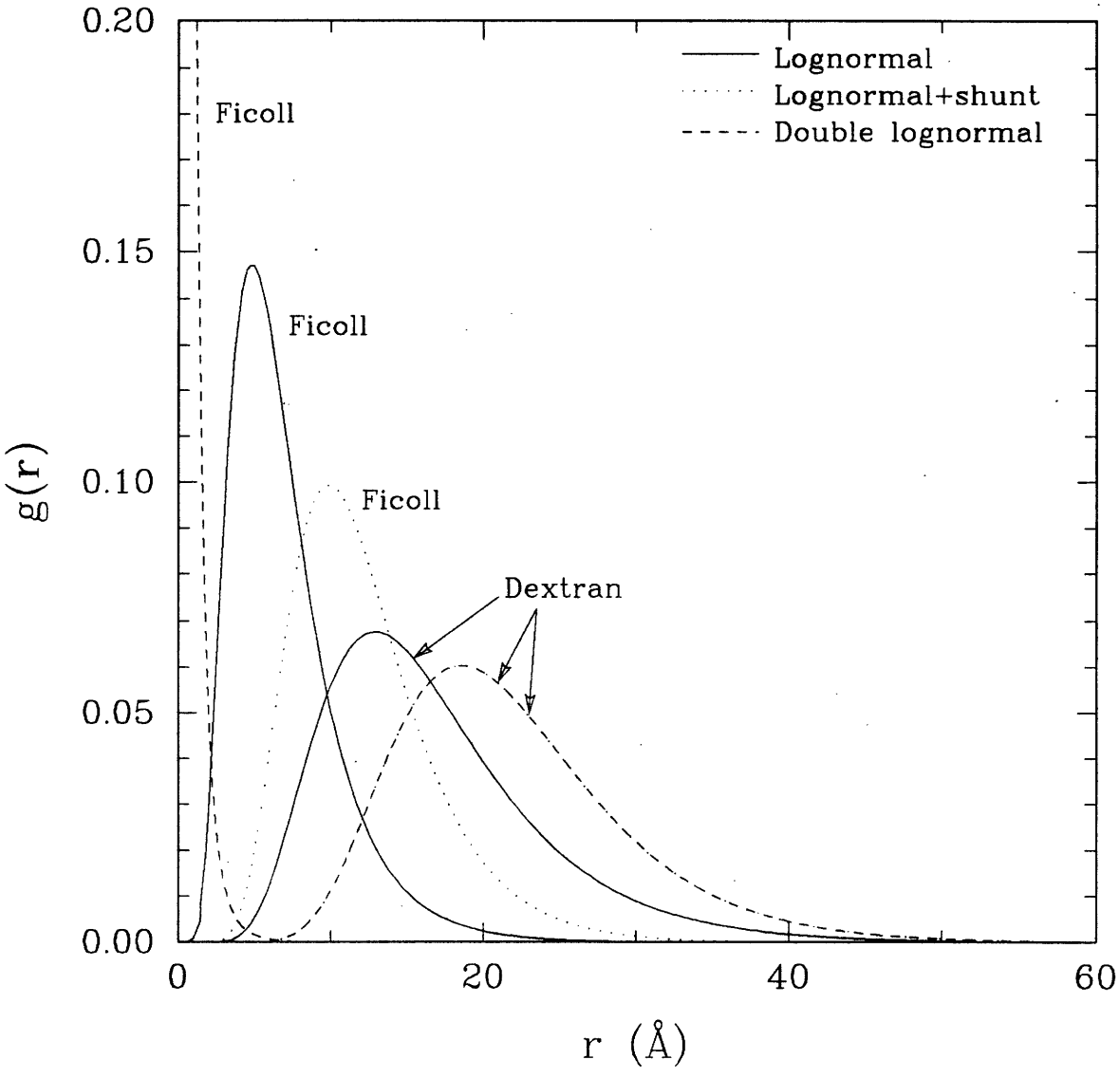

Figure 4-2: Pore number density distributions $g(r)$ for dextran and Ficoll heteroporous fits to data. Plots are based on the values of Table 4.4. Curves for dextran lognormal + shunt and double lognormal models are indistinguishable. Ficoll double lognormal curves appears to merge with the dextran lognormal + shunt and double lognormal curves around $r_s = 6$ Å. The curves are actually separate with one going to zero and the other two rising from zero.

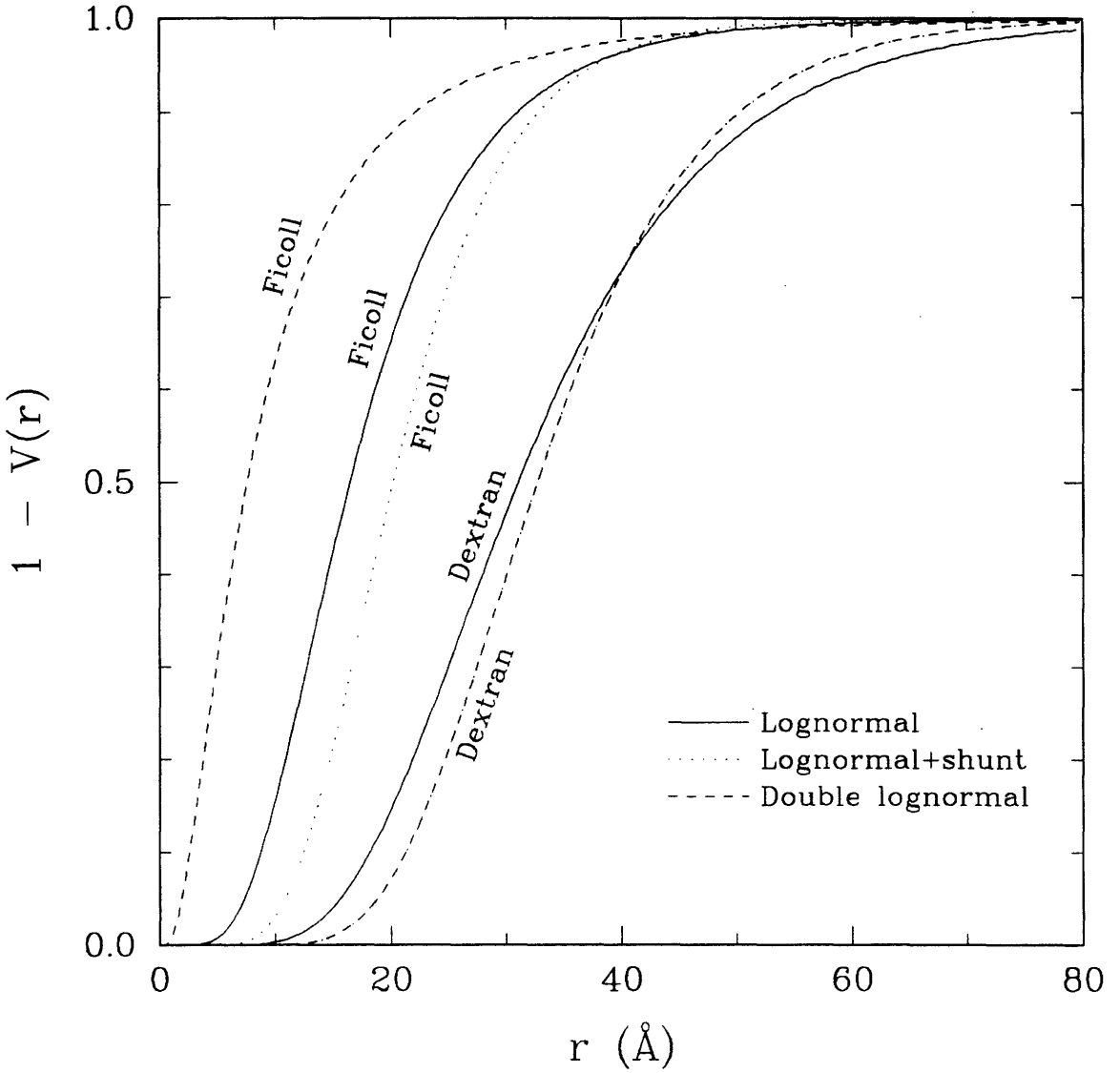

Figure 4-3: Integral volume flux $(1 - V)$ for dextran and Ficoll heteroporous fits to data. Plots based on the values of Table 4.4. Curves for dextran lognormal + shunt and double lognormal models are indistinguishable.

Model			Dextran Case				Ficoll Case			
			1	2	3	4	1	2	3	4
Isoporous	r_0	(Å)	44.3	45.1	45.5	44.8	29.1	29.7	30.0	29.5
+shunt	ω_0	$\times 10^3$	5.02	5.86	6.22	5.52	0.526	0.617	0.657	0.579
Lognormal	u	(Å)	15.4	12.6	12.7	12.7	6.19	5.03	6.18	6.19
	s		1.52	1.58	1.58	1.58	1.64	1.70	1.64	1.64
Lognormal	u	(Å)	20.8	20.8	20.8	20.8	11.4	11.4	11.4	11.4
+shunt	s	1.40	1.40	1.40	1.40	1.40	1.46	1.46	1.46	1.46
	ω_0	$\times 10^3$	3.04	3.54	3.75	3.34	0.382	0.452	0.479	0.424
Double	u_1	(Å)	20.8	21.6	21.7	21.4	0.46	0.46	0.46	0.46
Lognormal	s_1		1.40	1.39	1.38	1.39	2.31	2.31	2.31	2.31
	u_2	(Å)	104	103	102	103	24.1	24.3	24.4	24.3
	s_2		1.90	1.89	1.88	1.89	1.20	1.20	1.20	1.20
	q_2	$\times 10^6$	1.01	1.22	1.29	1.18	22.2	22.2	21.4	22.2

Table 4.6: Sensitivity of parameter fits to hemodynamic inputs. Case numbers correspond to values reported in the text.

groups was also considered in terms of its expected effect on the sieving curves. To do this, we chose as a reference condition the theoretical sieving curves obtained by fitting the dextran or Ficoll data (with single nephron hemodynamic inputs) with the isoporous + shunt, lognormal, and lognormal + shunt models. We then varied Q_A by $\pm$ 10% from the reference value of 172 nl/min, for both dextran and Ficoll. The resulting set of sieving curves encompasses a variety of situations, including up to a 20% difference in plasma flow rates between the dextran and Ficoll groups. As shown in Figures 4-4 and 4-5, altering Q_A had relatively minor effects on the computed sieving curves, and the range of sieving coefficients for dextran remained very distinct from that for Ficoll. This demonstrates that variations in plasma flow rate of this magnitude are incapable of explaining the large differences in the observed sieving behavior of the two polymers.

4.4 Discussion

The present study confirms the finding of Bohrer *et al.*[31] that, for a given value of r_s, dextran passes across the glomerular capillary wall more readily than does Ficoll. While qualitatively similar to the earlier results, the present data show a significantly greater separation between the sieving curves for dextran and Ficoll. One factor which may have contributed to these quantitative differences is a difference in experimental design. The study by Bohrer *et al.*[31] involved two experimental periods in each animal, one with dextran and one with Ficoll. The order of the dextran and Ficoll infusions was varied and an effort was made to wait long enough between the experimental periods to allow the first polymer to be cleared completely. Nonetheless, a small amount of the tritiated polymer from the first period may have been present during the second. This would tend of minimize the observed

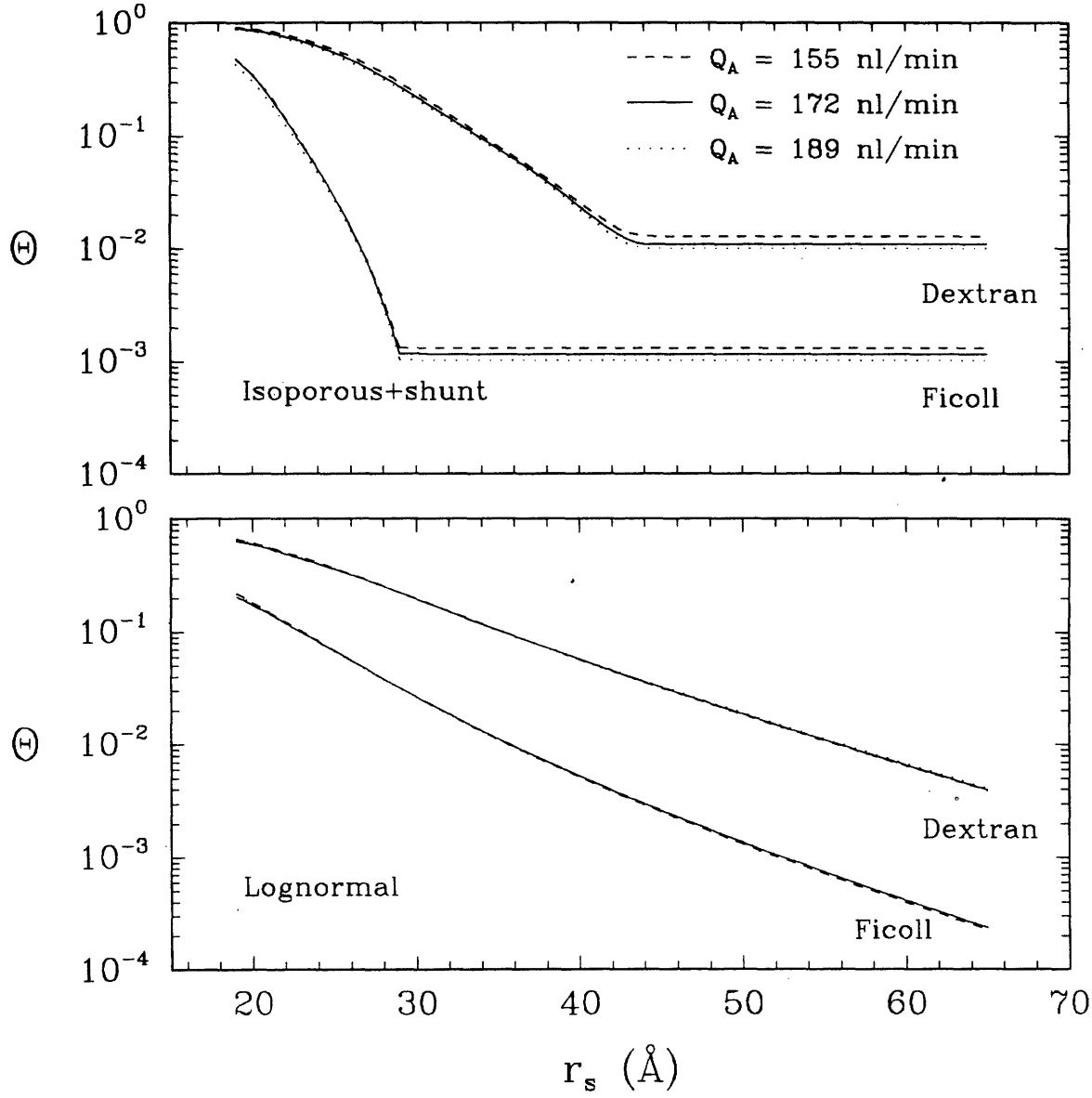

Figure 4-4: Sensitivity of theoretical sieving curves to changes in Q_A for isoporous + shunt and lognormal models.

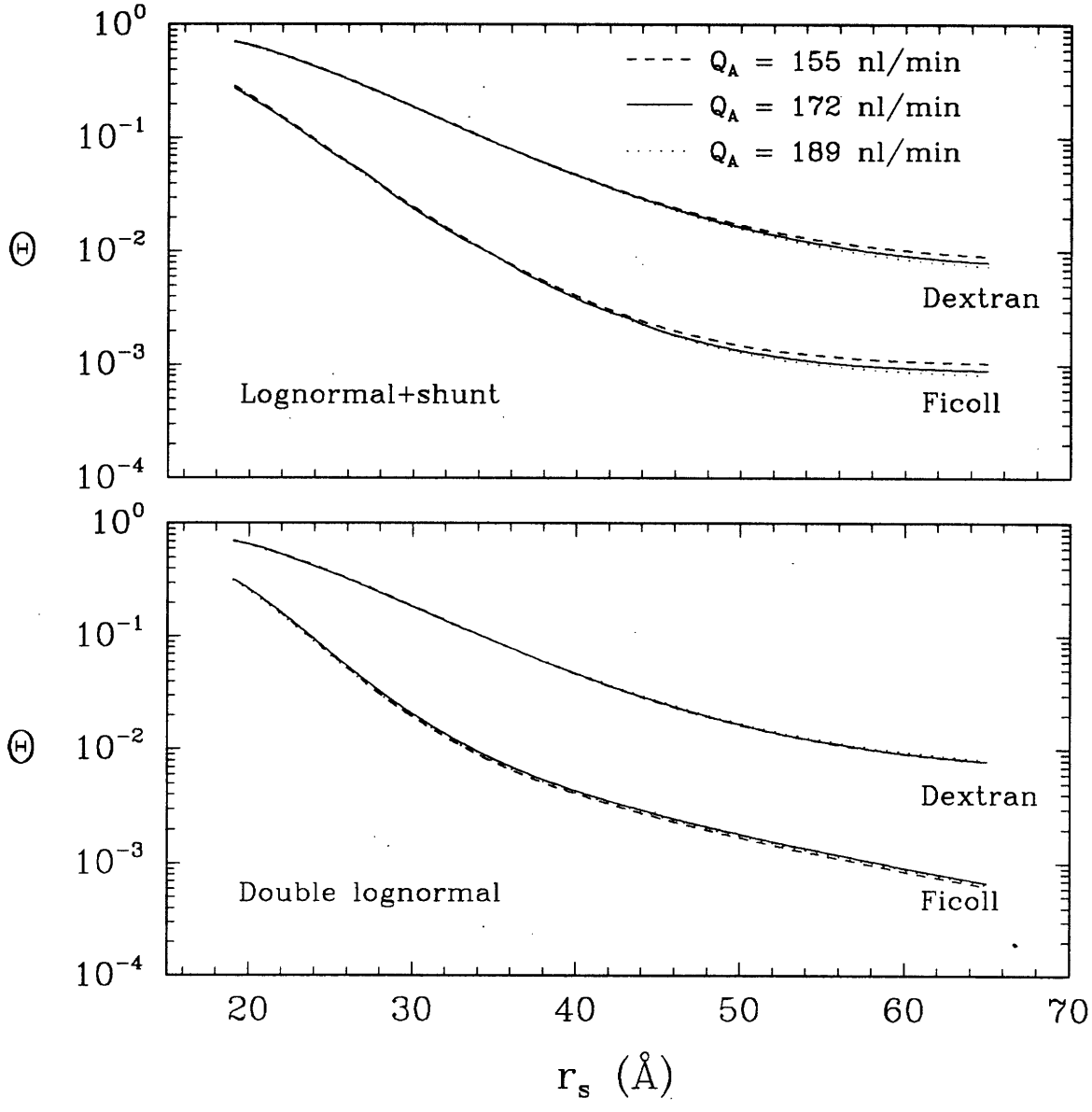

Figure 4-5: Sensitivity of theoretical sieving curves to changes in Q_A for lognormal + shunt and double lognormal models.

differences between dextran and Ficoll, especially for the largest molecules, which are cleared more slowly. To avoid this potential problem in the present study, we deliberately chose to study dextran and Ficoll in separate groups of animals. This was especially important because the present study included molecular radii up to 65 Å, whereas that of Bohrer *et al.*[31] did not go beyond 44 Å.

A second possible explanation is suggested by the observation that, while dextran values for this study are comparable to that of Bohrer *et al.*,[31] the Ficoll values of the present work are considerably lower. This would be consistent with a hypothesis of some sort of reversible or irreversible adsorption to the Sephacryl columns of this study relative to the Sephadex columns of Bohrer *et al.*[31] This possibility motivated the work described in Chapter 3, in which it was shown that Ficoll chromatography in both Sephadex and Sephacryl columns was not concentration dependent, and thus polymer absorption plays no discernible role in Ficoll elution.

For dextran radii up to approximately 40–50 Å the values of Θ obtained by us are comparable to those reported previously for normal rats.[30,31,63,198,210,252,261–263] For larger dextran sizes, however, the present values of Θ begin to exceed those in other studies,[198,210,252,261–263] reaching more than a ten-fold difference at $r_s = 60$ Å. The reasons for this discrepancy are not clear, but a contributing factor may have been differences in gel column calibration. As discussed in Chapter 3, the customary use of protein standards for column calibration may lead to errors in the molecular radius of dextran (or other non-protein polymers such as Ficoll), the magnitude of the error being dependent on the column packing material. To avoid this source of error, we employed nearly monodisperse samples of dextran or Ficoll for column calibration, with r_s determined for each standard by quasielastic light scattering. Because different column packings were employed in the various studies cited above, the correction factors of Chapter 3 are not applicable, and we are unable to estimate the extent to which this factor may have contributed to the discrepancies in Θ for dextran. Of course, physiological differences among the groups of animals studies, or other technical differences, may also have contributed.

The diffusion rates of Ficoll through synthetic membranes of known pore radius suggests that Ficoll molecules behave as ideal, neutral, rigid spheres.[32,71] Given that Ficoll is uncharged, that its crosslinked structure should confer rigidity, and that sedimentation and viscosity data suggest that it is approximately spherical,[31] this behavior is not unexpected. In contrast, the diffusion rates of dextran through the same synthetic membranes have been found to greatly exceed theoretical predictions for neutral spheres. There appears to be no simple explanation for the behavior of dextran. The most obvious difference between dextran and Ficoll is that whereas Ficoll is crosslinked and approximately spherical, dextran is flexible and roughly linear, existing in solution as an approximately random coil. The available theory for neutral random coils,[72] however, suggests that the observable rate of transmembrane diffusion should be less rapid, not more rapid, than that of a neutral solid sphere of equivalent r_s. Consistent with this prediction is the finding that the effective diffusivity

of PEG in track-etch polycarbonate membranes is lower than that of Ficoll.[71] The anomalous enhancement of dextran diffusion rates might be explained by weak attractive interactions between dextran and the membrane material, which would tend to elevate dextran concentrations in membrane pores.[71,74] Whatever the explanation, the relative rates of dextran and Ficoll diffusion through synthetic membranes mimic the behavior of these polymers in the glomerulus.

The structure of Ficoll, and its diffusion behavior *in vitro*, suggest that it may be a much better marker than dextran for the glomerular filtration of neutral, globular proteins. Supporting this is our finding that the ratio of Θ for Ficoll to Θ for dextran at $r_s = 30$ Å is ≈ 0.11. This value is very similar to the analogous sieving coefficient ratio for a neutral globular protein of ≈ 30 Å radius (horseradish peroxidase) and dextran.[216] With regard to IgG, a group of molecules with $r_s \approx 55$ Å and little net charge on average, less precise comparisons are possible because Θ for IgG has not been determined simultaneously with that for Ficoll or dextran. Our value for Θ for Ficoll at $r_s = 55$ Å (1.23×10^{-3}) is roughly comparable to that reported for IgG in rats (5×10^{-3}), the latter value based on tubule fluid samples.[104] Thus, the available evidence *in vivo* supports the view that Ficoll is a good marker for filtration of neutral proteins. The aforementioned value of Θ for Ficoll at $r_s = 55$ Å provides a much more satisfactory explanation for the normal absence of immunoglobulinuria than does the ten-fold higher values of Θ for dextran.

Analyses of tubule fluid samples obtained by micropuncture in rats suggests than $\Theta \approx 3 \times 10^{-4}$ for serum albumin.[14,22,94,98,104,105,161,164,166,193–195,235,249,264] This is about 30 times lower than the present value of Θ for Ficoll at this molecular size ($r_s = 35$ Å) and about 300 times lower than the value of Θ for dextran. The fact that this negatively charged protein is filtered much less readily than Ficoll is consistent with the concept that the normal absence of albuminuria is dependent in part on the charge-selectivity of the glomerular barrier. The present results, however, imply that the concentration of fixed negative charges in the glomerular capillary wall does not need to be as large as previously reported.[78] That is, attempting to explain the 300-fold difference between albumin and dextran on the basis of charge alone requires that one postulate many more fixed charges than are needed to account for the 30-fold difference between albumin and Ficoll. While it remains likely that a loss of charge-selectivity would contribute significantly to albuminuria, the results for Ficoll set a new and lower bound on the potential contribution of charge defects to proteinuria.

Previously, a variety of theoretical pore-size distributions were compared using fractional clearance data for dextran in normal and nephrotic humans.[79] In those comparisons the isoporous + shunt model was somewhat superior to the lognormal distribution. For that reason, and because the values of r_0 and ω_0 have a simpler interpretation than those of u and s, the isoporous + shunt model has been preferred in subsequent clinical studies with dextran. The curve-fitting results in Table 4.4 and Figure 4-1 indicate that for the present data the double lognormal and lognormal distributions are superior to the isoporous+shunt model. Remuzzi *et al.*[210] had previously reached

the conclusion that the lognormal model was superior to the isoporous +shunt model based on fits to dextran data in rats. It is less easy to judge whether the double lognormal and lognormal + shunt models, introduced here, offer a significant improvement over the lognormal distribution. The newer models have more degrees of freedom (5 and 3 parameters vs. 2 for the other models) and should yield smaller values of the error measure, χ^2, on that basis alone. The F-test results of Table 4.5 indicate that this improvement is statistically significant for the lognormal + shunt model with both sets of data, and for the double lognormal model with Ficoll, but not for the double lognormal model and dextran.

Another way to judge the performance of the models is to consider the values of χ^2 in relation to the number of data points per sieving curve, m. Based on the definition of χ^2 (Eq. 4.6), if the computed sieving coefficients differed from the measured values by exactly one standard error at all molecular sizes, then $\chi^2 = m$. If one accepts that fitting the experimental sieving curves more accurately than this is probably not meaningful, then one should discount the importance of achieving values of $\chi^2 < m$. In the present study $m = 24$, and the lognormal + shunt model reduced χ^2 from 35.4 to 1.05 for dextran, and from 64.6 to 12.5 for Ficoll, relative to the lognormal model (Table 4.4). Thus, by this measure, the improvement obtained with the lognormal + shunt model for dextran is probably unimportant. However, the improvement seen for Ficoll is more significant. We therefore conclude that the lognormal + shunt model merits further examination in future studies, at least with Ficoll. By the same token, the improvement provided by double lognormal model is probably not important. Combined with the fact that it was more difficult to achieve convergence with the double lognormal model, it appears that there is not enough justification to further pursue this distribution in any detail.

The alternative theoretical models for the glomerular barrier considered here are highly idealized, in that they are all based on the concept of hindered transport of neutral spheres through cylindrical membrane pores. We have discussed above the evidence from studies *in vitro* that Ficoll does in fact closely resemble an ideal, neutral sphere. It seems likely then that the opportunities for future advances in the description of Ficoll movement through the glomerular capillary wall lies much more in a closer representation of the actual ultrastructure of the barrier than in some improvement in the representation of the permeating molecule. Because Ficoll behaves much like an ideal sphere, and because it possesses the other desirable characteristics for an *in vivo* tracer which have led to the widespread use of dextran, we recommend that Ficoll be preferred over dextran in future studies of glomerular size-selectivity.

The situation with dextran is much more complicated, in that currently available models are unable to predict its transport rates even in synthetic membranes with well-defined pores of known size. In Chapter 5, we examine one proposed mechanism for dextran transport and apply it to the data of this section.

Chapter 5

Application of the Random Coil Model of Hindered Transport to Dextran Sieving Data

5.1 Chemical Structure of Dextran

The representation of dextran molecules as solid spheres in the model of glomerular permselectivity is a simplification born of the previous lack of suitable hydrodynamic theories for any other type of configuration. Since a dextran is a chain of α-1,6-D-glucopyranose monomers, it would be more properly modeled as a flexible linear coil. The consequences of this difference can be expected to be significant since a sphere cannot penetrate a pore with a smaller radius, while a flexible chain will have some finite probability of access even if the pore radius r_0 is much smaller than the chain radius of gyration r_g. Additionally, a coiled polymer would be permeable to solvent flow, which would lower the frictional drag on the molecule. Such configurational effects are proposed to be the principal reason why sieving data of different probe molecules vary substantially.[31,139,216,246]

As discussed in Section F.2.6, chemical analysis of dextran's structure indicates that it is a linear molecular with only a small number of branches. Measurements of its physical properties, however, suggest that dextran in aqueous solution behaves as a molecule with a significant degree of branching. From thermodynamic excess properties and intrinsic viscosity, dextran exhibits properties of a random coil at molecular weights of around 2000.[114] It appears that whatever effective contraction of the molecular dimensions exists due to branching is counterbalanced by the excluded volume effects resulting from expansion of dextran in water. Thus, though it is not strictly a theta system, dextran in water at 20–25 °C exhibits the behavior of a linear molecule with no excluded volume.

5.2 Review of Previous Theoretical Work

5.2.1 General Approach

Departures from the hydrodynamic theory for solid spheres will be manifested in the model as alternate forms of expression for the diffusive hindrance factor H and the convective hindrance factor W in Eq. 2.14. In their most general form, the hindrance factors for very dilute polymer solutions in a long cylindrical pore are defined by

$$H \equiv 2\int_0^1 K^{-1}(\lambda,\hat{r})p(\lambda,\hat{r})\hat{r}\,d\hat{r}, \tag{5.1}$$

$$W \equiv 4\int_0^1 G(\lambda,\hat{r})p(\lambda,\hat{r})(1-\hat{r}^2)\hat{r}\,d\hat{r}, \tag{5.2}$$

where λ is the molecule-to-pore size ratio (usually either $\lambda_s = r_s/r_0$ or $\lambda_g = r_g/r_0$, where r_g is the root-mean-square radius of gyration), $\hat{r}$ is the dimensionless radial position of the molecule's center of mass (or some other locator point), and p is the probability that the molecule will fit completely within the pore at $\hat{r}$. K is the *enhanced drag*, defined as the ratio of the frictional drag on the molecule in the pore to that in bulk solution. G is the *lag coefficient*, the ratio of particle-to-fluid velocity at an equivalent radial position. Each of these quantities is an average over all possible chain conformations.

In practice, "centerline" approximations are used, where the radial dependence of the hydrodynamic coefficients is ignored and replaced by the value at $\hat{r} = 0$:

$$H \approx K^{-1}(\lambda, 0) \cdot 2 \int_0^1 p(\lambda, \hat{r}) \hat{r}\, d\hat{r} = K^{-1}(\lambda, 0)\Phi, \tag{5.3}$$

$$G \approx G(\lambda, 0) \cdot 4 \int_0^1 p(\lambda, \hat{r})(1 - \hat{r}^2) \hat{r}\, d\hat{r} = G(\lambda, 0)\Omega, \tag{5.4}$$

where

$$\Phi \equiv 2 \int_0^1 p(\lambda, \hat{r}) \hat{r}\, d\hat{r}, \tag{5.5}$$

$$\Omega \equiv 4 \int_0^1 p(\lambda, \hat{r})(1 - \hat{r}^2) \hat{r}\, d\hat{r}. \tag{5.6}$$

Φ is the *partition coefficient*, which equals the ratio of the average solute concentration in the pore to that in bulk solution at equilibrium. Ω is an analogous coefficient for the flow-weighted average radial distribution. Each hindrance factor is then seen to be the product of a hydrodynamic term (K^{-1} or G) and a steric term (Φ or Ω). For non-interacting solutes, Φ, Ω, K^{-1}, and G all equal 1 in the limit $\lambda \to 0$. In the limit of large λ, Φ, Ω, and K^{-1} approach 0 and G approaches 0.5. The next sections review methods for calculating steric and hydrodynamic factors for random coils.

5.2.2 Calculation of Steric Parameters

5.2.2.1 Monte Carlo Method

Davidson *et al.*[74] developed a method for calculating Φ and Ω for random-flight chains based on Monte Carlo-generated ensembles of chain configurations. A chain is characterized by l, the length of a chain segment, and n, the number of chain segments. (Davidson *et al.*[70,74] defined n as the number of mass points in the chain, thus their n is equal to $n+1$ of this work.) For large n, $r_g \approx \sqrt{nl^2/6}$.[259] The advantage of this method is that, in theory, it can be applied to any combination of chain and pore parameters. Practically, computational limits preclude its use for very large chains: Davidson *et al.*[74] obtained results for $\lambda_g \leq 1.2$ and $n + 1 \leq 400$. Results are available only in tabular form, as there is no satisfactory means of expressing the data analytically.

5.2.2.2 *Diffusion Equation Model*

Casassa[51] devised a method for calculating Φ in the limit $n \rightarrow \infty$ ($= \Phi_\infty$) based on the analogy between a random walk of infinitesimal step size and molecular diffusion. This "diffusion equation" approach has the principal advantage of providing a closed-form expression for Φ_∞. Casassa's result is

$$\Phi_\infty = 4\sum_{n=0}^{\infty} \frac{e^{-\lambda_s^2 \beta_n^2}}{\beta_n^2}, \tag{5.7a}$$

$$J_0(\beta_n) = 0, \tag{5.7b}$$

where β_n are the roots of the characteristic equation given by Eq. 5.7b and J_0 is the Bessel function of zeroth order. An asymptotic approach to Φ_∞ is seen as n increases in the results from Monte Carlo simulations.[70,74]

A major disadvantage of the diffusion equation model is that Φ is very sensitive to n, especially at large λ_g. Thus, Eq. 5.7a does not provide an acceptable estimate for chains of finite n at large λ_g. Additionally, there is no analogous direct method of calculating Ω, although it could be estimated from a Ω/Φ ratio dependence (see Section 5.5.3).

5.2.3 Hydrodynamic Parameters

Davidson and Deen[72] developed a method for calculating K and G by representing the coil as a porous body with a radially- and axially-dependent solvent permeability. The pertinent molecular parameters in addition to λ_g are the resistance to solvent flow through the porous body (a function of r_s/r_g) and the Mark-Houwink exponent. The Brinkman equation[46] for flow through porous media was then solved to calculate the drag on the body. Values were tabulated for $\lambda_g \leq 1.6$.

5.2.4 Model Results

The model predicts that, for a noninteracting molecule of $\lambda_s < 1$, transport of a linear chain is actually more restricted than that of a solid sphere of equivalent size (*i.e.*, $H_{\text{coil}} < H_{\text{sphere}}, W_{\text{coil}} < W_{\text{sphere}}$).[72] This is because while the chain experiences less frictional drag (K^{-1} and G are larger), it is excluded from the pore (Φ and Ω are smaller) to a much greater degree. The model is in good agreement with hindered diffusion studies of polystyrene in organic solvents through synthetic porous membranes.[72]

Davidson and Deen[71] measured the diffusion of four polymers (dextran, Ficoll, polyethylene oxide (PEO), and polyvinylpyrrolidone (PVP)) in water through synthetic membranes. Dextran and PVP were found to behave similarly *in vitro*, with measured H values exceeding those predicted by the theory for solid spheres and, hence, exceeding to an even greater degree those predicted by the random coil theory. Ficoll data correlated well with the solid sphere theory, while the PEO values

were smaller than predicted for solid spheres, though still exceeding the random coil predictions. The data for dextran and Ficoll confirmed that reported in an earlier study by Bohrer *et al.*[32] This relative order parallels measurements of glomerular permselectivity using the same molecules.[31,139,216,246]

The *in vitro* data indicate that, for dextran (and PVP and, to a lesser degree, PEO), either the hydrodynamic coefficient K^{-1} or the steric coefficient Φ is underestimated. It will be seen later, in Section 5.9, that underestimation of K^{-1} is not sufficient to explain the discrepancy. One possible mechanism for an increased Φ that has been examined in some depth is the existence of attractive chain/pore interactions. Davidson *et al.*[74] demonstrated that this effect could be achieved by a square-well potential which affects chain segments in a region close to the pore wall. Equivalent analyses for solute/pore interactions using the diffusion equation model also have been presented by Davidson and Deen[73] and Lin and Deen.[167]

There exist unexplained discrepancies between hindered diffusion and hindered convection studies. Specifically, Mitchell and Deen[179] report that the convective hindrance for dextran-in-water systems is *greater* (W is smaller) than that predicted by the solid sphere theory. Similar results of increased hindrance have been reported for Ficoll,[179] PEO,[268] and bovine serum albumin.[179]

5.3 Goals

The remainder of this chapter details work performed to incorporate the Davidson *et al.* random coil method into the model of glomerular permselectivity. Because of the difficulty in representing the steric and hydrodynamic parameters analytically, we focused our efforts on generating tables of values covering a wide range of conditions which could be used for lookup and interpolation.

Since the steric parameters from Davidson *et al.*[74] were available only for $\lambda_g \leq 1.2$ and $n+1 \leq 400$, we performed additional calculations to extend the range of utility. Additional work was necessary to extrapolate values for very large λ_g, where Monte Carlo computation was impractical, and these estimated values were also added to the interpolation tables. Estimation of the hydrodynamic parameters at large λ_g was made by a straightforward analytical extrapolation. Finally, we applied the random coil model of glomerular permselectivity to the dextran sieving data of Chapter 4, as discussed in Section 5.9.

5.4 Calculation of Steric Parameters at Small λ_g

5.4.1 Methods

The method of Davidson *et al.*,[74] described subsequently, was used to generate tables of Φ and Ω values for $\lambda_g = 0.2$ to 1.8. All Monte Carlo simulations were performed at the MIT Supercomputing Facility on a Cray X-MP EA/464. The FORTRAN code was written to maximize vectorization. The two rate-limiting steps in the code were chain generation and testing of the configuration at

each radial position within the pore, neither of which could be vectorized.

The model geometry (Figure 5-1) was a cross-sectional circular pore with m radial mesh positions from the centerline to the pore wall. A square-well potential was assumed to exist: an interaction distance d was chosen with attractive pore/solute interactions in the region $m - d \leq r \leq m$. For given values of λ_g and n, the segment length l is then calculated as[150]

$$l = \lambda_g m \sqrt{\frac{6(n+1)}{n(n+2)}}. \tag{5.8}$$

The following algorithm was used for determining the weighted probability distribution $p(\lambda_g, \hat{r})$ at the discrete mesh positions in the pore:

1. A $(2m+1) \times n$ array **S** was initialized to zero. This array was used to keep track of the number of successful configurations.

2. A single chain was constructed: Beginning at the origin (0,0) with respect to the chain, a three-dimensional random walk step of length l was taken using the method of Marsaglia.[172] The (x, y) coordinate of each step was taken as the location of a mass point and the starting point for the next step. Generation of n such steps constituted a chain.

3. The center of mass of the chain was placed at pore radial position $(-m, 0)$.

4. Each mass point in the chain was tested to see if it fit within the pore.

   (a) If every mass point fit, then the number of mass points m_d that fit within the square-well was counted. The success was recorded by incrementing the ij-th element in **S**: $s_{ij}^{t+1} = s_{ij}^{t} + 1$, where i corresponded to the diameter position and $j = m_d$.

   (b) If any mass point fell outside of the pore lumen, no success was recorded.

5. The chain was moved one position to the right. Step 4 was repeated over the diameter of the pore.

6. Steps 2 to 5 were repeated for M_c chains, where M_c was large enough to insure a representative ensemble of chains.

Each mass point that lay within the interaction region was taken to have an energy $\epsilon k_B T$, where k_B is Boltzmann's constant and T is absolute temperature. Negative values of ϵ correspond to attractive interactions, while positive values indicate repulsive forces. For a given ensemble of chains and values of d and ϵ, the weighted probability of success $p(\lambda_g, \hat{r}_i)$ with center of mass at position $\hat{r}_i$ in the pore was then calculated from the Boltzmann-weighted sum of success divided by

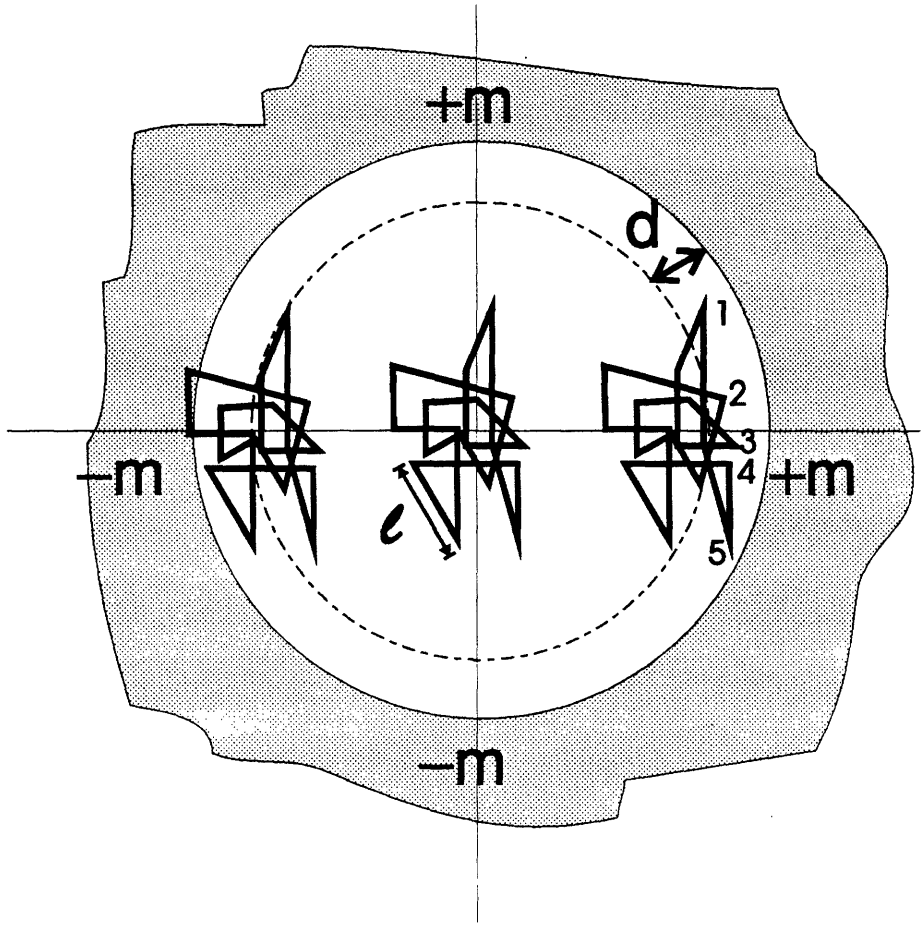

Figure 5-1: Model geometry for Monte Carlo simulations. The pore radius is divided into m positions with an interaction region a distance d from the wall. The chain is modeled as a three-dimensional random walk of step size l. The left configuration is not recorded as a success. The middle configuration is recorded as a success with zero pore wall interactions. The right configuration is recorded as a success with five mass points (*labeled*) experiencing pore wall interactions.

the total number of chains generated:

$$p(\lambda_g, \hat{r}_i) = \frac{\sum_{j=0}^{n} s_{ij} \exp(-\epsilon j)}{M_c}. \tag{5.9}$$

Once **S** was calculated, $p(\lambda_g, \hat{r}_i)$ could be rapidly determined for any ϵ. The steric parameters was then calculated by Simpson's rule:

$$\Phi = 2\sum_{i=0}^{m} \alpha_i p(\lambda_g, \hat{r}_i)\hat{r}_i(\Delta\hat{r}), \tag{5.10a}$$

$$\Omega = 4\sum_{i=0}^{m} \alpha_i p(\lambda_g, \hat{r}_i)(1-\hat{r}_i^2)\hat{r}_i(\Delta\hat{r}), \tag{5.10b}$$

where α_i are the Simpson's rule coefficients and $\Delta\hat{r}$ are the fixed radial step sizes. Propagation of errors in these calculations is discussed in Appendix E.

Molecule-to-pore size ratios were varied from $\lambda_g = 0.2$ to 1.8 in increments of 0.2. The number of chain segments n ranged from 20 to 800. The energy parameter ϵ was varied from -0.4 to 0 in increments of 0.01. The interaction region d was set equal to l for all calculations ($d = l$ case), as this seemed a reasonable assumption for short-range interactions. Additionally, the limiting case of a potential extending across the entire pore ($d = r_0$ case), affecting all $n+1$ mass points, was calculated directly from the $\epsilon = 0$ results as

$$\Phi|_{d=r_0} = \exp[-\epsilon(n+1)] \cdot \Phi|_{\epsilon=0}, \tag{5.11a}$$

$$\Omega|_{d=r_0} = \exp[-\epsilon(n+1)] \cdot \Omega|_{\epsilon=0}. \tag{5.11b}$$

5.4.2 Results

5.4.2.1 Computation Time

The amount of CPU time required to generate **S** for different cases is shown in Table 5.1. Computation time scaled roughly with M_c, the number of chains generated, and n. For $\lambda_g = 1.8$, the time requirements had become prohibitive, as even the simplest chains required an hour.

5.4.2.2 Steric Parameters

Calculated results for Φ and Ω are tabulated in Appendix D. Values were in excellent agreement with the results of Davidson *et al.*[74] for $\lambda_g \leq 1.2$, and for their small n results for $\lambda_g > 1.2$.

Values for Φ and Ω for the $d = l$ case are shown in Figures 5-2 and 5-3 for varying ϵ and constant $n = 200$. As will be discussed in Section 5.4.2.3, values for $\lambda_g = 1.8$ are deemed unreliable, and they are not shown in Figures 5-2 to 5-5.

Solute/pore interactions are seen to have a large effect on the steric parameters, more so with

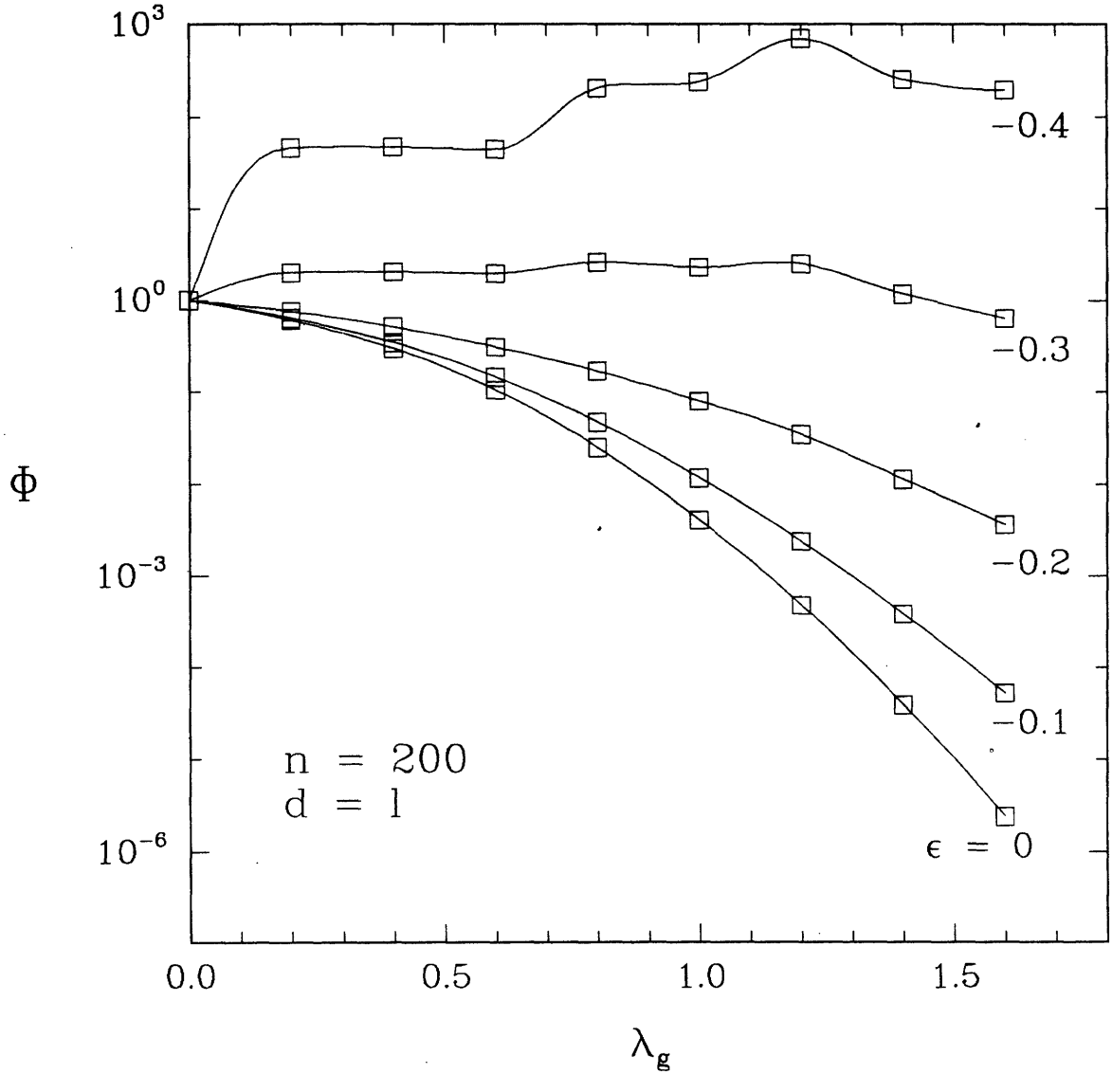

Figure 5-2: Partition coefficient (Φ) as a function of energy parameter (ϵ) for $n = 200$, $d = l$ case.

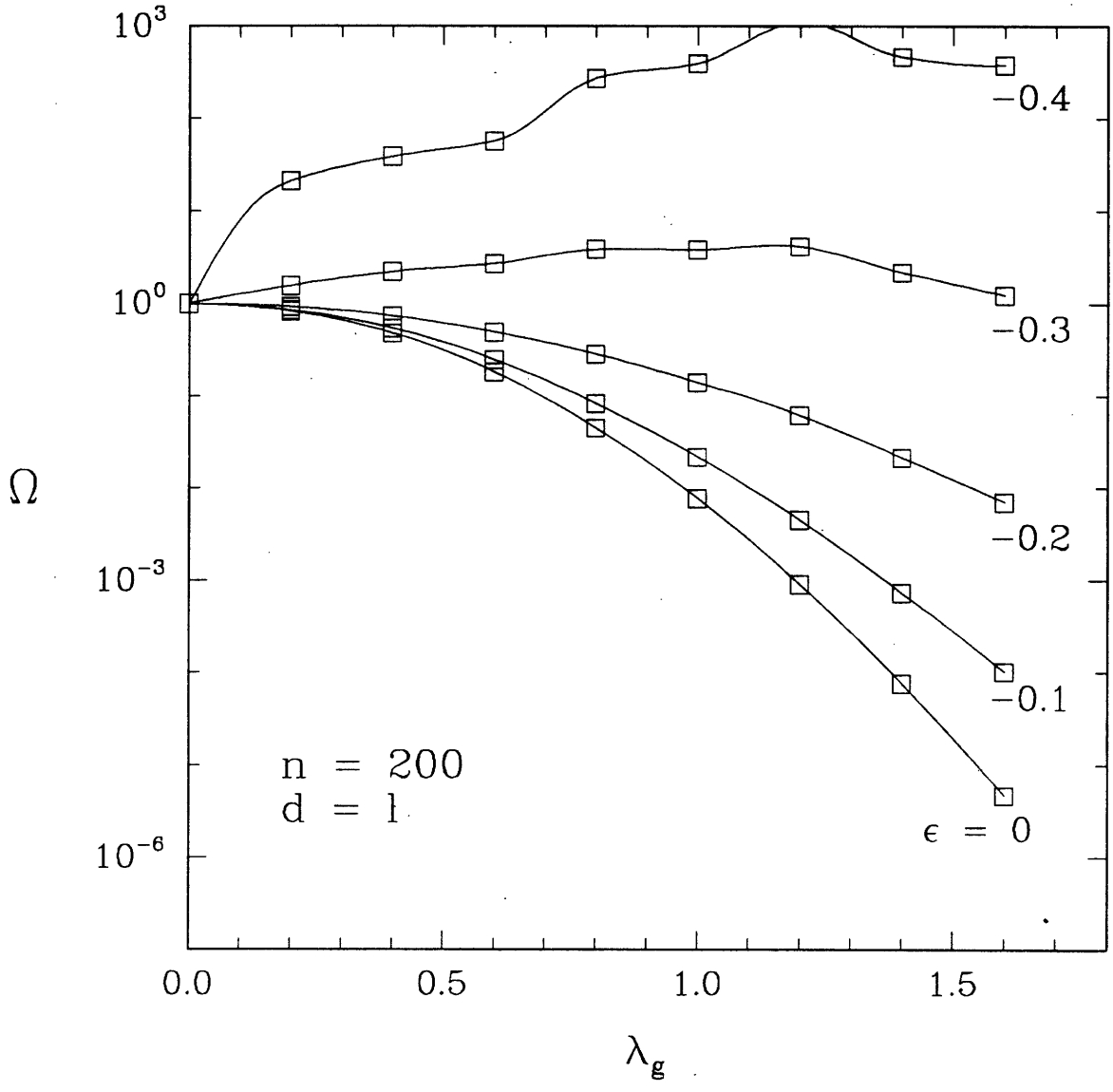

Figure 5-3: Flow-weighted average steric parameter (Ω) as a function of energy parameter (ϵ) for $n = 200$, $d = l$ case.

λ_g	0.2	0.4	0.6	0.8	1.0	1.2	1.4	1.6	1.8
M_c (in 10^3)	80	80	120	600	800	3000	6000	8000	20,000
$n = 20$	0.8	0.7	0.8	2.8	2.8	9.3	17.6	23.1	57.0
$n = 50$	1.3	1.1	1.4	5.3	6.0	20.6	41.3	54.7	134.4
$n = 100$	2.3	2.0	2.4	9.6	11.3	39.8	79.4	107.4	252.8
$n = 200$	4.2	3.7	4.5	18.1	21.8	78.0	157.3	210.7	510.7
$n = 400$	7.9	6.9	8.5	35.3	42.2	153.4	314.0	410.0	997.0
$n = 800$	15.4	13.4	16.6	69.2	84.0	304.2	623.0	828.1	1977.7
Total	31.9	27.8	34.2	140.2	168.1	605.3	1232.6	1633.9	3929.6

Table 5.1: CPU minutes required for Monte Carlo simulations on a Cray X-MP EA/464.

increasing λ_g. A Boltzmann energy of $-0.2k_BT$ per mass point, less than the energy of hydrogen bonding (which is roughly $-3k_BT$ to $-16k_BT$),[165] is enough to increase Φ and Ω by three orders of magnitude. At $\epsilon \approx -0.3$, the steric parameters begin to exceed unity. This is an indication that ϵ is near the critical energy for absorption onto the pore wall.[117,269] Considerable fluctuations are seen in the curves for $\epsilon < -0.3$, demonstrating large statistical uncertainly in these values.

Results for the full-pore potential ($d = r_0$) are shown in Figures 5-4 and 5-5. In this case, the energy parameter also has a significant effect on partitioning, with two differences from the $d = l$ model: comparable increases are shown at energies ten times smaller, and the increase is relatively uniform (on a log scale) at all λ_g, even in the limit as $\lambda_g \to 0$. It has been noted previously that Φ and Ω are more sensitive to changes in d than to ϵ.[74]

The effect of n on the partition coefficient Φ is demonstrated in Figure 5-6 for the neutral case. Also shown is the Casassa equation, Eq. 5.7a, for the $n \to \infty$ limit. Again the effect is most noticeable at large λ_g, with nearly two orders of magnitude separating $n = 20$ and $n = 800$ at $\lambda_g = 1.6$. Also noteworthy is that at $\lambda_g = 1.6$, a significant difference still exists between $n = 800$ and the Casassa limit.

The analogous plot for the $\epsilon = -0.2$, $d = l$ case is shown in Figure 5-7. The effect of n on Φ in the presence of attractive interaction is more complicated. For small λ_g, exclusion effects dominate and the curves have the same trend as the neutral case, Φ decreasing with increasing n. At $\lambda_g = 1.6$, however, crossing of the curves is observed. This happens because the interaction length d is fixed to the segment length l. For a given n, there is a value

$$\lambda_g|_{l=r_0} = \sqrt{\frac{n(n+2)}{6(n+1)}} \tag{5.12}$$

where $d = l = r_0$ and the $d = l$ case collapses to the full-pore ($d = r_0$) potential. Thus, as λ_g increases, d/r_0 becomes equal to or greater than one, and m_d, the number of mass points in the square well, approaches $n + 1$. The exponential weighting then begins to scale as $n + 1$, and so

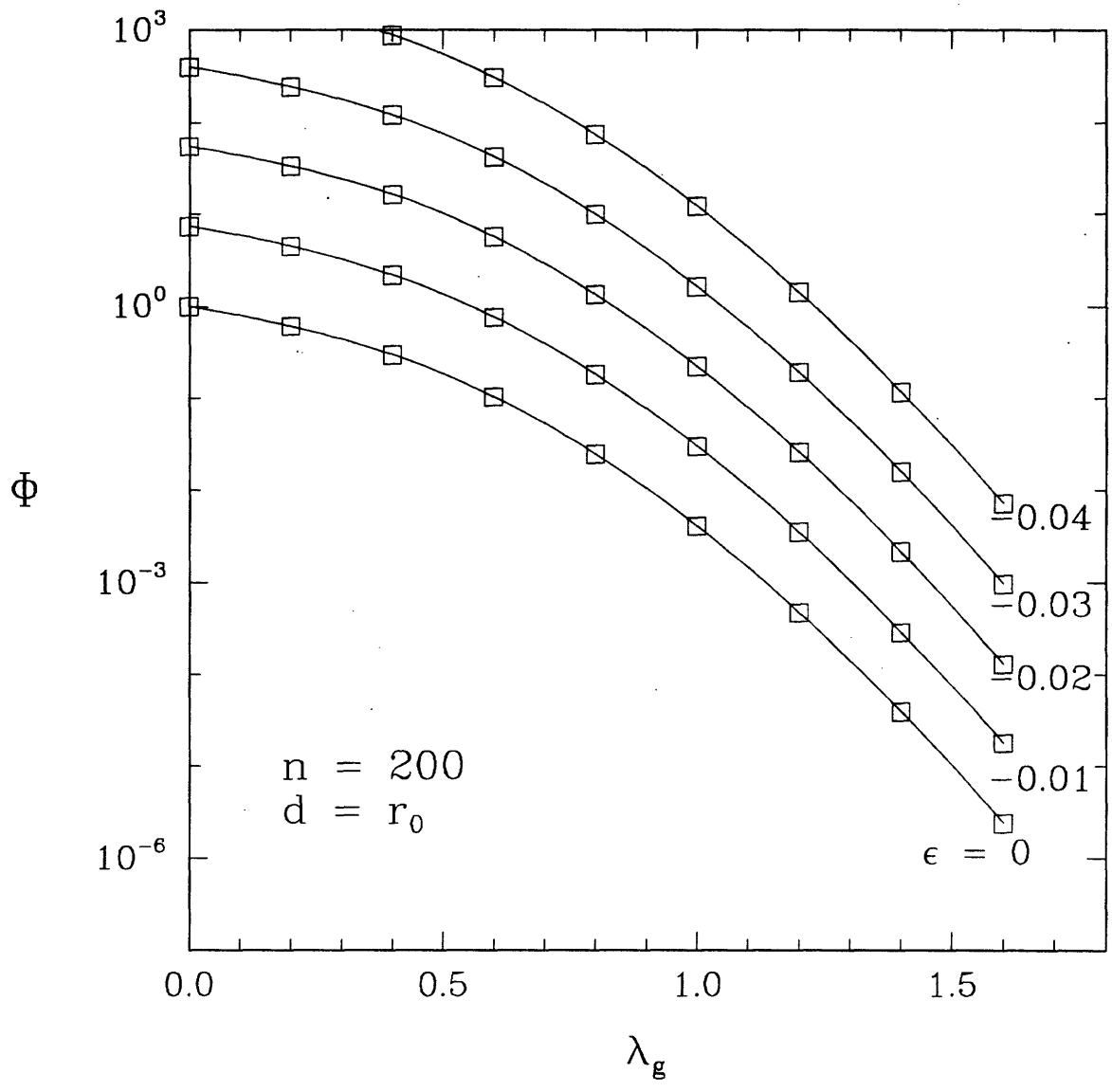

Figure 5-4: Partition coefficient (Φ) as a function of energy parameter (ϵ) for $n = 200$, $d = r_0$ case.

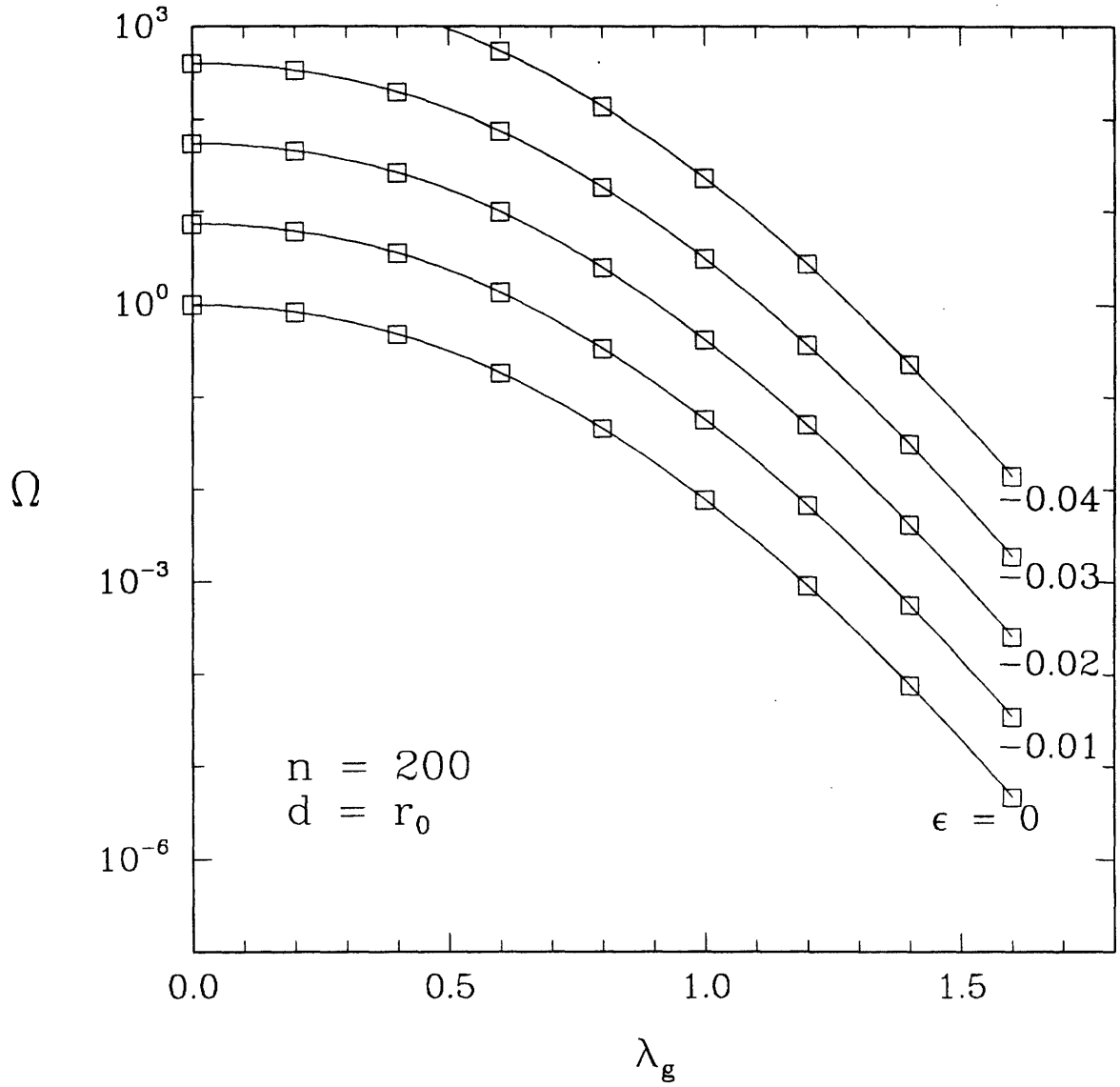

Figure 5-5: Flow-weighted average steric parameter (Ω) as a function of energy parameter (ϵ) for $n = 200$, $d = r_0$ case.

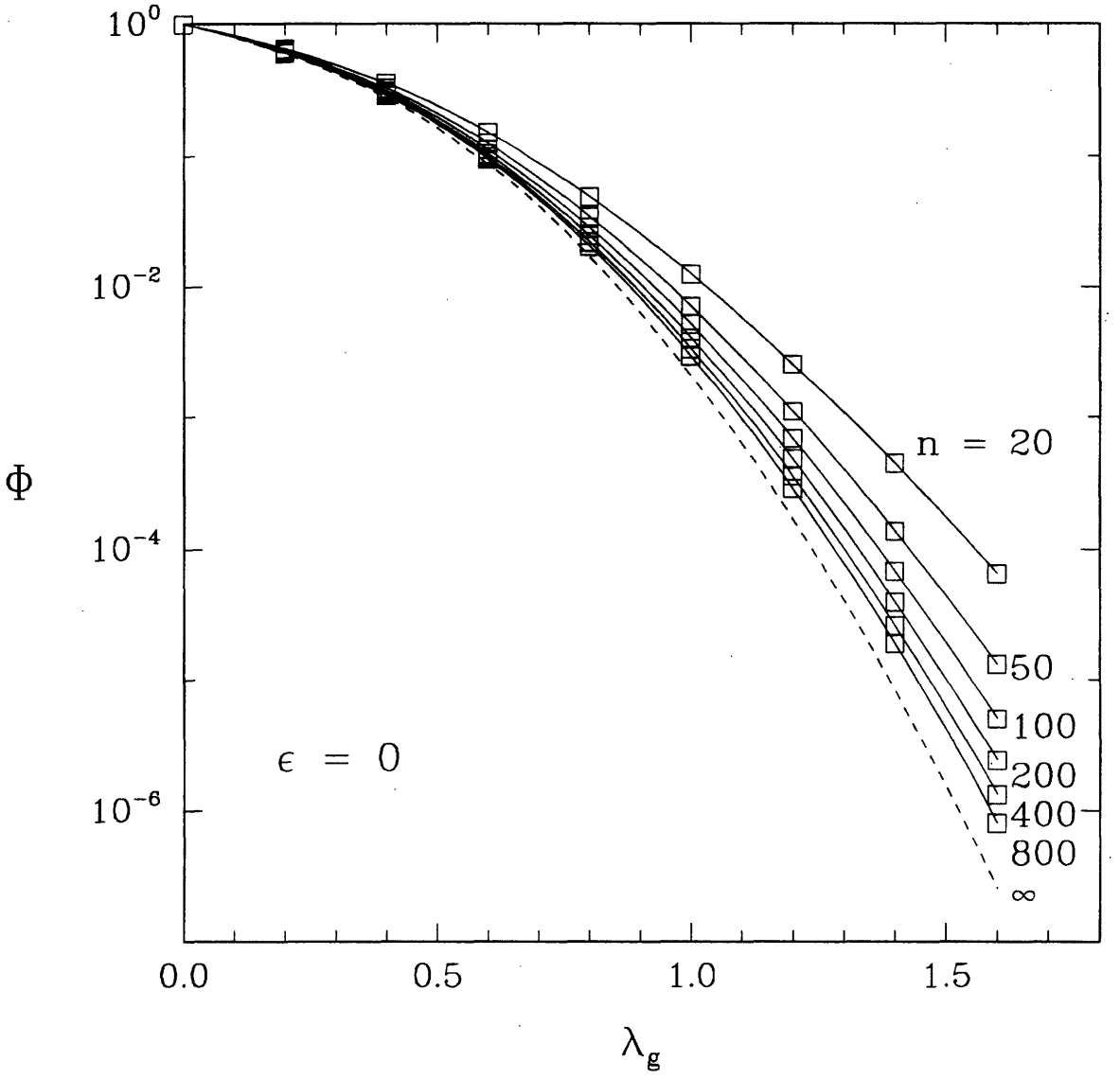

Figure 5-6: Partition coefficient (Φ) as a function of number of chain segments (n) for neutral ($\epsilon = 0$) case. Dashed line shows the $n \rightarrow \infty$ limit of the Casassa equation, Eq. 5.7a.

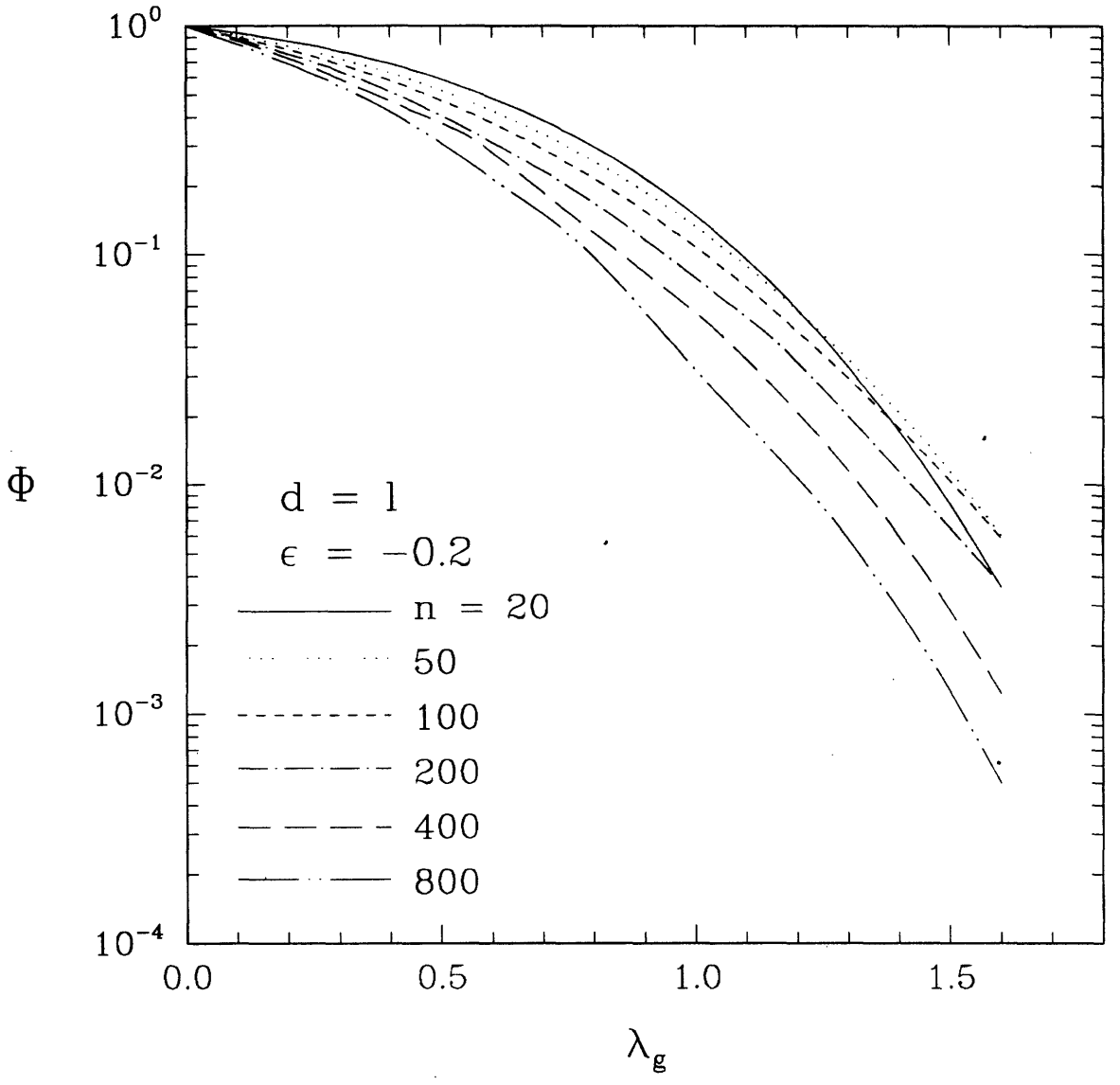

Figure 5-7: Partition coefficient (Φ) as a function of number of chain segments (n) for $\epsilon = -0.2$, $d = l$. For clarity, only the interpolating lines and not the discrete calculated points are shown.

chains with more mass points receive greater enhancement, and a reverse trend with n is obtained. Eventually, as λ_g becomes large enough, the exclusion effects will dominate again and the curves will re-cross. This second reversal is shown in Figure 5-8 for the full-pore potential with $\epsilon = -0.02$. In this figure, for small λ_g, attractive forces dominate and Φ varies inversely with n, but starting around $\lambda_g = 1$, exclusion effects dominate and the curves begin to cross.

5.4.2.3 Error Estimations

As discussed in Appendix E, any calculation of statistical variance for the derived quantities Φ and Ω presupposes that the calculated probabilities are good estimators of the true probabilities. Thus it is theoretically possible to calculate low variances even when the estimators are poor. Since we have no *a priori* means of knowing what the probabilities should be, several different methods were used to gauge the reliability of the results. Only Φ will be discussed here, as the results for Ω are nearly the same.

In general, for a given number of chain configurations M_c, errors will increase as n increases (because more chain configurations are possible, and fewer of them are successful), as ϵ becomes more negative (because small fluctuations are magnified), and as λ_g increases (because fewer configurations are successful). Once convergence on the probabilities is reached, errors will scale exactly as $1/\sqrt{M_c}$ (see Appendix E).

The "gold standard" for determining convergence would be to increase M_c until $\mathrm{Var}(\Phi)$ and $\mathrm{Var}(\Omega)$ vary linearly with $1/\sqrt{M_c}$. For large chains, where $M_c \sim 10^7$, this is not practical. Instead, approximate variances and confidence limits on the parameters were calculated assuming that the Monte Carlo-derived probabilities had converged. In addition, we assessed accuracy by considering two other parameters, the 95% confidence limits on Φ and the asymmetry factor.

The 95% confidence limits on Φ, defined as $2\sqrt{\mathrm{Var}(\Phi)}$ and expressed as a percentage of Φ, are shown in Figure 5-9 for the limiting cases of $n = 20$ and 800. For $n = 20$, the interval is less than 6% at all ϵ. For $n = 800$, it is less than 10% for the neutral case when $\lambda_g \leq 1.4$ and less than 40% for all λ_g. At $\lambda_g = 1.8$, the values are unreliable for even modest negative values of ϵ. For all λ_g at $n = 800$ and $\epsilon = -0.4$, the uncertainty is near 100%. For $\lambda_g < 1.8$ with $n = 800$ and $\epsilon = -0.2$, the uncertainties are on the range of 10–60%.

The asymmetry factor is defined as $|\Phi_{\mathrm{left}} - \Phi_{\mathrm{right}}|/\Phi_{\mathrm{avg}}$ where Φ_{left} and Φ_{right} are values obtained from integration on the "left" side (mesh points $-m$ to 0) and on the "right" side (mesh points 0 to m) of the pore, respectively, and Φ_{avg} is the value obtained from integration across the entire pore (mesh points $-m$ to m). It is a measure of the effects of skew in chain generation, with a minimum value of 0 and a maximum value of 2 (or 200%). Figure 5-10 shows values for the asymmetry factor for the limiting cases of $n = 20$ and 800, and $\epsilon = 0$, -0.2, and -0.4. For $n = 20$, the factor is less than 5% at all values of ϵ. For $n = 800$, the factor is less than 10% for all λ_g when $\epsilon = 0$, but reaches

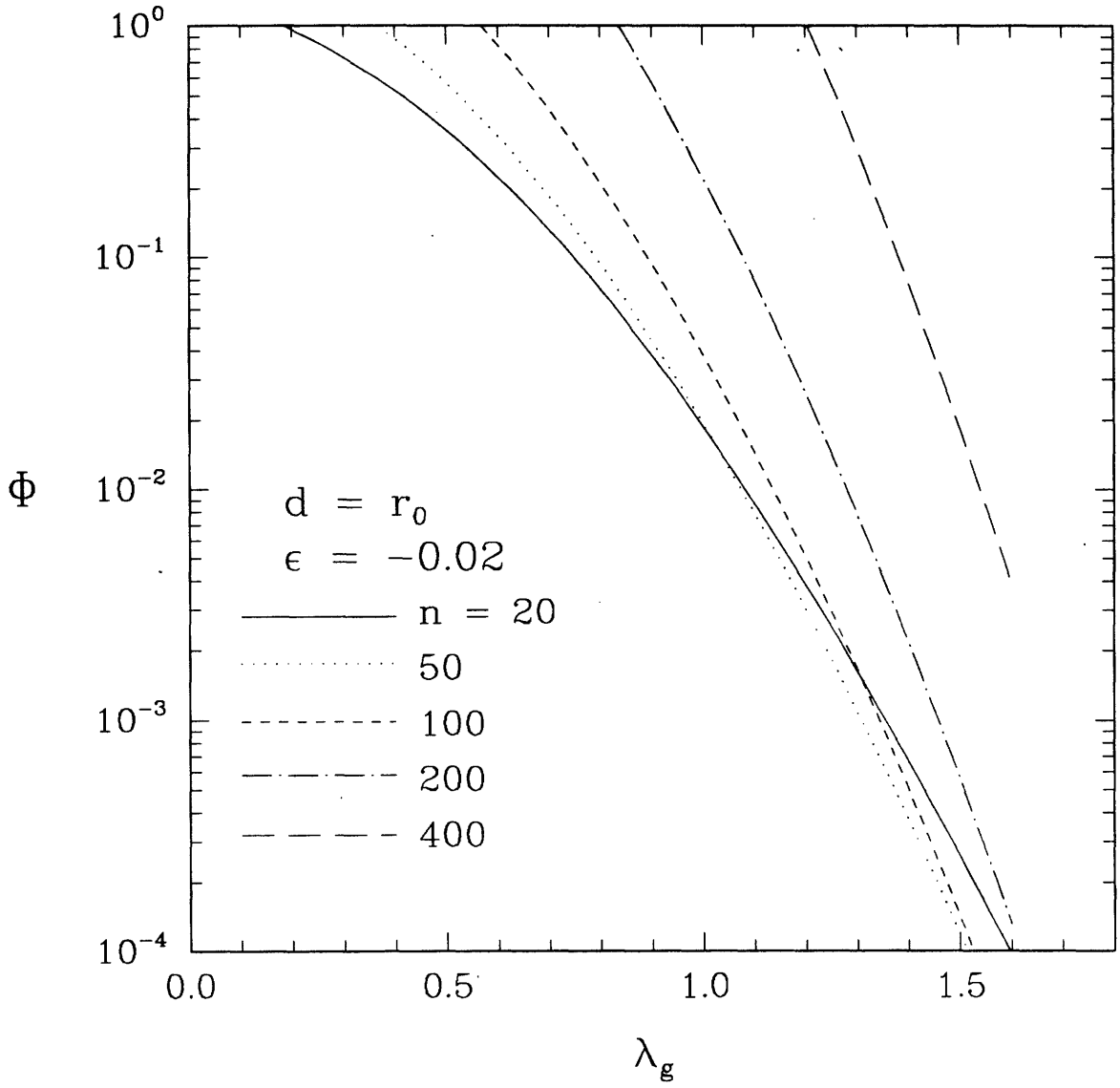

Figure 5-8: Partition coefficient (Φ) as a function of number of chain segments (n) for $\epsilon = -0.02$, $d = r_0$. For clarity, only the interpolating lines and not the discrete calculated points are shown.

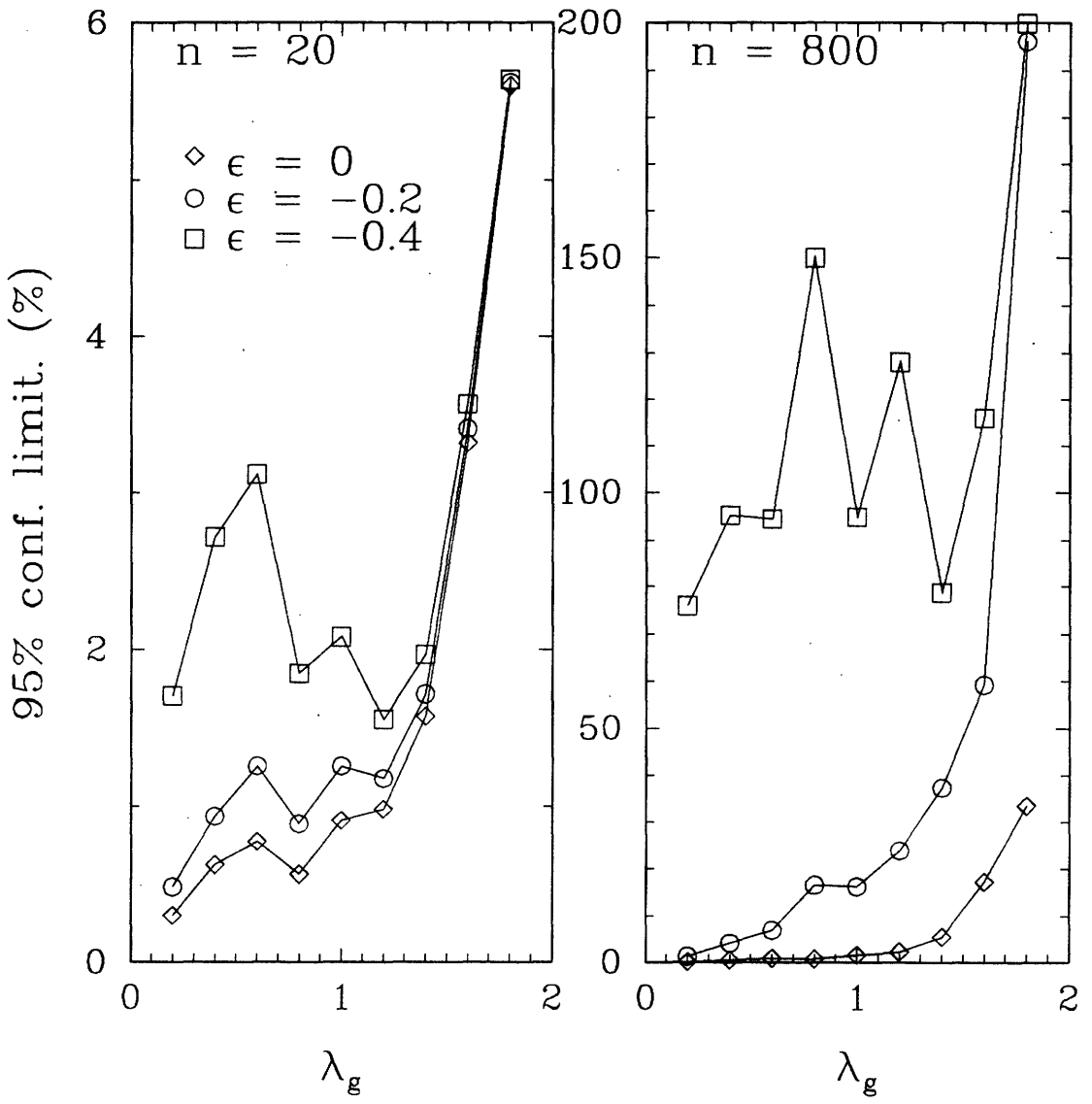

Figure 5-9: 95% confidence limits on Φ for $n = 20$ and $n = 800$.

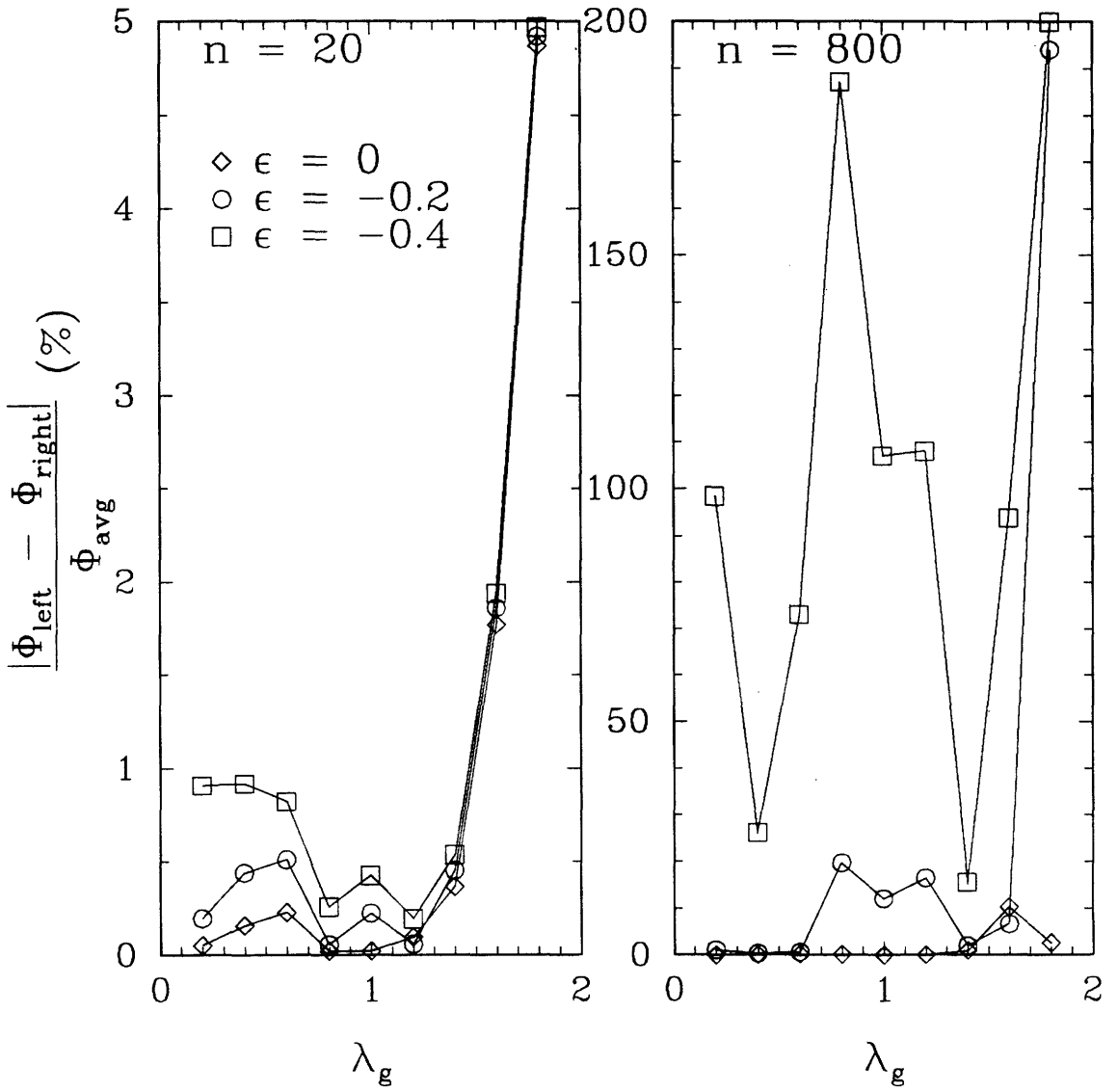

Figure 5-10: Asymmetry factor $|\Phi_{\text{left}} - \Phi_{\text{right}}|/\Phi_{\text{avg}}$ for $n = 20$ and $n = 800$.

the upper limit of 200% for even modest ϵ values when $\lambda_g = 1.8$. There is great uncertainty in the results for all λ_g at $n = 800$ when the magnitude of ϵ exceeds 0.3. In summary, the asymmetry factor qualitatively reinforces the conclusions reached from assessing the 95% confidence limits.

The ratio of Ω/Φ, discussed further in Section 5.5.3, was used as a third means of assessing quality of the results. Values of this ratio for $\lambda_g = 1.8, \epsilon < 0$ were not consistent with the asymptotic limit demonstrated by values at other λ_g, again indicating uncertainty. Based on the asymmetry factor, confidence limits, and Φ/Ω ratio, only results for $\lambda_g \leq 1.6$ and $\epsilon \geq -0.30$ were used for further calculations.

5.5 Estimation of Steric Parameters at Large λ_g

5.5.1 General Approach

As mentioned previously, Davidson *et al.*[74] were unable to find an adequate means of expressing the Monte Carlo results in analytical form. Of particular concern for application to dextran sieving is a means of extrapolating results to large λ_g. From the Ficoll results of Chapter 4, heteroporous distributions had a mode on the order of 10 Å or less. It is apparent then that a significant portion of the large dextran (> 60 Å) will be transported through pores where $\lambda_g > 2.0$, especially when pore attractions exist. An empirical method of extrapolating Φ for large values of λ_g is developed below. Ω was then calculated from Φ by a semi-empirical relationship.

For the purposes of modeling glomerular filtration, it is not necessary to have highly accurate estimations at large λ_g. For one thing, measured sieving coefficients have a high degree of uncertainty at large r_g, as reflected in experimental standard errors. For another, it is expected that most of the transport of large molecules will be through very large pores, even in the presence of attractive interactions. Finally, at large λ_g, Φ decreases several orders of magnitude with even small increases in λ_g. Estimation of steric parameters to within one or two order of magnitude should be suitable for our purposes at the larger values of λ_g.

5.5.2 Partition Coefficient (Φ)

One obvious means of performing an extrapolation would be to use limiting expressions for both low n and $n \to \infty$, at a constant value of the energy parameter, and then to develop expressions for $\Phi(n)|_\epsilon$. For the neutral coil ($\epsilon = 0$), this is easily done because, as seen in Figure 5-6, iso-n lines do not cross and are proportionally spaced as λ_g increases. For the attractive ($\epsilon < 0$) coil, however, the iso-n lines cross as λ_g increases (Figures 5-7 and 5-8).

An alternative method is suggested by comparing isoenthalpic curves in planes of constant n, as in Figures 5-2 and 5-4. Such curves will never cross, and the relative distance of the lines from each other remains roughly proportional. On this basis, the following empirical procedure was devised to

calculate $\Phi(\lambda_g > 1.6, \epsilon < 0)$. First, the neutral value $\ln \Phi(\lambda_g, 0)$ was determined. We then calculated $\ln \Phi$ at arbitrary ϵ_n by increments from the neutral value:

$$\ln \Phi(\lambda_g, \epsilon_n) = \ln \Phi(\lambda_g, 0) + \sum_{i=0}^{n-1} \delta\epsilon_i \cdot \frac{\partial \ln \Phi}{\partial \epsilon_i}(\lambda_g, \epsilon_i). \tag{5.13}$$

Thus the problem is reduced to finding separate expressions for the neutral partition coefficient and the gradient at $\lambda_g > 1.6$.

Values of $\Phi(\lambda_g, 0)$ for $\lambda_g > 1.6$ were calculated by a polynomial extrapolation from $\Phi(1.2, 0)$, $\Phi(1.4, 0)$, and $\Phi(1.6, 0)$. Such an extrapolation will be defined as one from an *endpoint* of $\lambda_g = 1.6$. Similarly, an endpoint of $\lambda_g = 1.0$ would imply that $\Phi(0.6, 0)$, $\Phi(0.8, 0)$, and $\Phi(1.0, 0)$ were fit. As a test of the extrapolation accuracy, polynomial extrapolations to $\Phi(1.6, 0)$ from endpoints of 1.0, 1.2, and 1.4 were calculated. Extrapolations were found to be within 20% of the true value at all values of n, as shown in Figure 5-11. Extrapolation to $\lambda_g > 1.6$ from λ_g endpoints smaller than 1.6 were still within two orders of magnitude of the 1.6 endpoint results, as shown in Figure 5-12. Thus, though extrapolation from endpoints larger than 1.6 would provide better estimates than the ones we have obtained, Figure 5-12 indicates that the results would not be significantly different for our purposes.

To develop a means of calculating the gradient term of Eq. 5.13 for $\lambda_g > 1.6$, we first examined the behavior of the gradient for $\lambda_g < 1.6$. The gradient was numerically approximately as

$$\frac{\partial \ln(\Phi)}{\partial \epsilon_i}(\lambda_g, \epsilon_i) \approx \frac{\ln \Phi(\epsilon_i + \delta\epsilon_i) - \ln \Phi(\epsilon_i)}{\delta\epsilon_i} \tag{5.14}$$

and calculated directly from the tabulated values, with $\delta\epsilon_i = -0.01$. The values were roughly linear in λ_g (see symbols on Figures 5-13 and 5-14). An additional consideration is that for $\lambda_g \geq \sqrt{n(n+2)/6(n+1)}$, $l \geq r_0$ and the behavior must be that of the full-pore potential ($d = r_0$). In this case, $\Phi \sim \exp[-\epsilon(n+1)]$, and therefore

$$\left.\frac{\partial \ln(\Phi)}{\partial \epsilon}\right|_{l \geq r_0} = n + 1. \tag{5.15}$$

Calculated values of the gradient from the Monte Carlo simulations for small n, where $\lambda_g|_{l=r_0}$ was not much greater than 1.6, were consistent with this asymptote (Figure 5-13). A linear extrapolation was then used to calculate the gradient in the region between $\lambda_g = 1.6$ and $\lambda_g|_{l=r_0}$, shown by dashed lines in Figures 5-13 and 5-14.

Extrapolated values for Φ are compared to the Monte Carlo results in Figure 5-15. The behavior of the extrapolations is qualitatively reasonable, with a monotonic rise in Φ as the magnitude of ϵ increases. The relative distances of the extrapolated isoenthalpic lines from each other is consistent with those in the Monte Carlo regime.

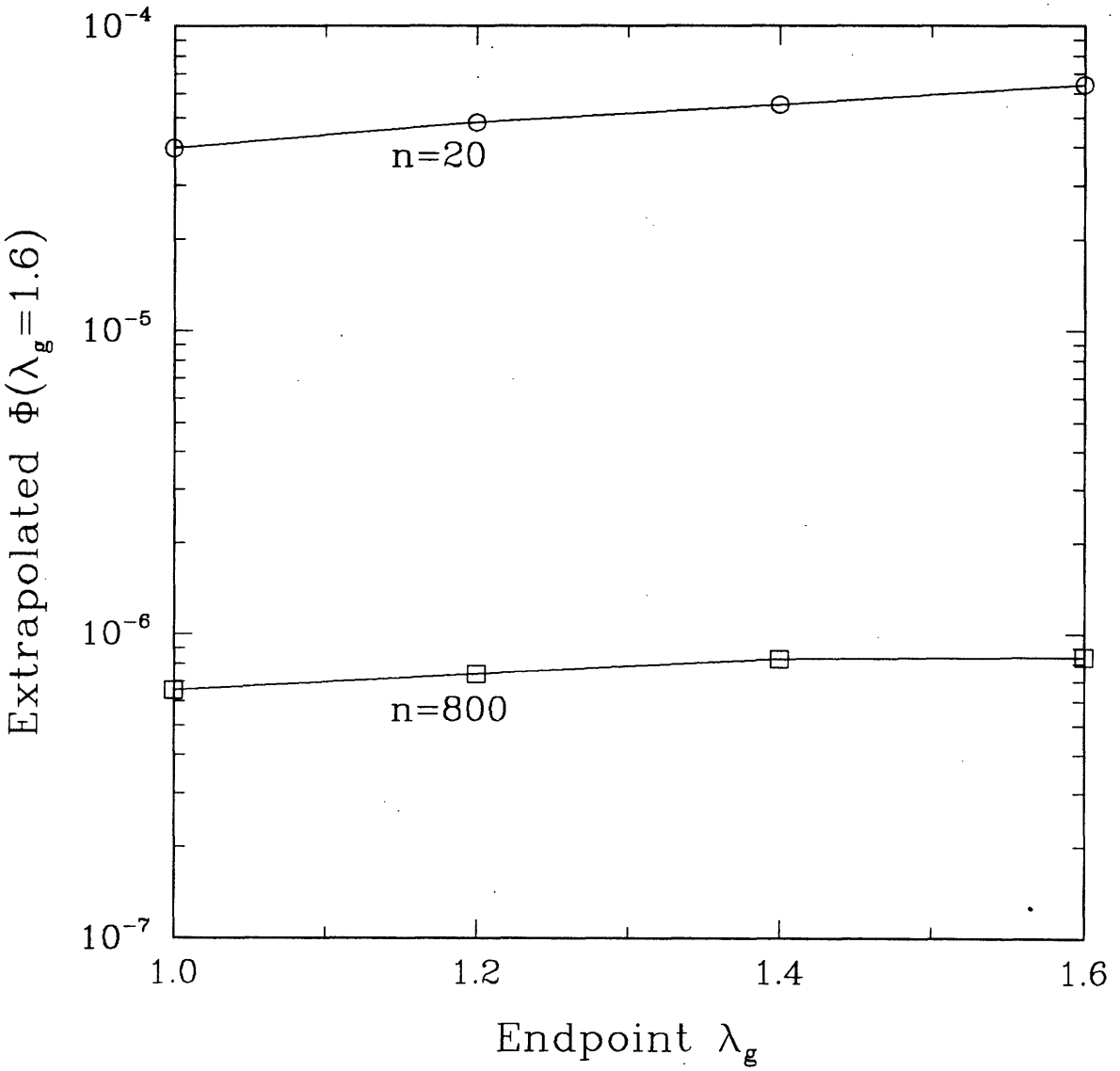

Figure 5-11: Polynomial extrapolation to $\Phi(1.6, 0)$ as a function of the extrapolation endpoint λ_g. By definition the values at endpoint $\lambda_g = 1.6$ are the true values.

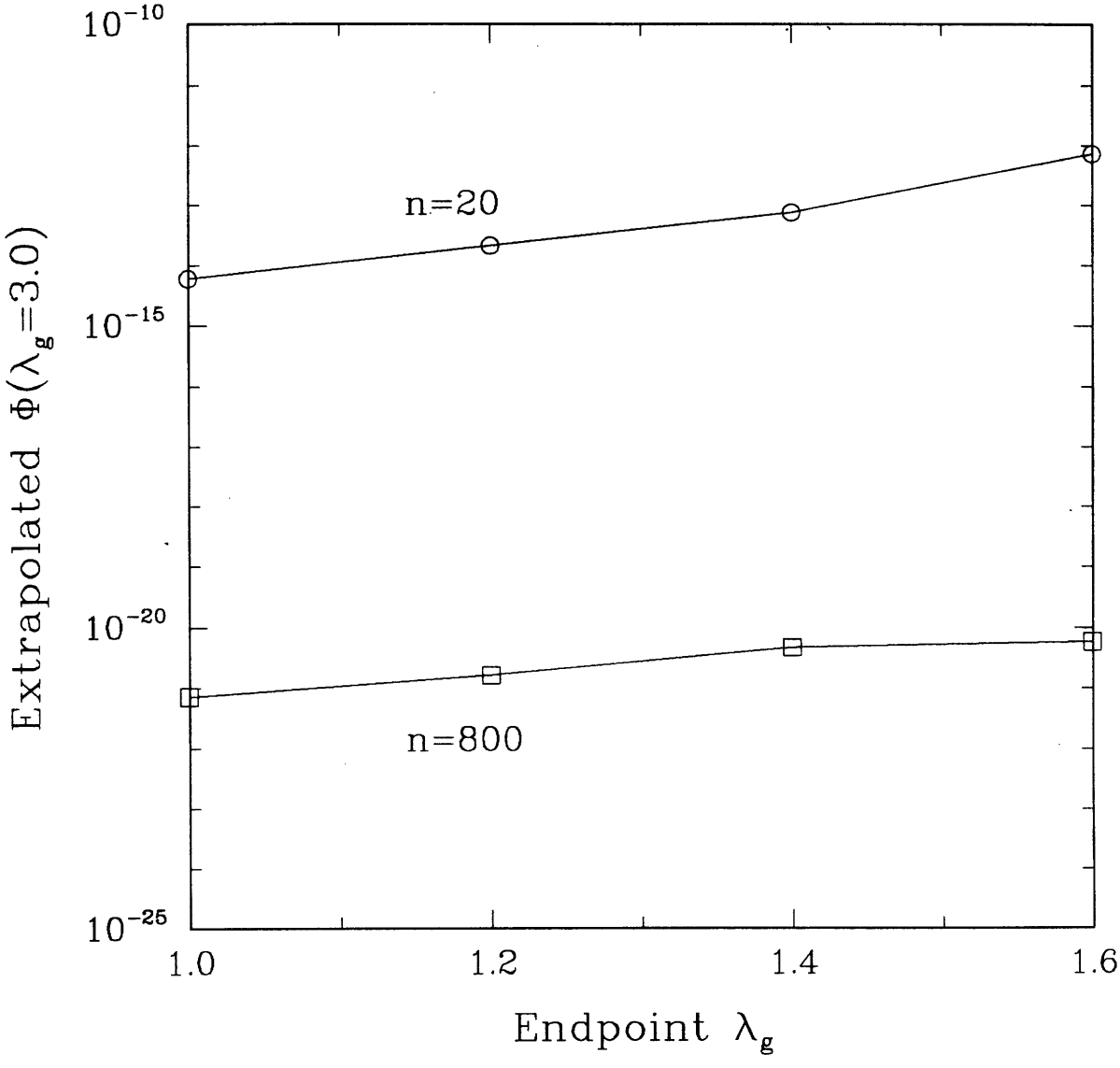

Figure 5-12: Polynomial extrapolation to $\Phi(3.0, 0)$ as a function of the extrapolation endpoint λ_g.

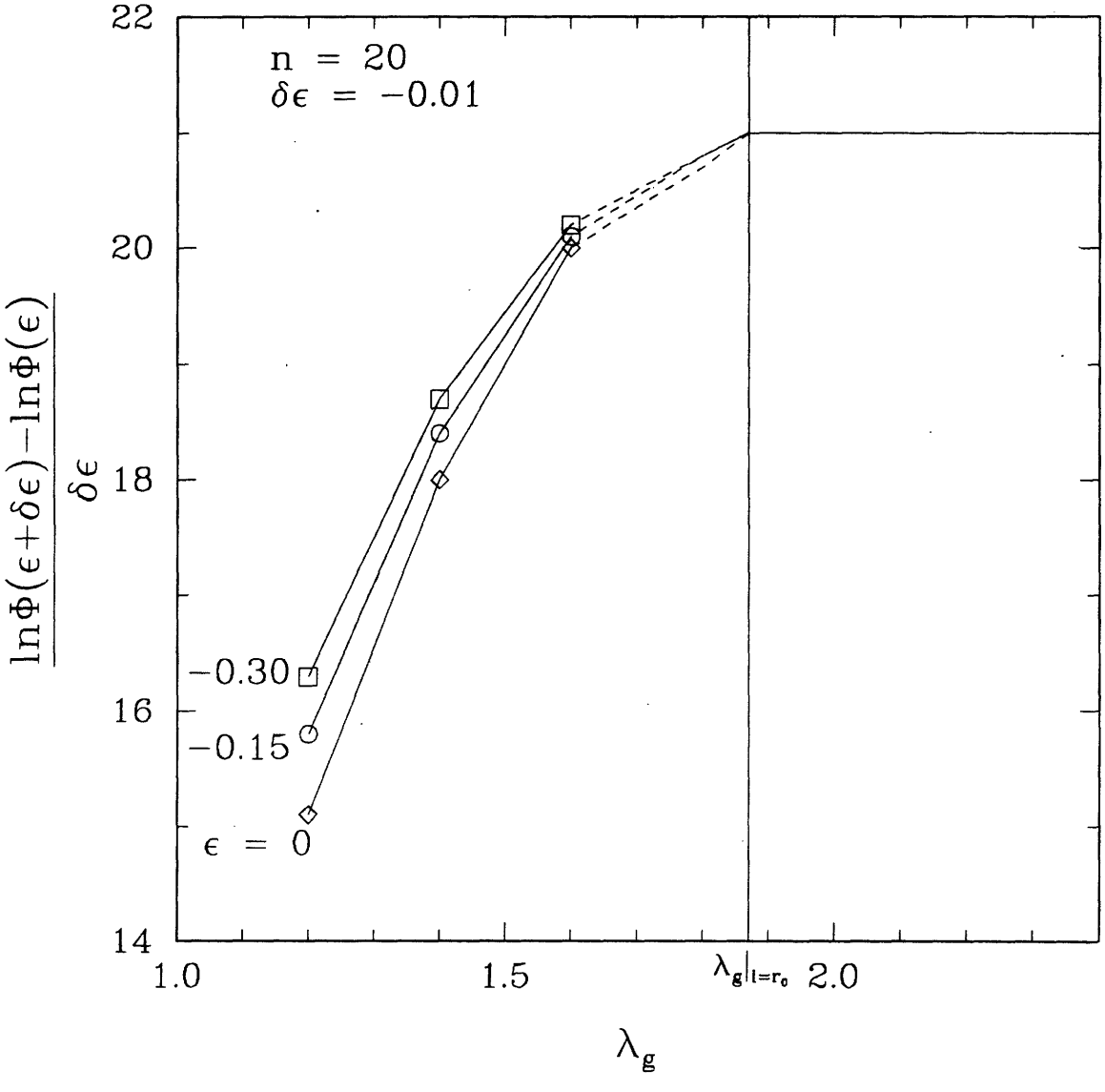

Figure 5-13: $\frac{\partial \ln(\Phi)}{\partial \epsilon} \approx \frac{\ln \Phi(\epsilon+\delta\epsilon)-\ln \Phi(\epsilon)}{\delta\epsilon}$ as a function of λ_g for $n = 20$. Symbols indicate values from Monte Carlo simulations, dotted lines are linear extrapolations from the value at $\lambda_g = 1.6$ to the value at $\lambda_g|_{l=r_0}$.

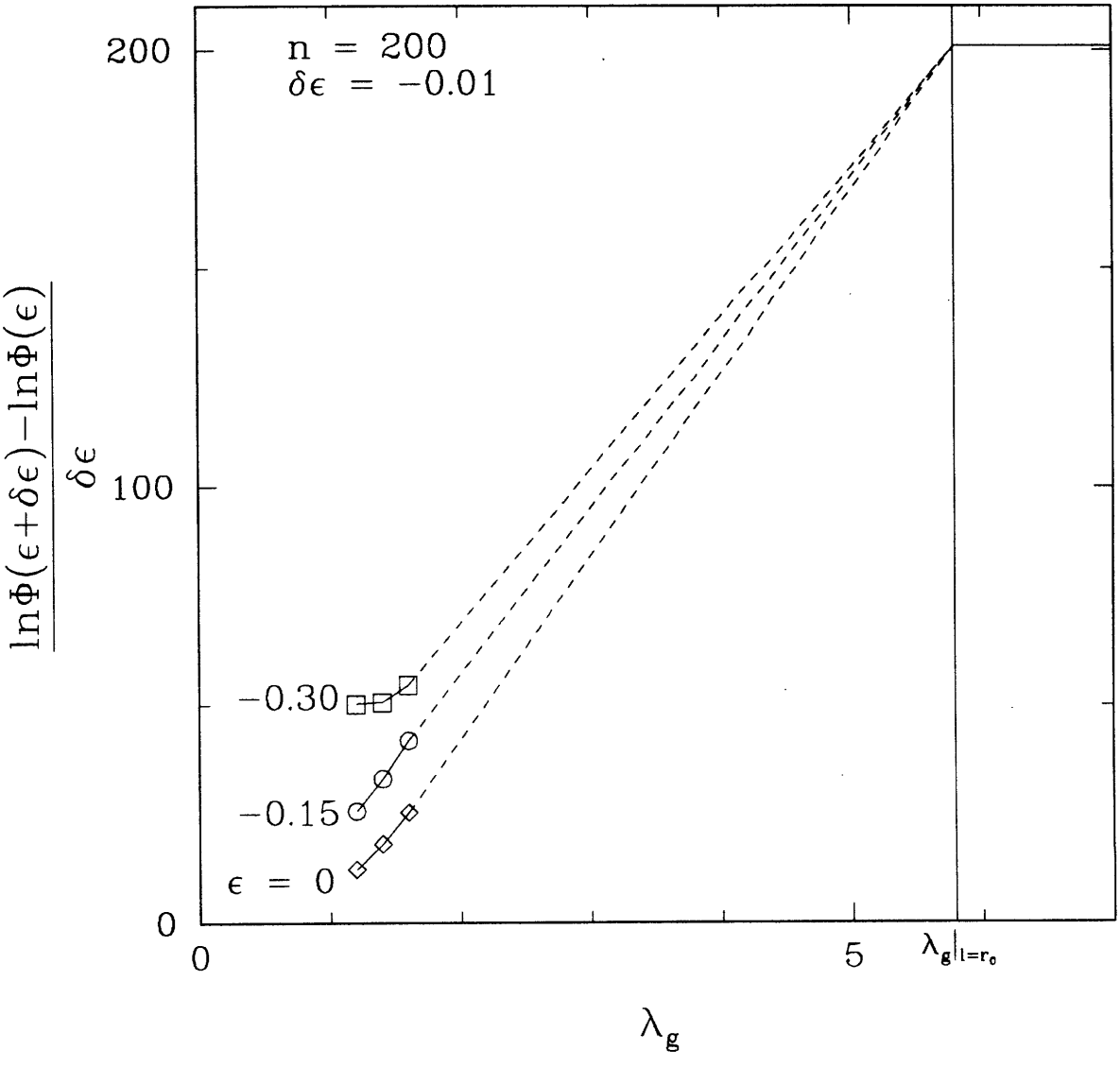

Figure 5-14: $\frac{\partial \ln(\Phi)}{\partial \epsilon} \approx \frac{\ln \Phi(\epsilon+\delta\epsilon) - \ln \Phi(\epsilon)}{\delta\epsilon}$ as a function of λ_g for $n = 200$. Symbols indicate values from Monte Carlo simulations, dotted lines are linear extrapolations from the value at $\lambda_g = 1.6$ to the value at $\lambda_g|_{l=r_0}$.

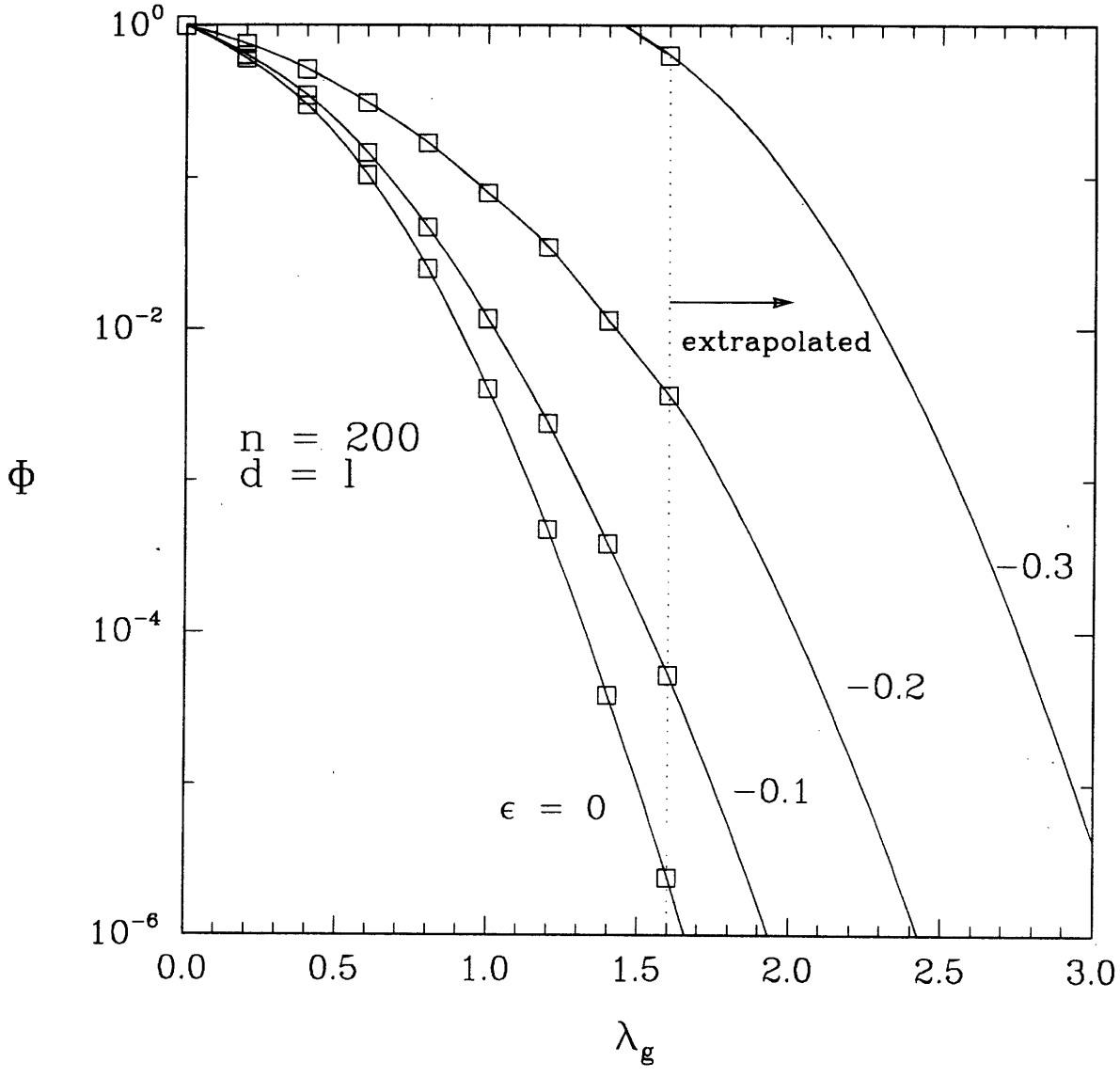

Figure 5-15: Extrapolated values ($\lambda_g > 1.6$) of Φ as a function of ϵ for $n = 200$.

5.5.3 Radial Flow-Averaged Steric Parameter (Ω)

One approach to calculating Ω at large λ_g would be to use a similar procedure to that just described for Φ. As an alternative to explicit calculation, we can devise a semi-empirical means of relating Ω to Φ. To begin, we note that, from Eqs. 5.3 and 5.4,

$$\Omega = 2\Phi - 4\int_0^1 p(\lambda, \hat{r})\hat{r}^3\, d\hat{r}. \tag{5.16}$$

Then, theoretically, $\lim_{p\to 0}\Omega = 2\Phi$. We then ask whether the limit as $\lambda_g \to \infty$ is equivalent:

$$\lim_{\lambda_g\to\infty}\Omega \stackrel{?}{=} \lim_{p\to 0}\Omega = 2\Phi. \tag{5.17}$$

For a solid sphere, this is true because $p = 0$ for $\lambda_g > 3/5$ (*e.g.*, $\lambda_s > 1$). For a random coil, Eq. 5.17 appears to be valid from the Monte Carlo results (see Figure 5-16). In fact, Ω/Φ is rather insensitive to both n and ϵ and can be approximated by a simple exponential dependence on λ_g. It should be noted that in the limit of large λ_g, the full pore potential is reached and Ω/Φ will be the same for all values of ϵ. At $\lambda_g > 1.6$,

$$\Omega/\Phi \approx 2 \tag{5.18}$$

provides a reasonable approximation, and this was the relation used to calculate Ω. Values of Ω for $n = 200$ are plotted in Figure 5-17.

As mentioned in Section 5.4.2.3, the ratio was also used a means of assessing the quality of the Monte Carlo results. Anomalous behavior such as that shown by the data for $\lambda_g = 1.8$, $\epsilon = -0.2$ (Figure 5-16) was one of the reasons the results at $\lambda_g = 1.8$ were not used for further calculations.

The physical significance of this ratio and its asymptotic limit is not clear. The ratio can be written as

$$\frac{\Omega}{\Phi} = 2 - 2\frac{\int_0^1 p(\lambda_g, \hat{r})\hat{r}^3\, d\hat{r}}{\int_0^1 p(\lambda_g, \hat{r})\hat{r}\, d\hat{r}} \equiv 2 - 2\xi, \tag{5.19}$$

where ξ is the ratio of the third moment of p to its first moment. From moment theory[254] we can construct bounds on ξ:

$$\left(\frac{\Phi}{\langle p\rangle}\right)^3 \leq \xi \leq \frac{\Phi}{\langle p\rangle}, \tag{5.20a}$$

$$\langle p\rangle \equiv \int_0^1 p(\lambda_g, \hat{r})\, d\hat{r} = 0^{th} \text{ moment.} \tag{5.20b}$$

(5.20c)

And so it seems a more detailed examination of $\Phi/\langle p\rangle$ would give some insight into the physical significance. Unfortunately, since information on $\langle p\rangle$ is not normally available, this is not generally useful.

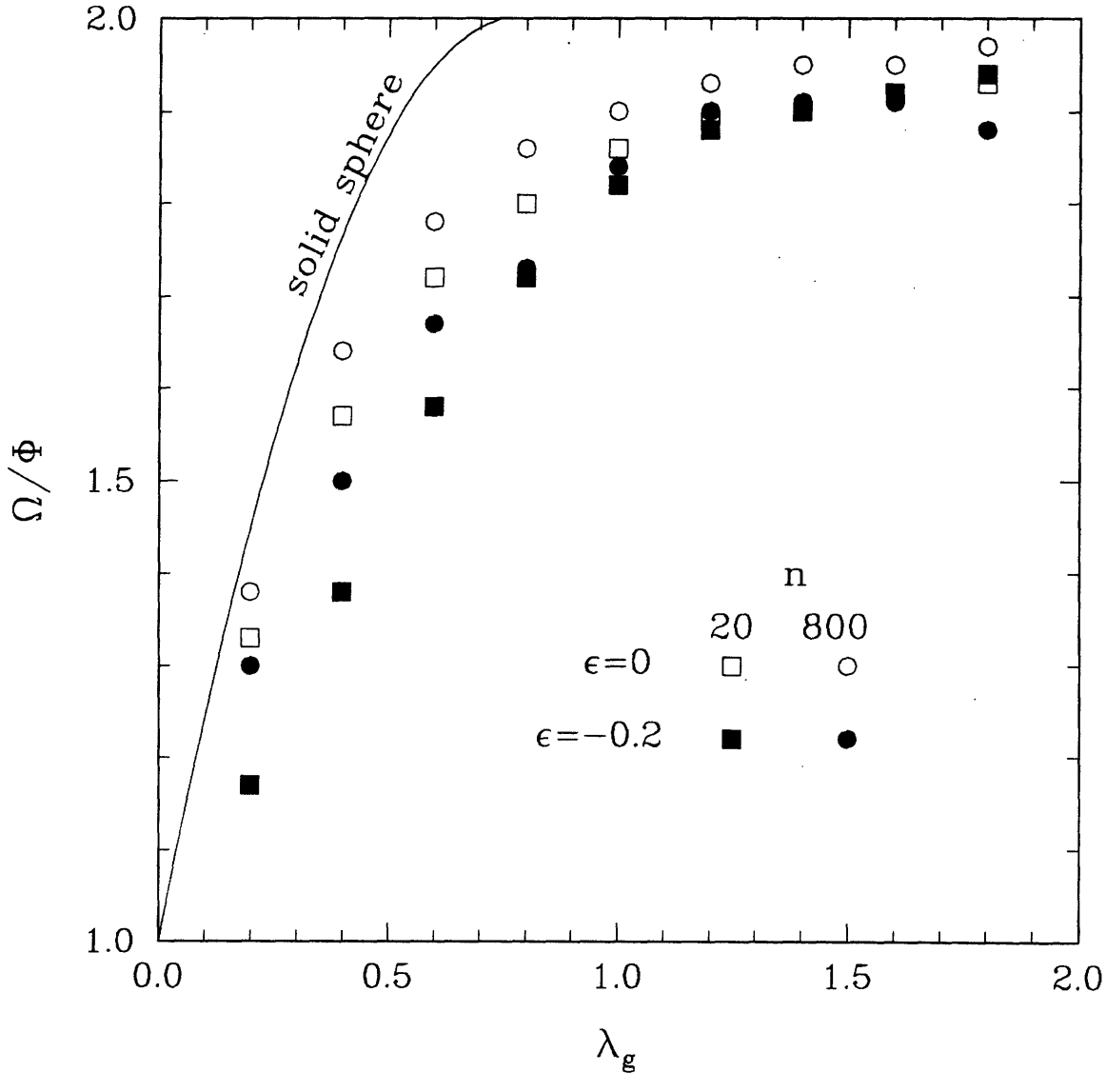

Figure 5-16: Ω/Φ for $n = 20$ and $n = 800$. Solid sphere theory is shown by solid curve.

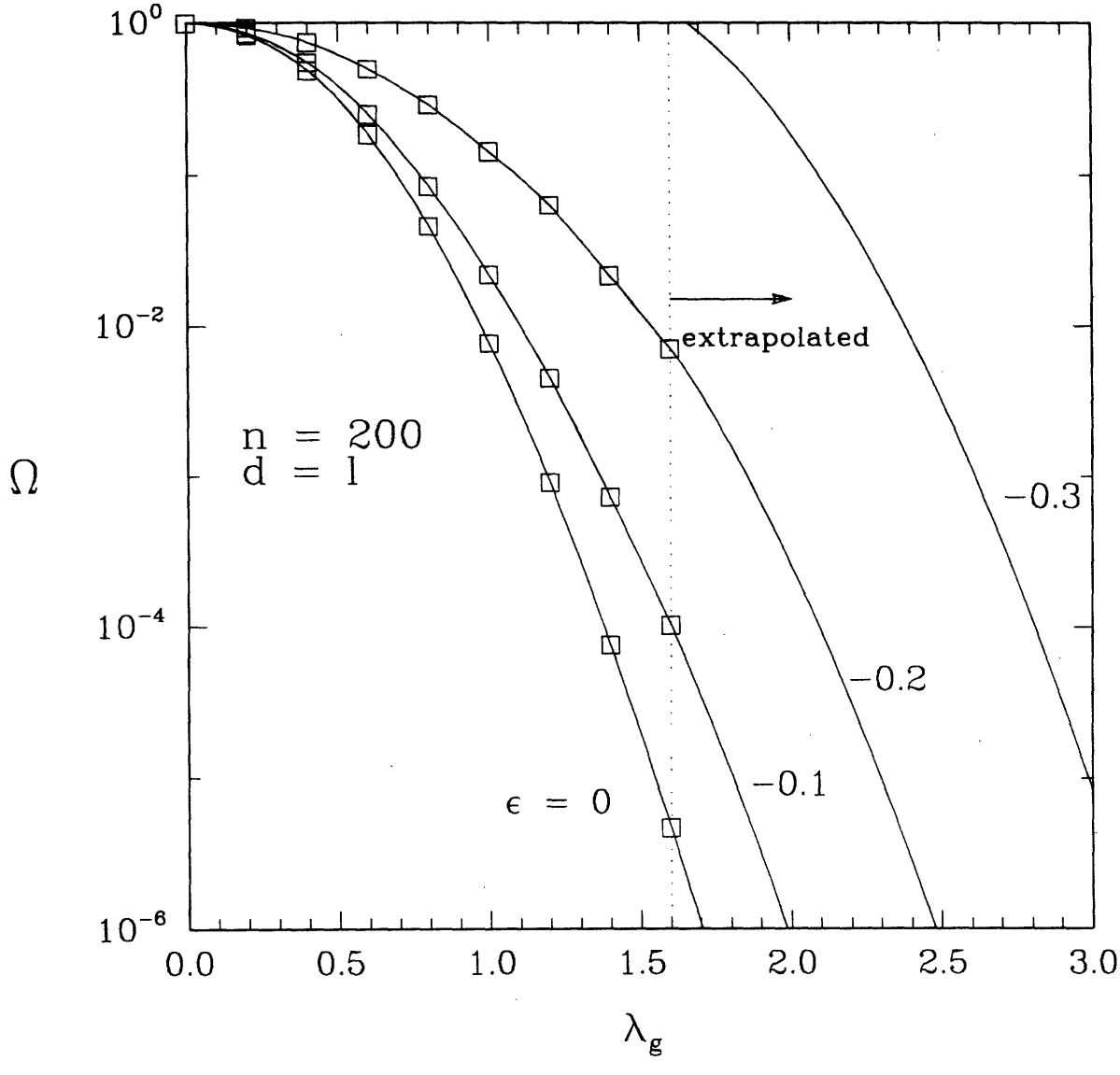

Figure 5-17: Extrapolated values ($\lambda_g > 1.6$) of Ω as a function of ϵ for $n = 200$.

5.6 Estimation of Hydrodynamic Parameters at Large λ_g

Extrapolation of the hydrodynamic parameters K^{-1} and G to large λ_g is less problematic because they vary roughly as $\exp(-\lambda_g)$, as opposed to Φ and Ω which vary almost as $\exp(-\lambda_g^2)$. Thus, the order of magnitude of H and W are insensitive to K^{-1} and G at large λ_g, and any simple function which satisfies the asymptote should be acceptable. We fit the data of Davidson and Deen[72] to the following exponentials:

$$K^{-1} = \exp(-1.798\lambda_g), \tag{5.21a}$$

$$G = 0.5\exp(-0.6146\lambda_g) + 0.5. \tag{5.21b}$$

These equations were fitted using their data for all three values of α_H, a parameter which is a measure of the flow resistance through the interior of the coil and which is a function of r_s/r_g:[72]

$$\alpha_H = \frac{5.77 \times (2.5981(r_s/r_g))}{2.22 - (2.5981(r_s/r_g))}. \tag{5.22}$$

The values of α_H used (10, 34, and 60) correspond to $r_s/r_g = 0.54$, 0.73 and 0.78. The hydrodynamic coefficients are actually relatively insensitive to α_H, and in fact use of any one the three values would give nearly the same result for the sieving coefficient.

5.7 Interpolation Procedure for Sieving Calculations

Tables of $\ln\Phi$ and $\ln\Omega$ as functions of number of chain segments (n = 20, 50, 100, 200, 400, 800), λ_g (= 0.0 to 7.0 by 0.2) and ϵ (= −0.30 to 0.0 by 0.01) were created, with values for $0 \leq \lambda_g \leq 1.6$ calculated by Monte Carlo simulation and values for $1.6 \leq \lambda_g \leq 7.0$ calculated by the extrapolation procedure of Section 5.5. For the full-pore potential, Φ and Ω were calculated for the neutral case, and energetic attractions were added by applying Eqs. 5.11.

Similar tables for K^{-1} and G as functions of λ_g (= 0.0 to 1.6 by 0.2) and α_H (= 10, 34, and 60) were constructed from the data of Davidson and Deen.[72] Values for $\lambda_g > 1.6$ were calculated from Eqs. 5.21.

A multidimensional interpolation scheme[206] was used to perform the calculations, with the algorithm of Akima[3,4] as the method of interpolation in each dimension.

In order to maintain consistency for comparison with the *in vitro* measurements of Davidson and Deen,[71] the following correlations for dextran molecular radii were used, fitted to data of Callaghan and Pinder[48] for r_s and that of Garg and Stivala[109] for r_g, with the radii in Å:

$$r_s = 0.245M_w^{0.5}, \tag{5.23a}$$

$$r_g = 0.323M_w^{0.5}. \tag{5.23b}$$

Eqs. 5.23 were fit assuming ideal coil behavior (*i.e.*, the exponent fixed at 0.5). For determination of n, a monomer was taken to be an equivalent Kuhn segment, and so $n = M_w/162$.

5.8 Theoretical Effect of ϵ on Glomerular Sieving

Theoretical sieving curves for dextran random coils which follow Eqs. 5.23 are compared to that of a neutral solid sphere in Figure 5-18. An isoporous membrane radius of 50 Å was assumed, using as hemodynamic inputs the single nephron values of Table 4.2 for combined dextran and Ficoll rats. As expected from the results for H and W of Davidson and Deen,[72] Θ for a neutral random coil of intermediate r_s is lower than that of a neutral solid sphere. An energetic attraction of between -0.1 and $-0.2\ k_BT$ per mass point is required for $\Theta_{coil} \approx \Theta_{sphere}$. Because $\Theta_{sphere} = 0$ for $r_s \geq 50$ Å, $\Theta_{coil} > \Theta_{sphere}$ for sufficiently large r_s, at any value of the energy parameter. Figure 5-19 shows the equivalent plot for the full-pore potential. There is little qualitative difference between the two figures, although the energy value at which $\Theta_{coil} \approx \Theta_{sphere}$ is now approximately $-0.01 k_BT$.

The presence of even very small attractive energies is seen to have significant effects on the sieving coefficients, especially for large molecules. The Θ of a 50 Å dextran is raised three orders of magnitude when ϵ changes from 0 to -0.25 in the $d = l$ model, or from 0 to -0.03 in the $d = r_0$ model.

5.9 Fit of Energy Parameter to Dextran Sieving Data

5.9.1 Methods

Values of ϵ were fit to the dextran data of Chapter 4 using Powell's method,[206] as described in Section 4.2.5. The isoporous + shunt, lognormal, lognormal + shunt, and double lognormal pore distributions were examined, with pore size parameters fixed at those obtained from Ficoll sieving curves (Table 4.4). The single nephron hemodynamic parameters for the combined dextran and Ficoll rats (Table 4.2) were used as model inputs. Pore/solute attractions were assumed to have no effect on coils traveling through the shunt.

5.9.2 Results

The best-fit values for ϵ are reported in Table 5.2 for each pore size distribution and are plotted in Figure 5-20 for the $d = l$ case and Figure 5-21 for the $d = r_0$ case. The values for the $d = l$ case are nearly identical for all distributions, with $\epsilon \approx -0.25$. In turn, this is very similar to the value of -0.26 reported by Davidson and Deen[71] using the same model for the transport of dextran through polycarbonate membranes. Thus it seems that the nature of dextran's enhanced transport is quantitatively independent of the medium through which it travels. The isoporous + shunt model does not provide a good description of the data because the energy term has no effect on sieving

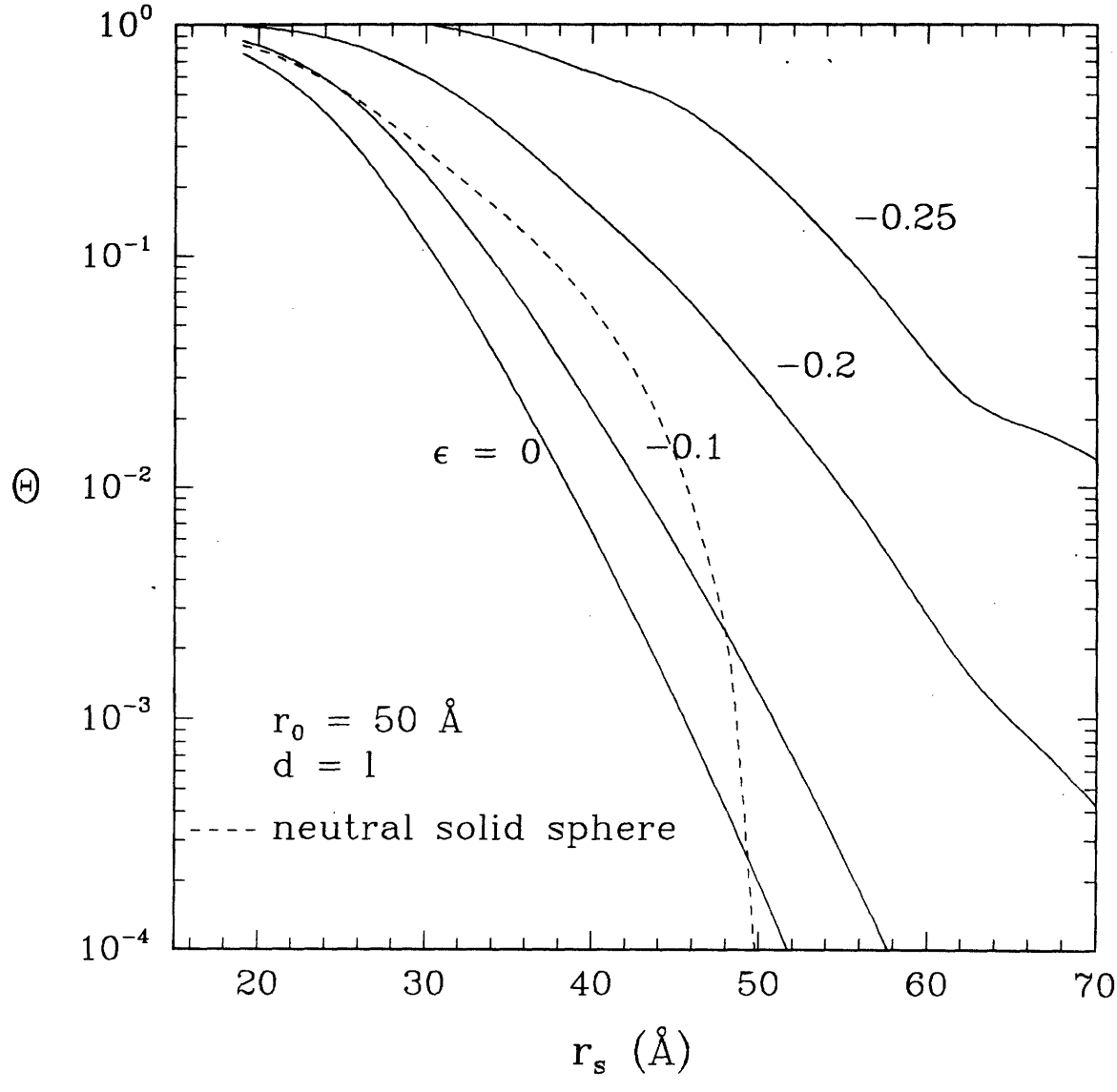

Figure 5-18: Effect of energy parameter ϵ on Θ for isoporous membrane with $r_0 = 50$ Å, $d = l$ case. Dashed lines represents results for neutral solid sphere. Hydrodynamic inputs are total single nephron values in Table 4.2.

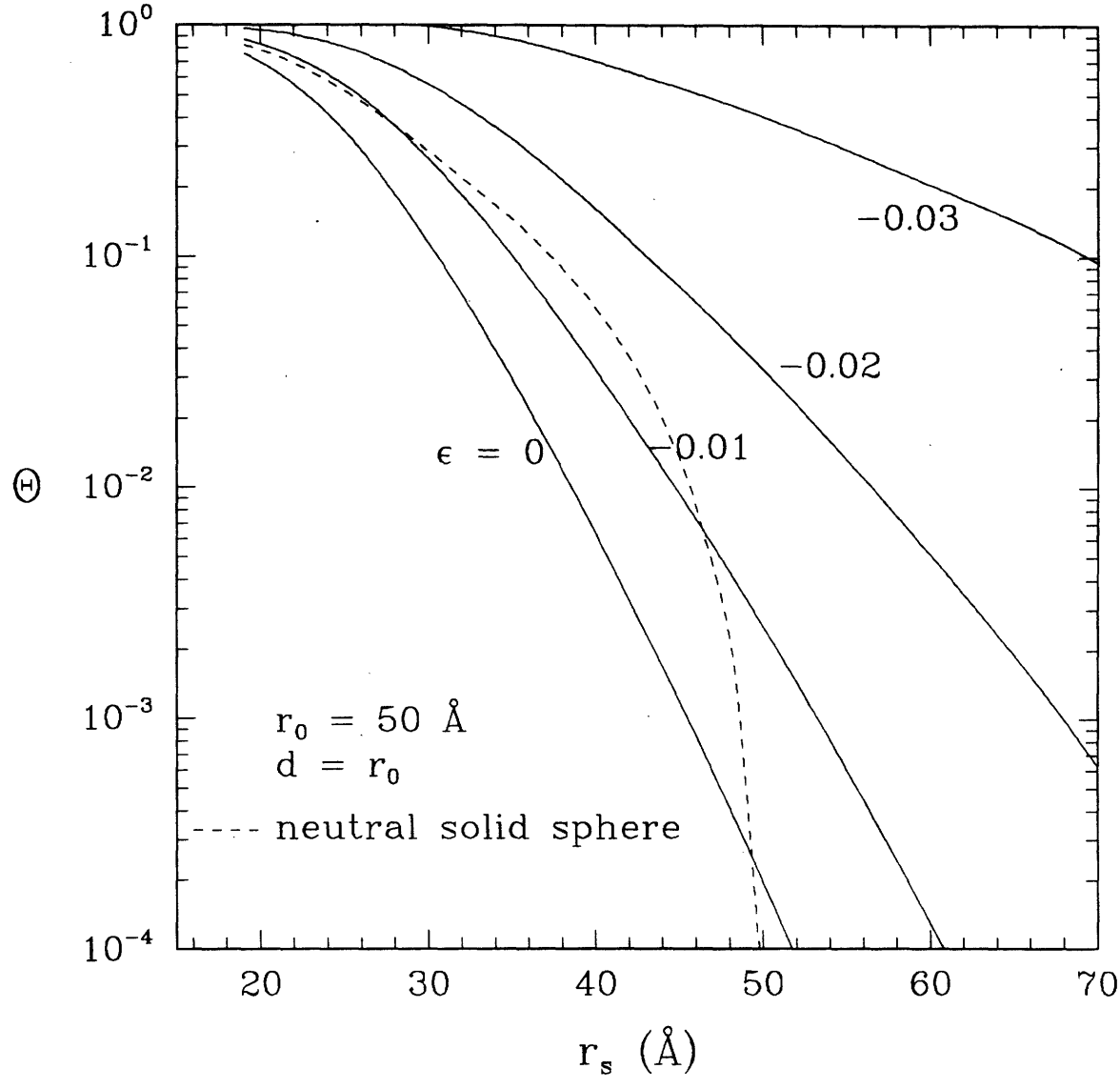

Figure 5-19: Effect of energy parameter ϵ on Θ for isoporous membrane with $r_0 = 50$ Å, $d = r_0$ case. Dashed lines represents results for neutral solid sphere. Hydrodynamic inputs are total single nephron values in Table 4.2.

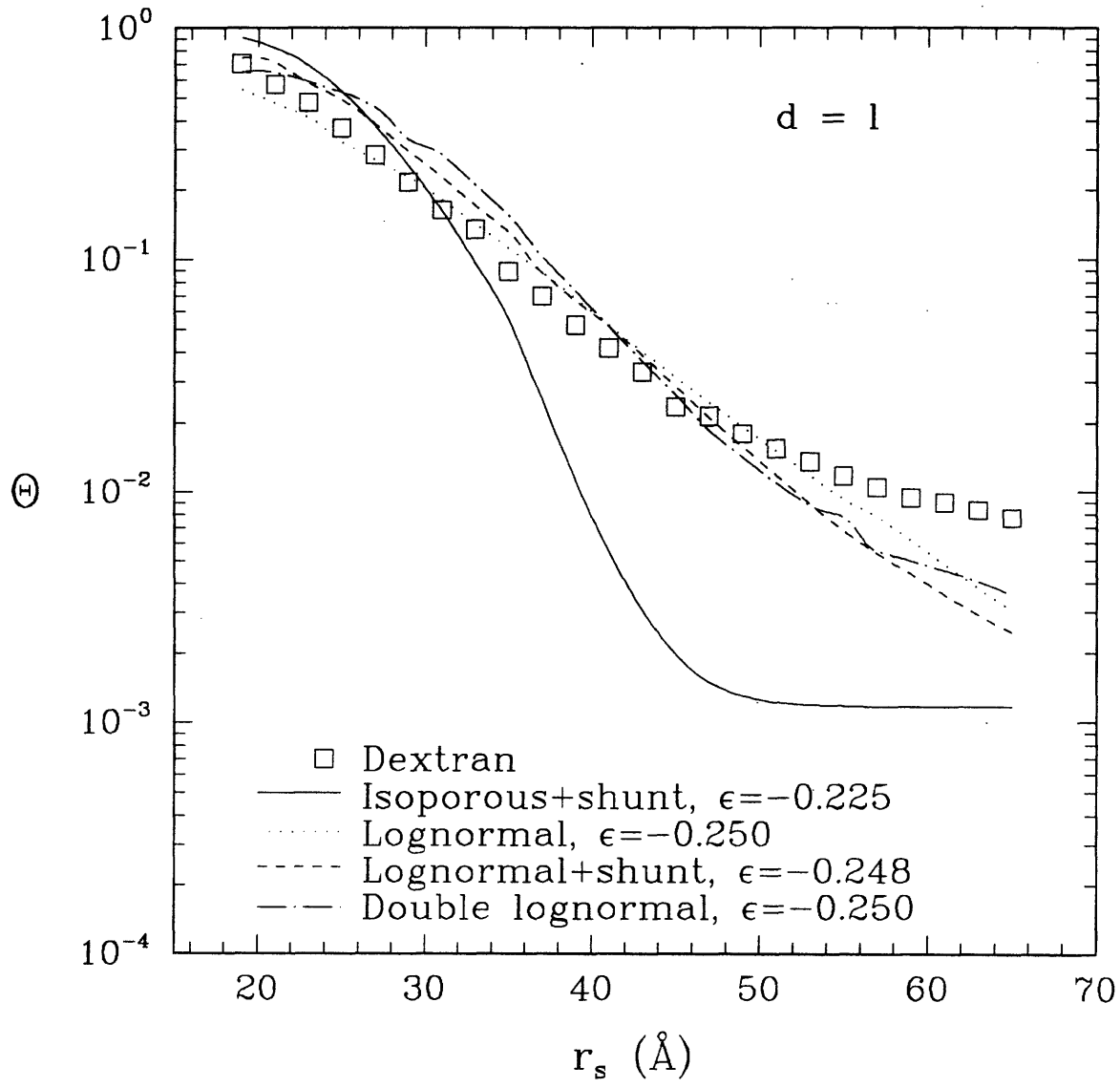

Figure 5-20: Fit of energy parameter ϵ to dextran data for various heteroporous models, $d = l$ case.

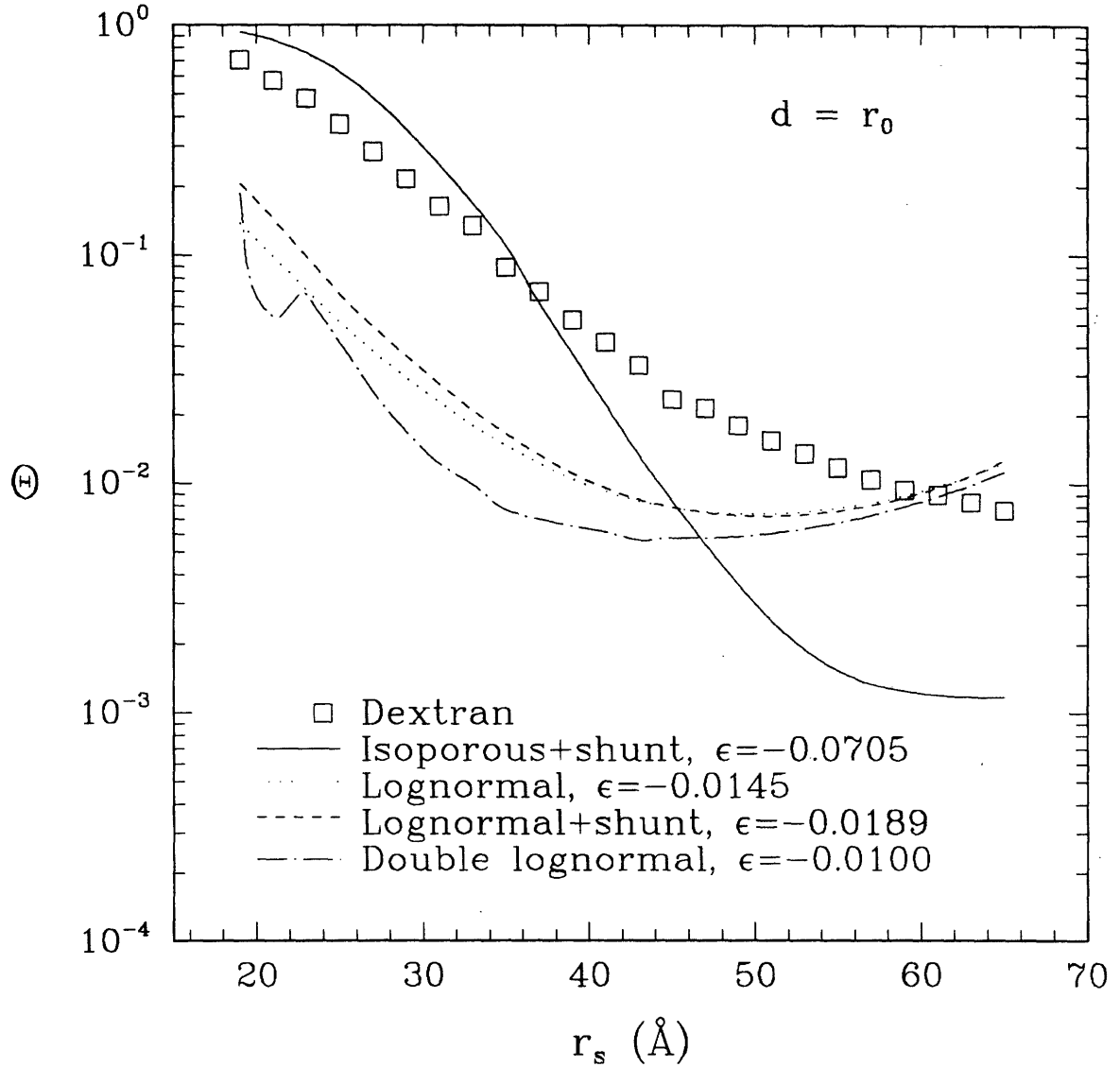

Figure 5-21: Fit of energy parameter ϵ to dextran data for various heteroporous models, $d = r_0$ case.

Model	$d =$	ϵ	χ^2
Isoporous	l	-0.225 ± 0.012	444
+shunt	r_0	-0.0705 ± 0.0023	386
Lognormal	l	-0.250 ± 0.017	60.6
	r_0	-0.0145 ± 0.0063	362
Lognormal	l	-0.248 ± 0.003	112
+shunt	r_0	-0.0192 ± 0.0007	349
Double	l	-0.250 ± 0.003	129
lognormal	r_0	-0.0100 ± 0.0007	409

Table 5.2: Fit of energy parameter ϵ to dextran data using Ficoll pore parameters of Table 4.4.

through the shunt and hence the transport of large molecules is not enhanced (Figure 5-20). The fits provided by the other three distributions are similar, with the lognormal model having the best-fit as measured by χ^2 values.

There is more variability in the values of ϵ for the $d = r_0$ cases, with the isoporous + shunt value being six to seven times that of the three continuous distributions. For the $d = r_0$ case, the isoporous + shunt model is similar to its $d = l$ counterpart (Figure 5-21). The plots for the other three distributions are in very poor agreement with the data. The curves anomalously reach a minimum around 40–50 Å and then begin to increase with r_s.

The explanation for this is seen when one examines the degree of sieving through large versus small pores. We define the value Θ_{extrap} as the amount of the sieving coefficient that is due to transport through pores smaller than $r_g/1.6$ (*i.e.*, $\lambda_g > 1.6$):

$$\Theta_{i,\text{extrap}} = \int_0^{r_g/1.6} \Theta_i(r)\omega(r)\,dr, \tag{5.24}$$

where $\Theta_i(r)$ is the isoporous sieving coefficient defined by Eq. B.1a and $\omega(r)$ is the fractional filtrate volume defined by Eq. B.1b. $\Theta_{i,\text{extrap}}$ corresponds to the part of the sieving coefficient calculated from the extrapolated approximations to large λ_g. These values are shown as a fraction of the total Θ_i in Table 5.3 for each distribution. For the $d = l$ cases, the extrapolated fractions are on the order of 5–30%, with higher percentages seen at the largest r_s for the lognormal and lognormal + shunt models, and in the middle values of r_s for the double lognormal model. For the $d = r_0$ cases, the trends are similar, but the amount of extrapolation is much smaller, less than 1% in all cases and predominantly less than 0.1%. This implies that, for the $d = r_0$ cases, even though there are very few large pores, they conduct the preponderance of the transport of large molecules due to the energetic attractions. For example, at $r_s = 65$ Å, $r_g/1.6 = 53.4$ Å. From the pore size distributions for the Ficoll data (Figure 4-3), 1% or less of the total volume flux is going through pores larger than 53.4 Å, yet these pores account for over 99% of the transport of the largest dextrans. This is

	$d = l$			$d = r_0$		
r_s	Lognormal	Lognormal + Shunt	Double Lognormal	Lognormal	Lognormal + Shunt	Double Lognormal
19	4.2	2.8	0.9	0.027	0.021	0.004
21	4.9	3.5	0.9	0.021	0.021	0.008
23	5.3	4.5	1.1	0.019	0.023	0.005
25	6.3	5.3	1.6	0.018	0.025	0.007
27	6.9	6.5	2.6	0.017	0.027	0.013
29	7.2	7.8	4.9	0.016	0.030	0.021
31	7.7	8.9	6.8	0.016	0.034	0.030
33	7.9	9.6	9.4	0.016	0.038	0.034
35	8.6	10.7	12.8	0.017	0.046	0.043
37	9.2	13.4	17.7	0.018	0.052	0.040
39	10.1	14.7	21.6	0.018	0.059	0.035
41	11.1	15.8	25.4	0.019	0.066	0.029
43	11.9	16.9	27.8	0.019	0.074	0.024
45	12.4	18.2	28.6	0.021	0.084	0.019
47	12.9	19.3	29.1	0.022	0.094	0.015
49	13.2	20.1	27.0	0.023	0.104	0.011
51	13.6	21.0	24.6	0.024	0.115	0.008
53	14.2	22.1	21.9	0.025	0.126	0.006
55	14.9	23.0	17.8	0.026	0.138	0.005
57	14.7	23.1	18.2	0.027	0.150	0.004
59	15.7	22.9	15.0	0.028	0.163	0.003
61	17.0	23.1	12.6	0.029	0.177	0.003
63	18.6	23.4	11.1	0.031	0.193	0.002
65	20.3	23.5	10.1	0.033	0.209	0.002

Table 5.3: $\Theta_{i,\mathrm{extrap}}/\Theta_i$ (in %) for random coil fits.

explained by noting that in the full-pore potential, enhancements from attractive energies are seen at all sizes, with significant adsorption at small λ_g (Figures 5-4 and 5-5). In contrast, in the $d = l$ case, only transport of molecules at large λ_g is enhanced (Figures 5-2 and 5-3). Thus, the presence of attractive energies makes transport through all pores more favorable in the $d = r_0$ case, whereas in the $d = l$ case it preferentially makes transport through small pores more favorable. The plots of Figure 5-21 represent the physically unrealistic situation of molecules highly adsorbed to a few large pores with steric parameters > 1. Since adsorption is predicted to increase with n, Θ is predicted to increase with λ_g.

The $d = l$ results are probably more physically realistic, but Θ_{extrap} is still relatively small, on the order of 10–20%. This suggest that greater accuracy in the extrapolation method would not make significant differences in the modeling results.

5.10 Discussion

Alternate possibilities exist for the mechanism behind the enhanced transport of dextran. One possibility is that the hydrodynamic coefficients K^{-1} and G are underestimated by the theory. This issue is easily addressed by modeling dextran as a free-draining coil, for which K^{-1} and G equal unity at all sizes. This case is shown in Figure 5-22 for the lognormal + shunt model in comparison with the results for a neutral coil and a coil with $\epsilon = -0.248$. The hydrodynamic effects are seen to account for at most 50% of the difference for small molecules, and less than 1% of the difference for large molecules.

A more important consideration is the determination of the values of l and n which truly characterize the physical properties of a given dextran molecule. All of the above calculations were performed assuming l corresponded to the length of one glucose monomer. This was consistent with the analysis of the *in vitro* data by Davidson and Deen[71] and would allow for direct comparison with their results. Although there is data to indicate that l may actually correspond to more monomers (see Appendix F), the range of alternative values is rather wide (between four and ten monomers), and this data is not consistent with other measurements that show that dextran exhibits the properties of a polymer at relative low molecular weight.[114] If one wanted to model behavior at different effective Kuhn lengths, a new set of Monte Carlo calculations would have to be performed since it would probably be desirable to still scale d with the size of a monomer, and not the effective Kuhn length.

Another possible explanation is that that chain branching reduces steric effects in a way that cannot be simply explained. The importance of branching for dextran unperturbed dimensions has not been resolved, but assuming that branching was significant, one would expect that a branched chain and a linear chain with equivalent r_g would have quite different distributions of intramolecular distance, with the branched chain being more compact. If each chain branch were only one or two

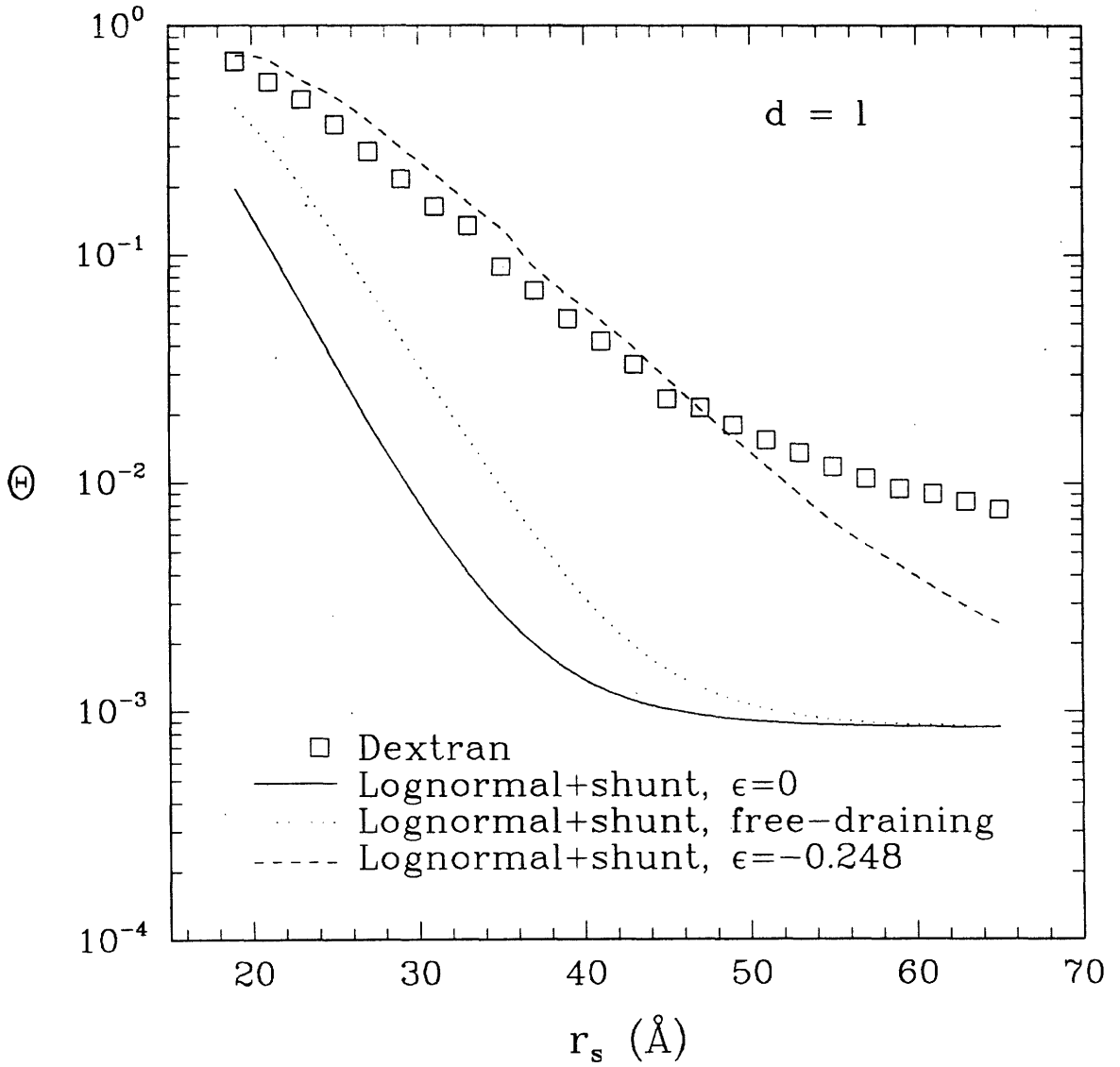

Figure 5-22: Comparison of free draining ($K^{-1} = 1$, $G = 1$) to neutral and attractive coil models. Pore parameters are for the lognormal + shunt model.

glucose residues, then a linear molecule might be justified as a suitable approximation. If, however, there are very large branches, this could have significant consequences. Casassa and Tagami[53] demonstrated that for a "star" configuration, consisting of identical random chains joined at a single branch point, Φ increased as the number of branches increased for a fixed total number of chain segments. Analytical expressions exist for volume correction factors for branched molecules with long side chains of identical length, or for molecules with a random distribution of branches,[154] and these could be applied as a first-order correction, but one must then determine the dependence of effective n and l on molecular weight. Most importantly, the effect on the partition coefficients would be much more significant than a simple adjustment for r_g.

In summary, we have used recent theoretical developments in the study of hindered transport to describe dextran sieving as the filtration of random coils through cylindrical pores. Dextran's transport both *in vivo* and *in vitro* is enhanced over that of a neutral coil, and it can be accounted for by the assumption of attractive solute/pore interactions. The magnitude of these interactions is nearly identical for the glomerulus and synthetic membranes, and indicates that the nature of the enhancement is independent of the medium through which dextran travels. This model is strictly descriptive, as there is no physical evidence to support the idea of solute/pore attractions. Nevertheless, such a model is the first step in attempting to understand the mechanism by which molecules of different configuration are filtered through the glomerular capillary.

Chapter 6

Ficoll Sieving in Fawn-Hooded Rats

6.1 Introduction

6.1.1 The Fawn-Hooded Rat

The fawn-hooded (FH) rat is a strain with a genetic predisposition to developing hypertension, hyperfiltration, proteinuria, and glomerulosclerosis at a young age.[151,153] As such, the FH rat model may serve as a closer approximation of essential renal disease in human beings than previous models. FH rats have increased $\overline{\Delta P}$ and *SNGFR* compared to normotensive Munich-Wistar rats.[230] A particular inbred substrain, denoted "FHH", has the highest susceptibility to hypertension, proteinuria, and sclerosis among the FH rats.

6.1.2 The Model of Renal Ablation

Surgical infarction of renal tissue ("renal ablation") is a well-studied model for chronic hypertension in the rat.[6,7,55,56,64,80,123,128,142,175,188,189,191,197,198,208,227] Common protocols are for the ablation of from 1/2 (uninephrectomy) to 15/16 of the renal mass. The animal responds by shifting renal blood flow to the remaining functional nephrons, resulting in larger values of Q_A and *SNGFR*. K_f is relatively unchanged, and thus *SNFF* falls. Transmural hydraulic pressure ($\overline{\Delta P}$) increases substantially, on the order of 5–15 mm Hg. Proteinuria ensues, and the remaining functional glomeruli eventually become sclerotic, establishing a cycle which ultimately leads to kidney failure. If a renal-ablated rat is treated with angiotensin I converting enzyme (ACE) inhibitor[6,7,175] or a low-protein diet,[175] $\overline{\Delta P}$ is normalized and K_f increases, with *SNGFR* maintained relatively constant. Depending on how early therapy commences, renal damage is either prevented or arrested. Conversely, a traditional "triple-drug" regimen for hypertension, which lowers systemic blood pressures but not $\overline{\Delta P}$, fails to stop progression of proteinuria and glomerulosclerosis.[7] Glomerular hypertension has thus been implicated as an important mediator in the progressive impairment of renal function.[35,38]

6.1.3 Enalapril and NAME

Two pharmacological agents are of particular importance to the work described in this chapter. Enalapril is an ACE inhibitor which has seen extensive use both clinically and in animal studies of glomerular hypertension and hyperfiltration.[7,124,125,131,173,175,183,202,204,212,213,221,266] Physiologically, it lowers efferent arteriolar resistance and increases K_f, resulting in the maintenance of *SNGFR* at lowered $\overline{\Delta P}$. In addition to pressure normalization, ACE inhibitors are believed to have

additional independent protective renal effects, including the raising of kinin activity.[99,130,131,183]

NAME (Nω-nitro L-arginine methyl ester) is a substituted L-arginine compound which blocks nitric oxide (NO) synthesis. Nitric oxide (also known as endothelial-derived relaxing factor) is made by the vascular endothelium and relaxes adjacent smooth muscle cells.[181] Other data suggest that NO and angiotensin II have directly antagonistic effects in glomerular filtration and tubular reabsorption.[75,229,241] Additionally, NO has been proposed as a mediator in the hyperfiltrative response of the glomerulus to amino acids.[75,143,241]

Blockage of NO synthesis (with NAME or other substituted L-arginine compounds) leads to acute increases in both systemic and glomerular blood pressure.[1,16,85,108,209,265] Chronic administration of NAME to rats has been shown to increase $\overline{\Delta P}$, proteinuria, and glomerulosclerosis.[18,58,217] Physiologically, NAME increases both afferent and efferent arteriolar resistances and decreases K_f. The result is decreased capillary blood flow and increased $\overline{\Delta P}$, with *SNGFR* maintained relatively constant.

6.1.4 Objectives

Ficoll sieving studies were performed on groups of FHH rats to study the effect of hyperfiltration and hypertension and subsequent pharmacological interventions on glomerular size-permselectivity. Uninephrectomy was performed on the FHH rats to accelerate the progression of the renal disease. Untreated and treated uninephrectomized rats were compared with two-kidney controls. These experiments also provided a database for the further study of pressure estimation from sieving curves (Chapter 7).

6.2 Materials and Methods

6.2.1 Preparation of Radiolabeled Polymers

Tritiated Ficoll was prepared as described in Section 4.2.1.

6.2.2 Animal Studies

Animal care and preparation, whole kidney measurements, and micropuncture studies were performed by Dr. Jacob L. Simons and Julia L. Troy of the Laboratory of Kidney and Electrolyte Physiology at Brigham and Women's Hospital.

6.2.2.1 Animals

A total of 43 male FHH rats were studied. All were fed *ad libitum* standard rat chow (Wayne Rodent Blox, Allied Mills, Chicago, IL) containing $\approx$ 24% protein by weight and allowed free access to water for the first eight weeks of life. At eight weeks, all rats were anesthetized with ethyl ether

and underwent either uninephrectomy or sham operation. For uninephrectomy, the right kidney was removed after exposure by a midline incision of the body wall and careful separation from the adrenal gland and associated connective tissue. For the sham operation, the right kidney was gently manipulated but otherwise left intact. All micropuncture and sieving studies were performed at twelve weeks of age.

The first group (2K, $n = 17$) consisted of normal two-kidney control animals which underwent the sham operation. After the operation, they resumed the normal diet. Micropuncture without Ficoll sieving analysis was performed on eight of the 2K animals, sieving analysis without micropuncture was performed on five, and four animals received both.

A second group of animals (UNX, $n = 9$) were uninephrectomized. After surgery, the rats resumed the standard diet and water. Both micropuncture and sieving studies were performed on all rats in this group.

A third group of rats (ENA, $n = 8$) also received uninephrectomy but after surgery were given a water supply containing 250 mg/l enalapril (Merck, Sharp & Dohme, West Point, PA). Both micropuncture and sieving studies were performed on all rats in this group.

The fourth group of rats (NAME, $n = 9$) were uninephrectomized and after surgery were given a water supply containing 50 mg/l NAME. The NAME was freshly made every other day and protected from exposure to light. Micropuncture plus sieving analysis was performed on four of these animals, while five received micropuncture only.

6.2.2.2 Surgical Preparation

Animals were prepared for micropuncture and tracer infusion as described in Section 4.2.2.2. Urine was collected from rats during two successive 24-hour periods for determination of urinary protein and albumin excretion.

6.2.2.3 Whole Kidney Hemodynamic Measurements

Whole kidney measurements were performed as described in Section 4.2.2.3.

6.2.2.4 Micropuncture Measurements

Micropuncture measurements were performed as described in Section 4.2.2.4 with the following differences. Since FH rats do not have surface glomeruli, glomerular pressures were measured by the stop-flow technique: time-averaged hydraulic pressures were measured directly in superficial proximal tubules under free-flow (P_T) and stop-flow (P_{SF}) conditions using a servo-null micropipette transducer system (Model 5A, Instrumentation for Physiology & Medicine, San Deigo, CA). Stop-flow conditions were obtained by injecting bone wax (Ethicon W-31G) blocks into proximal tubules using a wax blocking device (Research Instruments & Mfg., Corvallis, OR). At least 3 to 4 P_{SF}

recordings in different nephrons, with a minimum duration of 2 to 4 min each, were obtained during each experiment. Glomerular capillary hydraulic pressure was then calculated as $\overline{\Delta P} = P_{SF} + \pi_{SF} - P_T$.[115]

6.2.2.5 Tracer Infusion and Collection

Tracer infusion and collection was performed as described in Section 4.2.2.5.

6.2.2.6 Analytical Methods

Inulin, serum protein, PAH, and oncotic pressures were measured as described in Section 4.2.2.6.

Urinary total protein excretion ($U_p\dot{V}$) was measured by turbidimetric assay.[34] Urinary albumin excretion ($U_a\dot{V}$) was measured by immunodiffusion.[170] The urinary "non-albumin" excretion ($U_{(p-a)}\dot{V} \equiv U_p\dot{V} - U_a\dot{V}$) was calculated as the difference of the two. The non-albumin proteins are predominantly α-, β-, and γ-globulins, all with isoelectric points higher than albumin's. The fractional clearance of protein i is defined as

$$FRC_i = \frac{U_i\dot{V}}{GFR \cdot c_{i,A}}. \tag{6.1}$$

Since afferent albumin concentrations were not measured, they were estimated to be one-half the total serum protein concentration. It has been shown that the fraction of plasma albumin concentration to total plasma protein concentration does not change with uninephrectomy [Dr. A. P. Provoost, private communication]. Thus, although the absolute values of FRC_i may not be accurate, the relative values are valid for comparison. Unlike for Ficoll, for proteins $FRC \neq \Theta$ because they are actively reabsorbed in the tubules.

6.2.3 Fractionation of Radiolabeled Plasma and Urine Samples

Fractionation of the plasma and urine samples was performed as described in Section 4.2.3.

6.2.4 Calculation of Sieving Coefficients

Sieving coefficients were calculated as described in Section 4.2.4.

6.2.5 Data Analysis

Pore size parameters and their standard errors were calculated using the models and methods described in Section 4.2.5. Statistical comparisons were made using one-way analysis of variance, with Scheffe's test used to determine significant differences. The Pearson correlation coefficient was used to determine correlation between parameters.

	2K ($n = 9$)	UNX ($n = 9$)	ENA ($n = 8$)	NAME ($n = 4$)
BW (g)	287±5	265±7	260±8	263±12
$\overline{AP}$ (mm Hg)	124±1$^{(EN)}$	129±2$^{(EN)}$	96±3$^{(TUN)}$	160±4$^{(TUE)}$
Hematocrit	43.2±0.9$^{(N)}$	45.3±0.5	44.5±0.6	47.0±1.1$^{(T)}$
GFR (ml/min)	1.23±0.04$^{(UE)}$	1.98±0.12$^{(T)}$	1.86±0.18$^{(T)}$	1.47±0.09
RPF (ml/min)	4.90±0.16$^{(U)}$	6.89±0.31$^{(TN)}$	6.42±0.51	4.54±1.09$^{(U)}$
FF	0.25±0.01$^{(N)}$	0.29±0.04	0.29±0.01	0.35±0.04$^{(T)}$
$SNGFR$ (nl/min)	49.3±4.3$^{(UE4)}$	85.6±5.5$^{(T)}$	87.3±5$^{(T)}$	76.5±6.1
Q_A (nl/min)	177±20$^{(UE4)}$	296±17$^{(T)}$	304±22$^{(T)}$	208±40
$SNFF$	0.28±0.01$^{(N)}$	0.30±0.01$^{(N)}$	0.29±0.01$^{(N)}$	0.38±0.01$^{(TUE)}$
$c_{p,A}$ (g/dl)	5.4±0.1	5.2±0.1$^{(E)}$	5.6±0.1$^{(U)}$	5.4±0.1
$\overline{\Delta P}$ (mm Hg)	48.6±1.2$^{(UN4)}$	55.9±1.2$^{(TEN)}$	43.6±1.2$^{(UN)}$	64.6±3.3$^{(TUE)}$
K_f (nl/min/mm Hg)	1.91±0.19$^{(E4)}$	2.66±0.13$^{(E)}$	4.57±0.20$^{(TUN)}$	1.94±0.07$^{(E)}$
$U_p\dot{V}$ (mg/24 h)		40.7±6.9$^{(E)}$	12.0±1.8$^{(U)}$	30.3±5.2
$U_a\dot{V}$ (mg/24 h)		27.3±6.2$^{(E8)}$	1.87±1.04$^{(U)}$	20.9±6.6$^{(3)}$
$U_{(p-a)}\dot{V}$ (mg/24 h)		14.5±2.5$^{(8)}$	10.2±1.3	6.5±2.2$^{(3)}$
$U_a\dot{V}/U_p\dot{V}$		0.63±0.05$^{(E8)}$	0.13±0.05$^{(UN)}$	0.72±13$^{(E3)}$
$FRC_p \times 10^{-4}$		2.76±0.44$^{(E)}$	0.82±0.12$^{(UN)}$	2.67±0.49$^{(E)}$
$FRC_a \times 10^{-4}$		3.74±0.86$^{(E8)}$	0.28±0.15$^{(UN)}$	3.58±1.11$^{(E3)}$
$FRC_{(p-a)} \times 10^{-4}$		1.90±0.23$^{(8)}$	1.37±0.14	1.19±0.45$^{(3)}$
$\Theta_{F36} \cdot GFR$ (ml/min)	0.0863±0.0101$^{(UE)}$	0.174±0.024$^{(T)}$	0.176±0.024$^{(T)}$	0.159±0.033

Table 6.1: Hemodynamic values for fawn-hooded rats which underwent Ficoll sieving studies. Θ_{F36} = Ficoll Θ for $r_s = 36$ Å. Superscripted letters indicate $p < 0.05$: T—vs. 2K, U—vs. UNX, E—vs. ENA, N—vs. NAME. Superscripted numbers indicate n is different from column heading; 3: $n = 3$, 4: $n = 4$, 8: $n = 8$.

6.3 Results

6.3.1 Hemodynamic Data

The mean values ± one standard error of various systemic, single nephron, and whole kidney quantities are shown in Table 6.1 for rats on which Ficoll sieving was performed, and in Table 6.2 for all rats. (The differences between rats which did and did not undergo sieving studies will be discussed subsequently.) Considering the data for all rats (Table 6.2), untreated uninephrectomy significantly increased plasma flow rate (RPF or Q_A), filtration rates (GFR or $SNGFR$), filtration pressures ($\overline{\Delta P}$), albumin excretion ($U_a\dot{V}$), and fractional albumin excretion ($U_a\dot{V}/U_p\dot{V}$) compared to two-kidney controls. Total protein excretion ($U_p\dot{V}$) also increased by a wide margin (40.7 vs. 13.3 mg/24 h), but the difference did not achieve significance because of the low number of 2K rats in which protein excretions were measured. The difference in non-albumin excretion was not substantial. These changes are in general agreement with those previously reported for renal ablation.[82,128]

Relative to untreated uninephrectomized rats, enalapril treatment of uninephrectomized rats lowered the mean arterial and glomerular filtration pressures, increased the ultrafiltration coefficient, and lowered total protein, albumin, and fractional albumin excretion. The changes in $\overline{\Delta P}$, K_f, and $U_p\dot{V}$, along with the lack of significant change in Q_A, $SNGFR$, and $SNFF$ are consistent with previously reported effect of enalapril on renal ablation.[6,7,175] Non-albumin excretion was unchanged.

	2K ($n = 17$)	UNX ($n = 9$)	ENA ($n = 8$)	NAME ($n = 9$)
BW (g)	283±8	265±6	260±8	258±6
$\overline{AP}$ (mm Hg)	123±2$^{(EN)}$	129±2$^{(EN)}$	96±3$^{(TUN)}$	168±6$^{(TUE)}$
Hematocrit	43.7±0.6$^{(N)}$	45.3±0.5$^{(N)}$	44.5±0.6$^{(N)}$	49.6±1.5$^{(TUE)}$
GFR (ml/min)	1.34±0.06$^{(UE)}$	1.98±0.12$^{(TN)}$	1.86±0.18$^{(TN)}$	1.05±0.14$^{(UE)}$
RPF (ml/min)	5.05±0.14$^{(UN)}$	6.89±0.31$^{(TN)}$	6.42±0.51$^{(N)}$	3.05±0.66$^{(TUE)}$
FF	0.27±0.01$^{(N)}$	0.28±0.01$^{(N)}$	0.29±0.01$^{(N)}$	0.38±0.02$^{(TUE)}$
$SNGFR$ (nl/min)	58.2±2.9$^{(UN12)}$	85.6±5.5$^{(T)}$	87.3±5$^{(T)}$	66.7±5.9
Q_A (nl/min)	180±9$^{(UE12)}$	296±17$^{(TN)}$	304±2$^{(TN)}$	169±2$^{(UE)}$
$SNFF$	0.32±0.01$^{(N12)}$	0.30±0.01$^{(N)}$	0.29±0.01$^{(N)}$	0.39±0.02$^{(TUE)}$
$c_{p,A}$ (g/dl)	5.3±0.1	5.2±0.1	5.6±0.1	5.3±0.1
$\overline{\Delta P}$ (mm Hg)	48.8±0.8$^{(UN12)}$	55.9±1.2$^{(TEN)}$	43.6±1.2$^{(UN)}$	67.6±2.8$^{(TUE)}$
K_f (nl/min/mm Hg)	2.28±0.13$^{(EN12)}$	2.66±0.13$^{(EN)}$	4.57±0.20$^{(TUN)}$	1.54±0.16$^{(TUE)}$
$U_p\dot{V}$ (mg/24 h)	13.3±0.6$^{(4)}$	40.7±6.9$^{(E)}$	12.0±1.8$^{(U)}$	39.4±10$^{(5)}$
$U_a\dot{V}$ (mg/24 h)	4.2±0.8$^{(U4)}$	27.3±6.2$^{(TE8)}$	1.8±1.0$^{(U)}$	20.9±6.6$^{(3)}$
$U_{(p-a)}\dot{V}$ (mg/24 h)	9.0±0.7$^{(4)}$	14.5±2.5$^{(8)}$	10.2±1.3	6.5±2.2$^{(3)}$
$U_a\dot{V}/U_p\dot{V}$	0.32±0.06$^{(UN4)}$	0.63±0.05$^{(TE8)}$	0.13±0.05$^{(UN)}$	0.72±0.13$^{(TE3)}$
$FRC_p \times 10^{-4}$	1.45±0.20$^{(4)}$	2.76±0.44	0.82±0.12$^{(N)}$	5.07±2.42$^{(E5)}$
$FRC_a \times 10^{-4}$	0.99±0.32$^{(4)}$	3.74±0.86$^{(E8)}$	0.28±0.15$^{(U)}$	3.58±1.11$^{(3)}$
$FRC_{(p-a)} \times 10^{-4}$	1.92±0.11	1.90±0.23	1.37±0.14	1.19±0.45
$\Theta_{F36} \cdot GFR$ (ml/min)	0.0863±0.0101$^{(UE9)}$	0.174±0.024$^{(T)}$	0.176±0.024$^{(T)}$	0.159±0.033$^{(4)}$

Table 6.2: Hemodynamic values for all fawn-hooded rats. Θ_{F36} = Ficoll Θ for $r_s = 36$ Å. Superscripted letters indicate $p < 0.05$: T—vs. 2K, U—vs. UNX, E—vs. ENA, N—vs. NAME. Superscripted numbers indicate n is different from column heading; 3: $n = 3$, 4: $n = 4$, 5: $n = 5$, 9: $n = 9$, 12: $n = 12$.

Pressures and protein excretions for ENA rats were lower even than those for 2K rats.

NAME-treated uninephrectomized rats, when compared to the untreated UNX group, had increased mean arterial and glomerular filtration pressures and lowered K_f, capillary plasma flow rate, and filtration rates. These effects are the same as those reported for Munich-Wistar rats.[18] Filtration fractions increased significantly from ≈ 0.3 for the other three groups to almost 0.4. Total protein and albumin excretion, and fractional albumin excretion were higher than in the 2K and ENA groups and comparable to those of the UNX group, while non-albumin excretion was unchanged. There was also an increase in hematocrit which might have resulted from a shift of the extracellular fluid volume from the vascular to the extravascular space, secondary to increased vascular pressures and resistance.

Figure 6-1 compares the 24-hour urinary protein excretions from the four experimental groups. The predominant source of the variation in $U_p\dot{V}$ between groups is $U_a\dot{V}$, $U_{(p-a)}\dot{V}$ being relatively constant. Stated another way, the fractional albumin excretion ($U_a\dot{V}/U_p\dot{V}$) increased with total protein excretion. The ratio $U_a\dot{V}/U_p\dot{V}$= 0.32 in 2K rats is similar to reported normal clinical values.[33] In UNX and NAME rats, the ratio is approximately double the 2K value, while in ENA rats, its is roughly a third of it. The sieving data will be discussed in the next section, but it is worth noting here that while the urinary excretion of albumin was increased in the UNX and NAME groups

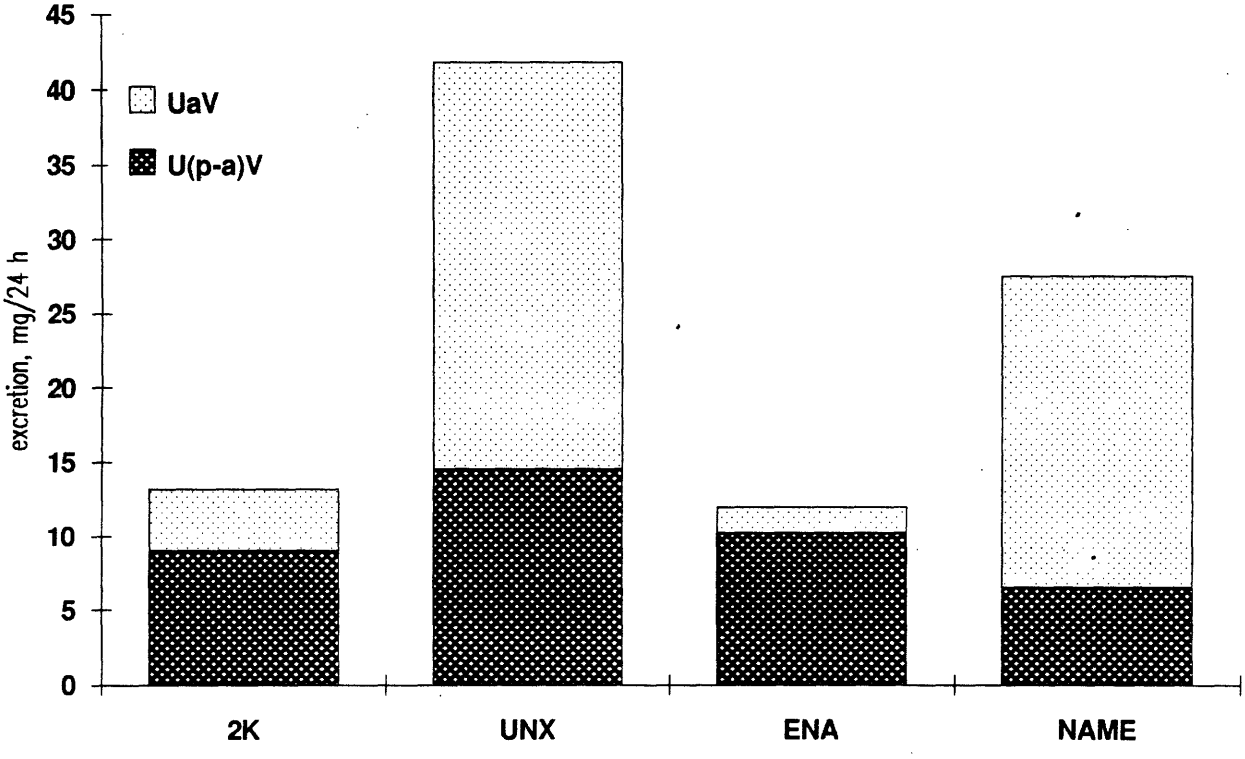

Figure 6-1: Comparison of average albumin and non-albumin protein excretions for experimental groups. Values shown are only for those rats in which both $U_p\dot{V}$ and $U_a\dot{V}$ were measured.

	Sieving only ($n = 5$)	Micropuncture only ($n = 8$)	Sieving +Micropuncture ($n = 4$)
BW (g)	279±7	278±2	298±5
$\overline{AP}$ (mm Hg)	124±2	122±4	125±2
Hematocrit	43.4±1.7	44.3±0.7	43.0±0.4
GFR (ml/min)	1.25±0.04	1.46±0.09	1.21±0.08
RPF (ml/min)	4.94±0.26	5.21±0.25	4.85±0.17
FF	0.25±0.02	0.28±0.02	0.25±0.013
$SNGFR$ (nl/min)		62.7±2.8*	49.3±4.3
Q_A (nl/min)		182±9	177±20
$SNFF$		0.34±0.01*	0.28±0.01
$c_{p,A}$ (g/dl)	5.4±0.1	5.2±0.1	5.3±0.1
$\overline{\Delta P}$ (mm Hg)		48.9±1.2	48.6±1.2
K_f (nl/min/mm Hg)		2.47±0.13*	1.91±0.19
$U_p\dot{V}$ (mg/24 h)		13.3±0.6	
$U_a\dot{V}$ (mg/24 h)		4.2±0.8	
$U_{(p-a)}\dot{V}$ (mg/24 h)		9.0±0.7	
$U_a\dot{V}/U_p\dot{V}$		0.32±0.06	
$FRC_p \times 10^{-4}$		1.45±0.20	
$FRC_a \times 10^{-4}$		0.99±0.32	
$FRC_{(p-a)} \times 10^{-4}$		1.92±0.11	

Table 6.3: Hemodynamic values for two-kidney rats. $^*p < 0.05$ vs. sieving + micropuncture group.

only, the filtered load of a 36 Å Ficoll molecule, shown as $\Theta_{F36} \cdot GFR$ in Table 6.2, was elevated in all three 1K groups. Thus, albumin excretion is normal in the ENA group even though excretion of 36 Å Ficoll is elevated.

Table 6.2 includes micropuncture data from eight 2K and five NAME rats which did not undergo Ficoll sieving studies. In Table 6.3 the data for the 2K rats is split into those which underwent sieving measurements only, those which underwent micropuncture only, and those which had both. For unknown reasons $SNGFR$, $SNFF$, and K_f were higher in micropuncture-only rats compared to rats with both. These could reflect effects of the various experimental procedures, methodological differences, or true differences in the population of the rats. Since Ficoll infusion occurred after micropuncture, it is doubtful that the sieving measurements themselves had anything to do with the difference between the micropuncture-only and sieving + micropuncture groups. For the analysis of the sieving data, only the average whole kidney and single nephron quantities for the rats which had sieving studies were used.

In Table 6.4, the data for the NAME rats which did and did not have sieving studies are presented. The rats which had sieving had larger K_f and GFR than those which did not, which was the opposite trend of the results from the 2K rats, indicating that such differences may have simply been due to chance.

	sieving ($n = 4$)	no sieving ($n = 5$)
BW (g)	263±12	254±7
$\overline{AP}$ (mm Hg)	160±4	175±10
Hematocrit	47.0±1.1	51.6±2.1
GFR (ml/min)	1.47±0.09*	0.73±0.05
RPF (ml/min)	4.54±1.09	1.86±0.18
FF	0.35±0.04	0.40±0.02
$SNGFR$ (nl/min)	76.5±6.1	58.9±8.3
Q_A (nl/min)	208±40	139±17
$SNFF$	0.38±0.01	0.39±0.02
$c_{p,A}$ (g/dl)	5.4±0.1	5.2±0.1
$\overline{\Delta P}$ (mm Hg)	64.6±3.3	70.1±4.3
K_f (nl/min/mm Hg)	1.94±0.07*	1.22±0.18
$U_p\dot{V}$ (mg/24 h)	30.3±5.2*	$76^{(1)}$
$U_a\dot{V}$ (mg/24 h)	$20.9\pm6.6^{(3)}$	
$U_{(p-a)}\dot{V}$ (mg/24 h)	$6.5\pm2.2^{(3)}$	
$U_a\dot{V}/U_p\dot{V}$	0.72±0.13	
$FRC_p \times 10^{-4}$	2.67±0.49*	$14.6^{(1)}$
$FRC_a \times 10^{-4}$	3.58±1.11	
$FRC_{(p-a)} \times 10^{-4}$	1.19±0.45	

Table 6.4: Hemodynamic values for NAME rats. $^*p < 0.05$ vs. no sieving group. Superscripted numbers indicate n is different from column heading; 1: $n = 1$, 3: $n = 3$.

Thus, though there were some significant unexplained variations in the subgroups of 2K and NAME rats which did and did not undergo sieving, such differences were in opposing directions and may have been random. In any case, the analysis of any data presented here is not affected, as averaged values were used only for those to which they were applicable.

6.3.2 Sieving Data

Ficoll sieving coefficients for each of the four groups are shown in Tables 6.5 and 6.6, and plotted in Figure 6-2 for the range $r_s = 20$ to 70 Å. The sieving curves in Figure 6-2 are more sigmoidal than the Ficoll curves for Munich-Wistar rats (Figure 4-1), the values for Θ at $r_s = 20$ Å being closer to one. At $r_s < 50$ Å, Θ for 2K fawn-hooded rats are somewhat greater than those for the normal Munich-Wistar rats reported in Chapter 4, while for $r_s = 60$ to 65 Å, values are lower ($\approx 3 \times 10^{-4}$ for FH rats vs. $\approx 7.5 \times 10^{-4}$ for Munich-Wistar rats). Because different investigators performed the micropuncture, however, it is difficult to draw absolute conclusions from the comparison.

The variances in Θ for each group were shown to be unequal by statistical analysis, violating the requirement of homoscedasticity necessary for ANOVA. A logarithmic transformation of the data satisfied this criterion, and so one-way ANOVA was performed on the values of $\log(\Theta)$ to determine significance.[144] No significant difference is seen between groups for $r_s < 45$ Å. For $r_s > 45$ Å only

r_s (Å)	2K (n=9)	UNX (n=9)
20	$8.51\times10^{-1}\pm9.04\times10^{-2}$	$7.36\times10^{-1}\pm7.04\times10^{-2}$
22	$7.74\times10^{-1}\pm8.09\times10^{-2}$	$6.73\times10^{-1}\pm5.97\times10^{-2}$
24	$6.51\times10^{-1}\pm7.02\times10^{-2}$	$5.61\times10^{-1}\pm4.89\times10^{-2}$
26	$5.03\times10^{-1}\pm5.28\times10^{-2}$	$4.47\times10^{-1}\pm3.48\times10^{-2}$
28	$3.60\times10^{-1}\pm3.32\times10^{-2}$	$3.37\times10^{-1}\pm2.32\times10^{-2}$
30	$2.71\times10^{-1}\pm3.75\times10^{-2}$	$2.47\times10^{-1}\pm1.76\times10^{-2}$
32	$1.70\times10^{-1}\pm1.76\times10^{-2}$	$1.76\times10^{-1}\pm1.23\times10^{-2}$
34	$1.07\times10^{-1}\pm1.25\times10^{-2}$	$1.23\times10^{-1}\pm1.18\times10^{-2}$
36	$7.02\times10^{-2}\pm8.15\times10^{-3}$	$8.78\times10^{-2}\pm1.01\times10^{-2}$
38	$4.24\times10^{-2}\pm4.95\times10^{-3}$	$6.10\times10^{-2}\pm8.45\times10^{-3}$
40	$2.59\times10^{-2}\pm3.61\times10^{-3}$	$4.19\times10^{-2}\pm7.36\times10^{-3}$
42	$1.57\times10^{-2}\pm2.44\times10^{-3}$	$3.06\times10^{-2}\pm6.12\times10^{-3}$
44	$9.51\times10^{-3}\pm1.60\times10^{-3}$	$2.22\times10^{-2}\pm5.12\times10^{-3}$
46	$5.64\times10^{-3}\pm1.04\times10^{-3}$	$1.64\times10^{-2}\pm4.34\times10^{-3*}$
48	$3.49\times10^{-3}\pm6.85\times10^{-4}$	$1.24\times10^{-2}\pm3.69\times10^{-3*}$
50	$2.29\times10^{-3}\pm4.73\times10^{-4}$	$9.79\times10^{-3}\pm3.23\times10^{-3*}$
52	$1.51\times10^{-3}\pm3.37\times10^{-4}$	$7.97\times10^{-3}\pm2.96\times10^{-3*}$
54	$1.03\times10^{-3}\pm2.46\times10^{-4}$	$6.59\times10^{-3}\pm2.71\times10^{-3*}$
56	$7.46\times10^{-4}\pm1.93\times10^{-4}$	$5.52\times10^{-3}\pm2.47\times10^{-3*}$
58	$5.46\times10^{-4}\pm1.44\times10^{-4}$	$4.67\times10^{-3}\pm2.23\times10^{-3*}$
60	$4.01\times10^{-4}\pm9.84\times10^{-5}$	$4.00\times10^{-3}\pm2.03\times10^{-3*}$
62	$3.09\times10^{-4}\pm7.28\times10^{-5}$	$3.43\times10^{-3}\pm1.86\times10^{-3*}$
64	$2.48\times10^{-4}\pm5.67\times10^{-5}$	$3.00\times10^{-3}\pm1.70\times10^{-3*}$
66	$2.04\times10^{-4}\pm4.19\times10^{-5}$	$2.65\times10^{-3}\pm1.54\times10^{-3*}$
68	$1.72\times10^{-4}\pm3.11\times10^{-5}$	$2.32\times10^{-3}\pm1.39\times10^{-3*}$
70	$1.50\times10^{-4}\pm2.59\times10^{-5}$	$2.03\times10^{-3}\pm1.25\times10^{-3*}$

Table 6.5: Ficoll sieving coefficients for two-kidney and UNX fawn-hooded rats. All values are given as mean ± standard error. $^*p < 0.05$ vs. 2K. p was not significant for all comparisons to ENA and NAME groups.

r_s (Å)	ENA (n=8)	NAME (n=4)
20	$9.34\times10^{-1}\pm9.00\times10^{-2}$	$8.43\times10^{-1}\pm5.83\times10^{-2}$
22	$8.59\times10^{-1}\pm8.37\times10^{-2}$	$7.93\times10^{-1}\pm6.72\times10^{-2}$
24	$7.40\times10^{-1}\pm7.13\times10^{-2}$	$6.77\times10^{-1}\pm4.57\times10^{-2}$
26	$5.91\times10^{-1}\pm5.60\times10^{-2}$	$5.55\times10^{-1}\pm4.05\times10^{-2}$
28	$4.39\times10^{-1}\pm4.34\times10^{-2}$	$4.30\times10^{-1}\pm3.75\times10^{-2}$
30	$3.08\times10^{-1}\pm3.25\times10^{-2}$	$3.18\times10^{-1}\pm2.65\times10^{-2}$
32	$2.16\times10^{-1}\pm2.25\times10^{-2}$	$2.19\times10^{-1}\pm2.72\times10^{-2}$
34	$1.44\times10^{-1}\pm1.53\times10^{-2}$	$1.56\times10^{-1}\pm2.37\times10^{-2}$
36	$9.55\times10^{-2}\pm1.13\times10^{-2}$	$1.08\times10^{-1}\pm2.08\times10^{-2}$
38	$6.36\times10^{-2}\pm8.16\times10^{-3}$	$7.32\times10^{-2}\pm1.83\times10^{-2}$
40	$4.20\times10^{-2}\pm6.09\times10^{-3}$	$4.95\times10^{-2}\pm1.48\times10^{-2}$
42	$2.78\times10^{-2}\pm4.55\times10^{-3}$	$3.39\times10^{-2}\pm1.22\times10^{-2}$
44	$1.87\times10^{-2}\pm3.25\times10^{-3}$	$2.34\times10^{-2}\pm9.29\times10^{-3}$
46	$1.31\times10^{-2}\pm2.53\times10^{-3}$	$1.72\times10^{-2}\pm7.47\times10^{-3}$
48	$9.49\times10^{-3}\pm2.08\times10^{-3}$	$1.25\times10^{-2}\pm5.93\times10^{-3}$
50	$7.15\times10^{-3}\pm1.75\times10^{-3}$	$8.94\times10^{-3}\pm4.62\times10^{-3}$
52	$5.48\times10^{-3}\pm1.46\times10^{-3}$	$6.76\times10^{-3}\pm3.72\times10^{-3}$
54	$4.28\times10^{-3}\pm1.22\times10^{-3}$	$5.12\times10^{-3}\pm2.96\times10^{-3}$
56	$3.31\times10^{-3}\pm9.88\times10^{-4}$	$4.15\times10^{-3}\pm2.48\times10^{-3}$
58	$2.68\times10^{-3}\pm8.67\times10^{-4}$	$3.48\times10^{-3}\pm2.18\times10^{-3}$
60	$2.19\times10^{-3}\pm7.60\times10^{-4}$	$2.82\times10^{-3}\pm1.85\times10^{-3}$
62	$1.80\times10^{-3}\pm6.46\times10^{-4}$	$2.22\times10^{-3}\pm1.50\times10^{-3}$
64	$1.49\times10^{-3}\pm5.45\times10^{-4}$	$1.83\times10^{-3}\pm1.26\times10^{-3}$
66	$1.24\times10^{-3}\pm4.74\times10^{-4}$	$1.59\times10^{-3}\pm1.12\times10^{-3}$
68	$1.05\times10^{-3}\pm4.23\times10^{-4}$	$1.38\times10^{-3}\pm9.95\times10^{-4}$
70	$8.92\times10^{-4}\pm3.71\times10^{-4}$	$1.19\times10^{-3}\pm8.72\times10^{-4}$

Table 6.6: Ficoll sieving coefficients for UNX+enalapril and UNX+NAME fawn-hooded rats. All values are given as mean ± standard error. p was not significant for all comparisons to each other and to 2K and UNX groups.

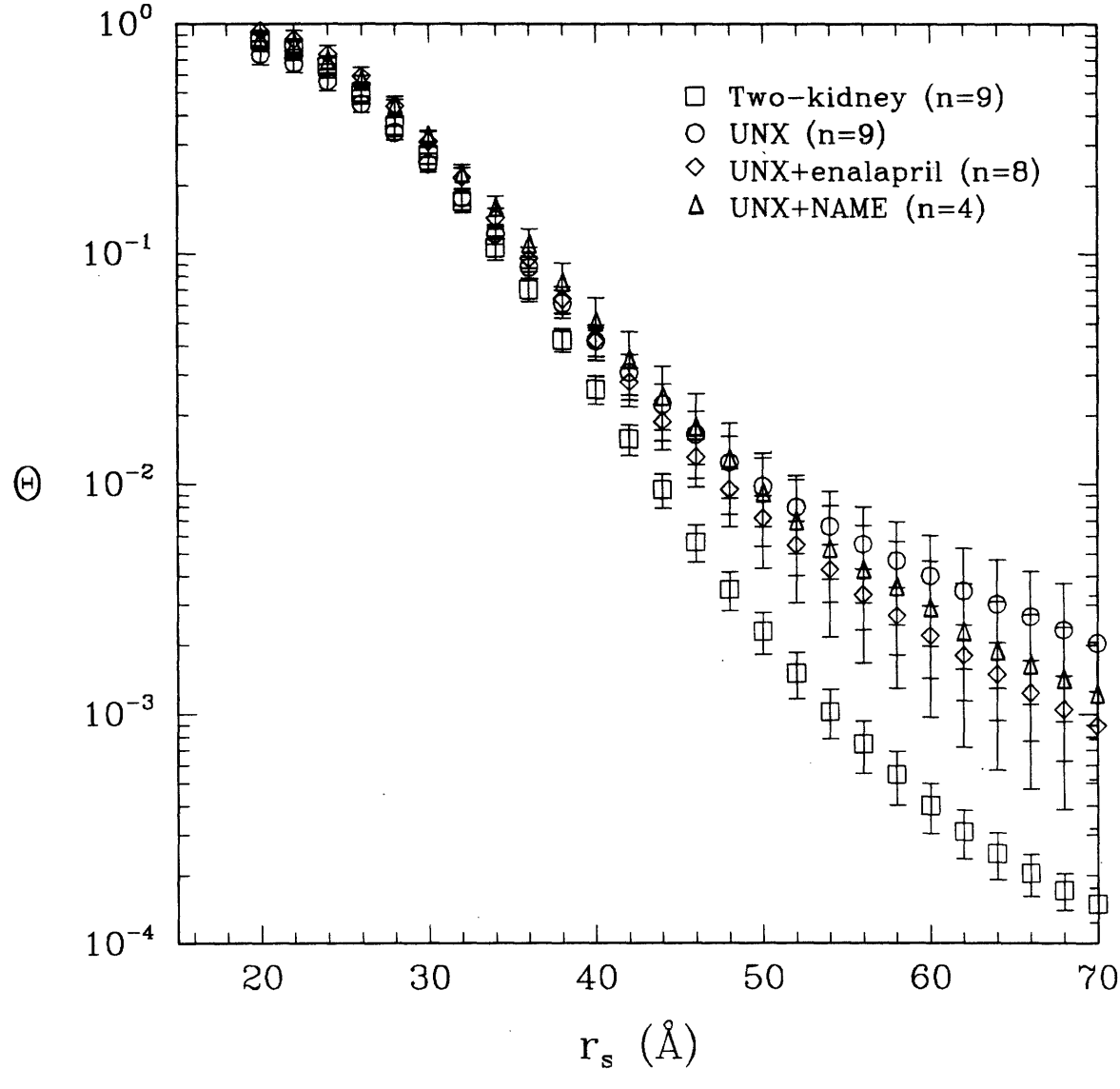

Figure 6-2: Sieving coefficients (Θ) for Ficoll-infused fawn-hooded rats as a function of molecular radius (r_s). Error bars denote ± one standard error of the mean.

Model			2K ($n = 9$)	UNX ($n = 9$)	ENA ($n = 8$)	NAME ($n = 4$)
Isoporous +shunt	r_0	(Å)	47.1±0.5	48.0±0.3	49.1±0.4	50.6±0.6
	ω_0	$\times 10^{-3}$	0.148±0.030	3.18±0.58	0.97±0.19	1.48±0.48
	χ^2		153	37.6	79.4	54.9
Lognormal	u	(Å)	30.7±1.7	28.5±1.1	36.0±2.1	36.4±1.3
	s		1.23±0.02	1.27±0.02	1.20±0.01	1.17±0.02
	$r^*(5\%)$	(Å)	51.2	53.0	55.5	52.0
	$r^*(1\%)$	(Å)	59.0	62.4	62.8	57.9
	χ^2		157	36.1	100	44.7
Lognormal +shunt	u	(Å)	34.2±0.9	30.6±0.6	38.6±1.2	37.4±0.3
	s		1.19±0.01	1.24±0.09	1.16±0.02	1.15±0.01
	ω_0	$\times 10^{-3}$	0.134±0.016	2.54±0.31	0.854±0.163	1.49±0.34
	$r^*(5\%)$	(Å)	50.8	51.9	53.9	50.9
	$r^*(1\%)$	(Å)	57.0	61.0	60.0	56.3
	χ^2		44.6	9.86	47.8	24.8

Table 6.7: Membrane pore parameter fits of fawn-hooded rat sieving coefficients to single nephron hemodynamic values of Table 6.1. Fitted values are shown ± one standard error.

	p-value			
Enhanced model:Simpler model	2K	UNX	ENA	NAME
Lognormal+shunt:Isoporous+shunt	2.7×10^{-7}	7.8×10^{-8}	1.4×10^{-3}	4.6×10^{-5}
Lognormal+shunt:Lognormal	2.0×10^{-7}	1.3×10^{-7}	9.1×10^{-5}	5.4×10^{-4}

Table 6.8: F-test comparisons of heteroporous model fits to fawn-hooded rat data. p values are those for the significance of the χ^2 reduction by the "enhanced" model over the "simple" one.

the 2K and UNX groups differed significantly, with the UNX values approximately an order of magnitude larger.

6.3.3 Pore Size Parameters

Membrane pore size parameters were fitted to the sieving data of Tables 6.5 and 6.6 using the single nephron hemodynamic data of Table 6.1. The results are shown in Table 6.7 for the isoporous + shunt, lognormal, and lognormal + shunt models previously discussed (Sections 2.6.5 and 4.2.5). For each group, the lognormal + shunt model gave the best fit of the three, with the isoporous + shunt and lognormal models giving approximately equivalent values of χ^2. This is in contrast to the Ficoll data from Munich-Wistar (Chapter 4), where the lognormal model was clearly superior to the isoporous + shunt model. F-test comparisons of the lognormal + shunt model to the other models are shown in Table 6.8 In all groups, the decrease in χ^2 provided by the lognormal + shunt model was highly significant, even though addition of the shunt to the lognormal model made only small

	GFR	$SNGFR$	RPF	Q_A	FF	$SNFF$	$\overline{\Delta P}$	K_f
$\overline{AP}$	−0.468*	−0.277	−0.592*	−0.518*	0.574*	0.616*	0.780*	−0.778*
	−0.597*	−0.476*	−0.668*	−0.700*	0.636*	0.706*	0.796*	−0.878*
GFR	1.000	0.659*	0.873*	0.767*	−0.118	−0.424*	−0.310	0.567*
	1.000	0.653*	0.911*	0.794*	−0.422*	−0.567*	−0.468*	0.545*
$SNGFR$		1.000	0.537*	0.699*	−0.034	−0.256	−0.039	0.563*
		1.000	0.604*	0.607*	−0.408*	−0.474*	−0.311	0.519*
RPF			1.000	0.788*	−0.554*	−0.653*	−0.486*	0.580*
			1.000	0.864*	−0.732*	−0.759*	−0.568*	0.592*
Q_A				1.000	−0.341*	−0.610*	−0.274	0.700*
				1.000	−0.676*	−0.780*	−0.521*	0.689*
FF					1.000	0.741*	0.581*	−0.341*
					1.000	0.854*	0.533*	−0.558*
$SNFF$						1.000	0.533*	−0.486*
						1.000	0.588*	−0.604*
$\overline{\Delta P}$							1.000	−0.664*
							1.000	−0.835*

Table 6.9: Correlation coefficients of whole kidney and single nephron hemodynamic quantities in fawn-hooded rats. Top number is correlation using rats from all four groups, bottom number is correlation using just 1K rats. $^*p < 0.05$.

changes in the values of u and s.

The models are plotted against the data for each of the groups in Figures 6-3, 6-4, 6-5, and 6-6. All three models tend to underpredict Θ at small r_s, a characteristic of the glomerular pore model as $\Theta \rightarrow 1$.[79,83] The models are roughly equivalent in the range 20 Å $\leq r_s \leq$ 40 Å. Above 50 Å, the lognormal model severely underpredicts the data.

The pore-size distributions for the lognormal and lognormal + shunt models are shown in Figure 6-7. Because of comparatively higher values of Θ at small r_s, the pores for the fawn-hooded rats are calculated to be considerably larger than those reported for Munich-Wistar rats in Chapter 4. For any group of rats, the differences between the two models is not large, nor is there much difference between the four groups for any one model. The UNX distributions in Figure 6-7 actually have the highest number of large pores, although this is not demonstrable on the scale of the figure.

6.3.4 Data Correlations

6.3.4.1 Correlation of Hemodynamic Parameters

Pearson correlation coefficients for whole kidney and single nephron parameters are shown in Table 6.9. A coefficient of ± 1 implies that the two parameters are perfectly correlated, while a value of zero means there is no correlation between the parameters. Separate coefficients were calculated for rats from all four groups (top number) and for rats from just the three 1K groups (bottom number), but little difference was observed. Body weight (not shown in the table) did not correlate with any of the hemodynamic quantities. As expected, $\overline{AP}$ and $\overline{\Delta P}$ correlated with each other and were similar in how they correlated with other parameters. Analogous statements could be made about

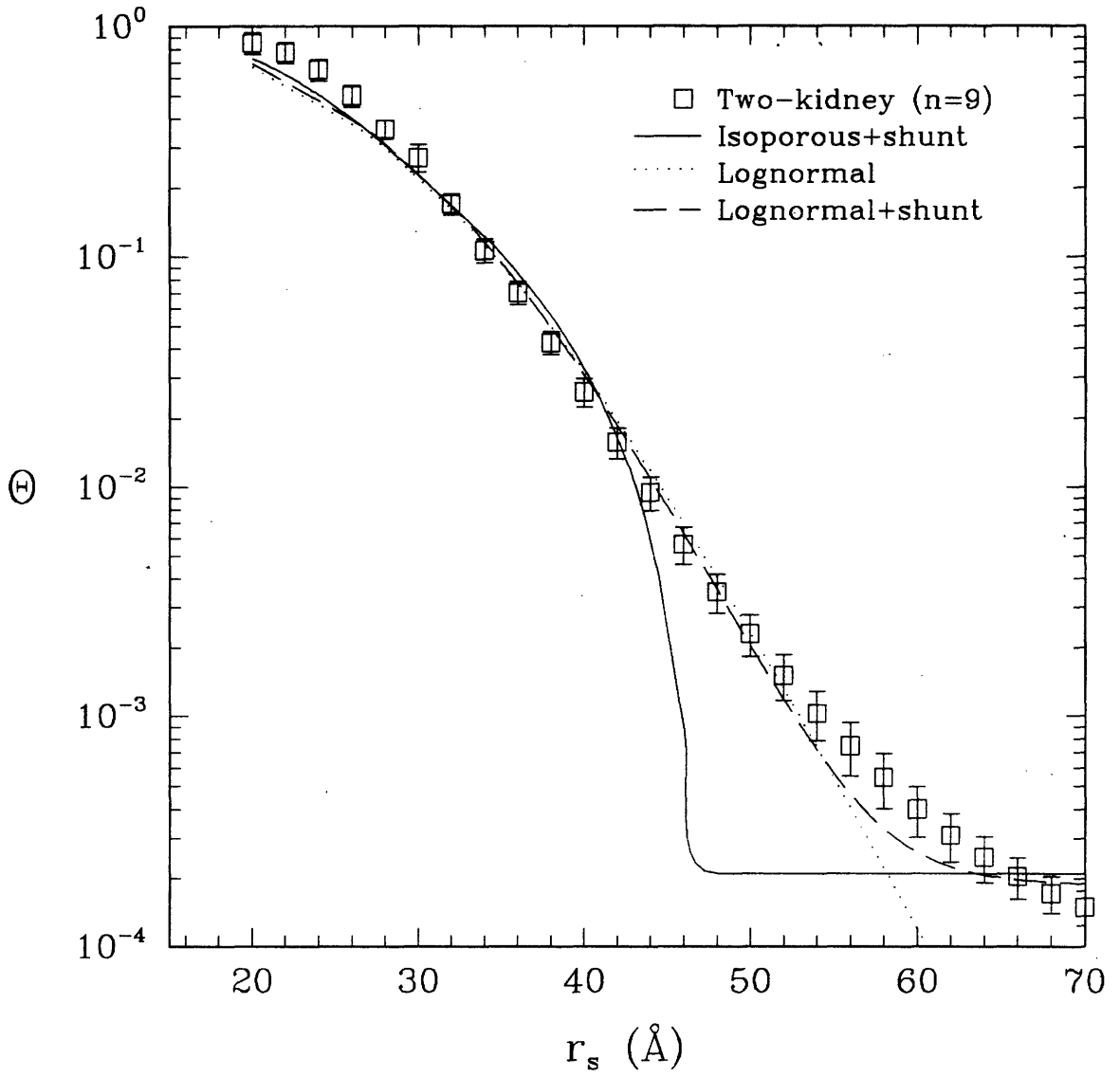

Figure 6-3: Fits of various heteroporous distribution models to two-kidney fawn-hooded rat data. Parameters are given in Table 6.7.

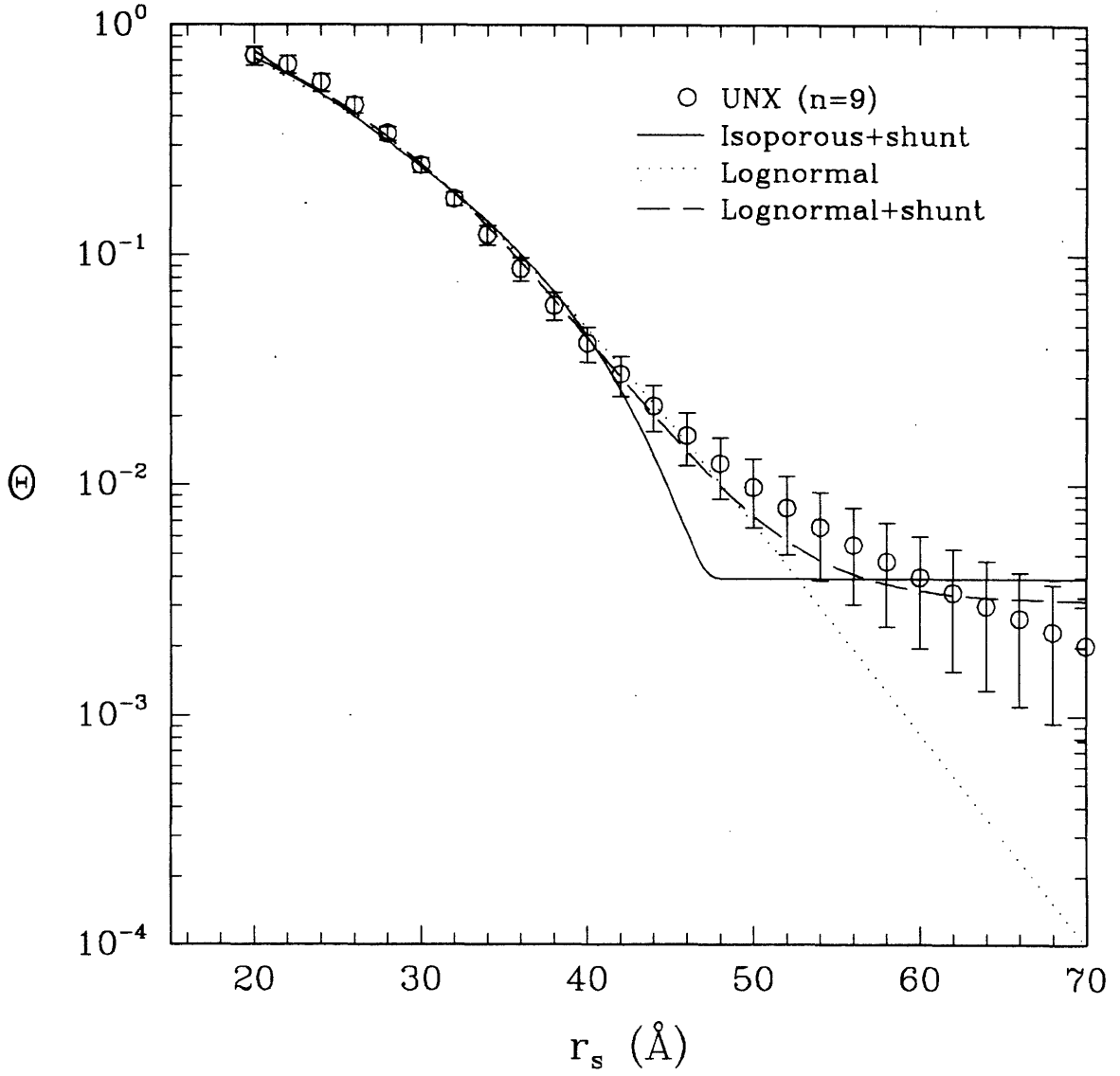

Figure 6-4: Fits of various heteroporous distribution models to uninephrectomized fawn-hooded rat data. Parameters are given in Table 6.7.

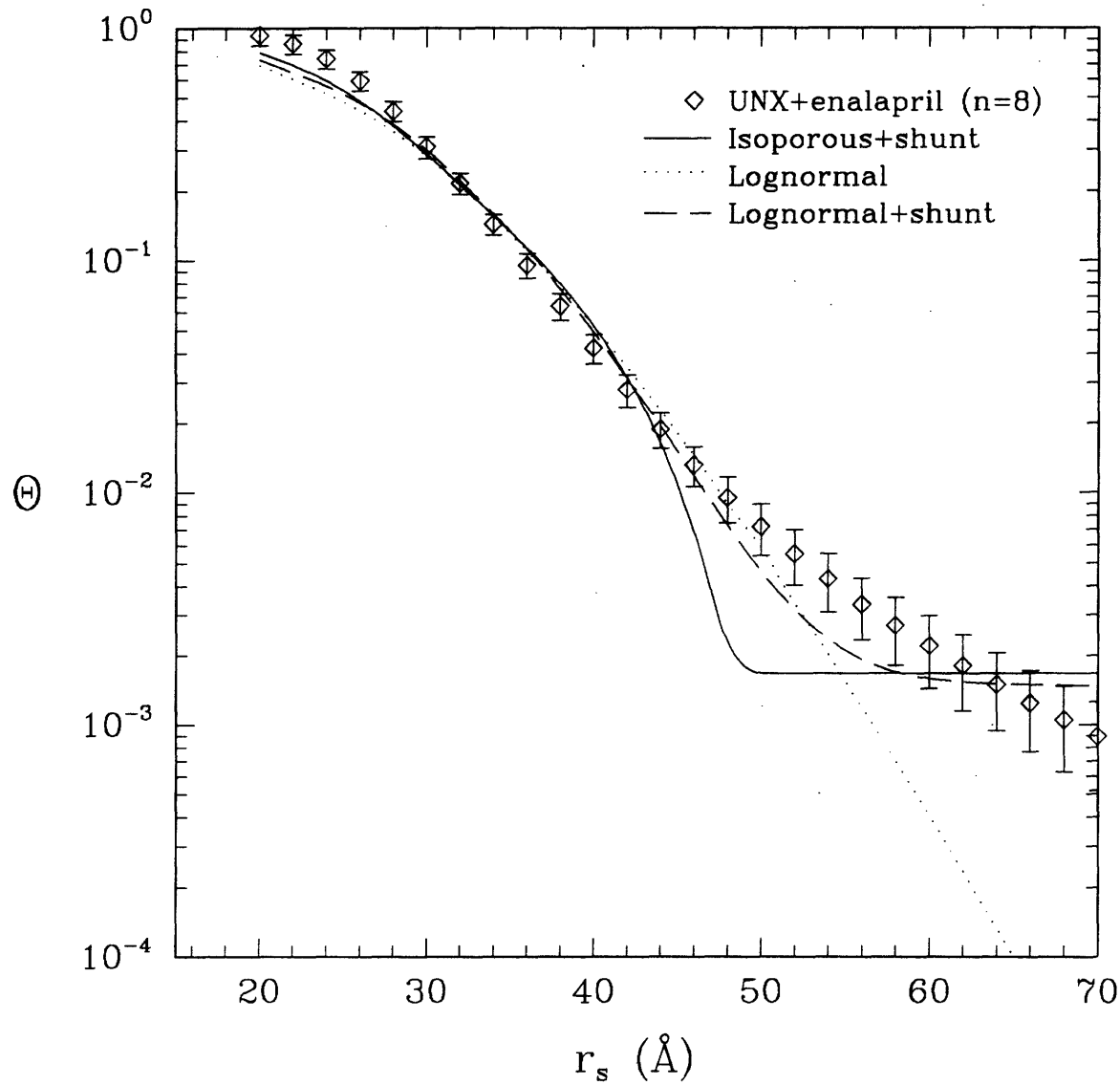

Figure 6-5: Fits of various heteroporous distribution models to uninephrectomized + enalapril-treated fawn-hooded rat data. Parameters are given in Table 6.7.

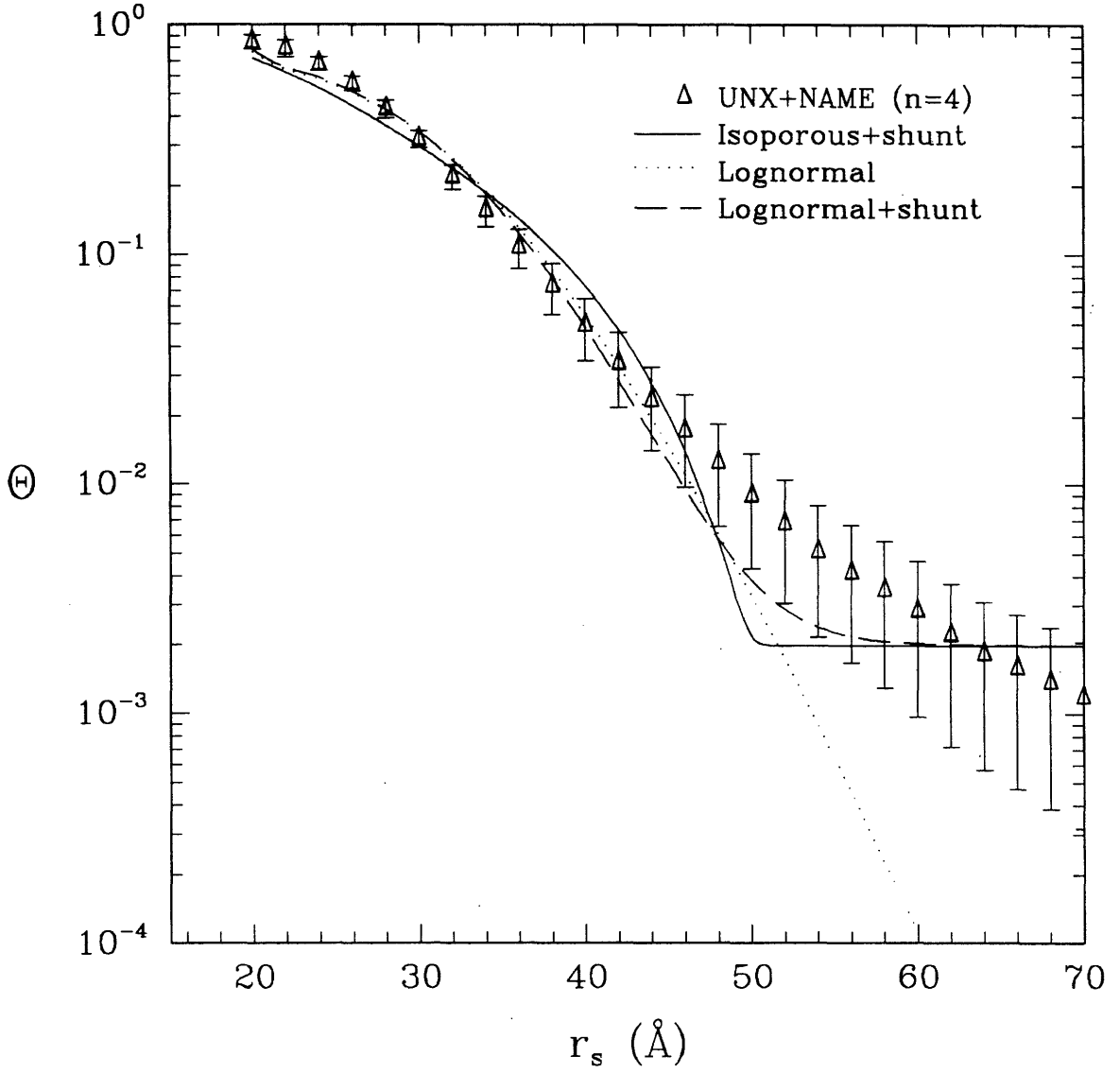

Figure 6-6: Fits of various heteroporous distribution models to uninephrectomized + NAME-treated fawn-hooded rat data. Parameters are given in Table 6.7.

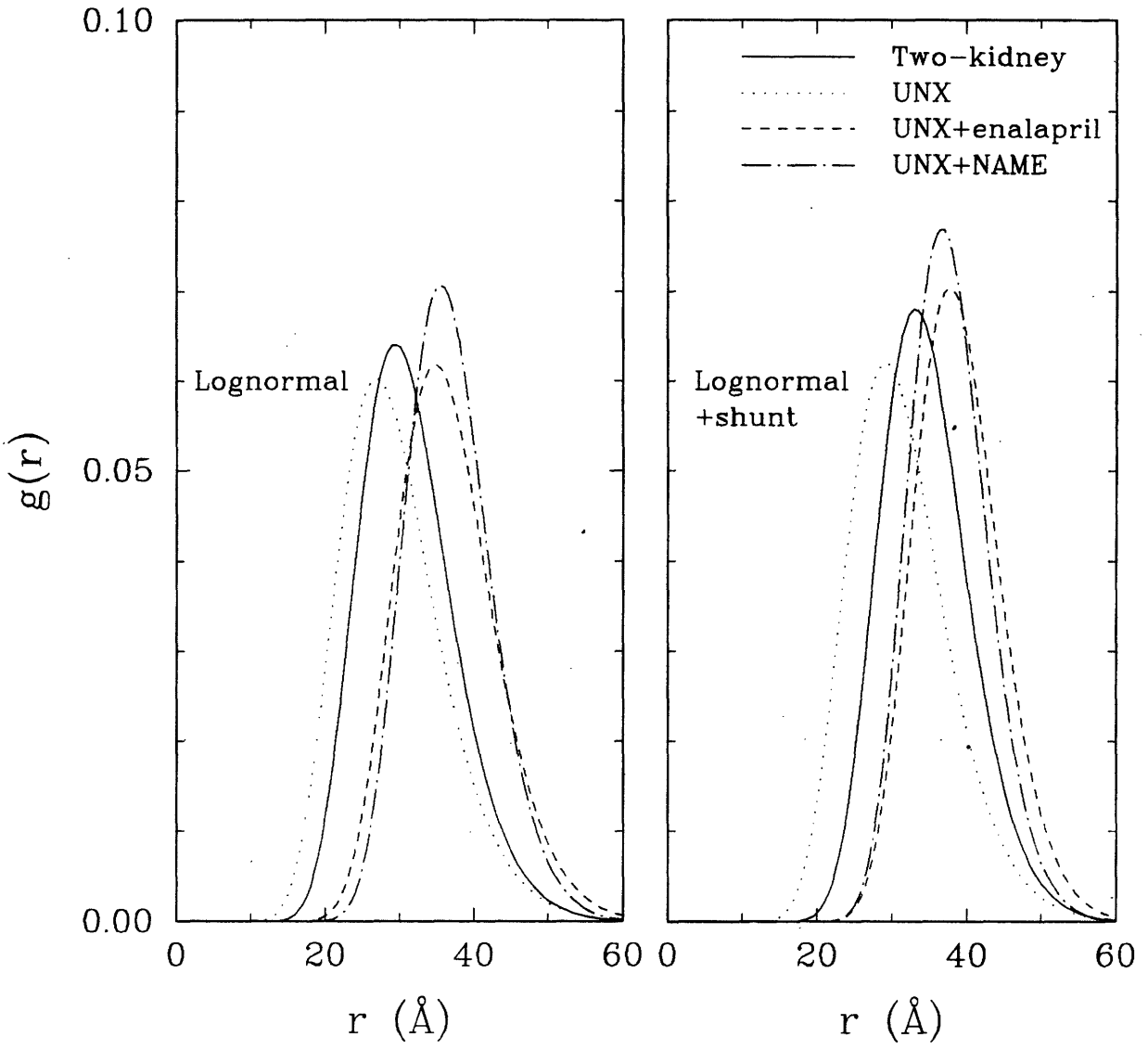

Figure 6-7: Pore number density distributions $g(r)$ for fits to fawn-hooded rat data. Plots are based on the values of Table 6.7.

the couplets of RPF and Q_A, $SNGFR$ and GFR, and FF and $SNFF$. In general, pressure increases correlated with decreases in capillary flow rate, indicating an increase in total arteriolar resistance. Glomerular filtration rates decreased due to both the drop in capillary flow rate and to an additional decrease in K_f. Filtration fraction, however, increased. The inverse correlation between $\overline{\Delta P}$ and K_f has been previously noted by Tucker and Blantz.[244]

Hemodynamic parameters are correlated to sieving and protein excretion data in Table 6.10. None of the sieving coefficients at any r_s displayed significant correlation with the hemodynamic parameters (shown are values for $r_s = 36$ and 60 Å). The filtered load of Ficoll ($\Theta \cdot GFR$) at all sizes correlated with GFR(as expected) and RPF, and not with $\overline{\Delta P}$.

Urinary excretion of total protein, $U_p\dot{V}$, showed a highly significant correlation with $\overline{\Delta P}$ (and thus an inverse correlation with K_f), as did the urinary albumin excretion ($U_a\dot{V}$) (Figure 6-8). Neither correlated with GFR. In contrast, excretion of non-albumin protein correlated with GFR but was uncorrelated with $\overline{\Delta P}$ (Figure 6-9). The fraction of albumin in the excreted urine, $U_a\dot{V}/U_p\dot{V}$ correlates solely with $\overline{\Delta P}$ (Figure 6-10). These data suggest that albumin excretion is governed by permselectivity alterations secondary to $\overline{\Delta P}$ changes, while non-albumin excretion is a function of the filtered load through the capillary, scaling with filtration rate. As albumin is the most anionic of the major proteins, the implication is that a decrease in the charge barrier to filtration is associated with increases in $\overline{\Delta P}$.

In support of this, the fractional clearance of total protein, FRC_p, showed a highly significant correlation with $\overline{\Delta P}$. (There were also significant correlations with GFR and RPF, though not with the corresponding single nephron quantities.) The fractional clearance of albumin, FRC_a, also was very significantly correlated to $\overline{\Delta P}$, but the fractional clearance of non-albumin proteins, $FRC_{(p-a)}$, was not. In contrast, none of the values of Θ for Ficoll at any size demonstrated correlation with any hemodynamic quantity.

6.4 Discussion

These studies suggest that there is a size defect introduced by uninephrectomy which persists through pharmacological interventions which both decrease (enalapril) and increase (NAME) $\overline{\Delta P}$. This defect is evidenced by the "tail" of the sieving curve at large r_s. This size defect, however, does not appear to be an important determinant of proteinuria, since Θ for Ficoll at $r_s = 36$ Å (corresponding to albumin size) is not affected. Rather, it is an apparent change in charge-selectivity which increases proteinuria, as suggested by a specific increase in albumin excretion.

A simple physical explanation for any possible charge/pressure interaction is unlikely. Compression of a membrane with a homogeneously distributed charge would increase the charge density and the resistance to transport of anions, and therefore reduce albumin excretion.

The interaction of renal hemodynamics with size- and charge-selectivity has been examined in a

	Θ_{F36}	Θ_{F60}	$\Theta_{F36} \cdot GFR$	$U_p\dot{V}$	$U_a\dot{V}$	$U_{(p-a)}\dot{V}$	$U_a\dot{V}/U_p\dot{V}$	FRC_p	FRC_a	$FRC_{(p-a)}$
GFR	0.134	0.341	0.618*	0.037	0.198	−0.591*	−0.098	−0.396*	0.009	−0.015
	−0.127	0.195	0.423	−0.084	0.089	0.591*	−0.179	−0.493*	−0.092	0.150
SNGFR	0.095	0.173	0.460*	0.003	−0.007	0.066	−0.107	−0.128	−0.149	−0.454*
	0.102	0.024	0.323	−0.225	−0.222	−0.038	−0.261	−0.272	−0.361	−0.391
RPF	0.148	0.359	0.579*	−0.175	0.027	0.294	−0.080	−0.486*	−0.102	−0.200
	0.002	0.267	0.477*	−0.262	−0.070	0.248	−0.125	−0.541*	−0.181	−0.121
Q_A	−0.155	0.202	0.312	0.071	0.212	0.333	−0.028	−0.257	0.067	−0.156
	−0.221	0.101	0.158	−0.102	0.064	0.304	−0.163	−0.400	−0.085	−0.008
FF	0.094	0.086	0.165	0.380	0.293	0.406	0.071	0.227	0.219	0.217
	−0.078	−0.065	−0.128	0.236	0.241	0.382	0.042	0.205	0.185	0.360
SNFF	0.048	−0.036	−0.067	0.135	0.077	0.158	0.085	0.138	0.139	0.448*
	0.059	−0.096	−0.171	0.243	0.203	0.240	0.164	0.196	0.252	0.417
$\overline{\Delta P}$	−0.015	0.128	−0.015	0.725*	0.692*	0.257	0.741*	0.700*	0.678*	0.190
	−0.020	0.091	−0.093	0.721*	0.703*	0.233	0.780*	0.706*	0.701*	0.271
K_f	0.019	−0.018	0.248	−0.421*	−0.412	0.071	−0.663*	−0.458*	−0.498*	−0.219
	0.008	−0.130	0.118	−0.560*	−0.577*	0.012	−0.807*	−0.535*	−0.648*	−0.153

Table 6.10: Correlation coefficients of sieving and proteinuria measurements with hemodynamic parameters. Top number is correlation using rats from all four groups, bottom number is correlation using just 1K rats. Θ_{F36} = Ficoll Θ for $r_s = 36$ Å; Θ_{F60} = Ficoll Θ for $r_s = 60$ Å; $^*p < 0.05$.

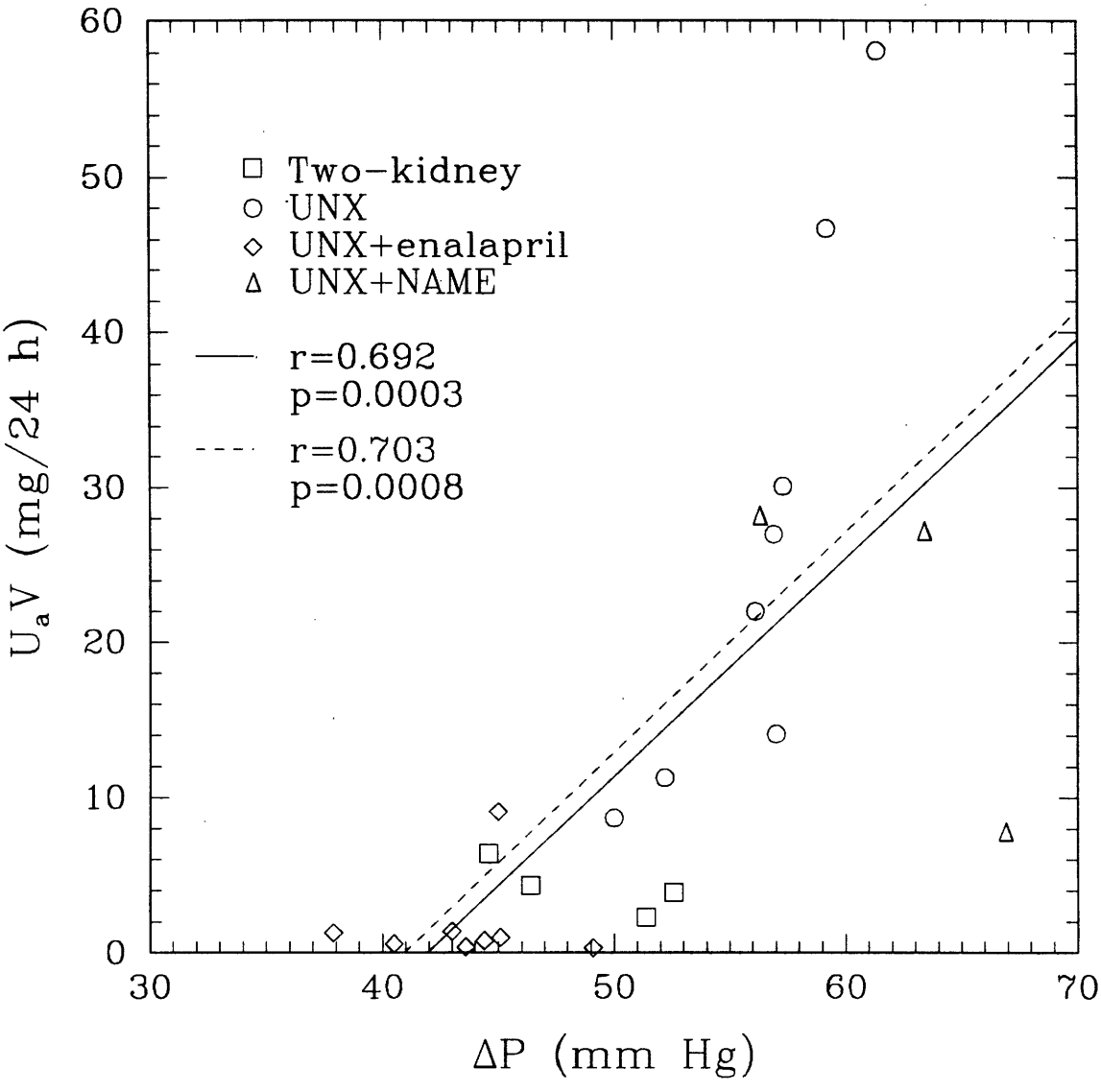

Figure 6-8: Correlation of filtration pressure ($\overline{\Delta P}$) to urinary albumin excretion ($U_a\dot{V}$). Solid lines are fit to all data, dashed lines are fit to the three 1K groups.

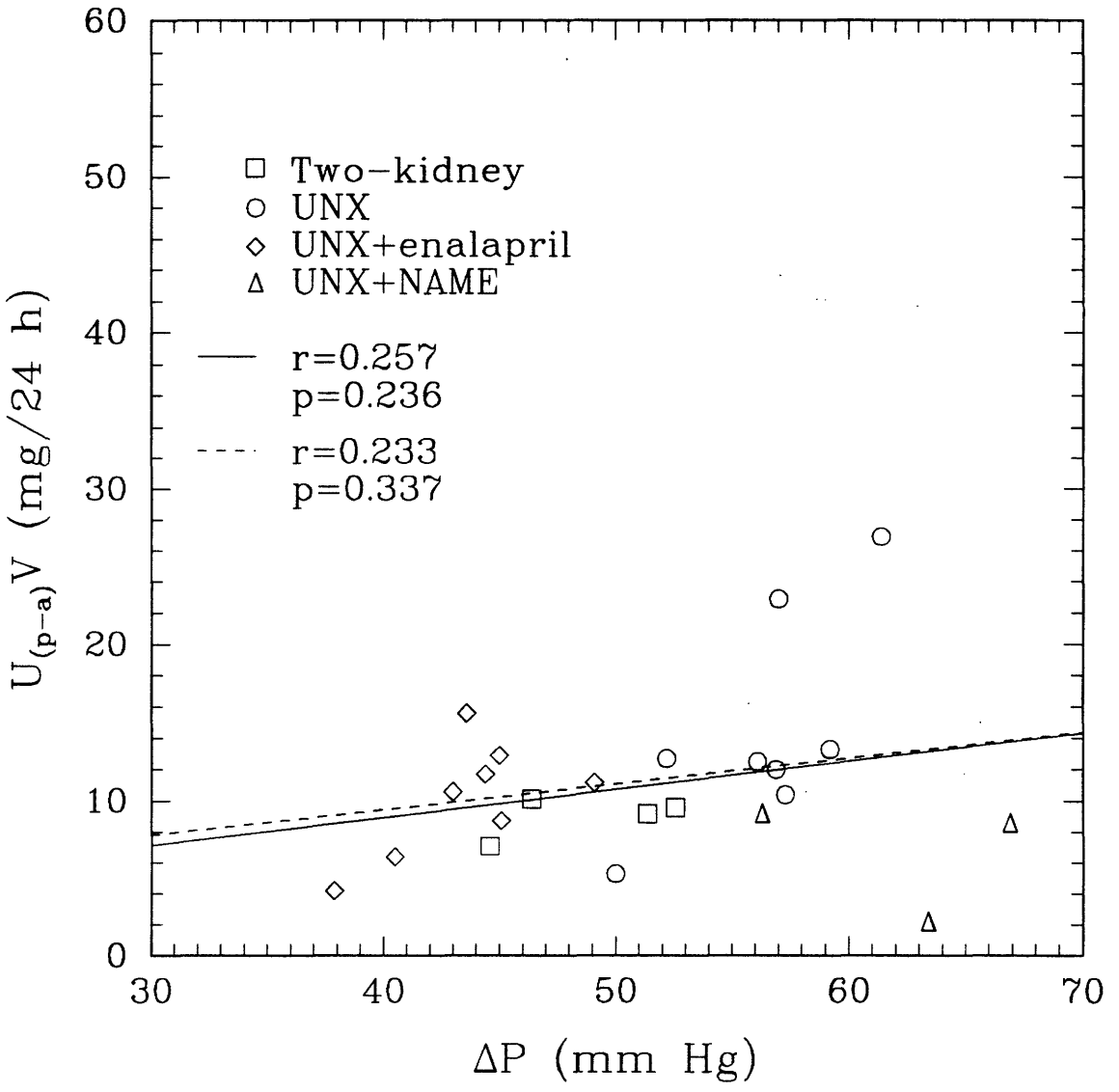

Figure 6-9: Correlation of filtration pressure ($\overline{\Delta P}$) to urinary non-albumin protein excretion ($U_{(p-a)}\dot{V}$). Solid lines are fit to all data, dashed lines are fit to the three 1K groups.

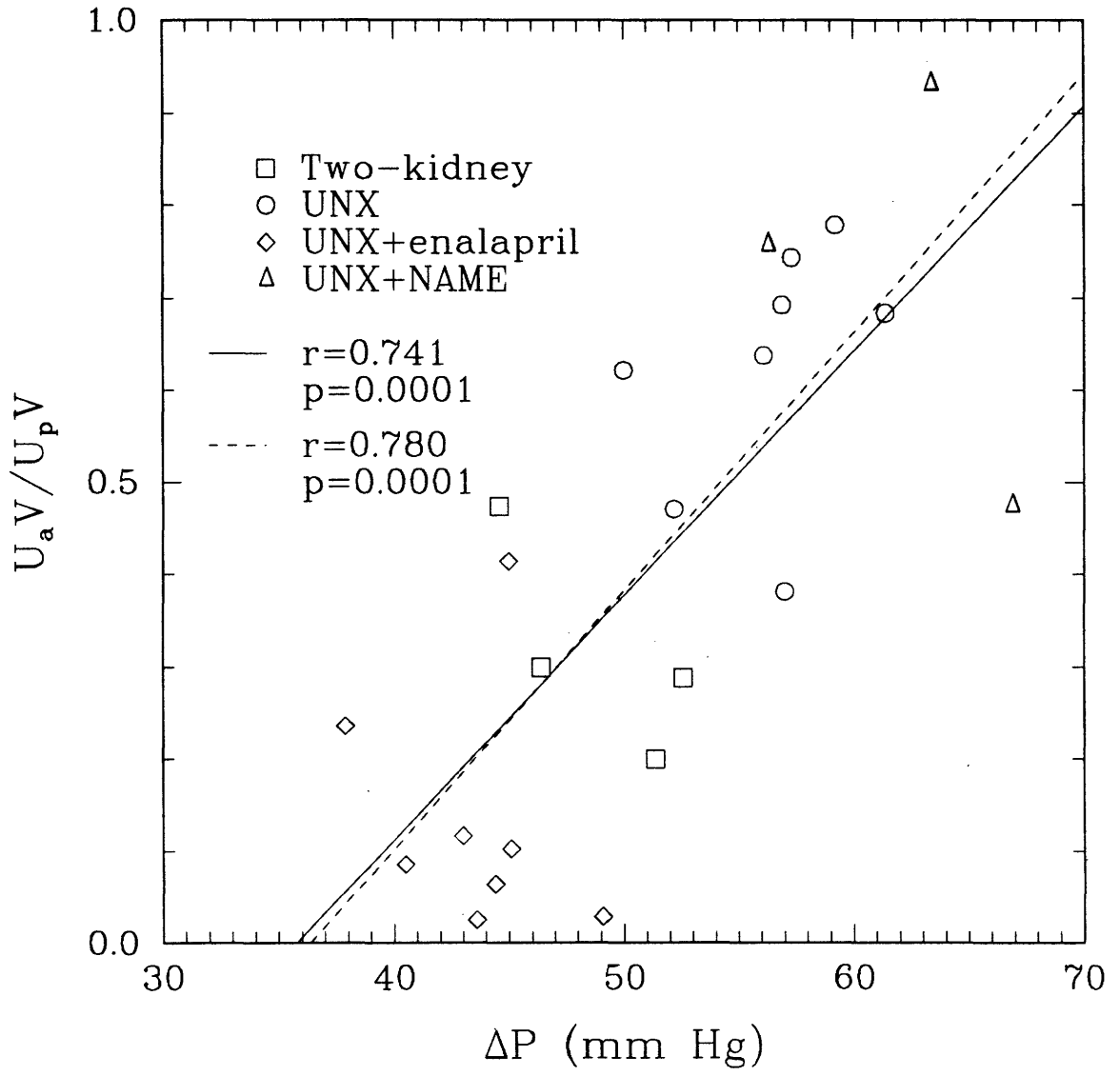

Figure 6-10: Correlation of filtration pressure ($\overline{\Delta P}$) to fractional albumin excretion ($U_a\dot{V}/U_p\dot{V}$). Solid lines are fit to all data, dashed lines are fit to the three 1K groups.

few studies, but a comprehensive picture of the mechanism has yet to emerge. Olson *et al.*[198] measured the sieving of neutral dextran, anionic dextran sulfate, and neutral, anionic, and cationic forms of horseradish peroxidase (HRP) in Munich-Wistar rats which had undergone 15/16 nephrectomy. Neutral HRP sieving coefficients and dextran sieving coefficients for $r_s = 16$ to 60 Å were not significantly different from controls. Micropuncture was not performed in this study. If their sieving data are interpreted using hemodynamic parameters from a similar study by the same investigators,[128] then the Olson *et al.* results are seen to be in agreement with those of the present work: renal ablation decreased the selectivity to large (> 50 Å) neutral molecules, but that to smaller molecules was relatively unaffected. In addition, values of Θ for anionic HRP and dextran sulfate were significantly increased, while those for cationic HRP were significantly decreased. This diminished charge-selectivity is also in concurrence with the results reported here.

Weening and van der Wal[253] studied the effects in rats of lowered perfusion pressure on charge-selectivity using charged horseradish peroxidases. Aortic ligation was used to lower $\overline{AP}$ from 105 to 56 mm Hg, though $\overline{\Delta P}$ was not measured. Fractional clearances of anionic, neutral, and cationic HRP were all unchanged. Thus, lowering of $\overline{\Delta P}$ to levels below physiologic may have no effect on permselectivity.

Mayer *et al.*[174] measured dextran sieving curves in rats along with the fractional clearance of 18 Å dextran sulfate. Renal ablation increased Θ for both dextran sulfate and large ($r_s > 55$ Å) dextrans. Treatment of the ablated rats with MK954, an angiotensin II receptor blocker, did not change Θ for dextran sulfate though both $\overline{\Delta P}$ and $U_p\dot{V}$ decreased and the size-selectivity to neutral dextran was restored to normal. Unlike the ACE inhibitor used in this study, pressure ameliorization by angiotensin II blockage demonstrated no effect on charge selectivity.

Treatment of uninephrectomized rats with ACE inhibitor did not substantially change size-selectivity to Ficoll in this study, although it did reduce proteinuria. In contrast, ACE inhibitors have been shown to improve size-selectivity in aging rats[213] and in patients with diabetic nephropathy[183] and IgA nephropathy.[212] These studies used dextran instead of Ficoll to assess size-selectivity, but this would not be expected to change the qualitative nature of the results. The reason for the different responses to ACE inhibition in the present study versus the others is not clear, but it may be related to different mechanisms of action. It has been suggested that in some disease models ACE inhibitors reduce proteinuria by increasing kinin activity rather than by decreasing angiotensin II activity.[130,131]

Thus, although both enalapril and angiotensin II antagonists reduce proteinuria in rats with reduced renal mass, enalapril appears to restore charge-selectivity without changing size-selectivity while A-II blockers restore size-selectivity without changing charge-selectivity. The possibility of different pharmacological mechanisms influencing the selectivity underscore the need for further research in this area.

This study is the first to report the effect of NO inhibition on glomerular size-selectivity. Despite changes in hemodynamics and the ultrafiltration coefficient, sieving coefficients from NAME rats were not different than those from UNX rats. It may be that any effects of NAME on size-selectivity are not detectable in the uninephrectomized state. Further studies of NO inhibition on two-kidney rats should be performed.

We used the ratio of urinary albumin excretion to total urinary protein excretion as a measure of effective membrane charge. In doing so, however, we did not distinguish the effect of changes in glomerular charge-selectivity from any potential changes in tubular reabsorption of protein. Since it is generally postulated that the reabsorption capacity of the tubules is overwhelmed in proteinuria, this is not believed to be a cause for concern. It should be recognized, however, that in the normal state cationic proteins are absorbed more rapidly along the length of the tubule, although the net absorption of both cationic and anionic proteins are the same.[66] There is no information on how pathological conditions such as renal ablation affect protein reabsorption, although it seems reasonable to continue to assume that it will have no effect on urinary protein excretion because of the high filtered load of protein. Nevertheless, to rigorously correlate charge-selectivity to proteinuria requires measurements of both protein excretion and the sieving coefficient of a suitable charged tracer (*i.e.*, one that is freely filtered and neither secreted nor reabsorbed in the tubules). Given the preference for Ficoll over dextran in sieving studies (Chapter 4) and the difficulties in interpreting dextran sulfate clearances because it binds to plasma proteins,[174] there is now strong motivation for developing a charged analog to Ficoll for use in studies of charge-selectivity. Ficoll sulfate is a likely candidate for this purpose. Ghitescu *et al.*[116] have developed anionic neutral, and cationic versions of DNP-bovine serum albumin which might also be used for such purposes. Alternatively, Di Mario and co-workers[86,87] have proposed using the ratio of anionic immunoglobulin (IgG4) excretion to total IgG excretion as a clinical parameter of charge selectivity. Sensitive immunoassays have been developed for measuring IgG4 and total IgG in urine.[88,182] This method has the advantage of not requiring exogenous infusions.

The results presented here are indicative of the chronic effects of altered pressure on glomerular permselectivity. Effects of short-term pressure changes by the acute administration of enalapril and NAME, in both 1K and 2K rats, should be examined.

Chapter 7

Estimation of Glomerular Transcapillary Hydraulic Pressure in the Rat from Sieving Curves

7.1 Introduction

7.1.1 Previous Work

The clinical motivation to monitor filtration pressure is strong in light of evidence that hyperfiltration, and in particular an elevated $\overline{\Delta P}$, is associated with a progression of glomerular damage and renal disease regardless of the etiology of the hemodynamic changes. Rat models in which $\overline{\Delta P}$ has been shown to play a significant role include surgical infarction of renal tissue,[6,7,106,107,128,175,198] desoxycorticosterone-salt hypertension,[92] and streptozotocin-induced diabetes mellitus.[266,267] In all of these cases $\overline{\Delta P}$ is elevated along with the glomerular plasma flow rate Q_A and the single nephron glomerular filtration rate *SNGFR*. Therapy in these animals which selectively reduces $\overline{\Delta P}$ (while leaving Q_A and *SNGFR* elevated), such as treatment with angiotensin I converting enzyme (ACE) inhibitors, slows the progression of glomerular sclerosis even in the persistence of systemic hypertension or underlying metabolic disease.[6,7,107,175,266] Additionally, treatment of systemic hypertension in a manner which does not lower $\overline{\Delta P}$ is not as effective at preventing further renal damage.[7,91] Acute or chronic elevations in $\overline{\Delta P}$ are also associated with proteinuria.[29,261,262] A method for obtaining clinical values of $\overline{\Delta P}$, or at least determining changes in $\overline{\Delta P}$, is required to fully evaluate the results of human trials.

The estimation of filtration pressures from sieving curve data has been of interest for some time. Early attempts[11,110,111,159,160,247] were based on the Pappenheimer-Renkin mathematical model (Section 2.6.3) and therefore suffer from its limitations. Least-squares fit values for an effective glomerular ultrafiltration pressure, equivalent to $\overline{\Delta P} - \int_0^1 \pi_{GC}(y)\,dy$, range from 9 to 30 mm Hg in these early studies. The differences in the fits principally reflect variations in the method used to calculate the hindrance factors, with the lower values obtained with the most recent methods. These estimates are all based on data from dogs and human beings, so there are no direct measurements of $\overline{\Delta P}$ with which to compare. Du Bois and Stoupel[90] tested the Pappenheimer-Renkin model *in vitro* by measuring PVP transport through artificial membranes. Reported results showed good agreement with the theory; the ratio of actual $\overline{\Delta P}$ to fitted values based on sieving curves was 1.036.

Lambert and Gassee and co-workers[112,158] fit pressures in the dog glomerulus using a pore model, but also included a term for the hydraulic pressure drop along the length of the capillary.

In order to get realistic results, they found it necessary to modify the boundary condition for solute concentration at the membrane/Bowman's space interface as a hybrid of two possibilities previously discussed (Section 2.6.4): the first and last quarter of capillary length used the local concentration condition while the middle two quarters used the well-mixed condition. Using this model afferent and efferent $\overline{\Delta P}$ values of 50 and 42 mm Hg were obtained. Again, no confirming measurements were obtainable.

Chang,[59] in a retrospective study, used the pore model to fit filtration pressures to dextran sieving literature data for Munich-Wistar rats.[60,63] His fit values for $\overline{\Delta P}$ were consistently lower than the experimental values by 2-9 mm Hg, with corresponding higher K_f values and lower r_0 values than reported originally. The range of $\overline{\Delta P}$ measured in the studies was not wide, ranging only from 34 to 40 mm Hg.

Most recently, Chan *et al.* have used dextran sieving data to estimate $\overline{\Delta P}$ in a clinical study of dietary protein effects.[57] Employing the isoporous model, they obtained values for control subjects of $\overline{\Delta P} = 34$ mm Hg and 38 mm Hg in the preprandial and postprandial periods, respectively. Fits to results from patients with chronic glomerular disease (preprandial $\overline{\Delta P} = 34$ mm Hg) were insensitive to changes in $\overline{\Delta P}$ up to 38 mm Hg.

This chapter begins with a discussion of the theoretical basis for estimating $\overline{\Delta P}$ from sieving data, followed by a comprehensive review of fitting isoporous-model pressures to available dextran experimental data. We then examined pressure fitting using recent data with more optimal conditions of exogenous tracer, greater range in measured pressures, and more recent heteroporous models.

The fawn-hooded rat study of Chapter 6 is one of the few experiments to date in which both micropuncture and sieving measurements were performed and in which large alterations in $\overline{\Delta P}$ were achieved. As such, it provides an important new source of data with several advantages pertaining to pressure estimation. Ficoll sieving data was used, which is better suited to the theoretical model than that for dextran. Through GPC calibration with Ficoll standards, the molecular sizes were more accurately determined than had been previously, and a larger range of r_s was used. The animal protocols resulted in a wider range of $\overline{\Delta P}$ than usually reported. Finally, newer and more realistic heteroporous models were employed.

7.1.2 Theoretical Considerations

Any method which attempts to determine changes in $\overline{\Delta P}$ from sieving curves must distinguish between those effects due to alterations in permselectivity and those from alterations in hemodynamics. The situation of most interest for deriving pressures is that of $\overline{\Delta P}$ changes at constant $SNGFR$, since this corresponds to the clinical case where the information on flow rates (RPF, GFR) is at hand while $\overline{\Delta P}$ and K_f are unknown.

Figure 7-1 compares the effects of changes in r_0 to those of changes in $\overline{\Delta P}$ at constant *SNGFR* using the isoporous model. As would be expected, a r_0 increase is accompanied by a rise in Θ at all values of r_s. The effect is more noticeable at larger sizes. A rise in $\overline{\Delta P}$ increases the net solute clearance but increases *GFR* to an even greater degree, and so the fractional clearance decreases. Decreasing plasma osmotic pressure has essentially the same effect. In contrast to a change in r_0, the sieving coefficients for large molecules are less sensitive to pressure then those for small molecules. Good agreement with this prediction is shown by the findings of Gassee *et al.*,[111] where, at comparable renal flow rates, sieving curves were generally lower in dogs with higher mean arterial blood pressures, but the curves merged at large solute radius.

As pointed out by Du Bois and Stoupel,[90] the sieving curves are steeper—the membrane showing greater permselectivity—at lower pressures, where the diffusive forces play a more important role. For large solutes, the sieving curves are relatively independent of pressure, a consequence of convection-domination. Qualitatively, then, it can be seen that permselectivity changes have different effects than hemodynamic changes. The question remains whether the sensitivity of the measurements or of the models is sufficient to allow $\overline{\Delta P}$ to be inferred.

7.2 Preliminary Calculations

As an initial assessment, we retrospectively applied the isoporous, solid-sphere model of Section 2.6.4 to all experimental studies in the rat where both fractional clearances of neutral dextrans were obtained and $\overline{\Delta P}$ was measured by micropuncture. These results are summarized in Table 7.1. Each of the cases shown involves paired groups of animals; one group serves as a baseline or control group and the other is a group in which some sort of intervention was made. Using the mathematical model, best-fit values of $\overline{\Delta P}$ (along with r_0) were calculated from the data as described in Section 7.3.1 and compared to those actually measured. Similarly to Chang,[59] fitted values generally underpredict the actual ones. The more central clinical issue of measuring *changes* in $\overline{\Delta P}$ is shown in Figure 7-2 for the paired groups. The correct direction is calculated in six of the nine cases, but the magnitude of the change is generally lower than measured. The mathematical analysis failed to correspond to the actual results in three cases, for no apparent reason. In summary, while the theory gives reasonable agreement with the data, it is questionable whether the conventional model is a clinically reliable means of estimating $\overline{\Delta P}$, or directional changes in $\overline{\Delta P}$.

7.3 Fitting of $\overline{\Delta P}$ to Fawn-Hooded Rat Data

7.3.1 Methods

Pore size parameters plus $\overline{\Delta P}$ were fitted simultaneously to sieving data using the χ^2 criterion of Section 4.2.5. Both data from the individual rats and averaged data for the experimental groups were

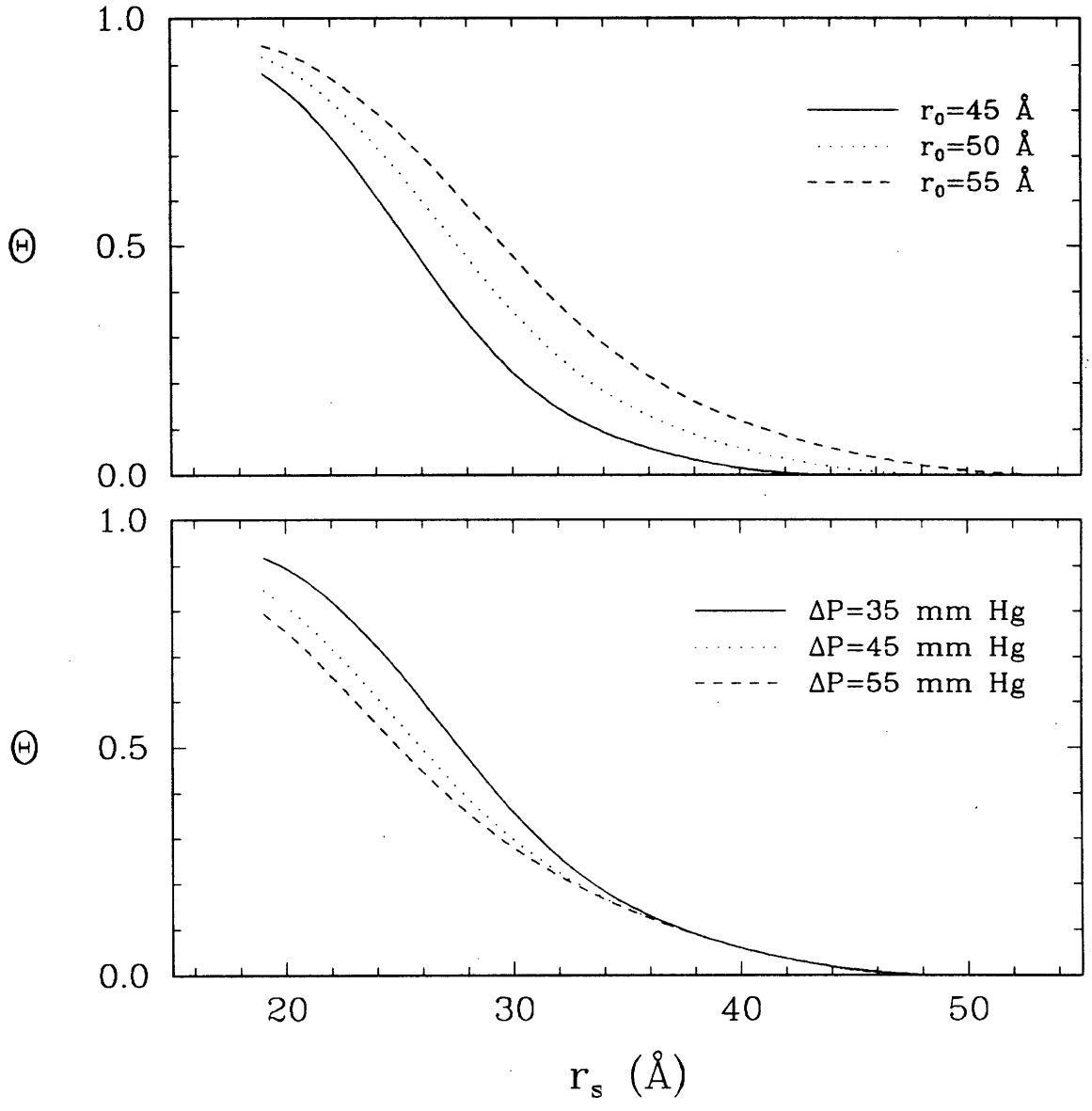

Figure 7-1: Theoretical effects of changes in isoporous r_0 (*top*) compared to changes in $\overline{\Delta P}$ (*bottom*) at constant *SNGFR*. Unless otherwise shown, input parameters were r_0 = 50 Å, *SNGFR* = 49.8 nl/min, Q_A = 172 nl/min, $\overline{\Delta P}$ = 35 mm Hg.

Conditions	Reference	$\overline{\Delta P}$, mm Hg Measured	Calculated	Measured/ Calculated
1. Normal hydropenia	30	34.0	33.8	1.01
Hydropenia + AII		43.0	45.6	0.94
2. NSN hydropenia	60	39.0	29.0	1.34
NSN + PVE		40.0	30.3	1.32
3. Normal hydropenia	63	34.0	32.0	1.06
Normal + PVE		38.0	27.0	1.41
4. Normal euvolemia	133	33.9	21.9	1.55
Normal+Histamine		39.5	23.5	1.68
5. Normal control	178	39.9	30.7	1.30
Diabetes		34.5	30.8	1.12
6. Normal euvolemia	261	33.0	36.8	0.90
Normal + RVC		42.0	39.5	1.06
7. PHN baseline	262	40.0	42.5	0.94
PHN + AII		52.0	45.6	1.14
8. PHN baseline	262	42.0	49.4	0.85
PHN + ACh		35.0	50.2	0.70
9. Renal ablation	263	51.9	41.5	1.25
Ablation + Ver		34.0	35.5	0.96

Table 7.1: Comparison of measured and fitted $\overline{\Delta P}$ from published fractional clearance data for dextran in rats using the isoporous, solid-sphere model. *Abbreviations*: AII–angiotensin II, NSN–nephrotoxic serum nephritis, PVE–plasma volume expansion, PHN–Passive Heymann's nephritis, ACh–acetylcholine, Ver-verapamil.

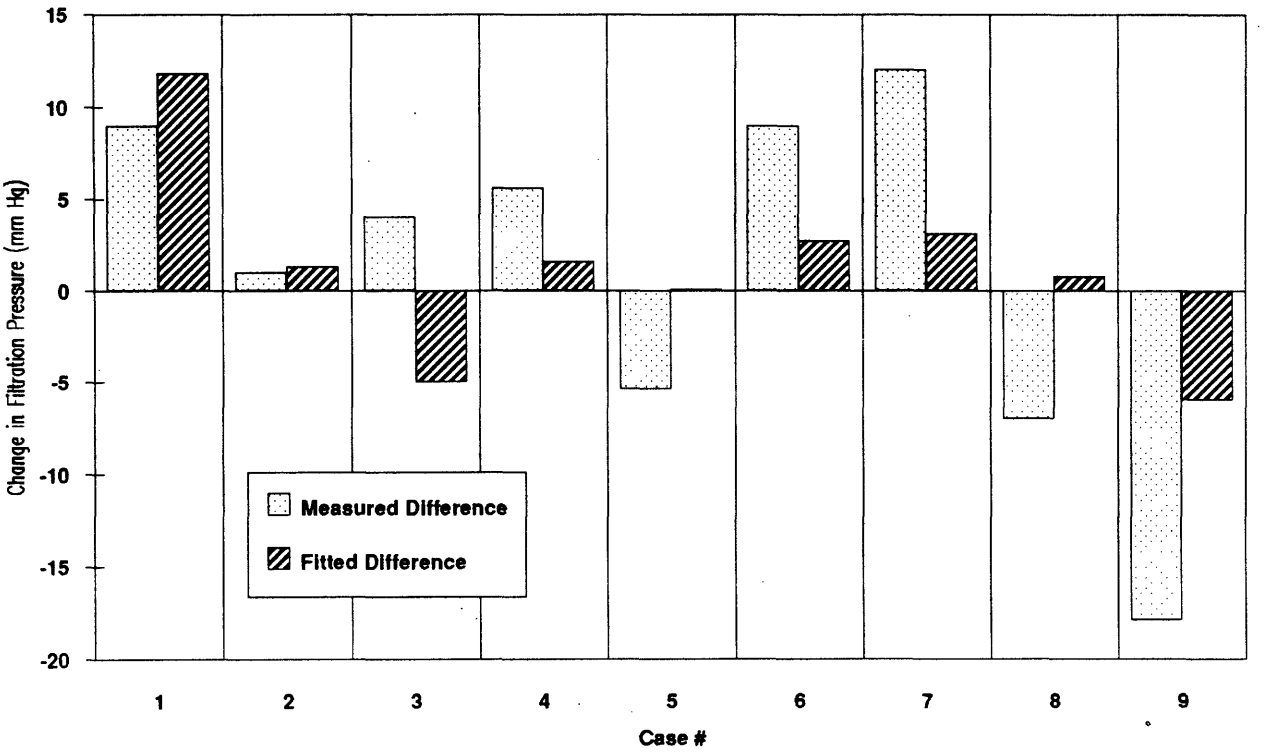

Figure 7-2: Comparison of measured changes in $\overline{\Delta P}$ to those fitted from dextran sieving data using the isoporous, solid-sphere model. Case number correspond to those in Table 7.1.

used. The group-mean sieving coefficients of Tables 6.5 and 6.6 were fitted using the appropriate hemodynamic parameters from Table 6.1. For fits to individual rat sieving curves, data was used only from the 25 animals (2K=4, UNX=9, END=8, NAME=4) on which both micropuncture and sieving studies were performed. When data from a single rat was fitted, the standard error $\sigma_{i,\text{exp}}$ was set equal to $\Theta_{i,\text{exp}}$ in Eq. 4.6.

Either Powell's method[206] or the donwhill simplex method[206] was used to determine the best-fit set of parameters. Pearson's correlation coefficient was used to determine significance of correlation between parameters.

7.3.2 Results and Discussion

In order to first determine whether specific ranges of the sieving curves showed greater sensitivity to $\overline{\Delta P}$ changes, we examined the individual sieving and micropuncture data from the 25 rats which underwent both studies. Correlation coefficients between $\overline{\Delta P}$ and Θ were calculated for each value of r_s. The results are shown in Figure 7-3. The correlation was not significant at any value of r_s, but the trend itself is of some interest. The correlation coefficient was negative for 20 Å $< r_s <$ 38 Å. This implies that Θ varied inversely with $\overline{\Delta P}$ at small $r_s$and varied with $\overline{\Delta P}$ at large r_s, in agreement with the predicted effect from Figure 7-1. For 50 Å$< r_s <$ 70 Å, the correlation was a constant positive value, with a lower magnitude than that for small r_s. While it seems that Θ at small r_s may be more sensitive to $\overline{\Delta P}$ changes, the correlation is not significant enough to justify using specific size ranges of sieving data to fit $\overline{\Delta P}$.

To demonstrate the equivalence of using single nephron versus whole kidney parameters in pressure fits, the four sets of experimental group data were fitted using both single nephron and whole kidney hemodynamic data of Table 6.1. The results are shown in Table 7.2. Little difference is seen between the results from single nephron versus whole kidney parameters. Fitted $\overline{\Delta P}$ uniformly underpredicted measured values by a considerable amount. None of the models predicted that $\overline{\Delta P}$ for the NAME was was substantially higher than the other groups. The isoporous + shunt model gave results closer to those measured, and it correctly demonstrated that the UNX and NAME pressures were higher than the 2K and ENA pressure. Even though they provided better overall fits to the sieving coefficients, the lognormal and lognormal + shunt fits indicated that the ENA and NAME pressure were either higher than or similar to those for 2K and UNX.

Finally, pressures were fitted to the sieving data of each of the 25 double-study rats and compared to the micropuncture value. Whole kidney hemodynamic parameters were used for the inputs. The results are shown in Figures 7-4, 7-5, and 7-6.

Again, fitted $\overline{\Delta P}$ tended to underestimate measured $\overline{\Delta P}$. For the isoporous + shunt model, $\overline{\delta P}_{\text{fitted}} - \overline{\delta P}_{\text{measured}}$ averaged -13.6 mm Hg, with a range of from $+6.7$ to -61.4 mm Hg. For the lognormal model, the average was -21.2 mm Hg with a range of from -8.3 to 36.7 mm Hg, and for

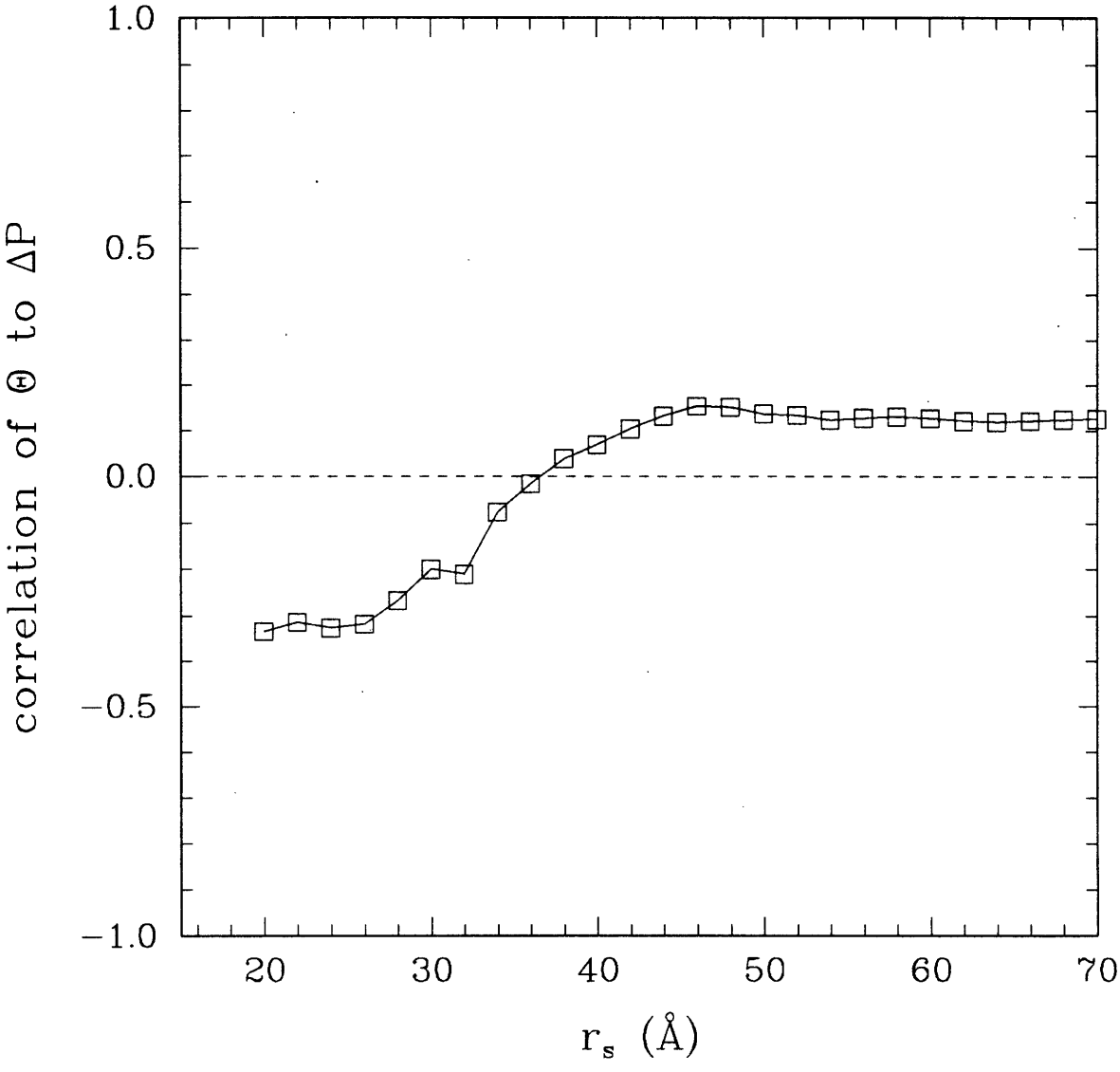

Figure 7-3: Correlation of $\Theta(r_s)$ with $\overline{\Delta P}$ for fawn-hooded rats.

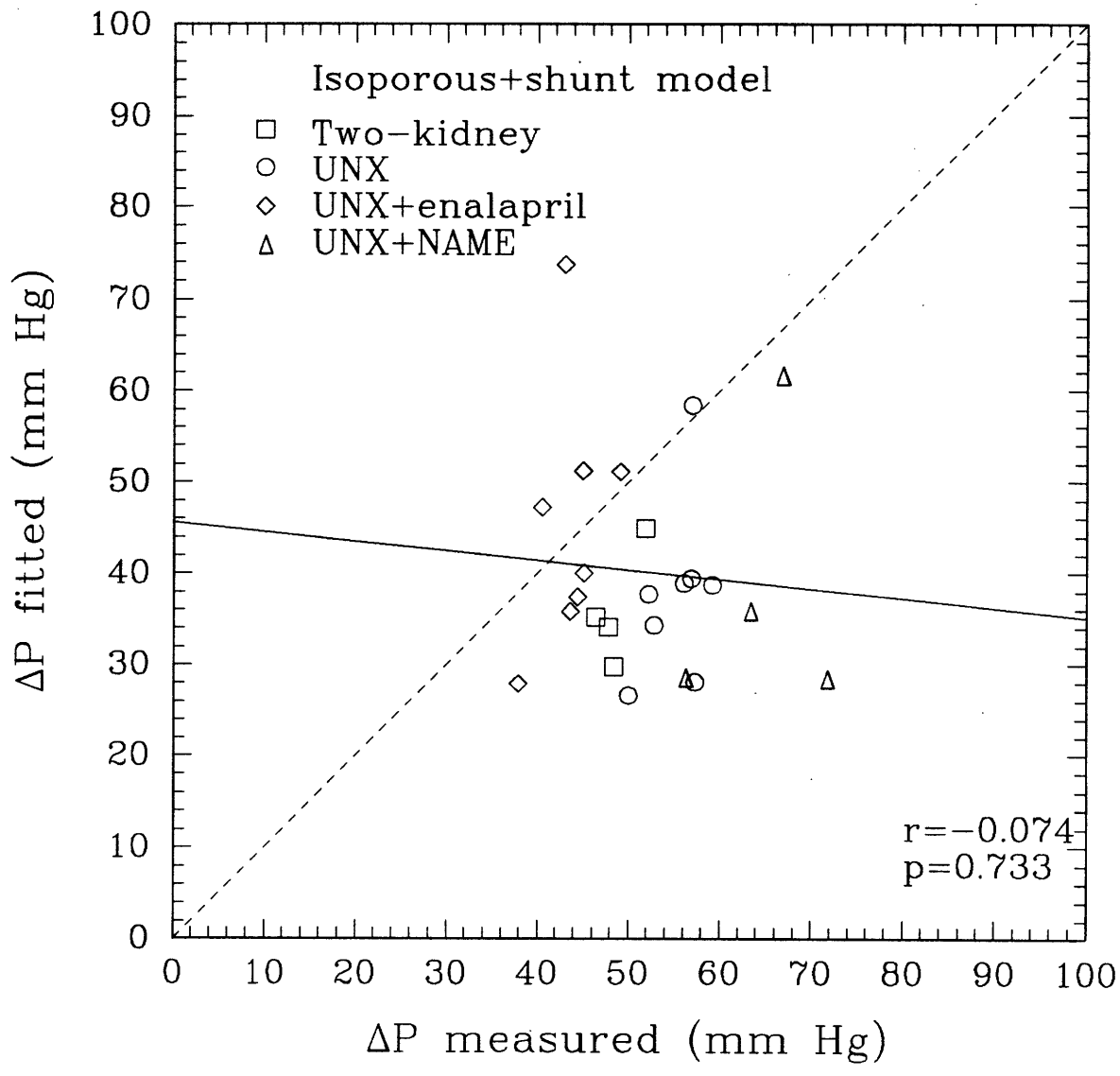

Figure 7-4: Correlation of measured to fitted $\overline{\Delta P}$ for isoporous + shunt model. Solid line is a linear fit to the data. Dashed line is $\overline{\Delta P}_{\text{fit}} = \overline{\Delta P}_{\text{measured}}$.

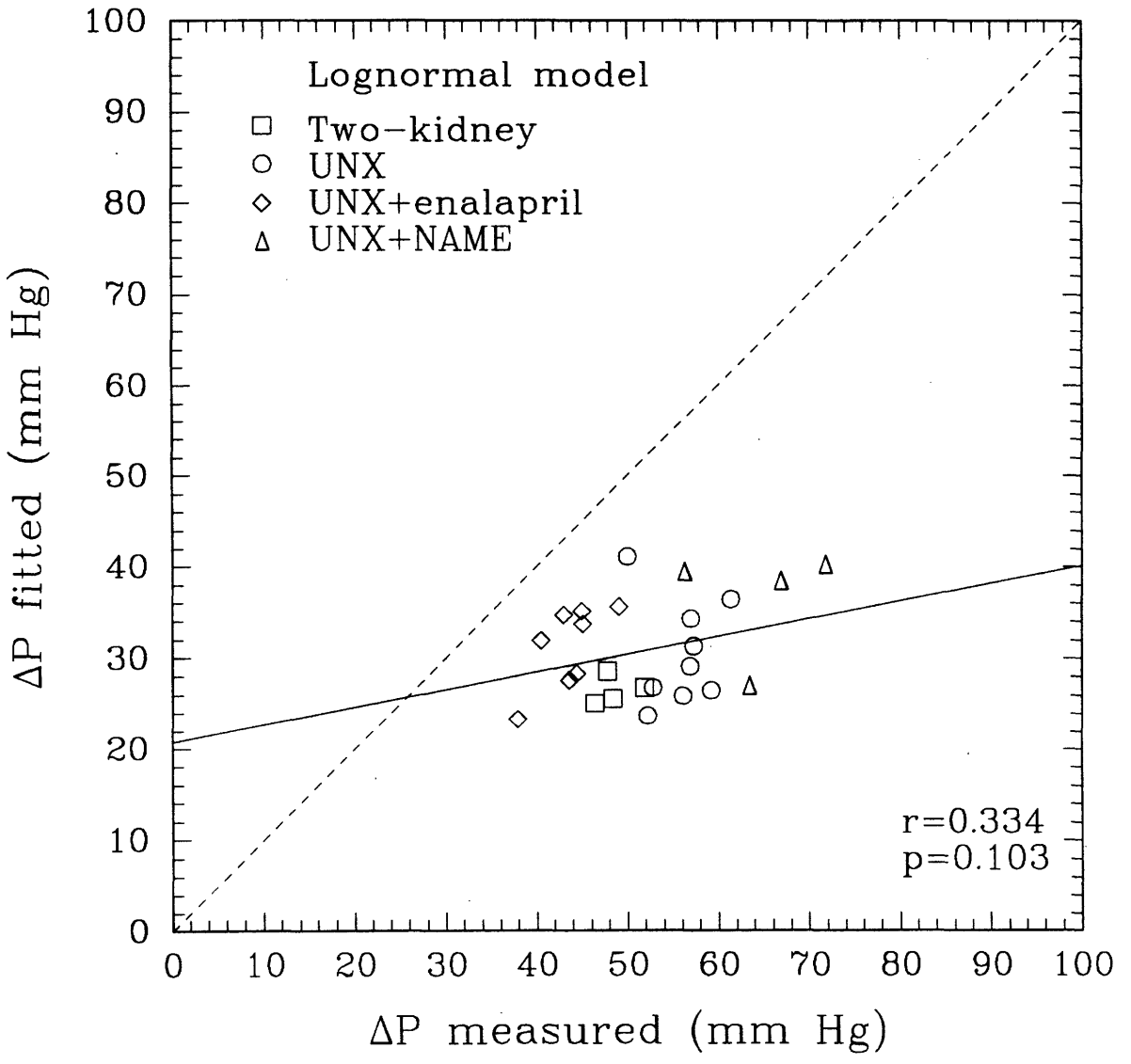

Figure 7-5: Correlation of measured to fitted $\overline{\Delta P}$ for lognormal model. Solid line is a linear fit to the data. Dashed line is $\overline{\Delta P}_{\text{fit}} = \overline{\Delta P}_{\text{measured}}$.

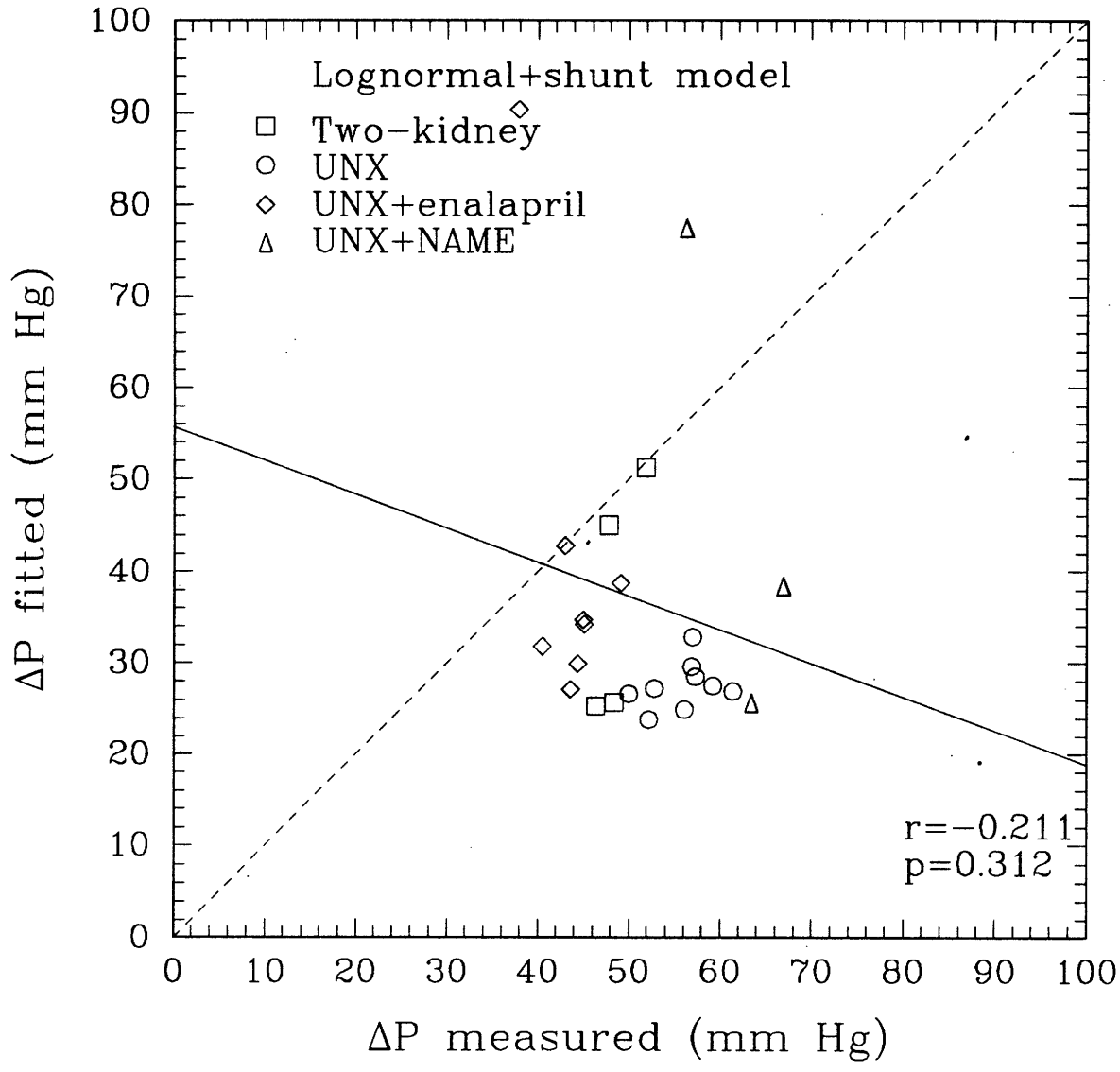

Figure 7-6: Correlation of measured to fitted $\overline{\Delta P}$ for lognormal + shunt model. Solid line is a linear fit to the data. Dashed line is $\overline{\Delta P}_{\text{fit}} = \overline{\Delta P}_{\text{measured}}$.

Group			2K		UNX		ENA		NAME	
$\overline{\Delta P}_{measured}$ (mm Hg)			48.6 ± 1.2		55.9 ± 1.2		43.6 ± 1.2		64.6 ± 3.3	
parameters			WK	SN	WK	SN	WK	SN	WK	SN
Isoporous	r_0	(Å)	46.9	46.8	47.7	47.8	48.6	48.7	49.0	48.7
+shunt	ω_0	(10^{-4})	1.07	1.05	27.4	27.3	7.18	7.23	9.43	8.69
	$\overline{\Delta P}_{flt}$	(mm Hg)	35.8	37.0	44.8	45.2	37.0	36.9	38.5	40.8
Lognormal	u	(Å)	29.7	29.8	26.6	26.0	32.5	32.5	33.4	33.9
	s		1.26	1.26	1.33	1.34	1.26	1.26	1.25	1.24
	$\overline{\Delta P}_{flt}$	(mm Hg)	27.2	28.7	29.1	28.8	31.4	31.2	32.1	35.6
Lognormal	u	(Å)	34.1	35.4	31.9	27.6	35.8	34.5	34.2	35.6
+shunt	s		1.21	1.19	1.25	1.31	1.20	1.22	1.23	1.22
	ω_0	(10^{-4})	0.314	0.415	13.8	4.48	0.905	0.891	1.13	1.31
	$\overline{\Delta P}_{flt}$	(mm Hg)	27.6	29.7	35.2	28.4	31.1	30.9	31.7	35.6

Table 7.2: Fits of pore parameters plus $\overline{\Delta P}$ to group-averaged sieving coefficients. WK: whole kidney hemodynamic parameters; SN: single nephron hemodynamic parameters.

the lognormal + shunt model the average was -16.0 mm Hg with a range of from $+52.4$ to -38.1 mm Hg. For the isoporous + shunt and lognormal models, there were a few cases in which the values were overestimated. There was no apparent pattern to the overestimation, however. None of the correlations between fitted and measured $\overline{\Delta P}$ were significant ($p = 0.733$ for the isoporous + shunt model, $p = 0.103$ for the lognormal, $p = 0.312$ for the lognormal + shunt). For the lognormal + shunt model, the pressures were inversely correlated.

In summary, neither the use of newer heteroporous models nor fitting of individual sieving data instead of group means improves the ability of the present models of glomerular permselectivity to infer glomerular hydraulic pressures. It is not clear whether this failure is intrinsic to the model or to the experimental accuracy of the sieving coefficients and hemodynamic data. Further evaluation of the model and the sensitivity of pressure fitting to experimental variance in Θ is necessary to determine whether estimation of $\overline{\Delta P}$ from sieving coefficients is viable.

Chapter 8

Conclusions and Recommendations

In this thesis we examined several technical and theoretical aspects in the use of sieving curves to analyze the effects of hemodynamic changes on glomerular permselectivity. In Chapter 3, errors in dextran and Ficoll molecular radius resulting from the use of protein calibration curves were shown to be small, on the order of 5 Å, for Sephacryl 300-HR columns. Correction factors could be easily obtained from calibrations using monodisperse polysaccharide standards. Dispersive effects were seen to be noncontributory to the calculation of sieving curves.

The importance of molecular configuration in glomerular filtration was demonstrated in Chapter 4. Ficoll and dextran were shown to behave *in vivo* in a fashion qualitatively similarly to their diffusion through synthetic membranes; that is, dextran transport at all sizes was greatly enhanced over that of Ficoll. The data from Ficoll indicates that the capillary wall is more size-restrictive than had previously been suggested by dextran sieving curves. Since Ficoll has been shown to follow the predicted behavior of a solid neutral sphere, pore size parameters from Ficoll studies will be more directly interpretable in terms of the pathophysiology of proteinuria. It is recommended that Ficoll be used for all future analysis of glomerular permselectivity. There is a vast body of dextran sieving data in various experimental protocols, both clinically and in animals. While Ficoll would be expected to show roughly parallel behavior, it will nevertheless be important to perform Ficoll sieving studies in at least some of the more important protocols (*e.g.*, renal ablation, diabetes, and glomerulonephritis) versus control animals.

Dextran filtration *in vivo* was described using a recently-developed model for the transport of random coils through cylindrical pores (Chapter 5). While the precise nature of dextran's enhanced transport remains unknown, it was shown to be quantitatively equivalent to a solute/pore attraction energy of about $-0.25k_BT$, nearly the same as that demonstrated *in vitro*. It thus appears that the phenomenon is independent of the system and may be intrinsic to the dextran/water system. Along these lines, dextran's physical dimensions have been measured by several methods and seen to be consistent with a more compact molecule than would be expected from its chemical structure (Appendix F). It may prove interesting to model dextran's transport behavior in other ways, such as by a factor which reduces the equivalent radius of gyration of the dextran molecule or by calculating steric parameters for a branched molecule.

We have introduced a new means of describing the heteroporous nature of the glomerular capillary wall, the lognormal + shunt model (Chapter 4 and 6). In order to reduce computation time, the approximate methods developed by Deen *et al.*[79] have been used in the calculation of hetero-

porous membrane parameters. While these methods have been shown to be accurate in previous applications, future experiments may involve other types of pore size distributions and the sieving data will be for tracers at higher r_s (and hence lower Θ) than previously measured. With the advent of high-speed workstations and wider access to supercomputers, the time required to implement the full mathematical model will not be prohibitive, and it is recommended that in the future it be employed in sieving analysis.

It should be emphasized that all such models represent only functional equivalents of the capillary wall. As such, changes in pore size parameters cannot be correlated to true changes in the wall ultrastructure. As newer ultrastructurally-based theories become available, they should be incorporated into the model.

The fawn-hooded rat experiments of Chapter 6 represent the first use of Ficoll to evaluate changes in glomerular disease and were performed in a species of rat for which no previous sieving data exists. In addition to continued evaluation of the fawn-hooded rat model, further work using Ficoll in Munich-Wistar models and in clinical studies is recommended, where results can be compared to previous studies using dextran.

The fawn-hooded rat experiments suggest that loss of charge permselectivity is more significant than loss of size-permselectivity in the pathophysiology of proteinuria secondary to renal ablation. In the absence of a suitable charged tracer for evaluation of charge-permselectivity, these conclusions were based on measurements of urinary fractional albumin excretion. Development and characterization of a charged analog of Ficoll such as Ficoll sulfate should be made a high priority, as it is necessary for more direct assessments of charge-permselectivity.

Assuming the eventual development of a charged tracer, several interesting studies suggest themselves. A comparison of the effects of ACE inhibitors versus angiotensin II antagonists on charge- and size-selectivity and proteinuria are recommended, as the data of Chapter 6 and the results of Mayer *et al.*[174] suggest different mechanisms are at work. Such a study would ideally involve both control and uninephrectomized animals with measurement of neutral and charged Ficoll sieving, total urinary protein excretion, and fractional excretion of albumin, IgG, and IgG4.

A study comparing the acute effects of ACE inhibitors, angiotensin II antagonists, and NAME in normal and uninephrectomized rats would also be of great interest. A two-period sieving study—one before the administration of the drug and one after—would be required for these experiments.

The results from attempts to fit filtration pressures to sieving data were not encouraging (Chapter 7). The worst-case scenario is that Θ is not sufficiently sensitive to changes in $\overline{\Delta P}$ to allow for fitting. A more optimistic possibility is that the present mathematical model is simply not advanced enough to enable accurate estimation of $\overline{\Delta P}$. A more sophisticated examination of the sensitivity of the model to experimental errors may suggest an alternate approach, such as a definition of χ^2 modified for optimization of $\overline{\Delta P}$ fitting.

Bibliography

[1] K. Aisaka, S. S. Gross, O. W. Griffith, and R. Levi. N^G-methylarginine, an inhibitor of endothelium-derived nitric oxide synthesis, is a potent pressor agent in the guinea pig: Does nitric oxide regulate blood pressure *in vivo*? *Biochem. Biophys. Res. Commun.*, 160:881–885, 1989.

[2] J. Aitchison and J. A. C. Brown. *The Lognormal Distribution With Special References to its Uses in Economics.* University Press, Cambridge, 1970.

[3] H. Akima. A new method of interpolation and smooth curve fitting based on local procedures. *J. ACM*, 17:589–602, 1970.

[4] H. Akima. Interpolation and smooth curve fitting based on local procedures. *Comm. ACM*, 15:914–918, 1972.

[5] J. L. Anderson and J. A. Quinn. Restricted transport in small pores. A model for steric exclusion and hindered particle motion. *Biophys. J.*, 14:130–150, 1974.

[6] S. Anderson, T. W. Meyer, H. G. Rennke, and B. M. Brenner. Control of glomerular hypertension limits glomerular injury in rats with reduced renal mass. *J. Clin. Invest.*, 76:612–619, 1985.

[7] S. Anderson, H. G. Rennke, and B. M. Brenner. Therapeutic advantage of converting enzyme inhibitors in arresting progressive renal disease associated with systemic hypertension in the rat. *J. Clin. Invest.*, 77:1993–2000, 1986.

[8] P. M. Andrews. Scanning electron microscopy of the nephrotic kidney. *Virchows Arch. B. Cell Pathol.*, 17:195–211, 1975.

[9] R. Aris. On the dispersion of a solute in a fluid flowing through a tube. *Proc. Roy. Soc. London, Ser. A.*, 235:67–77, 1956.

[10] V. S. Arpaci. *Conduction Heat Transfer.* Addison-Wesley, Reading, MA, 1966.

[11] G. Arturson, T. Groth, and G. Grotte. Human glomerular membrane porosity and filtration pressure: Dextran clearance data analyzed by theoretical models. *Clin. Sci.*, 40:137–158, 1971.

[12] D. A. Ausiello, J. I. Kreisberg, C. Roy, and M. J. Karnovsky. Contraction of cultured rat glomerular cells of apparent mesangial origin after stimulation with angiotensin II and arginine vasopressin. *J. Clin. Invest.*, 65:754–760, 1980.

[13] P. S. Avasthi and A. P. Evan. Glomerular permeability in aminonucleoside-induced nephrosis in rats. A proposed role of endothelial cells. *J. Lab. Clin. Med.*, 93:266–276, 1979.

[14] C. A. Baldamus, R. Galaske, G. M. Eisenbach, H. P. Krause, and H. Stolte. Glomerular protein filtration in normal and nephrotic rats. *Contrib. Nephrol.*, 1:37–49, 1975.

[15] A. M. Basedow, K. H. Ebert, H. Ederer, and H. Hunger. Die Bestimmung der Molekulargewichtsverteilung von Polymeren durch Permeationscromotographie en porosen Glas, 1. Dextrane bis zu einem Molekulargewicht von 600,000. *Makromol. Chem.*, 177:1501–1524, 1976.

[16] C. Baylis, P. Harton, and K. Engels. Endothelial-derived relaxing factor controls renal hemodynamics in the normal rat kidney. *J. Am. Soc. Nephr.*, 1:875–881, 1990.

[17] C. Baylis, I. Ichikawa, W. T. Willis, C. B. Wilson, and B. M. Brenner. Dynamics of glomerular ultrafiltration. IX. Effects of plasma protein concentration. *Am. J. Physiol.*, 232:F58–71, 1977.

[18] C. Baylis, B. Mitruka, and A. Deng. Chronic blockade of nitric oxide synthesis in the rat produces systemic hypertension and glomerular damage. *J. Clin. Invest.*, 90:278–281, 1992.

[19] B. G. Belenkii, L. Z. Vilenchik, V. V. Nesterov, V. J. Kolegov, and S. Y. Frenkel. Peculiarities in gel permeation chromatography of flexible-chain polymers on macroporous swelling sorbents. *J. Chromatogr.*, 109:233–238, 1975.

[20] C. M. Bennett, R. J. Glasscock, R. L. S. Chang, W. M. Deen, C. R. Robertson, and B. M. Brenner. Permselectivity of the glomerular capillary wall. Studies of experimental glomerulonephritis in the rat using dextran sulfate. *J. Clin. Invest.*, 57:1287–1294, 1976.

[21] H. Benoit, Z. Grubisic, P. Rempp, D. Decker, and J. G. Zilliox. Liquid-phase chromatographic study of branched and linear polystyrenes of known structure. *J. Chim. Phys.*, 63:1507–1514, 1966.

[22] J. A. Bertolatus and L. G. Hunsicker. Glomerular sieving of anionic and neutral bovine albumins in proteinuric rats. *Kidney Int.*, 28:467–476, 1985.

[23] R. C. Blantz. Effect of mannitol on glomerular ultrafiltration in the hydropenic rat. *J. Clin. Invest.*, 54:1135–1143, 1974.

[24] R. C. Blantz, K. S. Konnen, and B. J. Tucker. Angiotensin II effects upon the glomerular microcirculation and ultrafiltration coefficient in the rat. *J. Clin. Invest.*, 57:419–434, 1976.

[25] R. C. Blantz, F. C. Rector, Jr., and D. W. Seldin. Effect of hyperoncotic albumin expansion upon glomerular ultrafiltration in the rat. *Kidney Int.*, 6:209–221, 1974.

[26] R. C. Blantz and C. B. Wilson. Acute effects of antiglomerular basement membrane antibody on the process of glomerular filtration in the rat. *J. Clin. Invest.*, 58:899–911, 1976.

[27] M. Bohdanecky and J. Kovar. *Viscosity of Polymer Solutions.* Elsevier Scientific Publishing Company, New York, 1982.

[28] M. P. Bohrer, C. Baylis, H. D. Humes, R. J. Glasscock, C. R. Robertson, and B. M. Brenner. Permselectivity of the glomerular capillary wall. Facilitated filtration of circulating polycations. *J. Clin. Invest.*, 61:72–78, 1978.

[29] M. P. Bohrer, C. Baylis, C. R. Robertson, and B. M. Brenner. Mechanisms of the puromycin-induced defects in the transglomerular passages of water and macromolecules. *J. Clin. Invest.*, 60:152–161, 1977.

[30] M. P. Bohrer, W. M. Deen, C. R. Robertson, and B. M. Brenner. Mechanism of angiotensin II-induced protenuria in the rat. *Am. J. Physiol.*, 233:F13–F21, 1977.

[31] M. P. Bohrer, W. M. Deen, C. R. Robertson, J. L. Troy, and B. M. Brenner. Influence of molecular configuration on the passage of macromolecules across the glomerular capillary wall. *J. Gen. Physiol.*, 74:583–593, 1979.

[32] M. P. Bohrer, G. D. Patterson, and P. J. Carroll. Hindered diffusion of dextran and ficoll in microporous membranes. *Macromolecules*, 17:1170–1173, 1984.

[33] M. Bradley and G. B. Schumann. Examination of urine. In J. B. Henry, editor, *Clinical Diagnosis and Management by Laboratory Methods*, chapter 18, pages 408–409. W. B. Saunders Co., Philadelphia, 17th edition, 1984.

[34] M. Bradley, G. B. Schumann, and P. C. J. Ward. Examination of urine. In J. B. Henry, editor, *Clinical Diagnosis and Management by Laboratory Methods*, pages 604–605. W. B. Saunders Co., Philadelphia, 16th edition, 1979.

[35] B. M. Brenner. Nephron adaptation to renal injury or ablation. *Am. J. Physiol.*, 249:F324–F337, 1985.

[36] B. M. Brenner, F. L. Coe, and F. C. Rector. *Renal Physiology in Health and Disease.* W. B. Saunders Co., Philadelphia, 1987.

[37] B. M. Brenner, L. D. Dworkin, and I. Ichikawa. Glomerular ultrafiltration. In Brenner and Rector,[39] chapter 4, pages 124–144.

[38] B. M. Brenner, T. W. Meyer, and T. H. Hostetter. Dietary protein intake and the progressive nature of kidney disease: The role of hemodynamically mediated glomerular injury in the pathogenesis of progressive glomerular sclerosis in aging, renal ablation, and intrinsic renal disease. *N. Eng. J. Med.*, 307:652–660, 1982.

[39] B. M. Brenner and F. C. Rector, Jr., editors. *The Kidney.* W. B. Saunders Co., Philadelphia, third edition, 1986.

[40] B. M. Brenner, J. L. Troy, T. M. Daugharty, W. M. Deen, and C. R. Robertson. Dynamics of glomerular ultrafiltration in the rat. II. Plasma-flow dependence of GFR. *Am. J. Physiol.*, 223:1184–1190, 1972.

[41] B. M. Brenner, R. Zatz, and I. Ichikawa. The renal circulations. In Brenner and Rector,[39] chapter 3, pages 93–123.

[42] H. Brenner and L. J. Gaydos. The constrained Brownian movement of spherical particles in cylindrical pores of comparable radius. Models of the diffusive and convective transport of solute molecules in membranes and porous media. *J. Colloid Interface Sci.*, 58:312–356, 1977.

[43] M. Brezis, S. Rosen, and F. H. Epstein. Acute renal failure. In Brenner and Rector,[39] chapter 19, pages 735–799.

[44] C. R. Bridges, B. D. Myers, B. M. Brenner, and W. M. Deen. Glomerular charge alterations in human minimal change nephropathy. *Kidney Int.*, 22:677–684, 1982.

[45] C. R. Bridges, Jr. *Mechanisms of Clinical and Experimental Proteinuria: Analysis using Theoretical Models of Macromolecular Transport.* Sc.D. thesis, Massachusetts Institute of Technology, 1984.

[46] H. C. Brinkman. A calculation of the viscous force exerted by a flowing fluid on a dense swarm of particles. *Appl. Sci. Res.*, A1:27–34, 1947.

[47] P. M. Bungay and H. Brenner. The motion of a closely-fitting sphere in a fluid-filled tube. *Int. J. Multiphase Flow*, 1:25–56, 1973.

[48] P. T. Callaghan and D. N. Pinder. A pulsed field gradient NMR study of self-diffusion in a polydisperse system: Dextran in water. *Macromolecules*, 16:968–973, 1983.

[49] B. J. Carrie and B. D. Myers. Proteinuria and functional characteristics of the glomerular capillary barrier in diabetic nephropathy. *Kidney Int.*, 17:669–676, 1980.

[50] B. J. Carrie, W. R. Salyer, and B. D. Myers. Minimal change nephropathy: An electrochemical disorder of the glomerular membrane. *Am. J. Med.*, 70:262–268, 1981.

[51] E. F. Casassa. Equilibrium distribution of flexible polymer chains between a macroscopic solution phase and small voids. *J. Polym. Sci. B*, 5:773–777, 1967.

[52] E. F. Casassa and G. C. Berry. Angular distribution of intensity of Rayliegh scattering from comblike branched molecules. *J. Polym. Sci. A-2*, 4:881–897, 1966.

[53] E. F. Casassa and Y. Tagami. An equilibrium theory for exclusion chromatography of branched and linear polymer chains. *Macromolecules*, 2:14–26, 1969.

[54] R. Cecil and A. G. Ogston. Determination of sedimentation and diffusion constants of horseradish peroxidase. *Biochem. J.*, 49:105–106, 1951.

[55] G. Celsi, S. O. Bohman, and A. Aperia. Development of focal glomerulosclerosis after unilateral nephrectomy to infant rats. *Pediatr. Nephr.*, 1:290–296, 1987.

[56] G. Celsi, L. Larsson, I. Seri, V. Savin, and I. Aperia. Glomerular adaptation in uninephrectomized young rats. *Pediatr. Nephr.*, 3:280–285, 1989.

[57] A. Y. M. Chan, M.-L. L. Cheng, L. C. Keil, and B. D. Myers. Functional response of healthy and diseased glomeruli to a large, protein-rich meal. *J. Clin. Invest.*, 81:245–254, 1988.

[58] P. N. Chandler, P. O'Brien, and C. T. Stier. N-nitro-L-arginine (L-NMA) markedly accelerates the development of malignant nephrosclerosis in stroke-prone SHR (SHRSP). *J. Am. Soc. Nephr.*, 2:501A, 1991.

[59] R. L. S. Chang. A model to study the dynamics of glomerular ultrafiltration and glomerular capillary permselectivity characteristics. *Microvasc. Res.*, 16:141–150, 1978.

[60] R. L. S. Chang, W. M. Deen, C. R. Robertson, C. M. Bennett, R. J. Glasscock, and B. M. Brenner. Permselectivity of the glomerular capillary wall. Studies of experimental glomerulonephritis in the rat using neutral dextran. *J. Clin. Invest.*, 57:1272–1286, 1976.

[61] R. L. S. Chang, W. M. Deen, C. R. Robertson, and B. M. Brenner. Permselectivity of the glomerular capillary wall. III. Restricted transport of polyanions. *Kidney Int.*, 8:212–218, 1975.

[62] R. L. S. Chang, C. R. Robertson, W. M. Deen, and B. M. Brenner. Permselectivity of the glomerular capillary wall to macromolecules. I. Theoretical considerations. *Biophys. J.*, 15:861–886, 1975.

[63] R. L. S. Chang, I. F. Ueki, J. L. Troy, W. M. Deen, C. R. Robertson, and B. M. Brenner. Permselectivity of the glomerular capillary wall to macromolecules. II. Experimental studies in rats using neutral dextran. *Biophys. J.*, 15:887–906, 1975.

[64] A. Chanutin and E. B. Ferris. Experimental renal insufficiency produced by partial nephrectomy: I. Control diet. *Arch. Intern. Med.*, 49:767–787, 1932.

[65] H. Chasis, J. Redish, W. Goldring, H. A. Ramges, and H. W. Smith. Use of sodium *p*-aminohippurate for functional evaluation of human kidney. *J. Clin. Invest.*, 24:583–591, 1945.

[66] E. L. Christensen, H. G. Rennke, and F. A. Carone. Renal tubular uptake of protein: Effect of molecular charge. *Am. J. Physiol.*, 244:F436–F441, 1983.

[67] K. L. Chung. *Elementary Probability Theory with Stochastic Processes.* Springer-Verlag, New York, 1979.

[68] R. L. Cleland. Ionic polysaccharides. IV. Free-rotation dimensions for disaccharide polymers. Comparison with experiments for hyaluronic acid. *Biopolymers*, 9:811–824, 1970.

[69] E. L. Cussler. *Diffusion: Mass Transfer in Fluid Systems.* Cambridge University Press, New York, 1984.

[70] M. G. Davidson. *The Effects of Molecular Configuration on the Hindered Transport of Macromolecules in Microporous Membranes.* Ph.D. thesis, Massachusetts Institute of Technology, 1988.

[71] M. G. Davidson and W. M. Deen. Hindered diffusion of water-soluble macromolecules in membranes. *Macromolecules*, 21:3474–3481, 1988.

[72] M. G. Davidson and W. M. Deen. Hydrodynamic theory for the hindered transport of flexible macromolecules in porous membranes. *J. Membrane Sci.*, 35:167–192, 1988.

[73] M. G. Davidson and W. M. Deen. Equilibrium partitioning of long-chain polymers between bulk solution and pores in the presence of short-range attractions. *J. Polym. Sci. Polym. Phys.*, 28:2555–2563, 1990.

[74] M. G. Davidson, U. W. Suter, and W. M. Deen. Equilibrium partitioning of flexible macromolecules between bulk solution and cylindrical pores. *Macromolecules*, 20:1141–1146, 1987.

[75] L. De Nicola, R. C. Blantz, and F. B. Gabbai. Nitric oxide and angiotensin II. *J. Clin. Invest.*, 89:1248–1256, 1992.

[76] W. M. Deen. Hindered transport of large molecules in liquid-filled pores. *AIChE J.*, 33:1409–1425, 1987.

[77] W. M. Deen, M. P. Bohrer, and N. B. Epstein. Effects of molecular size and configuration on diffusion in microporous membranes. *AIChE J.*, 27:952–959, 1981.

[78] W. M. Deen, C. R. Bridges, and B. M. Brenner. Biophysical basis of glomerular permselectivity. *J. Memb. Bio.*, 71:1–10, 1983.

[79] W. M. Deen, C. R. Bridges, B. M. Brenner, and B. D. Myers. Heteroporous model of glomerular size selectivity: Application to normal and nephrotic humans. *Am. J. Physiol.*, 249:F374–F389, 1985.

[80] W. M. Deen, D. A. Maddox, C. R. Robertson, and B. M. Brenner. Dynamics of glomerular ultrafiltration in the rat. VII. Response to reduced renal mass. *Am. J. Physiol.*, 227:556–562, 1974.

[81] W. M. Deen, C. R. Robertson, and B. M. Brenner. A model of glomerular ultrafiltration in the rat. *Am. J. Physiol.*, 223:1178–1183, 1972.

[82] W. M. Deen, C. R. Robertson, and B. M. Brenner. Concentration polarization in an ultrafiltering capillary. *Biophys. J.*, 14:412–431, 1974.

[83] W. M. Deen, B. Satvat, and J. M. Jamieson. Theoretical model for glomerular filtration of charged solutes. *Am. J. Physiol.*, 238:F126–F139, 1980.

[84] W. M. Deen, J. L. Troy, C. R. Robertson, and B. M. Brenner. Dynamics of glomerular ultrafiltration in the rat. IV. Determination of the ultrafiltration coefficient. *J. Clin. Invest.*, 52:1500–1508, 1973.

[85] A. Deng, L. Samsell, and C. Baylis. Locally produced endothelial-derived relaxing factor (EDRF) control preglomerular (R_A) arteriolar tone and the glomerular capillary ultrafiltration coefficient, K_f. *J. Am. Soc. Nephr.*, 2:503A, 1991.

[86] U. Di Mario, S. Bacci, S. Morano, G. Pugliese, P. Pietravalle, D. Andreani, S. Morabito, B. Simonetti, and A. Pierucci. Selective decrement of anoinic immunoglobulin clearance after induced renal hemodynamic changes in diabetic patients. *Am. J. Physiol.*, 262:F381–F388, 1992.

[87] U. Di Mario, S. Morano, A. Cancelli, S. Bacci, S. Frontoni, P. Pietravalle, S. Gambardella, and D. Andreani. New parameters to monitor the progression of diabetic nephropathy. *Am. J. Kid. Dis.*, 13:45–48, 1989.

[88] U. Di Mario, S. Morano, M. Mancuso, P. Pietravalle, A. Napoli, S. Gambardella, and D. Andreani. Urinary immunoglobulin G: A routine and highly sensitive technique based on competitive binding. *J. Clin. Lab. Immunol.*, 20:155–158, 1986.

[89] R. Du Bois, P. Decoodt, J. P. Gassee, A. Verniory, and P. P. Lambert. Determination of glomerular intracapillary and transcapillary pressure gradients from sieving data. I. A mathematical model. *Pflugers Arch.*, 356:299–316, 1975.

[90] R. Du Bois and E. Stoupel. Permeability of artificial membranes to a pluridisperse solution of ^{125}I-polyvinylpyrrolidone. *Biophys. J.*, 16:1427–1445, 1976.

[91] L. D. Dworkin, H. D. Feiner, and J. Randazzo. Glomerular hypertension and injury in desoxycorticosterone-salt rats on anti-hypertensive therapy. *Kidney Int.*, 31:718–724, 1987.

[92] L. D. Dworkin, T. H. Hostetter, H. G. Rennke, and B. M. Brenner. Hemodynamic basis for glomerular injury in rats with desoxycorticosterone-salt hypertension. *J. Clin. Invest.*, pages 1448–1461, 1984.

[93] R. M. Edwards. Segmental effects of norepinephrine and angiotensin II on isolated renal microvessels. *Am. J. Physiol.*, 244:F526–F534, 1983.

[94] G. M. Eisenbach, J. B. V. Liew, and J. W. Boylan. Effect of angiotensin on the filtration of protein in the rat kidney: A micropuncture study. *Kidney Int.*, 8:80–87, 1975.

[95] H. Elias, A. Hossman, I. B. Barth, and A. Solmar. Blood flow in the renal glomerulus. *J. Urology*, 83:790–798, 1960.

[96] H.-G. Elias. *Macromolecules: Structures and Properties*, volume I. Plenum Press, New York, second edition, 1984.

[97] M. G. Farquhar. The glomerular basement membrane: A selective macromolecular filter. In E. D. Hay, editor, *The Cell Biology of the Extracellular Matrix*, chapter 11, pages 335–378. Plenum Press, New York, 1982.

[98] L. G. Feld, J. B. Van Liew, R. G. Galaske, and J. W. Boylan. Selectivity of renal injury and proteinuria in the spontaneously hypertensive rat. *Kidney Int.*, 12:332–343, 1977.

[99] A. Fogo, Y. Yoshida, A. D. Glick, T. Homma, and I. Ichikawa. Serial micropuncture analysis of glomerular function in two rat models of glomerular sclerosis. *J. Clin. Invest.*, 82:322–330, 1988.

[100] R. P. Forster and J. P. Maes. Effect of experimental neurogenic hypertension on renal blood flow and glomerular filtration rate in intact denervated kidneys of unanesthetized rabbits with adrenal glands demedullated. *Am. J. Physiol.*, 150:534–540, 1947.

[101] S. Friedman, H. W. Jones III, H. V. Golbetz, J. A. Lee, H. L. Little, and B. D. Myers. Mechanisms of proteinuria in diabetic nephropathy. II. A study of the size selective glomerular filtration barrier. *Diabetes*, 32 (suppl. 2):40–46, 1983.

[102] R. P. Frigon, J. K. Leypoldt, S. Uyeji, and L. W. Henderson. Disparity between Stokes radii of dextrans and proteins as determined by retention volume in gel permeation chromatography. *Anal. Chem.*, 55:1349–1354, 1983.

[103] J. Führ, J. Kazmarczyk, and C. D. Krüttgen. Eine einfache colorimetrische Methode zur Inulinbestimmung für Nierenclearance-Untersuchungen bei Stoffwechsel Gesunden und Diabetikern. *Klin. Wochenschr.*, 33:729–730, 1955.

[104] R. G. Galaske, C. A. Baldamus, and H. Stolte. Plasma protein handling in the rat kidney: Micropuncture experiments in the acute heterologous phase of anti-GBM nephritis. *Pflugers Arch.*, 375:269–277, 1978.

[105] R. G. Galaske, J. B. Van Liew, and L. G. Feld. Filtration and reabsorption of endogenous low-molecular-weight protein in the rat kidney. *Kidney Int.*, 16:394–403, 1979.

[106] D. L. Garcia, S. Anderson, H. G. Rennke, and B. M. Brenner. Anemia lessens and its prevention with recombinant human erythropoietin worsens glomerular injury and hypertension in rats with reduced renal mass. *Proc. Natl. Acad. Sci. (USA)*, 85:6142–6146, 1988.

[107] D. L. Garcia, H. G. Rennke, B. M. Brenner, and S. Anderson. Chronic glucorticord therapy amplifies glomerular injury in rats with renal ablation. *J. Clin. Invest.*, 80:867–874, 1987.

[108] S. M. Gardiner, A. M. Compton, T. Bennet, R. J. M. Palmer, and S. Moncada. Control of regional blood flow by endothelium-derived nitric oxide. *Hypertension (NY)*, 15:486–492, 1990.

[109] S. K. Garg and S. S. Stivala. Assessment of branching in polymers from small-angle x-ray scattering (SAXS). *J. Polym. Sci. Polym. Phys.*, 16:1419–1434, 1978.

[110] J. P. Gassee. Effects of acetylcholine on glomerular sieving of macromolecules. *Pflugers Arch.*, 342:239–254, 1973.

[111] J. P. Gassee, P. Decoodt, A. Verniory, and P. P. Lambert. Autoregulation of effective glomerular filtration pressure. *Am. J. Physiol.*, 226:616–623, 1974.

[112] J. P. Gassee, R. Du Bois, M. Staroukine, and P. P. Lambert. Determination of glomerular intracapillary and transcapillary pressure gradients from sieving data. III. The effect of angiotensin II. *Pflugers Arch.*, 367:15–24, 1976.

[113] K. Gekko. Physicochemical studies of oligodextran. II. Intrinsic viscosity-molecular weight relationship. *Makromol. Chem.*, 148:229–238, 1971.

[114] K. Gekko. Solution properites of dextran and its ionic derivatives. *ACS Symp. Ser.*, 150:415–438, 1981.

[115] K. H. Gertz, J. A. Mangos, G. Braun, and H. D. Pagel. Pressure in the glomerular capillaries of the rat kidney and its relation to arterial blood pressure. *Pflugers Archiv.*, 288:269–374, 1966.

[116] L. Ghitescu, M. Desjardins, and M. Bendayan. Immunocytochemical study of glomerular permeability to anionic, neutral, and cationic albumins. *Kidney Int.*, 42:25–32, 1992.

[117] A. A. Gorbunov, E. B. Zhulina, and A. M. Skvortsov. Theory of adsorption of macromolecules in cylindrical pores and at surface of cylindrical shape. *Polymer*, 23:1133–1142, 1982.

[118] V. R. Gowariker, N. V. Viswanathan, and J. Sreedhar. *Polymer Science.* Halsted Press, New York, 1986.

[119] K. A. Granath. Solution properties of branched dextrans. *J. Colloid Sci.*, 13:308–328, 1958.

[120] A. Guasch, H. Hashimoto, R. K. Sibley, W. M. Deen, and B. D. Myers. Glomerular dysfunction in nephrotic humans with minimal changes or focal glomerulosclerosis. *Am. J. Physiol.*, 260:F728–F737, 1991.

[121] D. P. Haley, M. Sarrafian, R. E. Bulger, D. C. Dobyan, and G. Eknoyan. Structural and functional correlates of effects of angiotensin-induced changes in rat glomerulus. *Am. J. Physiol.*, 253:F111–F119, 1987.

[122] A. E. Hamielec. Correction for axial dispersion. In J. Janca, editor, *Steric Exclusion Liquid Chromatography of Polymers*, chapter 3, pages 117–160. Marcel Dekker, Inc., New York, 1984.

[123] J. P. Hayslett. Functional adaptation to reduction in renal mass. *Physiol. Rev.*, 59:137–164, 1979.

[124] J. E. Heeg, P. E. de Jong, G. K. van der Hem, and D. de Zeeuw. Efficacy and variability of the antiproteinuric effect of ACE inhibition by lisnopril. *Kidney Int.*, 36:272–279, 1989.

[125] J. E. Heeg, P. E. de Jong, G. K. van der Hem, and D. de Zeeuw. Angiotensin II does not acutely reverse the reduction of proteinuria by long-term ACE inhibition. *Kidney Int.*, 40:734–741, 1991.

[126] J. J. Hermans. Role of diffusion in gel permeation chromatography. *J. Polym. Sci. A-2*, 6:1217–1226, 1968.

[127] H. Hornich, M. Beaufils, and G. Richet. The effect of exogenous angiotensin on superficial and deep glomeruli in the rat kidney. *Kidney Int.*, 2:336–343, 1972.

[128] T. H. Hostetter, J. L. Olson, H. G. Rennke, M. A. Venkatachalam, and B. M. Brenner. Hyperfiltration in remnant nephrons: A potentially adverse response to renal ablation. *Am. J. Physiol.*, 241:F85–F93, 1981.

[129] T. H. Hostetter, J. L. Troy, and B. M. Brenner. Glomerular hemodynamics in experimental diabetes mellitus. *Kidney Int.*, 19:410–415, 1981.

[130] F. N. Hutchison and V. I. Martin. Effects of modulation of renal kallikrein-kinin system in the nephrotic syndrome. *Am. J. Physiol.*, 258:F1237–F1244, 1990.

[131] F. N. Hutchison, M. Schambelan, and G. A. Kaysen. Modulation of albuminuria by dietary protein and converting enzyme inhibition. *Am. J. Physiol.*, 253:F719–F725, 1987.

[132] I. Ichikawa. Direct analysis of the effector mechanism of the tubuloglomerular feedback system. *Am. J. Physiol.*, 243:F447–F455, 1982.

[133] I. Ichikawa and B. M. Brenner. Mechanisms of action of histamine and histamine antagonists on the glomerular microcirculation in the rat. *Circ. Res.*, 45:737–745, 1979.

[134] I. Ichikawa, J. R. Hoyer, M. W. Seiler, and B. M. Brenner. Mechanism of glomerulotubular balance in the setting of heterogeneous glomerular injury. Preservation of a close functional linkage between individual nephrons and surrounding microvasculature. *J. Clin. Invest.*, 69:185–198, 1982.

[135] I. Ichikawa, D. A. Maddox, M. G. Cogan, and B. M. Brenner. Dynamics of glomerular ultrafiltration in euvolemic Munich-Wistar rats. *Renal Physiol.*, 1:121–131, 1978.

[136] I. Ichikawa, J. F. Miele, and B. M. Brenner. Reversal of the renal cortical actions of angiotensin II by verapamil and manganese. *Kidney Int.*, 16:137–147, 1979.

[137] I. Ichikawa, H. G. Rennke, J. R. Hoyer, K. F. Badr, N. Schor, J. L. Troy, C. P. Lechene, and B. M. Brenner. Role for intrarenal mechanisms in the imparied salt excretion of experimental nephrotic syndrome. *J. Clin. Invest.*, 71:91–103, 1983.

[138] H. Inagaki, H. Suzuki, and M. Kurata. A semiempirical method for estimating unperturbed dimensions of chain polymers from the intrinsic viscosity-molecular weight relationship. *J. Polym. Sci.*, C15:409–425, 1966.

[139] K. E. Jørgensen and J. V. Møller. Use of flexible polymers as probes of glomerular pore size. *Am. J. Physiol.*, 236:F103–F111, 1979.

[140] Y. S. Kanwar and M. G. Farquhar. Anionic sites in the glomerular basement membrane. *In vivo* and *in vitro* localization to the laminae rarae by cationic probes. *J. Cell Biol.*, 81:137–153, 1979.

[141] Y. S. Kanwar, A. Linker, and M. G. Farquhar. Increased permeability of the glomerular basement membrane to ferritin after removal of glycosaminoglycans (heparan sulfate) by enzyme digestion. *J. Cell Biol.*, 86:688–693, 1980.

[142] J. M. Kaufmann, R. Hardy, and J. P. Hayslett. Age-dependent characteristics of compensatory renal growth. *Kidney Int.*, 8:21–26, 1975.

[143] A. J. King, J. L. Troy, S. Anderson, J. R. Neuringer, M. Gunning, and B. M. Brenner. Nitric oxide: A potential mediator of amino-acid induced renal hyperemia and hyperfiltration. *J. Am. Soc. Nephr.*, 1:1271–1277, 1991.

[144] D. G. Kleinbaum, L. L. Kupper, and K. E. Muller. *Applied Regression Analysis and Other Multivariable Methods.* PWS-Kent Publishing Co., Boston, MA, 1988.

[145] K. D. Knierim and E. A. Mason. Heteroporous sieving membranes: Rigorous bounds on pore-size distributions and sieving curves. *J. Membrane Sci.*, 42:87–107, 1989.

[146] K. D. Knierim, M. Waldman, and E. A. Mason. Bounds on solute flux and pore-size distribution for non-sieving membranes. *J. Membrane Sci.*, 17:173–203, 1984.

[147] D. E. Koppel. Analyses of macromolecular polydispersity in intensity correlation spectroscopy: The method of cumulants. *J. Chem. Phys.*, 57:4814–4820, 1972.

[148] A. M. Kotliar. A critical evaluation of mathematical molecular weight distribution models proposed for real polymer distributions. I. Effects of a low molecular weight cut-off value. *J. Polym. Sci.*, A2:4303–4325, 1964.

[149] A. M. Kotliar. A critical evaluation of mathematical molecular weight distribution models proposed for real polymer distributions. II. Effects of a high molecular weight cut-off value. *J. Polym. Sci.*, A2:4327–4337, 1964.

[150] H. A. Kramers. The behavior of macromolecules in inhomogeneous flow. *J. Chem. Phys.*, 14:415–424, 1946.

[151] J. I. Kreisberg and M. J. Karnovsky. Focal glomerular sclerosis in the fawn-hooded rat. *Am. J. Path.*, 92:637–652, 1978.

[152] T. Kuge, K. Kobayashi, S. Kitamura, and H. Tanahashi. Degrees of long-chain branching in dextran. *Carbohydrate Res.*, 160:205–214, 1987.

[153] M. H. M. Kuijpers and E. Gruys. Spontaneous hypertension and hypertensive renal disease in the fawn-hooded rat. *Br. J. Exp. Path.*, 65:181–190, 1984.

[154] M. Kurata and M. Fukatsu. Unperturbed dimension and translational friction constant of branched polymers. *J. Chem. Phys.*, 41:2934–2944, 1964.

[155] M. Kurata and W. H. Stockmayer. Instrinsic viscosities and unperturbed dimension of long chain molecules. *Adv. Polymer Chem.*, 3:196–312, 1963.

[156] M. Kurata and H. Yamakawa. Theory of dilute polymer solution. II. Osmotic pressure and frictional properties. *J. Chem. Phys.*, 29:311–325, 1958.

[157] P. P. Lambert, B. Aeikens, A. Bohle, F. Hanus, S. Pegoff, and M. Van Damme. A network model of glomerular function. *Microvasc. Res.*, 23:99–128, 1982.

[158] P. P. Lambert, R. Du Bois, P. Decoodt, J. P. Gassee, and A. Verniory. Determination of glomerular intracapillary and transcapillary pressure gradients from sieving data. II. A physiological study in the normal dog. *Pflugers Arch.*, 359:1–22, 1975.

[159] P. P. Lambert, J. P. Gassee, A. Verniory, and P. Ficheroulle. Measurement of the glomerular filtration pressure from sieving data for macromolecules. *Pflugers Arch.*, 329:34–58, 1971.

[160] P. P. Lambert, A. Verniory, J. P. Gassee, and P. Ficheroulle. Sieving equations and effective glomerular filtration pressure. *Kidney Int.*, 2:131–146, 1972.

[161] D. M. Landwher, J. S. Carvalho, and D. E. Oken. Micropuncture studies of the filtration and absorption of albumin by nephrotic rats. *Kidney Int.*, 11:9–17, 1977.

[162] O. Larm, B. Lindberg, and S. Svenson. Studies on the length of the side chains of the dextran elaborated by *Leuconostic mesenteroides* NRRL B-512. *Carbohydrate Res.*, 20:39–48, 1971.

[163] A. Leaf and R. Cotran. *Renal Pathophysiology.* Oxford University Press, New York, third edition, 1985.

[164] P. D. Leber and D. J. Marsh. Micropuncture study of concentration and fate of albumin in rat nephron. *Am. J. Physiol.*, 219:358–363, 1970.

[165] I. N. Levine. *Physical Chemistry.* McGraw-Hill, Inc., New York, second edition, 1983.

[166] J. E. Lewy and A. Pesce. Micropuncture study of albumin transfer in aminonucleoside nephrosis in the rat. *Pediatr. Res.*, 7:553–559, 1973.

[167] N. P. Lin and W. M. Deen. Effects of long-range polymer-pore interaction on the partitioning of linear polymers. *Macromolecules*, 23:2947–2955, 1990.

[168] D. A. Maddox, C. M. Bennett, W. M. Deen, R. J. Glasscock, D. Knutson, T. M. Daugharty, and B. M. Brenner. Determinants of glomerular filtration in experimental glomerulonephritis in the rat. *J. Clin. Invest.*, 55:305–318, 1975.

[169] D. A. Maddox, W. M. Deen, and B. M. Brenner. Glomerular filtration. In E. E. Windhager, editor, *Handbook of Physiology*, volume 1 of *Handbook of Physiology*, chapter 13, pages 545–638. American Physiological Society, New York, 1992.

[170] G. Mancini, A. O. Carnonara, and O. F. Hermans. Immunochemical quantitation of antigens by single radial immunodiffusion. *Immunochemistry*, 2:235–254, 1965.

[171] E. Margoliash and J. Lustgarten. Interconversion of horse heart cytochrome *c* monomer and polymers. *J. Biol. Chem.*, 237:3397–3405, 1962.

[172] G. Marsaglia. Choosing a point from the surface of a sphere. *Ann. Math. Stat.*, 43:645–646, 1972.

[173] E. R. Mathiesen, E. Hommel, J. Giese, and H. H. Parving. Efficacy of captopril in postponin nephropathy in normotensinve insulin dependent diabetic patients with microalbuminuria. *Br. Med. J.*, 303:81–87, 1991.

[174] G. Mayer, R. A. Lafayette, J. Oliver, W. M. Deen, B. D. Myers, and T. W. Meyer. Effects of angiotensin II receptor blockade on remnant glomerular permselectivity. *Kidney Int.* In press.

[175] T. W. Meyer, S. Anderson, H. G. Rennke, and B. M. Brenner. Reversing glomerular hypertension stabilizes established glomerular injury. *Kidney Int.*, 31:752–759, 1987.

[176] A. F. Michel, W. F. Keane, L. Raji, R. L. Vernier, and S. M. Mauer. The glomerular mesangium. *Kidney Int.*, 17:141–154, 1980.

[177] L. D. Michels, M. Davidman, and W. F. Keane. Determinants of glomerular filtration and plasma flow in experimental diabetic rats. *J. Lab. Clin. Med.*, 98:869–885, 1981.

[178] L. D. Michels, M. Davidman, and W. F. Keane. Glomerular permeability to neutral and anionic dextrans in experimental diabetes. *Kidney Int.*, 21:699–705, 1982.

[179] B. D. Mitchell and W. M. Deen. Effect of concentration on the rejection coefficients of rigid macromolecules in track-etch membranes. *J. Colloid Interface Sci.*, 113:132–142, 1986.

[180] C. E. Mogensen. Kidney function and glomerular permeability to macromolecules in early juvenile diabetes. *Scand. J. Clin. Lab. Invest.*, 28:79–90, 1971.

[181] S. Moncada, R. M. J. Palmer, and E. A. Higgs. Biosynthesis and endogenous role of nitric oxide. *Phramacol. Rev.*, 43:109–142, 1991.

[182] S. Morano, A. Cancelli, M. Mancuso, M. Sensi, M. Negri, S. Gambardella, and U. Di Mario. Sensitive imuujnoenzymatic assay for urinary immunoglobulin subclasses of different pH: Its significance in diabetic patients. *Diabetes Res.*, 6:181–185, 1987.

[183] E. Morelli, N. Loon, T. Meyer, W. Peters, and B. D. Myers. Effects of converting-enzyme inhibition on barrier function in diabetic glomerulopathy. *Diabetes*, 39:76–82, 1990.

[184] H. J. Motulsky and L. A. Ransnas. Fitting curves to data using nonlinear regression: A practical and nonmathematical review. *FASEB J.*, 1:365–374, 1987.

[185] B. D. Myers, W. M. Deen, and B. M. Brenner. Effects of norepinephrine and angiotensin II on the determinants of glomerular ultrafiltration and proximal tubule fluid reabsorption in the rat. *Circ. Res.*, 37:101–110, 1975.

[186] B. D. Myers, M. Hilberman, B. J. Carrie, R. J. Spencer, E. B. Stinson, and C. R. Robertson. Dynamics of glomerular ultrafiltration following open-heart surgery. *Kidney Int.*, 20:366–374, 1981.

[187] B. D. Myers, J. A. Winetz, F. Chui, and A. S. Michaels. Mechanisms of proteinuria in diabetic nephropathy: A study of glomerular barrier function. *Kidney Int.*, 21:633–641, 1982.

[188] M. Nagata and W. Kriz. Glomerular damage after uninephrectomy in young rats. II. Mechanical stress on podocytes as a pathway to sclerosis. *Kidney Int.*, 42:148–160, 1992.

[189] M. Nagata, K. Schärer, and W. Kriz. Glomerular damage after uninephrectomy in young rats. I. Hypertrophy and distortion of capillary architecture. *Kidney Int.*, 42:136–147, 1992.

[190] S. Newman, W. R. Krigbaum, C. Laugier, and P. J. Flory. Molecular dimensions in relation to intrinsic viscosities. *J. Polym. Sci.*, 14:451–462, 1954.

[191] M. P. O'Donnell, B. L. Kasiske, L. Raje, and W. F. Keane. Age is a determinant of the glomerular morphologic and functional processes to chronic nephron loss. *J. Lab. Clin. Med.*, 106:308–313, 1985.

[192] M. P. O'Donnell, L. Michels, B. Kasiske, L. Raij, and W. F. Keane. Adriamycin-induced chronic proteinuria: A structural and functional study. *J. Lab. Clin. Med.*, 106:62–67, 1985.

[193] D. E. Oken, S. C. Cotes, and C. W. Mende. Micropuncture study of tubular transport of albumin in rats with aminonucleoside nephrosis. *Kidney Int.*, 1:3–11, 1972.

[194] D. E. Oken and W. Flamenbaum. Micropuncture studies of proximal tubule transport of albumin in rats with aminonucleoside nephrosis. *J. Clin. Invest.*, 50:1498–1505, 1971.

[195] D. E. Oken, B. B. Kirschbaum, and D. M. Landwehr. Micropuncture studies of the mechanisms of normal and pathologic albuminuria. *Contr. Nephr.*, 24:1–7, 1981.

[196] D. E. Oken, S. R. Thomas, and D. C. Mikulecky. A network thermodynamic model of glomerular dynamics: Application in the rat. *Kidney Int.*, 19:359–373, 1981.

[197] S. Okuda, K. Motomura, T. Sanai, H. Tsuruda, Y. Oh, K. Onoyama, and M. Fujishima. Influence of age on determination of the remnant kidney in uninephrectomized rats. *Clin. Sci.*, 72:571–576, 1987.

[198] J. L. Olson, T. H. Hostetter, H. G. Rennke, B. M. Brenner, and M. A. Venkatachalam. Altered glomerular permselectivity and progressive sclerosis following extreme ablation of renal mass. *Kidney Int.*, 22:112–126, 1982.

[199] J. L. Olson, H. G. Rennke, and M. A. Venkatachalam. Alterations in the charge and size selectivity barrier of the glomerular filter in aminonucleoside nephrosis in rats. *Lab. Invest.*, 44:271–279, 1981.

[200] J. R. Pappenheimer. Passage of molecules through capillary walls. *Physiol. Rev.*, 33:384–423, 1953.

[201] J. R. Pappenheimer, E. M. Renkin, and L. M. Borrero. Filtration, diffusion, and molecular sieving through peripheral capillary membranes. A contribution to the pore theory of capillary permeability. *Am. J. Physiol.*, 167:13–46, 1951.

[202] H. H. Parving, E. Hommel, and U. M. Smidt. Protection of kidney function and decrease in albuminuria by captopril in insulin-dependent diabetics with nephropathy. *Br. Med. J.*, 297:1086–1091, 1988.

[203] D. C. Peace. Fine structures of the kidney seen by electron microscopy. *J. Histochem. Cytochem.*, 3:295–308, 1955.

[204] J. C. Pelayo, A. H. Quan, and P. F. Shanley. Angiotensin II control of the renal microcirculation in rats with reduced renal mass. *Am. J. Physiol.*, 258:F414–F422, 1990.

[205] J. P. Pennell, N. Yanagawa, K. H. Kwang, M. M. Millard, and J. J. Bourgoignie. Glomerular selective permeability to macromolecular neutral dextrans in experimental diabetes. *Diabetologica*, 20:223–227, 1981.

[206] W. H. Press, B. P. Flannery, S. A. Teukolsky, and W. T. Vetterling. *Numerical Recipes: The Art of Scientific Computing.* Cambridge University Press, New York, 1986.

[207] O. B. Ptitsyn. Geometry of linear polymers. VIII. An approximate statistical theory of the volume effects in linear polymer chains. *Vysokomolekul. Soedin.*, 3:1673–1683, 1961.

[208] M. L. Purkerson, P. E. Hoffsten, and S. Klahr. Pathogenesis of the glomerulopathy associated with renal infarction in rats. *Kidney Int.*, 9:407–417, 1976.

[209] D. D. Rees, R. M. J. Palmer, and S. Moncada. Role of endothelium-derived nitric oxide in the regulation of blood pressure. *Proc. Natl. Acad. Sci. (USA)*, 86:3375–3378, 1989.

[210] A. Remuzzi, C. Battaglia, L. Rossi, C. Zoja, and G. Remuzzi. Glomerular size selectivity in nephrotic rats exposed to diets with different protein content. *Am. J. Physiol.*, 253:F318–F327, 1987.

[211] A. Remuzzi and W. M. Deen. Theoretical effects of a distribution of capillary dimensions on glomerular ultrafiltration. *Microvasc. Res.*, 32:131–144, 1986.

[212] A. Remuzzi, E. Perticucci, P. Ruggenenti, L. Mosconi, M. Limonta, and G. Remuzzi. Angiotensin convertin enzyme inhibition improves glomerular size-selectivity in IgA nephropathy. *Kidney Int.*, 39:1267–1273, 1991.

[213] A. Remuzzi, S. Puntorieri, C. Battaglia, T. Bertani, and G. Remuzzi. Angiotensin converting enzyme inhibition amerliorates glomerular filtration of macromolecules and water and lessens glomerular injury in the rat. *J. Clin. Invest.*, 85:541–549, 1990.

[214] E. M. Renkin. Filtration, diffusion, and molecular sieving through porous cellulose membranes. *J. Gen. Physiol.*, 38:225–243, 1954.

[215] H. G. Rennke, Y. Patel, and M. A. Venkatachalam. Glomerular filtration of proteins: Clearance of anionic, neutral, and cationic horseradish peroxidase in the rat. *Kidney Int.*, 13:278–288, 1978.

[216] H. G. Rennke and M. A. Venkatachalam. Glomerular permeability of macromolecules. Effect of molecular configuration on the fractional clearance of uncharged dextrans and neutral horseradish peroxidase in the rat. *J. Clin. Invest.*, 63:713–717, 1979.

[217] M. O. Ribeiro, G. de Nucci, and R. Zatz. Persistent arterial hypertension by chronic blockade of nitric oxide sythesis. *J. Am. Soc. Nephr.*, 2:512A, 1991.

[218] C. R. Robertson, W. M. Deen, J. L. Troy, and B. M. Brenner. Dynamics of glomerular ultrafiltration in the rat. III. Hemodynamics and autoregulation. *Am. J. Physiol.*, 223:1191–1200, 1972.

[219] A. Rothen. Ferritin and apoferritin in the ultracentrifuge. Studies on the relationship of ferritin and apoferritin; precision measurements of the rates of sedimentation of apoferritin. *J. Biol. Chem.*, 152:679–693, 1944.

[220] SAS Institute, Inc., Cary, NC. *SAS/STAT User's Guide*, fourth edition, 1990.

[221] J. W. Scholey, P. L. Miller, H. G. Rennke, and T. W. Meyer. Effect of converting enzyme inhibition on the course of adriamycin-induced nephropathy. *Kidney Int.*, 36:816–822, 1989.

[222] M. W. Seiler, J. R. Hoyer, and T. E. Krueger. Altered localization of protamine-heparin complexes in aminonucleoside nephrosis. *Lab. Invest.*, 43:9–17, 1980.

[223] M. W. Seiler, M. A. Venkatachalam, and R. S. Cotran. Glomerular epithelium: Structural alterations induced by polycations. *Science*, 189:390–393, 1975.

[224] F. R. Senti, N. N. Hellman, N. H. Ludwig, G. E. Babcock, R. Tobin, C. A. Glass, and B. L. Lamberts. Viscosity, sedimentation, and light-scattering properties of fraction of an acid-hydrolyzed dextran. *J. Polym. Sci.*, 17:527–546, 1955.

[225] S. M. Shea and J. Raskova. Glomerular hemodynamics and vascular structure in uremia: A network analysis of glomerular path lengths and maximal blood transit times computed for a microvascular model reconstructed from subserial ultrathin sections. *Microvasc. Res.*, 28:37–50, 1984.

[226] O. Shemesh, H. W. Jones III, and B. D. Myers. Pathophysiology of proteinuria in diabetic nephropathy. In R. Robinson, editor, *Nephrology*, volume 2, pages 1081–1093. Springer-Verlag, New York, 1984. (Proc. 9th Int. Congr. Nephrology).

[227] T. Shimamura and A. B. Morrison. A progressive glomerulosclerosis occuring in partial five-sixths nephrectomized rats. *Am. J. Pathol.*, 79:95–106, 1975.

[228] A. R. Shultz. Polyvinylacetate. A light scattering and viscosity study. *J. Am. Chem. Soc.*, 76:3422–3430, 1954.

[229] P. J. Shultz, A. E. Schorer, and L. Raij. Effects of endothelium-derived relaxing factor and nitric oxide on rat mesangial cells. *Am. J. Physiol.*, 258:F162–F167, 1990.

[230] J. L. Simons, A. P. Provoost, S. Anderson, J. L. Troy, H. G. Rennke, D. J. Sandstrom, and B. M. Brenner. Glomerular capillary hypertension in the fawn-hooded rat. *In preparation.*

[231] K. L. Skorecki, S. P. Nadler, K. F. Badir, and B. M. Brenner. Renal and systemic manifestations of glomerular disease. In Brenner and Rector,[39] chapter 21, pages 891–928.

[232] P. G. Squire. Calculation of hydrodynamic parameters of random coil polymers from size exclusion chromatography and comparison with parameters by conventional methods. *J. Chromatogr.*, 210:433–442, 1981.

[233] W. H. Stockmayer and M. Fixman. Dilute solutions of branched polymers. *Ann. N.Y. Acad. Sci.*, 57:334–352, 1953.

[234] W. H. Stockmayer and M. Fixman. On the estimation of unperturbed dimensions from intrinsic viscosities. *J. Polym. Sci.*, C1:137–141, 1963.

[235] H. Stolte, H.-J. Schurek, and J. M. Alt. Glomerular albumin filtration: A comparison of micropuncture studies in the isolated perfused kidney with *in vivo* experiment conditions. *Kidney Int.*, 16:377–384, 1979.

[236] W. Sutter and A. Kuppel. Zum Einfluß der molekularen Uneinheitlichkeit auf molekulargewichtsabhängige Eigenschaften von Polymeren en Lösung. *Makromol. Chem.*, 149:271–289, 1971.

[237] N. Suzuki, A. Wada, and K. Suzuki. Study of dextran solutions by quasielastic light-scattering. *Carbohydrate Res.*, 109:242–258, 1982.

[238] G. I. Taylor. Dispersion of soluble matter in solvent flowing slowly through a tube. *Proc. Roy. Soc. Lond., Ser. A*, 219:186–203, 1953.

[239] H. Theorell. Kristallinisches Myoglobin. II. Mitteilung: Sedimentationskonstante und Molekulargewicht des Myoglobins. *Biochem. Z.*, 268:46–54, 1934.

[240] C. C. Tisher and K. M. Madsen. Anatomy of the kidney. In Brenner and Rector,[39] chapter 1, pages 3–60.

[241] J. P. Tolins and L. Raij. Effects of amino acid infusion on renal hemodynamics. Role of endothelial-derived relaxing factor. *Hypertension (Dallas)*, 17:1045–1051, 1991.

[242] S. Tomlanovich, W. M. Deen, H. W. Jones III, H. C. Schwartz, and B. D. Myers. Functional nature of glomerular injury in progressive diabetic glomerulopathy. *Diabetes*, 36:556–565, 1987.

[243] N. Tsoulfanidis. *Measurement and Detection of Radiation.* Hemisphere Publishing Corporation, Washington, 1983.

[244] B. J. Tucker and R. C. Blantz. Effects of glomerular filtration dynamics on the glomerular permeability coefficient. *Am. J. Physiol.*, 240:F245–F254, 1981.

[245] J. W. van Cleve, W. C. Schaefer, and C. E. Rist. The structure of NRRL B-512 dextran. Methylation studies. *J. Am. Chem. Soc.*, 78:4435–4438, 1956.

[246] Y. Vanrenterghem, R. Vanholder, M. Lammens-Verslijpe, and P. P. Lambert. Sieving studies in "urea-induced nephropathy" in the dog. *Clin. Sci.*, 58:65–75, 1980.

[247] A. Verniory, R. Dubois, P. DeCoodt, J. P. Gassee, and P. P. Lambert. Measurement of the permeability of biological membranes. Application to the glomerular wall. *J. Gen. Physiol.*, 62:489–507, 1973.

[248] J. W. Viets, W. M. Deen, J. L. Troy, and B. M. Brenner. Determination of serum protein concentration in nanoliter blood samples using fluorescamine or *o*-phthalaldehyde. *Anal. Biochem.*, 88:513–521, 1978.

[249] H. Von Baeyer, J. B. Van Liew, J. Klassen, and J. W. Boylan. Filtration of protien in the antiglomerular basment membrane nephritic rat: A micropuncture study. *Kidney Int.*, 10:425–437, 1976.

[250] G. C. Vurek and S. E. Pegram. Flurometric method for the determination of nanogram quantities of inulin. *Anal. Biochem.*, 16:409–416, 1966.

[251] M. Wales, P. A. Marshall, and S. G. Weissburg. Intrinsic viscosity-molecular weight relationships for dextran. *J. Polym. Sci.*, 10:229–240, 1953.

[252] J. J. Weening and H. G. Rennke. Glomerular permeability and polyanion in adriamycin nephrosis in the rat. *Kidney Int.*, 24:152–159, 1983.

[253] J. J. Weening and A. van der Wal. Effect of decreased perfusion pressure on glomerular permeability in the rat. *Lab. Invest.*, 57:144–149, 1987.

[254] J. C. Wheeler and R. G. Gordon. Bounds for averages using moment constraints. In G. A. Baker, Jr. and J. L. Gammel, editors, *The Padé Approximant in Theoretical Physics*, pages 99–128. Academic Press, New York, 1970.

[255] J. A. Winetz, H. V. Golbetz, R. J. Spencer, J. A. Lee, and B. D. Myers. Glomerular function in advanced human diabetic nephropathy. *Kidney Int.*, 21:750–756, 1982.

[256] J. A. Winetz, C. R. Robertson, H. V. Golbetz, B. J. Carrie, W. R. Salyer, and B. D. Myers. The nature of the glomerular injury in minimal change and focal sclerosing glomerulopathies. *Am. J. Kidney Dis.*, 1:91–98, 1981.

[257] J. Wishart. Cumulants of multivariate multinomial distributions. *Biometrika*, 36:47–58, 1949.

[258] F. S. Wright and J. P. Briggs. Feedback control of glomerular blood flow, pressure, and filtration rate. *Physiol. Rev.*, 59:958–1006, 1979.

[259] H. Yamakawa. *Modern Theory of Polymer Solutions*. Harper & Row, New York, 1971.

[260] W. W. Yau, J. J. Kirkland, and D. D. Bly. Band broadening. In *Modern Size-Exclusion Liquid Chromatography: Practice of Gel Permeation and Gel Filtration Chromatography*, chapter 3, pages 53–95. John Wiley & Sons, New York, 1979.

[261] T. Yoshioka, T. Mitarai, V. Kon, W. M. Deen, H. G. Rennke, and I. Ichikawa. Role for angiotensin II in an overt functional proteinuria. *Kidney Int.*, 30:538–545, 1986.

[262] T. Yoshioka, H. G. Rennke, D. J. Salant, W. M. Deen, and I. Ichikawa. Role of abnormally high transmural pressure in the permselectivity defect of glomerular capillary wall: A study in early passive Heymann nephritis. *Circ. Res.*, 61:531–538, 1987.

[263] T. Yoshioka, H. Shiraga, Y. Yoshida, A. Fogo, A. D. Glick, W. M. Deen, J. R. Hoyer, and I. Ichikawa. "Intact nehprons" as the primary origin of proteinuria in chronic renal disease. Study in the rat model of subtotal nephrectomy. *J. Clin. Invest.*, 82:1614–1623, 1988.

[264] M. J. Zamlauski-Tucker, J. B. Van Liew, and B. Noble. Pathophysiology of the kidney in rats with Heymann nephritis. *Kidney Int.*, 28:504–512, 1985.

[265] R. Zatz and G. de Nucci. Effects of acute nitric oxide inhibition of rat glomerular microcirculation. *Am. J. Physiol.*, 30:F360–F363, 1991.

[266] R. Zatz, B. R. Dunn, T. W. Meyer, S. Anderson, H. G. Rennke, and B. M. Brenner. Prevention of diabetic glomerulopathy by pharmacological amelioration of glomerular capillary hypertension. *J. Clin. Invest.*, 77:1925–1930, 1986.

[267] R. Zatz, T. W. Meyer, H. G. Rennke, and B. M. Brenner. Predominance of hemodynamic rather than metabolic factor in the pathogenesis of diabetic glomerulopathy. *Proc. Natl. Acad. Sci. (USA)*, 82:5963–5967, 1985.

[268] L. Zeman and M. Wales. Steric rejection of polymeric solutes by membranes with uniform size distribution. *Sep. Sci. Technol.*, 16:275–290, 1981.

[269] E. B. Zhulina, A. A. Gorbunov, T. M. Birshtein, and A. M. Skvortsov. Adsorption of the polypeptides on a solid surface. III. Behavior of stiff chains in a pore. *Biopolymers*, 21:1021–1036, 1982.

Appendix A

List of Principal Symbols

The dimensions are given in terms of mass (M), length (L), time (t), temperature (T), and charge (Q). When no dimensions are listed, the units are dimensionless or variable.

$\overline{AP}$ mean systemic arterial pressure, $ML^{-1}t^{-2}$

$c_{i,A}$ afferent concentration of solute i, ML^{-3}

$\langle c_{i,B} \rangle$ average concentration of solute i in Bowman's space, ML^{-3}

$c_{p,A}$ afferent protein concentration, ML^{-3}

$c_{p,E}$ efferent protein concentration, ML^{-3}

$\dot{C}_i$ renal clearance of solute i, L^3t^{-1}

$\mathcal{D}$ translational diffusion coefficient, L^2t^{-1}

d interaction distance for Monte Carlo square-well potential, L

f capillary wall porosity

f' protein volume correction factor

FF filtration fraction $= GFR/RBF$

FRC_i fractional clearance of solute i, $= \dot{C}_i/GFR$

$g(r)$ pore radius size distribution function

G solute lag coefficient

GFR glomerular filtration rate, L^3t^{-1}

H diffusion hindrance factor

J_i solute flux, $ML^{-2}t^{-1}$

J_v solvent flux, Lt^{-1}

k_B Boltzmann's constant, $ML^2t^{-2}T^{-1}$

K solute enhanced drag coefficient

K_{av} approximate fractional elution volume of solute

K_f ultrafiltration coefficient, $M^{-1}L^4t$

$\mathcal{K}$ Taylor dispersion coefficient, L^2t^{-1}

l length of chain segment in random coil, L

ℓ capillary membrane thickness, L

L capillary length, L

m 1) number of data points to fit 2) number of radial mesh points for Monte Carlo simulation

m_d number of mass points fitting within the square-well interaction region

M molecular weight, M/g-mole

M_c number of chains generated in a Monte Carlo simulation

M_n number-averaged molecular weight, M/g-mole

M_w weight-averaged molecular weight, M/g-mole

n number of chain segments in random coil

N_A Avogardo's number, (g-mole)$^{-1}$

p probability that a molecule will fit in pore at position $\hat{r}$

P_A afferent arteriole hydraulic pressure, $ML^{-1}t^{-2}$

P_E efferent arteriole hydraulic pressure, $ML^{-1}t^{-2}$

P_{GC} glomerular capillary hydraulic pressure, $ML^{-1}t^{-2}$

P_T tubular hydraulic pressure, $ML^{-1}t^{-2}$

$\overline{P}_{UF}$ net ultrafiltration pressure, $ML^{-1}t^{-2}$

$\overline{\Delta P}$ average capillary transmural hydraulic pressure difference, $ML^{-1}t^{-2}$

Pe Peclet number, $= WJ_v\ell/fH\mathcal{D}$

q_2 lognormal + shunt pore distribution parameter

Q_A single nephron afferent capillary plasma flow rate, L^3t^{-1}

Q_E single nephron efferent capillary plasma flow rate, L^3t^{-1}

r pore radial coordinate, L

r^* characteristic pore radius for heteroporous distributions, L

$\hat{r}$ dimensionless pore radial coordinate, $= r/r_p$

r_g root mean-square radius of gyration, L

r_p pore radius, L

r_s Stokes-Einstein radius, L

$\tilde{r}_s$ Stokes-Einstein radius as determined by protein calibrated GPC, L

r_0 isoporous pore radius, L

R chain end-to-end distance, L

R_A afferent arteriole resistance, $ML^{-4}t^{-1}$

R_E efferent arteriole resistance, $ML^{-4}t^{-1}$

R_T total arteriole resistance $= R_A + R_E$, $ML^{-4}t^{-1}$

RBF renal blood flow, L^3t^{-1}

RPF renal plasma flow, L^3t^{-1}

s lognormal distribution parameter

S capillary wall surface area, L^2

$SNFF$ single nephron filtration fraction, $= SNGFR/Q_A$

$SNGFR$ single nephron glomerular filtration rate, L^3t^{-1}

T absolute temperature, T

u lognormal distribution parameter, L

(U/P) urinary-to-plasma concentration ratio

$\dot{U}$ urinary flow rate, L^3t^{-1}

V_e elution volume of solute i, L^3

V_t total column volume, L^3

V_0 void volume of column, L^3

W convective hindrance factor

x pore axial coordinate, L

y capillary axial coordinate, L

$\hat{y}$ dimensionless capillary axial coordinate, $= y/L$

Greek symbols

α_i coefficients for Simpson's rule

ϵ dimensionless Boltzmann attractive energy term

$[\eta]$ intrinsic viscosity

Θ_i sieving coefficient of solute i, $= \langle c_{i,B} \rangle / c_{i,a}$

λ_g solute gyration-to-pore radius ratio, $= r_g/r_0$

λ_s solute Stokes-Einstein-to-pore radius ratio, $= r_s/r_0$

μ solvent viscosity, $ML^{-1}t^{-1}$

π 3.14159...

π_A afferent arteriole oncotic pressure, $ML^{-1}t^{-2}$

π_E efferent arteriole oncotic pressure, $ML^{-1}t^{-2}$

$\Delta\pi$ capillary transmural oncotic pressure difference, $ML^{-1}t^{-2}$

σ standard error of the mean

Φ steric partition coefficient

χ^2 sum of squared residuals

ω_0 shunt parameter for heteroporous models

Ω radial flow-weight averaged concentration parameter

Appendix B

Modifications to Numerical Integrations for Heteroporous Models

B.1 Scheme for Faster Calculation of Approximation Integrals

For heteroporous models, the sieving coefficient is a weighted average of the isoporous values over the volume flux distribution:[79]

$$\Theta_i = \int_0^\infty \omega(r)\Theta_i(r)\,dr, \tag{B.1a}$$

$$\omega(r) \approx \frac{r^4 g(r)}{\int_0^\infty r^4 g(r)\,dr}, \tag{B.1b}$$

where $\omega(r)$ is the fractional filtrate volume through pores with radii between r and $r+dr$, $g(r)$ is the fractional number of pores with radii between r and $r+dr$, and

$$\Theta_i(r) = \frac{1}{c_{i,A}} \frac{\int_0^1 J_i(\hat{y},r)\,d\hat{y}}{\int_0^1 J_v(\hat{y},r)\,d\hat{y}} \tag{B.2}$$

is the isoporous sieving coefficient of solute i through those corresponding pores. $J_i(\hat{y},r)$ is the solute flux at dimensionless position $\hat{y}$ along the capillary through pores with radii betwen r and $r+dr$, while $J_v(\hat{y},r)$ is the corresponding volume flux.

In the approximate method devised by Deen *et al.*,[79] Eq. B.2 is calculated as

$$\Theta_i(r) = \frac{bW_i}{1-e^{-b}} \int_0^1 \frac{\left[1+a_i(1-e^{-b\hat{y}})\right] e^{-b\hat{y}}}{1-e^{-Pe(\hat{y})}(1-W_i)}\,d\hat{y}, \tag{B.3}$$

$$Pe(\hat{y}) = \frac{W_i(\Delta P - \pi_A)e^{-b\hat{y}}}{H_i \mathcal{D}_i}\left(\frac{r^2}{8\mu}\right), \tag{B.4}$$

where a_i and b are constants. This approximation is necessary to reduce computation time to reasonable lengths, and was shown to result in not more than 5% error in cases of marked filtration pressure disequilibrium (with a maximum error of 10%), while requiring 1% of the computation time.[79]

Here we show that computation time can be further reduced by making the following substitutions,

$$A = \frac{bW_i}{1-e^{-b}}, \tag{B.5}$$

$$B = Pe(\hat{y})/e^{-b\hat{y}}$$

$$= \frac{W_i(\Delta P - \pi_A)}{H_i \mathcal{D}_i}\left(\frac{r^2}{8\mu}\right), \tag{B.6}$$

$$C = 1 - W_i, \tag{B.7}$$

$$q(\hat{y}) = e^{-b\hat{y}}, \tag{B.8}$$

where A, B, and C are constants and $q(\hat{y})$ is the spatially-varying parameter. Eq. B.3 is then rewritten as

$$\Theta_i(r) = -\frac{A}{b}\int_1^{e^{-b}} \frac{1 + a_i - a_i q}{1 - Ce^{-Bq}}\, dq. \tag{B.9}$$

The first two terms in the quotient of Eq. B.9 can be integrated directly, leaving only integration of the third term to be carried out by numerical means:

$$\Theta_i(r) = -\frac{A}{b}(1 + a_i)\cdot\left(e^{-b} - 1 + \frac{1}{B}\ln\left[\frac{1 - C\exp(-Be^{-b})}{1 - Ce^{-B}}\right]\right) - \frac{Aa_i}{b}\int_1^{e^{-b}} \frac{q}{1 - Ce^{-Bq}}\, dq. \tag{B.10}$$

Implementation of Eq. B.10 in place of Eq. B.3 decreased the CPU time required for parameter fitting by approximately a factor of 2.

B.2 Endpoint Calculation for Lognormal Distribution Integrations

Calculation of Eq. B.1a requires integration over the range $r = 0$ to ∞. In the actual numerical procedure, a value r_{stop} is chosen as the upper limit such that

$$\Theta_i = \int_0^\infty \omega(r)\Theta_i(r)\, dr \approx \int_0^{r_{\text{stop}}} \omega(r)\Theta_i(r)\, dr = \frac{\int_0^{r_{\text{stop}}} r^4 g(r)\Theta_i(r)\, dr}{\int_0^{r_{\text{stop}}} r^4 g(r)\, dr}, \tag{B.11}$$

and such that the fractional error ξ is small, where

$$\xi = \frac{\int_{r_{\text{stop}}}^\infty \omega(r)\Theta_i(r)\, dr}{\int_0^{r_{\text{stop}}} \omega(r)\Theta_i(r)\, dr}, \tag{B.12}$$

$$= \frac{\int_{r_{\text{stop}}}^\infty r^4 g(r)\Theta_i(r)\, dr / \int_{r_{\text{stop}}}^\infty r^4 g(r)\, dr}{\int_0^{r_{\text{stop}}} r^4 g(r)\Theta_i(r)\, dr / \int_0^{r_{\text{stop}}} r^4 g(r)\, dr}, \tag{B.13}$$

$$= \frac{\int_{r_{\text{stop}}}^\infty r^4 g(r)\Theta_i(r)\, dr}{\int_0^{r_{\text{stop}}} r^4 g(r)\Theta_i(r)\, dr} \cdot \frac{\int_0^{r_{\text{stop}}} r^4 g(r)\, dr}{\int_{r_{\text{stop}}}^\infty r^4 g(r)\, dr}, \tag{B.14}$$

For the lognormal distribution $\int_{r_{\text{stop}}}^\infty r^4 g(r)\, dr$ can be evaluated exactly as[2]

$$\int_{r_{\text{stop}}}^\infty r^4 g(r)\, dr = \exp(4\ln u + 8\ln^2 s)\cdot\frac{1}{2}\left[1 - \text{erf}\left(\frac{t_{\text{stop}} - 4\ln s}{\sqrt{2}}\right)\right], \tag{B.15}$$

$$t_{\text{stop}} = \frac{\ln(r_{\text{stop}}/u)}{\ln s},$$

and therefore,

$$\int_0^\infty r^4 g(r)\,dr = \exp(4\ln u + 8\ln^2 s). \tag{B.16}$$

The approximate sieving coefficient and error bound are then given by

$$\Theta_i \approx \int_0^{r_{stop}} \omega(r)\Theta_i(r)\,dr = \frac{\int_0^{r_{stop}} r^4 g(r)\Theta_i(r)\,dr}{\int_0^\infty r^4 g(r)\,dr} = \frac{\int_0^{r_{stop}} r^4 g(r)\Theta_i(r)\,dr}{\exp(4\ln u + 8\ln^2 s)}, \tag{B.17}$$

$$\xi = \frac{\int_{r_{stop}}^\infty r^4 g(r)\Theta_i(r)\,dr}{\int_0^{r_{stop}} r^4 g(r)\Theta_i(r)\,dr}, \tag{B.18}$$

$$< \frac{\int_{r_{stop}}^\infty r^4 g(r)\,dr}{\int_0^{r_{stop}} r^4 g(r)\Theta_i(r)\,dr} = \frac{\exp(4\ln u + 8\ln^2 s)\cdot\frac{1}{2}\left[1-\mathrm{erf}\left(\frac{t_{stop}-4\ln s}{\sqrt{2}}\right)\right]}{\int_0^{r_{stop}} r^4 g(r)\Theta_i(r)\,dr}, \tag{B.19}$$

where the inequality in Eq. B.19 holds since $\Theta_i(r) \leq 1$ for all r. Similarly, the bound for the double lognormal distribution is given by

$$\xi < \frac{\int_{r_{stop}}^\infty r^4\left[(1-q_2)g_1(r)+q_2 g_2(r)\right]\,dr}{\int_0^{r_{stop}} r^4\left[(1-q_2)g_1(r)+q_2 g_2(r)\right]\Theta_i(r)\,dr}, \tag{B.20}$$

where g_1 and g_2 are the two distributions. Values of $\xi = 10^{-4}$ were used to insure accuracy to three significant figures.

Bridges[45] established a single bound on the integrals $\int_{r_{stop}}^\infty r^4 g(r)\,dr$ and $\int_{r_{stop}}^\infty r^4 g(r)\Theta_i(r)\,dr$ to estimate ξ. His expression for the lognormal distribution contains an algebraic error; the corrected result is

$$\int_{r_{stop}}^\infty r^4 g(r)\,dr < u^4\sqrt{\frac{q}{8}}\exp\left(-\frac{t_{stop}^2}{2q}\right), \tag{B.21}$$

$$t_{stop} = \frac{\ln(r_{stop}/u)}{\ln s},$$

$$q = \frac{2t_{stop}}{t_{stop} - 8\ln s}.$$

Bridges[45] used Eq. B.21 to bound both the numerator and denominator of Eq. B.11. For smaller molecules ($r_s < 45$ Å), bounding the individual integrals also provides convergence on the quotient. For larger molecules ($r_s > 60$ Å), however, bounding the numerator and denominator separately does *not* guarantee convergence on the quotient, because the numerator is many orders of magnitude smaller than the denominator.

Appendix C

Statistics of Scintillation Counting and Determination of Minimum Acceptable Levels of Detection

This Appendix summarizes the relevant statistical analysis for the counting of radioisotopes and determination of minimal acceptable counting levels. The development is that of Tsoulfanidis [243, Chapter 2].

C.1 Standard Error of Total Counts

The radioactive decay of nuclei is described by Poisson statistics. Thus, if m is the mean number of decays over time t and n is the number of decays measured over one particular interval of time, then the variance and standard deviation of n are given by

$$V(n) = m, \tag{C.1}$$

$$\sigma_n = \sqrt{m}. \tag{C.2}$$

Note that this is true only for the total number of counts and not the counting rate. As $m \to \infty$, the Poisson distribution approaches the normal distribution. For $m > 20$, the Poisson distribution is for all practical purposes equivalent to the normal distribution.

Since the true mean m is not known, n (for one measurement) or $\overline{n}$ (for multiple measurements) is taken as the best estimator of m. Though the value of a single measurement follows Poisson statistics, the distribution of the average of N measurements is Gaussian. The standard deviation of $\overline{n}$ is given by

$$\sigma_{\overline{n}} = \frac{\sigma_n}{\sqrt{N}} = \sqrt{\frac{m}{N}} \approx \sqrt{\frac{\overline{n}}{N}}. \tag{C.3}$$

C.2 Standard Error of Counting Rate

The net counting rate r is given by

$$r = g - b = \frac{G}{t_G} - \frac{B}{t_B}, \tag{C.4}$$

where g and b are the gross and background counting rates, equal to the total counts (G and B) divided by the counting time (t_G and t_B). Assuming G, B, t_G, and t_B are all independent, then

$$\sigma_r = \sqrt{\sum_i \left(\frac{\partial r}{\partial x_i}\right)^2 \sigma_{x_i}^2}, \tag{C.5}$$

where the x_i are independent variables. Assuming that time is measured accurately, then $\sigma_{t_G}, \sigma_{t_B} \ll \sigma_G, \sigma_B$ and

$$\begin{aligned} \sigma_r &= \sqrt{\left(\frac{\partial r}{\partial G}\right)^2 \sigma_G^2 + \left(\frac{\partial r}{\partial B}\right)^2 \sigma_B^2}, \\ &= \sqrt{\frac{G}{t_G^2} + \frac{B}{t_B^2}} = \sqrt{\frac{g}{t_G} + \frac{b}{t_B}}, \\ &= \sqrt{\sigma_g^2 + \sigma_b^2}, \end{aligned} \tag{C.6}$$

where the last equality comes from the fact that $\sigma_g = \sigma_G/t_G = \sqrt{G}/t_G$ and similarly for σ_b.

C.3 Minimum Acceptable Activity

One way to define a criterion for the minimum detectable activity is to set a bound f on the relative error:

$$\begin{aligned} f &\geq \frac{\sigma_r}{r}, \\ &\geq \frac{1}{r} \cdot \sqrt{\frac{g}{t_G} + \frac{b}{t_B}}. \end{aligned} \tag{C.7}$$

Substituting $g = r + b$ and solving the resulting quadratic for positive r gives,

$$r \geq \frac{1 + \sqrt{1 + 4f^2 b t_G + 4f^2 t_G^2 \sigma_b^2}}{2f^2 t_G}. \tag{C.8}$$

Thus given a known background rate b and associated error σ_b, either the error for a given counting rate or the counting rate required to achieve a predefined accuracy can be determined.

C.4 Calculations

The Tric-Carb Model 4530 scintillation counter (Packard Instrument Co., Downers Grove, IL) uses a single detector and can be set to count until either a preset error (i.e., total counts) or a maximum time is reached. The values were set for $\sigma = 2.5\%$ (i.e., 1600 counts since $\sigma = \sqrt{1600}/1600 = 2.5\%$)

or a maximum time of 5 minutes. Thus for $g \geq (1600/5 =)$ 320 cpm, the counting time is given by

$$t_G = \frac{1600}{g}, \tag{C.9}$$

while for $g \leq 320$ cpm, the counting time is 5 minutes.

The minimum acceptable levels for r can then be calculated directly from Eq. C.7. For $g \geq 320$,

$$\begin{aligned} r &\geq \frac{1}{f} \cdot \sqrt{\frac{g}{t_G} + \frac{b}{t_B}}, \\ &\geq \frac{1}{f} \cdot \sqrt{\frac{g^2}{1600} + \frac{b}{t_B}}, \\ &\geq \frac{1}{f} \cdot \sqrt{\frac{(r+b)^2}{1600} + \frac{b}{t_B}}, \end{aligned} \tag{C.10}$$

while for $g \leq 320$,

$$r \geq \frac{1}{f} \cdot \sqrt{\frac{(r+b)}{5} + \frac{b}{t_B}}. \tag{C.11}$$

The average of 36 background counts (t_b = 5 min) on the scintillation counter gave $b = 19.55$ cpm. When these values for b and t_B are substituted in the right-hand side of Eqs. C.10 and C.11, it can be shown that when $f = 0.05$ Eq. C.10 is satisfied for all $r > 54.0$, while Eq. C.11 is satisfied for all $r > 108.8$. Thus it appears using a net counting rate of 120 cpm as a cutoff conservatively insures no more than a 5% counting error.

Appendix D

Tabulated Parameters from Monte Carlo Simulations

The following tables summarize the calculated values of Φ and Ω from the Monte Carlo simulations. Values are shown for the $d = l$ case with $\lambda_g = 0.2$ to 1.6 , $n = 20$ to 800, and $\epsilon = 0$ to -0.30.

	n					
λ_g	20	50	100	200	400	800
0.2	6.452×10^{-1}	6.248×10^{-1}	6.147×10^{-1}	6.069×10^{-1}	6.020×10^{-1}	5.983×10^{-1}
0.4	3.539×10^{-1}	3.237×10^{-1}	3.091×10^{-1}	2.982×10^{-1}	2.913×10^{-1}	2.863×10^{-1}
0.6	1.502×10^{-1}	1.245×10^{-1}	1.122×10^{-1}	1.039×10^{-1}	9.860×10^{-2}	9.476×10^{-2}
0.8	4.898×10^{-2}	3.451×10^{-2}	2.849×10^{-2}	2.467×10^{-2}	2.212×10^{-2}	2.053×10^{-2}
1.0	1.251×10^{-2}	7.098×10^{-3}	5.173×10^{-3}	4.073×10^{-3}	3.374×10^{-3}	2.948×10^{-3}
1.2	2.560×10^{-3}	1.105×10^{-3}	6.834×10^{-4}	4.767×10^{-4}	3.551×10^{-4}	2.860×10^{-4}
1.4	4.415×10^{-4}	1.359×10^{-4}	6.755×10^{-5}	3.933×10^{-5}	2.583×10^{-5}	1.884×10^{-5}
1.6	6.464×10^{-5}	1.312×10^{-5}	5.024×10^{-6}	2.407×10^{-6}	1.320×10^{-6}	8.038×10^{-7}

Table D.1: Monte Carlo calculations for Φ, $\epsilon = 0$, $d = l$.

	n					
λ_g	20	50	100	200	400	800
0.2	8.613×10^{-1}	8.462×10^{-1}	8.385×10^{-1}	8.324×10^{-1}	8.286×10^{-1}	8.256×10^{-1}
0.4	5.568×10^{-1}	5.181×10^{-1}	4.989×10^{-1}	4.844×10^{-1}	4.750×10^{-1}	4.682×10^{-1}
0.6	2.582×10^{-1}	2.173×10^{-1}	1.973×10^{-1}	1.837×10^{-1}	1.750×10^{-1}	1.686×10^{-1}
0.8	8.833×10^{-2}	6.306×10^{-2}	5.240×10^{-2}	4.559×10^{-2}	4.099×10^{-2}	3.815×10^{-2}
1.0	2.319×10^{-2}	1.331×10^{-2}	9.755×10^{-3}	7.710×10^{-3}	6.405×10^{-3}	5.607×10^{-3}
1.2	4.828×10^{-3}	2.105×10^{-3}	1.309×10^{-3}	9.155×10^{-4}	6.835×10^{-4}	5.516×10^{-4}
1.4	8.418×10^{-4}	2.615×10^{-4}	1.306×10^{-4}	7.627×10^{-5}	5.015×10^{-5}	3.665×10^{-5}
1.6	1.242×10^{-4}	2.545×10^{-5}	9.779×10^{-6}	4.701×10^{-6}	2.580×10^{-6}	1.572×10^{-6}

Table D.2: Monte Carlo calculations for Ω, $\epsilon = 0$, $d = l$.

	n					
λ_g	20	50	100	200	400	800
0.2	6.767×10^{-1}	6.481×10^{-1}	6.325×10^{-1}	6.201×10^{-1}	6.117×10^{-1}	6.053×10^{-1}
0.4	3.999×10^{-1}	3.574×10^{-1}	3.348×10^{-1}	3.171×10^{-1}	3.050×10^{-1}	2.961×10^{-1}
0.6	1.916×10^{-1}	1.539×10^{-1}	1.339×10^{-1}	1.193×10^{-1}	1.095×10^{-1}	1.025×10^{-1}
0.8	7.359×10^{-2}	5.068×10^{-2}	3.968×10^{-2}	3.225×10^{-2}	2.722×10^{-2}	2.401×10^{-2}
1.0	2.254×10^{-2}	1.307×10^{-2}	8.961×10^{-3}	6.433×10^{-3}	4.845×10^{-3}	3.879×10^{-3}
1.2	5.491×10^{-3}	2.656×10^{-3}	1.561×10^{-3}	9.690×10^{-4}	6.283×10^{-4}	4.460×10^{-4}
1.4	1.092×10^{-3}	4.366×10^{-4}	2.146×10^{-4}	1.096×10^{-4}	6.033×10^{-5}	3.676×10^{-5}
1.6	1.757×10^{-4}	5.687×10^{-5}	2.345×10^{-5}	9.880×10^{-6}	4.309×10^{-6}	2.091×10^{-6}

Table D.3: Monte Carlo calculations for Φ, $\epsilon = -0.05$, $d = l$.

	n					
λ_g	20	50	100	200	400	800
0.2	8.841×10^{-1}	8.632×10^{-1}	8.516×10^{-1}	8.423×10^{-1}	8.360×10^{-1}	8.310×10^{-1}
0.4	6.149×10^{-1}	5.610×10^{-1}	5.318×10^{-1}	5.089×10^{-1}	4.930×10^{-1}	4.812×10^{-1}
0.6	3.241×10^{-1}	2.642×10^{-1}	2.321×10^{-1}	2.087×10^{-1}	1.929×10^{-1}	1.814×10^{-1}
0.8	1.314×10^{-1}	9.147×10^{-2}	7.215×10^{-2}	5.906×10^{-2}	5.011×10^{-2}	4.439×10^{-2}
1.0	4.158×10^{-2}	2.431×10^{-2}	1.675×10^{-2}	1.209×10^{-2}	9.144×10^{-3}	7.348×10^{-3}
1.2	1.034×10^{-2}	5.035×10^{-3}	2.971×10^{-3}	1.850×10^{-3}	1.204×10^{-3}	8.572×10^{-4}
1.4	2.081×10^{-3}	8.375×10^{-4}	4.130×10^{-4}	2.117×10^{-4}	1.167×10^{-4}	7.125×10^{-5}
1.6	3.375×10^{-4}	1.101×10^{-4}	4.551×10^{-5}	1.922×10^{-5}	8.397×10^{-6}	4.075×10^{-6}

Table D.4: Monte Carlo calculations for Ω, $\epsilon = -0.05$, $d = l$.

	n					
λ_g	20	50	100	200	400	800
0.2	7.191×10^{-1}	6.818×10^{-1}	6.595×10^{-1}	6.408×10^{-1}	6.272×10^{-1}	6.165×10^{-1}
0.4	4.632×10^{-1}	4.075×10^{-1}	3.744×10^{-1}	3.470×10^{-1}	3.270×10^{-1}	3.121×10^{-1}
0.6	2.521×10^{-1}	2.005×10^{-1}	1.696×10^{-1}	1.452×10^{-1}	1.281×10^{-1}	1.157×10^{-1}
0.8	1.137×10^{-1}	7.969×10^{-2}	6.051×10^{-2}	4.650×10^{-2}	3.676×10^{-2}	3.040×10^{-2}
1.0	4.142×10^{-2}	2.594×10^{-2}	1.748×10^{-2}	1.173×10^{-2}	8.061×10^{-3}	5.817×10^{-3}
1.2	1.190×10^{-2}	6.855×10^{-3}	4.089×10^{-3}	2.385×10^{-3}	1.368×10^{-3}	8.467×10^{-4}
1.4	2.718×10^{-3}	1.489×10^{-3}	7.902×10^{-4}	3.832×10^{-4}	1.855×10^{-4}	9.515×10^{-5}
1.6	4.784×10^{-4}	2.575×10^{-4}	1.269×10^{-4}	5.304×10^{-5}	1.910×10^{-5}	7.868×10^{-6}

Table D.5: Monte Carlo calculations for Φ, $\epsilon = -0.10$, $d = l$.

	n					
λ_g	20	50	100	200	400	800
0.2	9.136×10^{-1}	8.867×10^{-1}	8.707×10^{-1}	8.573×10^{-1}	8.474×10^{-1}	8.395×10^{-1}
0.4	6.923×10^{-1}	6.223×10^{-1}	5.810×10^{-1}	5.468×10^{-1}	5.213×10^{-1}	5.022×10^{-1}
0.6	4.181×10^{-1}	3.365×10^{-1}	2.880×10^{-1}	2.498×10^{-1}	2.227×10^{-1}	2.027×10^{-1}
0.8	2.009×10^{-1}	1.416×10^{-1}	1.083×10^{-1}	8.398×10^{-2}	6.693×10^{-2}	5.575×10^{-2}
1.0	7.603×10^{-2}	4.777×10^{-2}	3.232×10^{-2}	2.181×10^{-2}	1.507×10^{-2}	1.094×10^{-2}
1.2	2.235×10^{-2}	1.292×10^{-2}	7.725×10^{-3}	4.516×10^{-3}	2.603×10^{-3}	1.618×10^{-3}
1.4	5.175×10^{-3}	2.845×10^{-3}	1.512×10^{-3}	7.354×10^{-4}	3.568×10^{-4}	1.834×10^{-4}
1.6	9.191×10^{-4}	4.974×10^{-4}	2.455×10^{-4}	1.027×10^{-4}	3.713×10^{-5}	1.523×10^{-5}

Table D.6: Monte Carlo calculations for Ω, $\epsilon = -0.10$, $d = l$.

	n					
λ_g	20	50	100	200	400	800
0.2	7.778×10^{-1}	7.339×10^{-1}	7.045×10^{-1}	6.776×10^{-1}	6.561×10^{-1}	6.373×10^{-1}
0.4	5.530×10^{-1}	4.868×10^{-1}	4.424×10^{-1}	4.009×10^{-1}	3.684×10^{-1}	3.430×10^{-1}
0.6	3.430×10^{-1}	2.797×10^{-1}	2.353×10^{-1}	1.947×10^{-1}	1.663×10^{-1}	1.424×10^{-1}
0.8	1.807×10^{-1}	1.360×10^{-1}	1.046×10^{-1}	7.821×10^{-2}	5.847×10^{-2}	4.513×10^{-2}
1.0	7.759×10^{-2}	5.598×10^{-2}	3.958×10^{-2}	2.632×10^{-2}	1.721×10^{-2}	1.104×10^{-2}
1.2	2.606×10^{-2}	1.906×10^{-2}	1.258×10^{-2}	7.608×10^{-3}	4.132×10^{-3}	2.264×10^{-3}
1.4	6.799×10^{-3}	5.387×10^{-3}	3.424×10^{-3}	1.773×10^{-3}	8.338×10^{-4}	3.866×10^{-4}
1.6	1.306×10^{-3}	1.218×10^{-3}	7.994×10^{-4}	3.828×10^{-4}	1.241×10^{-4}	4.907×10^{-5}

Table D.7: Monte Carlo calculations for Φ, $\epsilon = -0.15$, $d = l$.

	n					
λ_g	20	50	100	200	400	800
0.2	9.527×10^{-1}	9.211×10^{-1}	9.007×10^{-1}	8.825×10^{-1}	8.679×10^{-1}	8.547×10^{-1}
0.4	7.981×10^{-1}	7.150×10^{-1}	6.612×10^{-1}	6.121×10^{-1}	5.724×10^{-1}	5.412×10^{-1}
0.6	5.563×10^{-1}	4.556×10^{-1}	3.874×10^{-1}	3.260×10^{-1}	2.818×10^{-1}	2.452×10^{-1}
0.8	3.157×10^{-1}	2.369×10^{-1}	1.831×10^{-1}	1.382×10^{-1}	1.044×10^{-1}	8.146×10^{-2}
1.0	1.417×10^{-1}	1.019×10^{-1}	7.214×10^{-2}	4.817×10^{-2}	3.164×10^{-2}	2.054×10^{-2}
1.2	4.885×10^{-2}	3.566×10^{-2}	2.355×10^{-2}	1.423×10^{-2}	7.776×10^{-3}	4.296×10^{-3}
1.4	1.294×10^{-2}	1.026×10^{-2}	6.512×10^{-3}	3.377×10^{-3}	1.593×10^{-3}	7.398×10^{-4}
1.6	2.508×10^{-3}	2.348×10^{-3}	1.541×10^{-3}	7.386×10^{-4}	2.411×10^{-4}	9.415×10^{-5}

Table D.8: Monte Carlo calculations for Ω, $\epsilon = -0.15$, $d = l$.

	n					
λ_g	20	50	100	200	400	800
0.2	8.621×10^{-1}	8.210×10^{-1}	7.909×10^{-1}	7.578×10^{-1}	7.247×10^{-1}	6.845×10^{-1}
0.4	6.850×10^{-1}	6.241×10^{-1}	5.771×10^{-1}	5.168×10^{-1}	4.686×10^{-1}	4.216×10^{-1}
0.6	4.841×10^{-1}	4.272×10^{-1}	3.760×10^{-1}	3.094×10^{-1}	2.798×10^{-1}	2.153×10^{-1}
0.8	2.959×10^{-1}	2.558×10^{-1}	2.147×10^{-1}	1.682×10^{-1}	1.248×10^{-1}	9.804×10^{-2}
1.0	1.482×10^{-1}	1.325×10^{-1}	1.077×10^{-1}	7.914×10^{-2}	5.584×10^{-2}	3.184×10^{-2}
1.2	5.762×10^{-2}	5.721×10^{-2}	4.646×10^{-2}	3.427×10^{-2}	2.069×10^{-2}	1.072×10^{-2}
1.4	1.710×10^{-2}	2.070×10^{-2}	1.769×10^{-2}	1.137×10^{-2}	5.933×10^{-3}	2.823×10^{-3}
1.6	3.571×10^{-3}	6.016×10^{-3}	5.856×10^{-3}	3.660×10^{-3}	1.231×10^{-3}	4.974×10^{-4}

Table D.9: Monte Carlo calculations for Φ, $\epsilon = -0.20$, $d = l$.

	n					
λ_g	20	50	100	200	400	800
0.2	1.006×10^{0}	9.747×10^{-1}	9.534×10^{-1}	9.326×10^{-1}	9.133×10^{-1}	8.878×10^{-1}
0.4	9.476×10^{-1}	8.664×10^{-1}	8.091×10^{-1}	7.441×10^{-1}	6.887×10^{-1}	6.355×10^{-1}
0.6	7.657×10^{-1}	6.683×10^{-1}	5.900×10^{-1}	4.953×10^{-1}	4.456×10^{-1}	3.579×10^{-1}
0.8	5.105×10^{-1}	4.346×10^{-1}	3.640×10^{-1}	2.870×10^{-1}	2.156×10^{-1}	1.697×10^{-1}
1.0	2.691×10^{-1}	2.378×10^{-1}	1.928×10^{-1}	1.417×10^{-1}	9.963×10^{-2}	5.835×10^{-2}
1.2	1.078×10^{-1}	1.063×10^{-1}	8.605×10^{-2}	6.279×10^{-2}	3.847×10^{-2}	2.025×10^{-2}
1.4	3.252×10^{-2}	3.925×10^{-2}	3.340×10^{-2}	2.147×10^{-2}	1.127×10^{-2}	5.379×10^{-3}
1.6	6.860×10^{-3}	1.157×10^{-2}	1.125×10^{-2}	7.050×10^{-3}	2.398×10^{-3}	9.491×10^{-4}

Table D.10: Monte Carlo calculations for Ω, $\epsilon = -0.20$, $d = l$.

	n					
λ_g	20	50	100	200	400	800
0.2	9.876×10^{-1}	9.822×10^{-1}	9.956×10^{-1}	9.955×10^{-1}	9.572×10^{-1}	8.272×10^{-1}
0.4	8.862×10^{-1}	8.879×10^{-1}	9.053×10^{-1}	8.376×10^{-1}	8.297×10^{-1}	7.227×10^{-1}
0.6	7.109×10^{-1}	7.320×10^{-1}	7.449×10^{-1}	6.486×10^{-1}	9.147×10^{-1}	5.251×10^{-1}
0.8	4.989×10^{-1}	5.392×10^{-1}	5.513×10^{-1}	5.237×10^{-1}	4.219×10^{-1}	4.941×10^{-1}
1.0	2.882×10^{-1}	3.464×10^{-1}	3.636×10^{-1}	3.469×10^{-1}	3.162×10^{-1}	1.646×10^{-1}
1.2	1.287×10^{-1}	1.859×10^{-1}	2.095×10^{-1}	2.351×10^{-1}	1.947×10^{-1}	1.004×10^{-1}
1.4	4.322×10^{-2}	8.437×10^{-2}	1.100×10^{-1}	1.011×10^{-1}	6.491×10^{-2}	3.394×10^{-2}
1.6	9.787×10^{-3}	3.102×10^{-2}	4.955×10^{-2}	4.418×10^{-2}	1.773×10^{-2}	6.919×10^{-3}

Table D.11: onte Carlo calculations for Φ, $\epsilon = -0.25$, $d = l$.

	n					
λ_g	20	50	100	200	400	800
0.2	1.081×10^{0}	1.066×10^{0}	1.064×10^{0}	1.064×10^{0}	1.056×10^{0}	9.840×10^{-1}
0.4	1.166×10^{0}	1.137×10^{0}	1.136×10^{0}	1.080×10^{0}	1.075×10^{0}	9.753×10^{-1}
0.6	1.094×10^{0}	1.087×10^{0}	1.089×10^{0}	9.707×10^{-1}	1.270×10^{0}	8.259×10^{-1}
0.8	8.495×10^{-1}	8.879×10^{-1}	8.953×10^{-1}	8.474×10^{-1}	6.958×10^{-1}	7.804×10^{-1}
1.0	5.207×10^{-1}	6.119×10^{-1}	6.371×10^{-1}	6.058×10^{-1}	5.428×10^{-1}	2.979×10^{-1}
1.2	2.402×10^{-1}	3.425×10^{-1}	3.841×10^{-1}	4.167×10^{-1}	3.597×10^{-1}	1.908×10^{-1}
1.4	8.215×10^{-2}	1.593×10^{-1}	2.064×10^{-1}	1.894×10^{-1}	1.229×10^{-1}	6.472×10^{-2}
1.6	1.880×10^{-2}	5.953×10^{-2}	9.484×10^{-2}	8.517×10^{-2}	3.471×10^{-2}	1.319×10^{-2}

Table D.12: Monte Carlo calculations for Ω, $\epsilon = -0.25$, $d = l$.

	n					
λ_g	20	50	100	200	400	800
0.2	1.182×10^{0}	1.317×10^{0}	1.627×10^{0}	2.004×10^{0}	2.083×10^{0}	1.417×10^{0}
0.4	1.205×10^{0}	1.461×10^{0}	1.952×10^{0}	2.039×10^{0}	2.852×10^{0}	2.479×10^{0}
0.6	1.088×10^{0}	1.441×10^{0}	1.992×10^{0}	1.957×10^{0}	7.272×10^{0}	2.602×10^{0}
0.8	8.663×10^{-1}	1.293×10^{0}	1.838×10^{0}	2.591×10^{0}	2.355×10^{0}	6.035×10^{0}
1.0	5.711×10^{-1}	1.008×10^{0}	1.550×10^{0}	2.274×10^{0}	2.876×10^{0}	1.432×10^{0}
1.2	2.901×10^{-1}	6.549×10^{-1}	1.162×10^{0}	2.484×10^{0}	3.078×10^{0}	1.534×10^{0}
1.4	1.098×10^{-1}	3.646×10^{-1}	8.291×10^{-1}	1.172×10^{0}	9.664×10^{-1}	5.429×10^{-1}
1.6	2.687×10^{-2}	1.670×10^{-1}	4.784×10^{-1}	6.387×10^{-1}	3.296×10^{-1}	1.143×10^{-1}

Table D.13: Monte Carlo calculations for Φ, $\epsilon = -0.30$, $d = l$.

	n					
λ_g	20	50	100	200	400	800
0.2	1.191×10^{0}	1.237×10^{0}	1.357×10^{0}	1.557×10^{0}	1.704×10^{0}	1.372×10^{0}
0.4	1.498×10^{0}	1.682×10^{0}	2.056×10^{0}	2.218×10^{0}	3.104×10^{0}	2.865×10^{0}
0.6	1.624×10^{0}	2.009×10^{0}	2.650×10^{0}	2.714×10^{0}	8.890×10^{0}	3.947×10^{0}
0.8	1.455×10^{0}	2.051×10^{0}	2.838×10^{0}	3.920×10^{0}	3.722×10^{0}	8.787×10^{0}
1.0	1.026×10^{0}	1.748×10^{0}	2.655×10^{0}	3.882×10^{0}	4.795×10^{0}	2.579×10^{0}
1.2	5.405×10^{-1}	1.195×10^{0}	2.111×10^{0}	4.215×10^{0}	5.685×10^{0}	2.940×10^{0}
1.4	2.086×10^{-1}	6.852×10^{-1}	1.548×10^{0}	2.180×10^{0}	1.831×10^{0}	1.039×10^{0}
1.6	5.161×10^{-2}	3.196×10^{-1}	9.123×10^{-1}	1.235×10^{0}	6.480×10^{-1}	2.184×10^{-1}

Table D.14: Monte Carlo calculations for Ω, $\epsilon = -0.30$, $d = l$.

Appendix E

Error Analysis for Monte Carlo Simulations

E.1 Probability Estimate Error

Sources of errors in the Monte Carlo calculation of the steric factors can be divided into primary errors in the determination of the radial probability profile $p(\hat{r})$ and propagated errors in the integration of that profile. In general, rigorous determination of convergence on $p(\hat{r})$ would be by repeating simulations until no change is observed. Unfortunately, time and cost constraints make this prohibitive except in the case of small chains. As described in Section 5.4.2.3, the following methods were used as indirect means of determining convergence:

1. symmetry
2. Φ/Ω profiles
3. visual assessment of constant n, epsilon plots

E.2 Profile Integration Error

This section presents an analysis of the errors resulting from numerical integration of the probability profile $p(\hat{r})$. These errors are determined primarily by the value of the mesh size across the pore diameter and are in general much smaller than those resulting from inadequate convergence on $p(\hat{r})$. The following assumes that the estimated probabilities are an accurate measure of the true probabilities. Poor $p(\hat{r})$ estimates will result in fluctuations which are magnified by the Boltzmann weighting term, especially for large attractive energies, providing an indirect relative means of evaluating convergence on $p(\hat{r})$.

E.2.1 Definitions

We make the following definitions:

n_p = number of mass points per chain

m = number of mesh points across pore radius

$\hat{r}_j$ = dimensionless radial mesh point across pore, where $\hat{r}_{\pm m} = \pm 1$

p_i = "true" probability that a polymer chain is in state i, where $\sum_i p_i = 1$

M_c = number of chains generated

S_i = expected number of chains generated in state i based on p_i

$\tilde{S}_i$ = actual number of chains generated in state i

$\tilde{p}_i$ = estimated probability from $\tilde{S}_i$

For M_c trials, S_i and $\tilde{S}_i$ are the expected and actual number of observations in category i, so

$$M_c = \sum_i S_i = \sum_i \tilde{S}_i. \tag{E.1}$$

The exact value of each p_i is unknown but is estimated from $\tilde{p}_i$, where

$$p_i \approx \tilde{p}_i = \frac{\tilde{S}_i}{M_c}. \tag{E.2}$$

From multinomial statistics, the expected value (E) and variance (Var $= \sigma^2$) of $\tilde{S}_i$ are given by[67]

$$\mathrm{E}(\tilde{S}_i) = S_i, \tag{E.3}$$

$$\mathrm{Var}(\tilde{S}_i) = M_c \tilde{p}_i (1 - \tilde{p}_i). \tag{E.4}$$

E.2.2 Calculation of Steric Factor Variances

The steric factors Φ and Ω are calculated by Simpson integration of the Monte Carlo results, and thus they can be thought of as functions of two random variables: $\{S_i\}$, the vector of number of observations in each category, and $\{\hat{r}_j\}$, the vector of radial positions in the pore. Integration is done by evaluation at fixed points across the diameter, which is equivalent to assuming that each radial position occurs with uniform probability. A success is defined when every mass point of a chain fits within the pore.

E.2.2.1 Neutral Pore

The neutral case ($E = 0$) simplifies to a binomial probability distribution:

$$p_i = \begin{cases} p_0 & \text{if success } (i = 0) \\ \overline{p} = p_1 = 1 - p_0 & \text{if failure } (i = 1) \end{cases}$$

Then,

$$\Phi = \sum_{j=-m}^{m} a_j \frac{\tilde{S}_0(\hat{r}_j)}{M_c}, \tag{E.5}$$

$$\mathrm{Var}(\Phi) = \mathrm{Var}\left(\sum_{j=-m}^{m} a_j \frac{\tilde{S}_0(\hat{r}_j)}{M_c} \right),$$

$$= \sum_{j=-m}^{m} \sum_{jj=-m}^{m} \frac{a_j a_{jj}}{M_c^2} \mathrm{Cov}\left[\tilde{S}_0(\hat{r}_j), \tilde{S}_0(\hat{r}_{jj})\right], \tag{E.6}$$

where the a_j are coefficients from Simpson's rule:

$$\text{For } \Phi: \qquad a_j = 2\alpha_j(\Delta\hat{r})\hat{r}_j, \tag{E.7a}$$

$$\text{For } \Omega: \qquad a_j = 4\alpha_j(\Delta\hat{r})\hat{r}_j(1-\hat{r}_j^2), \tag{E.7b}$$

and $\Delta\hat{r}$ are the fixed radial step sizes.

The covariance term in Eq. E.6 is more precisely a binomial multivariate cross-covariance. Applying the general formulation of Wishart,[257]

$$\mathrm{Cov}\left[\tilde{S}_0(\hat{r}_j), \tilde{S}_0(\hat{r}_{jj})\right] = M_c\left\{\tilde{p}_0(\hat{r}_j \cap \hat{r}_{jj}) - \tilde{p}_0(\hat{r}_j)\tilde{p}_0(\hat{r}_{jj})\right\}, \tag{E.8}$$

where $\tilde{p}_0(\hat{r}_j \cap \hat{r}_{jj})$ is the probability of a single chain fitting at *both* $\hat{r}_j$ and $\hat{r}_{jj}$.

Substituting Eq. E.8 into Eq. E.6 and rearranging to maximize computation speed yields

$$\begin{aligned}\mathrm{Var}(\Phi) \;=\; & \sum_{j=-m}^{m} \frac{a_j^2}{M_c}\tilde{p}_0(\hat{r}_j)(1-\tilde{p}_0(\hat{r}_j)) \\ & +2\sum_{j=-m}^{m-1}\sum_{jj=j+1}^{m} \frac{a_j a_{jj}}{M_c}\left\{\tilde{p}_0(\hat{r}_j \cap \hat{r}_{jj}) - \tilde{p}_0(\hat{r}_j)\tilde{p}_0(\hat{r}_{jj})\right\}.\end{aligned} \tag{E.9}$$

For the Monte Carlo simulation, rigorous calculation of $\tilde{p}_0(\hat{r}_j \cap \hat{r}_{jj})$ requires additional bookkeeping in an $(2m+1)\times(2m+1)$ array. As a faster alternative, the cross-covariance can be conservatively estimated by using the fact that its absolute value is bound by the square root of the product of the individual variances:[67]

$$|\tilde{p}_0(\hat{r}_j \cap \hat{r}_{jj}) - \tilde{p}_0(\hat{r}_j)\tilde{p}_0(\hat{r}_{jj})| \le \sqrt{\tilde{p}_0(\hat{r}_j)(1-\tilde{p}_0(\hat{r}_j))\cdot\tilde{p}_0(\hat{r}_{jj})(1-\tilde{p}_0(\hat{r}_{jj}))}, \tag{E.10}$$

so that a bound for Φ is given by

$$\begin{aligned}\mathrm{Var}(\Phi) \;\lesssim\; & \sum_{j=-m}^{m} \frac{a_j^2}{M_c}\tilde{p}_0(\hat{r}_j)(1-\tilde{p}_0(\hat{r}_j)) \\ & +2\sum_{j=-m}^{m-1}\sum_{jj=j+1}^{m} \frac{a_j a_{jj}}{M_c}\sqrt{\tilde{p}_0(\hat{r}_j)(1-\tilde{p}_0(\hat{r}_j))\cdot\tilde{p}_0(\hat{r}_{jj})(1-\tilde{p}_0(\hat{r}_{jj}))}.\end{aligned} \tag{E.11}$$

The equation for $\mathrm{Var}(\Omega)$ is exactly the same with different values of a_j. Eq. E.11 was used by Davidson[70] for estimation of variances in the neutral pore case.

E.2.2.2 Pore with Square-well Potential

For a square-well potential acting on the mass points, we have an $(n_p + 1)$-nomial probability distribution:

$$p_i = \begin{cases} p_0 & \text{if success with zero mass-point interactions } (i = 0) \\ p_1 & \text{if success with one mass-point interaction } (i = 1) \\ \vdots & \\ p_{n_p} & \text{if success with } n_p \text{ mass-point interactions } (i = n_p) \\ \overline{p} = p_{n_p+1} & \text{if failure } (i = n_p + 1) \end{cases},$$

where the partition coefficient is now given by

$$\Phi = \sum_{j=-m}^{m} \sum_{i=0}^{n_p} a_j \frac{\tilde{S}_i(\hat{r}_j)}{M_c} \exp(-\epsilon i), \tag{E.12}$$

$$\text{Var}(\Phi) = \text{Var}\left(\sum_{j=-m}^{m} \sum_{i=0}^{n_p} a_j \frac{\tilde{S}_i(\hat{r}_j)}{M_c} \exp(-\epsilon i) \right). \tag{E.13}$$

Davidson originally provided a conservative estimate for Eq. E.13 using a graphical technique. Here we demonstrate an analytical solution by expanding Eq. E.13:

$$\text{Var}(\Phi) = \sum_{j=-m}^{m} \sum_{jj=-m}^{m} \sum_{i=0}^{n_p} \sum_{ii=0}^{n_p} \frac{a_j a_{jj} \exp(-\epsilon[i + ii])}{M_c^2} \text{Cov}\left[\tilde{S}_i(\hat{r}_j), \tilde{S}_{ii}(\hat{r}_{jj})\right]. \tag{E.14}$$

The covariance term is a generalized multinomial multivariate cross-covariance, given by Wishart[257] as

$$\text{Cov}\left[\tilde{S}_i(\hat{r}_j), \tilde{S}_{ii}(\hat{r}_{jj})\right] = M_c \left\{\tilde{p}_{i \cap ii}(\hat{r}_j \cap \hat{r}_{jj}) - \tilde{p}_i(\hat{r}_j)\tilde{p}_{ii}(\hat{r}_{jj})\right\}. \tag{E.15}$$

Here, $\tilde{p}_{i \cap ii}(\hat{r}_j \cap \hat{r}_{jj})$ is defined as the probability of a chain existing in both states i and ii at both $\hat{r}_j$ and $\hat{r}_{jj}$. The cross-covariance reduces to the following forms depending on the values of the indices:

$$\text{For } i \neq ii: \quad = -M_c \tilde{p}(\hat{r}_j)\tilde{p}_{ii}(\hat{r}_{jj}), \tag{E.16a}$$

$$\text{For } i = ii: \quad = M_c \left\{\tilde{p}_i(\hat{r}_j \cap \hat{r}_{jj}) - \tilde{p}_i(\hat{r}_j)\tilde{p}_i(\hat{r}_{jj})\right\}, \tag{E.16b}$$

$$\text{For } i = ii,\ j = jj: \quad = M_c \left\{\tilde{p}_i(\hat{r}_j)(1 - \tilde{p}(\hat{r}_j))\right\}, \tag{E.16c}$$

where Eq. E.16a results from the fact that states i and ii are mutually exclusive at a give r_j.

Substituting Eqs. E.15 and E.16 into Eq. E.14 gives

$$\text{Var}(\Phi) = \sum_{i=0}^{n_p} \sum_{j=-m}^{m} \frac{a_j^2 \exp(-2\epsilon i)}{M_c} \tilde{p}_i(\hat{r}_j)(1 - \tilde{p}_i(\hat{r}_j))$$

$$+2\sum_{i=0}^{n_p}\sum_{j=-m}^{m-1}\sum_{jj=j+1}^{m}\frac{a_j a_{jj}\exp(-2\epsilon i)}{M_c}\left\{\tilde{p}_i(\hat{r}_j\cap\hat{r}_{jj})-\tilde{p}_i(\hat{r}_j)\tilde{p}_i(\hat{r}_{jj})\right\}$$
$$-2\sum_{i=0}^{n_p-1}\sum_{ii=i+1}^{n_p}\sum_{j=-m}^{m}\frac{a_j^2\exp(-\epsilon[i+ii])}{M_c}\tilde{p}_i(\hat{r}_j)\tilde{p}_{ii}(\hat{r}_j)$$
$$-4\sum_{i=0}^{n_p-1}\sum_{ii=i+1}^{n_p}\sum_{j=-m}^{m-1}\sum_{jj=j+1}^{m}\frac{a_j a_{jj}\exp(-\epsilon[i+ii])}{M_c}\tilde{p}_i(\hat{r}_j)\tilde{p}_{ii}(\hat{r}_{jj}). \qquad \text{(E.17)}$$

And finally, rearranging for computational use:

$$\mathrm{Var}(\Phi) = \frac{1}{M_c}\left[\sum_{j=-m}^{m}a_j^2 Q(j)+2\sum_{j=-m}^{m-1}\sum_{jj=j+1}^{m}a_j a_{jj}V(j,jj)\right], \qquad \text{(E.18a)}$$

$$Q(j) = \sum_{i=0}^{n_p}\exp(-2\epsilon i)\tilde{p}_i(\hat{r}_j)(1-\tilde{p}_i(\hat{r}_j))$$
$$-2\sum_{i=0}^{n_p-1}\sum_{ii=i+1}^{n_p}\exp(-\epsilon[i+ii])\tilde{p}_i(\hat{r}_j)\tilde{p}_{ii}(\hat{r}_j), \qquad \text{(E.18b)}$$

$$V(j,jj) = \sum_{i=0}^{n_p}\exp(-2\epsilon i)\left\{\tilde{p}_i(\hat{r}_j\cap\hat{r}_{jj})-\tilde{p}_i(\hat{r}_j)\tilde{p}_i(\hat{r}_{jj})\right\}$$
$$-2\sum_{i=0}^{n_p-1}\sum_{ii=i+1}^{n_p}\exp(-\epsilon[i+ii])\tilde{p}_i(\hat{r}_j)\tilde{p}_{ii}(\hat{r}_{jj}). \qquad \text{(E.18c)}$$

Once again, rigorous calculation of the joint probability requires additional bookkeeping, this time in an $(2m+1)\times(2m+1)\times(n_p+1)$ array. Again, as a practial solution, Eq. E.10 was used as an upper bound. Finally, to avoid negative values for $\mathrm{Var}(\Phi)$ which result from lack of convergence on $p(\hat{r})$, only the additive terms of Eqs. E.18 and E.18 were used; since all terms in the summations are positive, this also insures an overestimation of the error.

Note that because of a mathematical artifact, the variance calculation for the multinomial case with $\epsilon = 0$ is not equivalent to the binomial neutral pore variance of Section E.2.2.1, i.e., Eq. E.18a with $\epsilon = 0$ does not reduce to Eq. E.9. This is because the multinomial case still considers chains with different numbers of points in the square well to be in different states, even though in the neutral case they contribute equally to the calculation of Φ and Ω.

Appendix F

Estimation of Molecular Dimensions of Dextran in Water

F.1 Overview and Summary

In this Appendix, we review methods for determining the characteristic dimensions of polymer molecules in solution from intrinsic viscosity data and radius-of-gyration correlations. In Section F.2, the pertinent theory and equations are summarized. Section F.3 presents a compilation of data available in the literature for dextran/water systems. Section F.4 gives the results for the perturbed dimensions obtained by these methods and the implications for restricted transport.

F.2 Summary of Theory and Equations

F.2.1 Relationship of Ideal and Real Chain Dimensions

The following development is a combination of methods found in Kurata and Stockmayer,[155] Yamakawa[259] and Gowariker *et al.*[118] A *random-flight* chain is defined as one with neither short-range interactions (*i. e.*, bond angle restriction) nor long-range interactions (*i. e.*, intramolecular van der Waals forces). All random-flight dimensions will be indicated by a "00" subscript, *e. g.*, r_{g00}. An *unperturbed* chain is one which does not experience long-range interactions (denoted by the subscript "0"), and a *real* chain is one which has both short- and long-range interactions (no subscript). The unperturbed number of chain segments n and chain length l are related to their real counterparts N and L by

$$N = n/(s\alpha_S^2 \frac{g}{g_0}), \tag{F.1a}$$

$$L = s\alpha_S^2 \frac{g}{g_0} l. \tag{F.1b}$$

Short-range interactions are accounted for by the skeletal factor $s > 1$, where for both the mean-square radius of gyration r_g^2 and the mean-square end-to-end distance $\langle R^2 \rangle$,

$$r_{g0}^2 = s r_{g00}^2, \tag{F.2a}$$

$$\langle R^2 \rangle_0 = s \langle R^2 \rangle_{00}. \tag{F.2b}$$

The expansion factors α_S and α_R relate the unperturbed radius of gyration and unperturbed end-to-end distance to the real radius of gyration and real end-to-end distance:

$$r_g^2 = \alpha_S^2 r_{g0}^2, \tag{F.3a}$$

$$\langle R^2 \rangle = \alpha_R^2 \langle R^2 \rangle_0. \tag{F.3b}$$

In general, the solvent expansion has a greater effect on end-to-end distance than radius of gyration and $\alpha_R > \alpha_S$. The factor g/g_0 is a correction term to account for chain branching. Relating unperturbed to real dimensions is thus a matter of determining s, α_S, and g/g_0, as discussed in the following sections. As will be seen, the present state of theoretical and experimental work in the field does not yet allow for a single rigorous means of making these calculations, and so we have chosen to examine a variety of methods and compare the results.

F.2.2 Determination of Unperturbed Molecular Dimensions from Intrinsic Viscosity Data

In a similar fashion to the radius of gyration, the unperturbed intrinsic viscosity is related to that at other conditions by an expansion factor $\alpha_\eta \leq \alpha_S$:

$$[\eta] = \alpha_\eta^3 [\eta]_0. \tag{F.4}$$

The difference between the expansion factors results from the fact that as excluded volume increases, the hydrodynamic radius increases less than the statistical physical radius. At theta conditions for a nondraining coil the unperturbed intrinsic viscosity $[\eta]_0$ is proportional to the square root of the molecular weight M and to the 3/2th-power of $\langle R^2 \rangle_0$.

$$[\eta]_0 = \kappa_0 M^{1/2}, \tag{F.5a}$$

$$\kappa_0 = \phi_0 A_0^3, \tag{F.5b}$$

$$A_0 = (\langle R^2 \rangle_0 / M)^{1/2}, \tag{F.5c}$$

$$\phi_0 \approx 2.5 \times 10^{23}, \tag{F.5d}$$

thus

$$[\eta] = \alpha_\eta^3 \kappa_0 M^{1/2}. \tag{F.6}$$

In the above equations, κ_0 has units of $cm^3\text{-}g^{-3/2}\text{-}mol^{1/2}$, A_0 has units of $cm\text{-}g^{-1/2}\text{-}mol^{1/2}$, and ϕ_0 is a viscosity constant for linear chains which has units of mol^{-1}. The value for ϕ_0 shown is experimentally derived from viscosity and light-scattering data and differs slightly from reported theoretical values.[259] Determination of the unperturbed dimensions from intrinsic viscosity data is

thus equivalent to calculation of A_0.

There is a body of methods based on the argument that as the chain size decreases, the expansion factors must approach unity, and $[\eta] \rightarrow [\eta]_0$. Therefore an extrapolation of $[\eta]$ to $M = 0$ provides a value of $[\eta]_0$ from which κ_0, and hence A_0, can be calculated. The particulars of each method differ in the functional representation used for α_S and α_η. The Stockmayer-Fixman method[234] results in

$$\frac{[\eta]}{M^{1/2}} = \kappa_0 + 0.51\phi_0 B M^{1/2}, \tag{F.7a}$$

$$B = \beta/M_{seg}^2 = (1-2\chi)(\bar{v}_p^2/V_s N_A), \tag{F.7b}$$

$$M_{seg} = M/n, \tag{F.7c}$$

where B has units of cm^3-g^{-2}-mol^2, M_{seg} is the segment molecular weight in g/mol, $\bar{v}_p$ is the partial specific volume of the polymer in cm^3/g, V_s is the molar volume of solvent in cm^3/mol, and N_A is Avogardo's number. The parameter B can be equivalently expressed as either a function of the segment excluded volume β or of the Flory-Huggins thermodynamics parameter χ. A plot of $[\eta]/M^{1/2}$ versus $M^{1/2}$ will have y-intercept κ_0. In practice, the Stockmayer-Fixman method has been shown to yield accurate results for good-solvent systems as long as the data is for relatively low molecular weights.[259] When data from higher molecular weights are used, the analysis tends to overestimate κ_0. This approach has been seen to be sensitive to different ranges of α_η, with modifications needed if α_η^3 is greater than 1.6 for any range of the data.[27]

Inagaki *et al.*[138] have proposed an alternative method which complements the Stockmayer-Fixman approach in that it works best with extrapolations from high molecular weight data. This expression, obtained from the use of an equation by Ptitsyn,[207] is

$$\frac{[\eta]^{4/5}}{M^{2/5}} = 0.786\kappa_0^{4/5} + 0.454\kappa_0^{2/15}\phi_0^{2/3}B^{2/3}M^{1/3}, \tag{F.8}$$

where a plot of $[\eta]^{4/5}/M^{2/5}$ versus $M^{1/3}$ has a y-intercept of $0.786\kappa_0^{4/5}$. When extrapolation is done from low molecular weights, the equation is modified so that the y-intercept is $\kappa_0^{4/5}$.

Finally, an expression of Berry's is suggested as showing linear behavior over a broader range of molecular weights:[96]

$$\sqrt{\frac{[\eta]}{M_w^{1/2}}} = \kappa_0^{1/2} + D\frac{M_w}{[\eta]}, \tag{F.9}$$

where M_w is the weight-averaged molecular weight and D is an adjustable parameter. A plot of $\sqrt{[\eta]/M_w^{1/2}}$ versus $M_w/[\eta]$ will have a y-intercept of $\kappa_0^{1/2}$.

F.2.3 Effect of Sample Polydispersity on Viscosity Measurements

Newman *et al.*[190] demonstrated that for polydisperse samples, number-averaged molecular weights and number-averaged radii of gyration should be used in calculations of molecular dimensions from

$[\eta]$. Shultz[228] has derived an expression for correcting viscosity data when either M_n or the number-averaged r_g are not available, and M_w or z-averaged r_g must be used. The correction is significant when M_w is used but the form of the radius of gyration has very minor effects. For our purposes, where M_n is available for almost all of the data, no such adjustments are necessary. In related work, Bohdanecky and Kovar[27] show that a correlation of M_n to $[\eta]$ from a polydisperse sample overestimates the true value of M_n. The inverse is true for correlations of M_w, but the magnitude of the effect is much smaller.

If an analytical form is assumed for the distribution of molecular weights, then it is possible to derive corrections for polydispersity. Probably the best such function is the Schulz-Zimm distribution for the mass fraction $f(M)$:

$$f(M) = \frac{r^{t+1}}{\Gamma(t+1)} \cdot M^t \cdot \exp(-rM), \tag{F.10}$$

where $t = (M_w/M_n - 1)^{-1}$, $r = t/M_n$, and Γ is the gamma function. The Schulz-Zimm distribution has been found superior to the lognormal distribution in describing fractionated samples, although the differences are small for $M_w/M_n < 2$.[148,149] A correction factor for the Stockmayer-Fixman equation (Eq. F.7a) using the Schulz-Zimm distribution and M_w is defined as[236]

$$\frac{[\eta]}{M_w^{1/2}} = Q\kappa_0 + 0.51\phi_0 B M_w^{1/2}, \tag{F.11a}$$

$$Q = \frac{\langle M^{1/2}\rangle_w}{M_w^{1/2}} = \frac{1}{(t+1)^{1/2}} \cdot \frac{\Gamma(t+1.5)}{\Gamma(t+1)}. \tag{F.11b}$$

For branched polymers, the effects of branching and polydispersity are difficult to separate as branching, when not uniform throughout the molecule, in effect introduces a second probability distribution into the description of the polymer.[233]

F.2.4 Determination of the Linear Expansion Coefficient α_S

Since there is not presently a unifying theoretical formulation for excluded volume effects, it is common for results from one type of empirical formulation to be incompatible with supposedly equivalent results from another formulation. The graphical extrapolation procedures give accurate values for the unperturbed dimensions, but are generally not useful for directly determining excluded volumes. In light of this, three alternate methods of calculating α_S will be considered. Two methods (using the intrinsic viscosity and the radius of gyration) require calculation of κ_0 or A_0 from one of the graphical methods previously discussed, and the other (using the second virial coefficient) requires measurement of the second virial coefficient and radius of gyration.

F.2.4.1 α_S from Intrinsic Viscosity Data

Calculation of α_S from viscosity data requires the assumption of a direct functional relationship to α_η. Such functions are usually of the form

$$\alpha_\eta^3 = \alpha_S^\delta, \tag{F.12}$$

where δ is an adjustable parameter so that

$$\alpha_S = \left(\frac{[\eta]}{\kappa_0 M^{1/2}}\right)^{1/\delta}. \tag{F.13}$$

According to Kurata and Yamakawa,[156] $\delta = 2.43$ is a suitable general solution.

F.2.4.2 α_S from Radius of Gyration Data

Having obtained A_0 from a graphical method, we can now solve directly for the unperturbed radius of gyration:

$$r_{g0} = \left(\frac{\langle R^2\rangle_0}{6}\right)^{1/2} = A_0(M/6)^{1/2}. \tag{F.14}$$

Given an independent correlation for the real radius of gyration as a function of molecular weight,

$$r_g = A' M^a, \tag{F.15}$$

a value for α_S can be obtained by combining Eqs. F.14 and F.15:

$$\alpha_S = r_g/r_{g0} = \frac{A'\sqrt{6}}{A_0} M^{(a-0.5)}. \tag{F.16}$$

F.2.4.3 α_S from Second Virial Coefficient Data

Yamakawa[259] gives a method for determining the expansion coefficient when data for both the second virial coefficient A_2 and the radius of gyration are available for individual fractions. His method first involves calculation of the variables Ψ and $\bar{z}$, where

$$\Psi = \frac{A_2 M^2}{4\pi^{3/2} N_A r_g^3}, \tag{F.17a}$$

$$\bar{z} = \frac{\left(1 - \frac{\Psi}{0.547}\right)^{-1/0.4683} - 1}{3.903}. \tag{F.17b}$$

An iterative solution is then made for α_S:

$$\alpha_S^2 = 0.541 + 0.459(1 + 6.04\bar{z}\alpha_S^3)^{0.46}. \tag{F.18}$$

F.2.5 Determination of Skeletal Factor s and Bond Dimensions n and l

The skeletal factor s can be decomposed into two parts: one factor due to bond angle restriction and the other to the impedance to internal rotations:

$$s = \frac{\langle R^2\rangle_0}{\langle R^2\rangle_{0,\mathrm{fr}}} \cdot \frac{\langle R^2\rangle_{0,\mathrm{fr}}}{\langle R^2\rangle_{00}}, \tag{F.19a}$$

$$= \sigma^2 \frac{\langle R^2\rangle_{0,\mathrm{fr}}}{nl^2}, \tag{F.19b}$$

where $\langle R^2\rangle_{0,\mathrm{fr}}$ is the mean-square end-to-end dimension of a molecule with fixed valence angles but free internal rotations and $\langle R^2\rangle_{00} = nl^2$. The conformation (or flexibility) factor σ^2 is defined as $\langle R^2\rangle_0/\langle R^2\rangle_{0,\mathrm{fr}}$. The dimensions n and l are determined by the assumption of some sort of model used to derive the free-rotation dimensions. Cleland[68] calculated the theoretical free-rotation value of $(\langle R^2\rangle_{0,\mathrm{fr}}/n)^{1/2}$ for mono- and disaccharide polymers based on an idealized pyranose monomer in the C1 chair conformation. For a α-1,6 glucose linkage, he reported values of $(\langle R^2\rangle_{0,\mathrm{fr}}/n)^{1/2} = 5.02$ or 5.40 Å, depending on the assumed bond angle. Both values are close to the end-to-end glucose monomer length of 5.15 Å, and so the approximations of $(\langle R^2\rangle_{0,\mathrm{fr}}/n)^{1/2} \approx (\langle R^2\rangle_{00}/n)^{1/2} = l$ and $s = \sigma^2$ are justified. Since Cleland used the length of a pyranose unit for l, n is the number of glucose monomers in a polymer $= M/M_{\mathrm{mon}}$, where $M_{\mathrm{mon}} = 162$ daltons. Then by substitution, $A_{00} = (\langle R^2\rangle_{0,\mathrm{fr}}/M)^{1/2} = 0.394$ or 0.424 Å-(mol/g)$^{1/2}$. The skeletal factor is thus given by

$$s = \left(\frac{A_0}{A_{00}}\right)^2. \tag{F.20}$$

An alternative method of deriving L is from persistence length measurements. The persistence length a^* is related to the radius of gyration for large chains by[109]

$$a^* = 3r_g^2/NL, \tag{F.21}$$

leading to

$$L = 2a^*. \tag{F.22}$$

F.2.6 Determination of Branching Factor g/g_0

The development so far strictly pertains to straight-chain molecules. Dextran is reported to be predominantly linear, but with a small amount (5-6%) of chain branching through α-1,3 linkages.[162,245] The length of these branches is the source of some controversy, with results from chemical analysis at odds with observed physical behavior. Recent studies on large (10^6-10^7 dalton) dextrans indicate a majority of the branches are short chains ($\approx$ 1 to 2 glucose residues) with a small number of long branches (50-100 residues).[152,162] Branch length increases with molecular weight, but at dextran

sizes of concern to us (less than 10^6 daltons), there is no evidence of long branches.[152,224]

The principal effect of branching is to reduce the effective volume of the molecule compared to a linear molecule of equivalent weight. This in turn lowers the intrinsic viscosity and radius of gyration relative to the linear molecule. The effect of chain branching is described by a factor $g_\eta < 1$ which relates the intrinsic viscosity of a branched chain to that of a linear molecule of equal molecular weight:

$$g_\eta = [\eta]_{\rm br}/[\eta]_{\rm lin}, \tag{F.23a}$$

$$= \left(\frac{r_{g0,\rm br}}{r_{g0,\rm lin}}\right)^{3/2} \cdot \left(\frac{\phi_{0,\rm br}}{\phi_{0,\rm lin}}\right) \cdot \left(\frac{\alpha^3_{\eta,\rm br}}{\alpha^3_{\eta,\rm lin}}\right), \tag{F.23b}$$

$$= g_0^{3/2} \cdot \left(\frac{\phi_{0,\rm br}}{\phi_{0,\rm lin}}\right) \cdot \left(\frac{\alpha^3_{\eta,\rm br}}{\alpha^3_{\eta,\rm lin}}\right). \tag{F.23c}$$

The branching effect is factored into three terms representing, respectively, the effect on unperturbed dimensions, the effect on the intramolecular hydrodynamics, and the effect on the excluded volume. Both g_η and g_0 decrease with increasing molecular weight at a constant degree of branching or increasing number of branches at constant molecular weight.

Analytical formulations for g_0 have been derived as a function of the branching geometry and the degree of branching.[154] The simplest physical model of dextran is a comb-like chain with uniform, regularly spaced short branches. The regular comb-like chain model is seen to uniformly underestimate experimental values of g_0 for several types of branched chains by up to 30-50%.[27] For a comb-like molecule with a total of m identical side chains dispersed at random points across the backbone, with each side chain containing $n_{\rm side}$ segments and the backbone having $n_{\rm back}$ segments, g_0 is given by[52]

$$g_0 = (1+mq)^{-3} \cdot \left[1 + 2mq + (2m+m^2)q^2 + (3m^2-2m)q^3\right], \tag{F.24}$$

where $q = n_{\rm side}/n_{\rm back}$. Eq. F.24 applies in a strict sense only to chains with large side branches ($n_{\rm side} \gg 1$) which can be assumed to obey random flight statistics. Applying it to low molecular weight dextran, which has mostly short branches, can only yield a rough estimate for g_0. Using the results implied from chemical analysis, 5% of the molecular weight of dextran is in branch chains and $n_{\rm side} = 1$, 2, or 3 segments. For molecular weights between 40,000 and 10,000, g_0 is then calculated to be around 0.95. This value does not change appreciably if the the effective segment size is adjusted to account for short-range interactions.

Experimental calculations of g_0, on the other hand, indicate a much greater effect of branching on unperturbed dimensions. Based on persistence length measurements, Garg and Stivala[109] determined values ranging from 0.95 at $M_n = 5700$ to 0.82 at $M_n = 27,800$ to 0.72 at $M_n = 48,500$.[109]

Source	Year	M_N range	M_w/M_n range	κ (ml/g)	a
Senti *et al.*[224]	1955	14,500 to 99,600	1.06 to 1.48	0.118	0.491
Granath[119]	1958	17,000 to 263,000	1.09 to 2.75	0.197	0.453
Gekko[113]	1971	32,100 to 410	unknown	0.0986	0.515
Basedow *et al.*[15]	1976	990 to 286,000	1.003 to 1.19	0.130	0.492
Garg and Stivala[109]	1978	5700 to 112,500	1.39 to 2.25	0.147	0.485
Kuge *et al.*[152]	1987	24,000 to 2,860,000	1.19 to 2.35	0.785	0.320

Table F.1: Summary of literature data available for the intrinsic viscosity of dextran in water solutions. κ and a are Mark-Houwink constants determined by fitting $[\eta] = \kappa M_n^a$ to the reported data.

Their values are consistent with data of Granath[119] and Wales *et al.*[251] and suggest a considerably higher degree of branching than indicated by chemical analysis. Dextran with $M_w = 1200$ is estimated to have 7% of the total molecular weight in side chains; for $M_w = 42,000$ it is 17%; for $M_w = 74,500$ it is 28%; and for $M_w = 246,000$ it is 46%. The basis for the discrepancy with the results from chemical analysis is not addressed by any of these workers.

Experimental studies with dextran have usually focused on calculating the equivalent of g_0 for perturbed conditions,

$$g = \frac{r_{g,\mathrm{br}}}{r_{g,\mathrm{lin}}} = g_0 \frac{\alpha^2_{S,\mathrm{br}}}{\alpha^2_{S,\mathrm{lin}}}, \tag{F.25}$$

where α_S^2 is calculated assuming a linear polymer and then adjusted by a factor g/g_0. Values for this ratio based on the data of Garg and Stivala[109] range from 1.02 at $M_n = 5700$ to 1.28 at $M_n = 48,500$.

The hydrodynamic term, the second quotient in Eq. F.23c, has been studied by Stockmayer and Fixman,[233] who arrived at

$$\frac{\phi_{0,\mathrm{br}}}{\phi_{0,\mathrm{lin}}} \approx \left(\frac{r_{s,\mathrm{br}}/r_{s,\mathrm{lin}}}{g_0^{1/2}} \right)^3, \tag{F.26}$$

where r_s is the Stokes-Einstein radius. There is to date no theoretical treatment of the excluded volume effect of branching, represented by the third quotient in Eq. F.23c. The available data indicate that the ratio is less than one for comb-like chains with regularly-spaced branching.[27] For dextran, values of the product of the hydrodynamic and excluded volume terms have been calculated by Senti *et al.* to be in the range of 0.9 to 0.7.[224]

F.3 Summary of Available Dextran/Water Solution Data

Table F.1 summarizes reported measurements of intrinsic viscosity for dextran-in-water systems at 25 °C. For each of these studies, M_w values were determined from light-scattering measurements and M_n was determined from end-group analysis. The Gekko[113] measurements did not include a determination of M_w. The data of Basedow *et al.*[15] covers the largest range of molecular weights

and is in general the most monodisperse, however, the agreement between the different sets was deemed good enough to justify use of all the data (see Figure F-1). At extremely high molecular weights ($> 10^6$), significant departure from ideality (*i.e.*, the square-root dependence on M_n) is seen, believed to be due to increased chain branching.

For use with the graphical calculations, correlations of r_g to M_n are needed. Results from light-scattering measurements for dextran from various sources[109,152,224,237] are shown in Figure F-2. There is some scatter in the data, but only that of Garg and Stivala[109] are in the molecular weight range of interest. Their data was correlated to

$$r_g = 0.812 M_n^{0.438} \tag{F.27}$$

where r_g is in Å.

Only two sources of values for second virial coefficients were found, from Senti *et al.*[224] and Kuge *et al.*.[152] These results are shown in Figure F-3. The agreement between the two sets is poor, but there is reason to believe that the data of Kuge *et al.* is more accurate. For one thing, it is the more recent and there have been significant improvements in the analysis of light-scattering data since the 1950s.[259] Also, use of the Senti *et al.* values led to unrealistically large values of Ψ in Eq. F.17a, precluding calculation of $\overline{z}$. Hence, though the Senti *et al.* data is more suitable for the molecular weight range of interest only calculations from the Kuge *et al.* data were used.

F.4 Results

F.4.1 Unperturbed Dimensions from Graphical Analyses

Since it is not clearly established what constitutes a "high" versus a "low" molecular weight range for dextran-water systems in the context of the graphical methods, all three (Stockmayer-Fixman, Inagaki-Ptitsyn, and Berry) were employed. The results of the plots for the data of Table F.1 are shown in Figures F-4, F-5, and F-6. For the Berry plot (Figure F-6), only the data for which M_w was available was used.

The data on each plot correlate reasonably well, with no observed trend for more recent or more monodisperse data. The solid lines indicate the best-fit for each group. In all cases, the data is nearly flat as $M \rightarrow 0$, indicative of near-theta conditions ($B = 0$ in Eqs. F.7a and F.8). The data at large M_n from Kuge *et al.*[152] show negative slope that is not consistent with the other data and may be the effects of significant chain branching. The intercepts of the lines are $\kappa_0 = 0.122$ cm^3-g$^{-3/2}$-mol$^{1/2}$ for the Stockmayer-Fixman plot, $0.786\kappa_0^{4/5} = 0.196 \rightarrow \kappa_0 = 0.176$ cm^3-g$^{-3/2}$-mol$^{1/2}$ for the Inagaki-Ptitsyn plot, and $\kappa_0^{1/2} = 0.323 \rightarrow \kappa_0 = 0.104$ cm^3-g$^{-3/2}$-mol$^{1/2}$ for the Berry plot. If the Inagaki-Ptitsyn intercept for low-molecular weight data is used, $\kappa_0^{4/5} = 0.176$ and $\kappa_0 = 0.113$ cm^3-g$^{-3/2}$-mol$^{1/2}$, which is more consistent with the Stockmayer-Fixman and Berry results. These

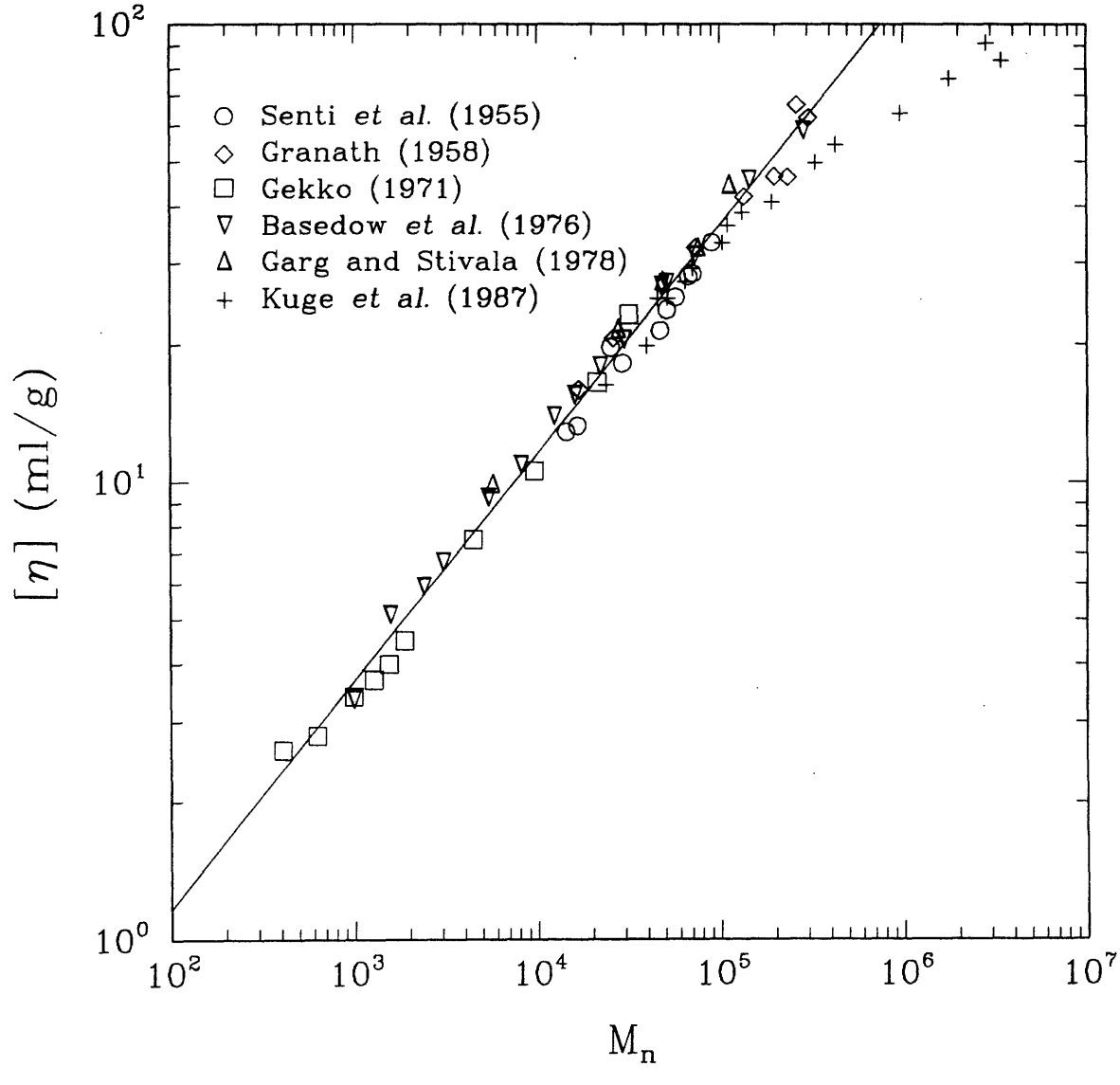

Figure F-1: Intrinsic viscosity versus molecular weight for data of Table F.1. Line represents best fit of $[\eta] = 0.118 M_n^{0.498}$ to data.

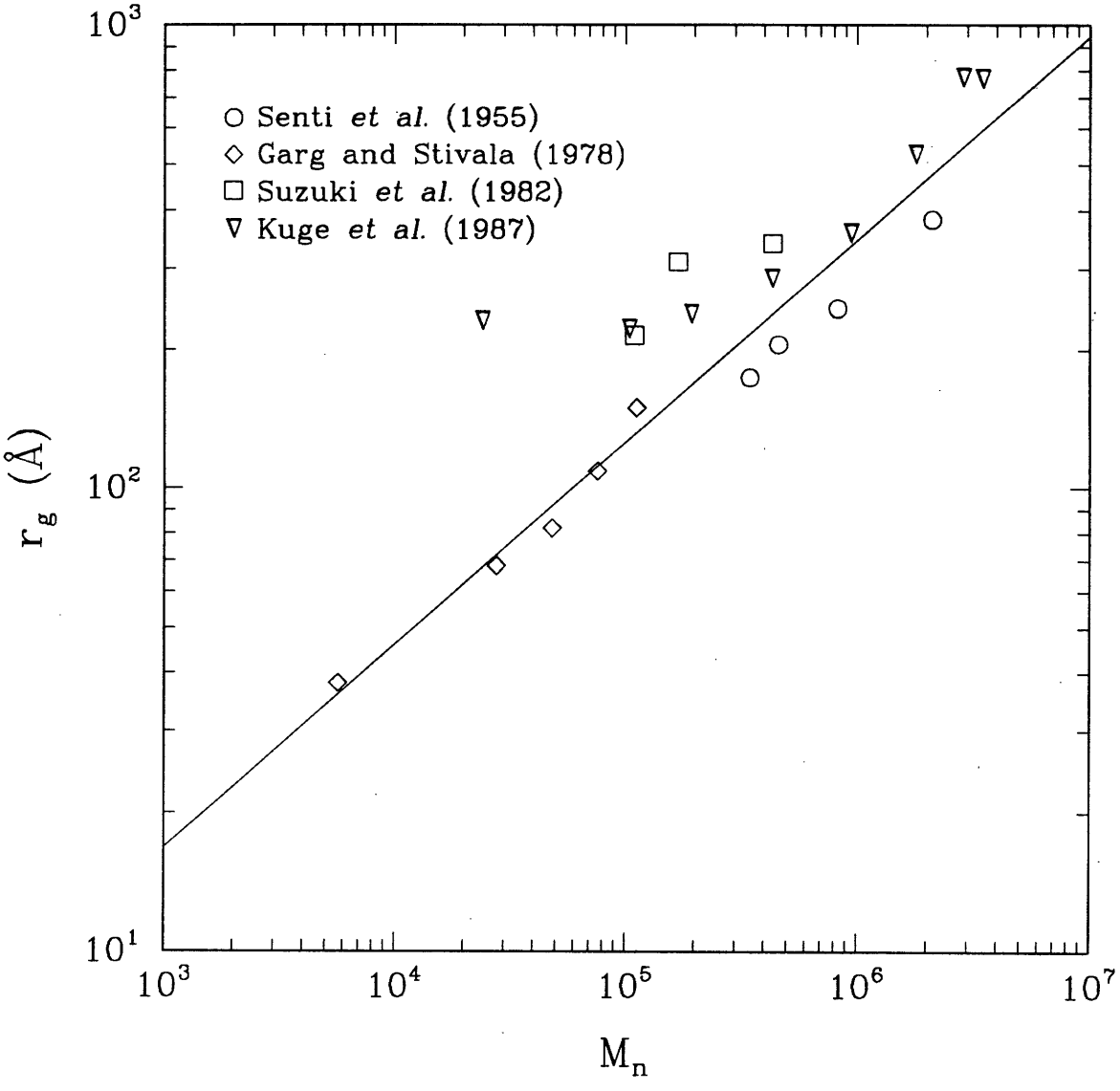

Figure F-2: Summary of reported values of r_g from light-scattering measurements for dextran/water systems. Line is corelation given by Eq. F.27.

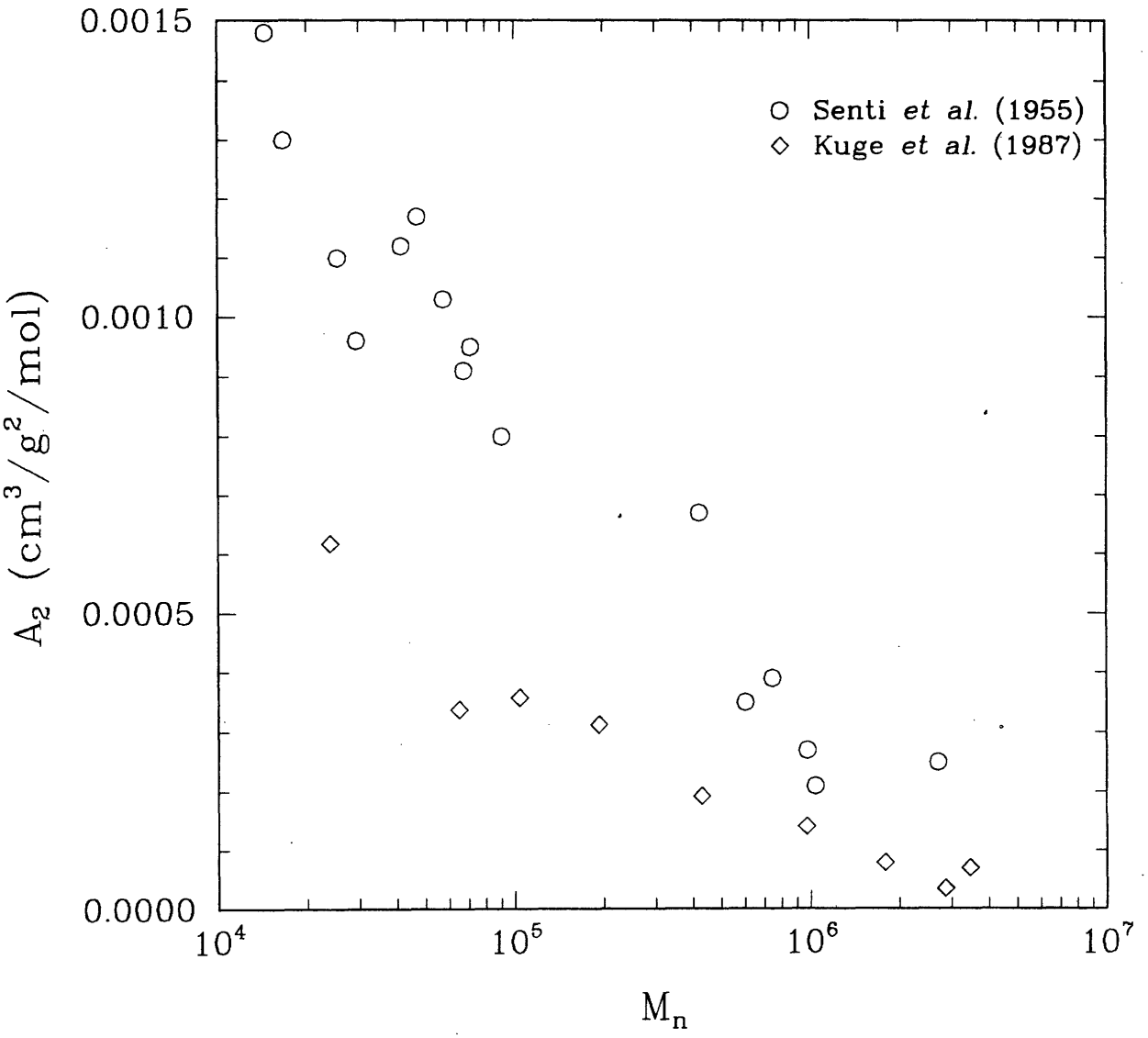

Figure F-3: Summary of reported values of the second virial coefficient (A_2) for dextran/water systems.

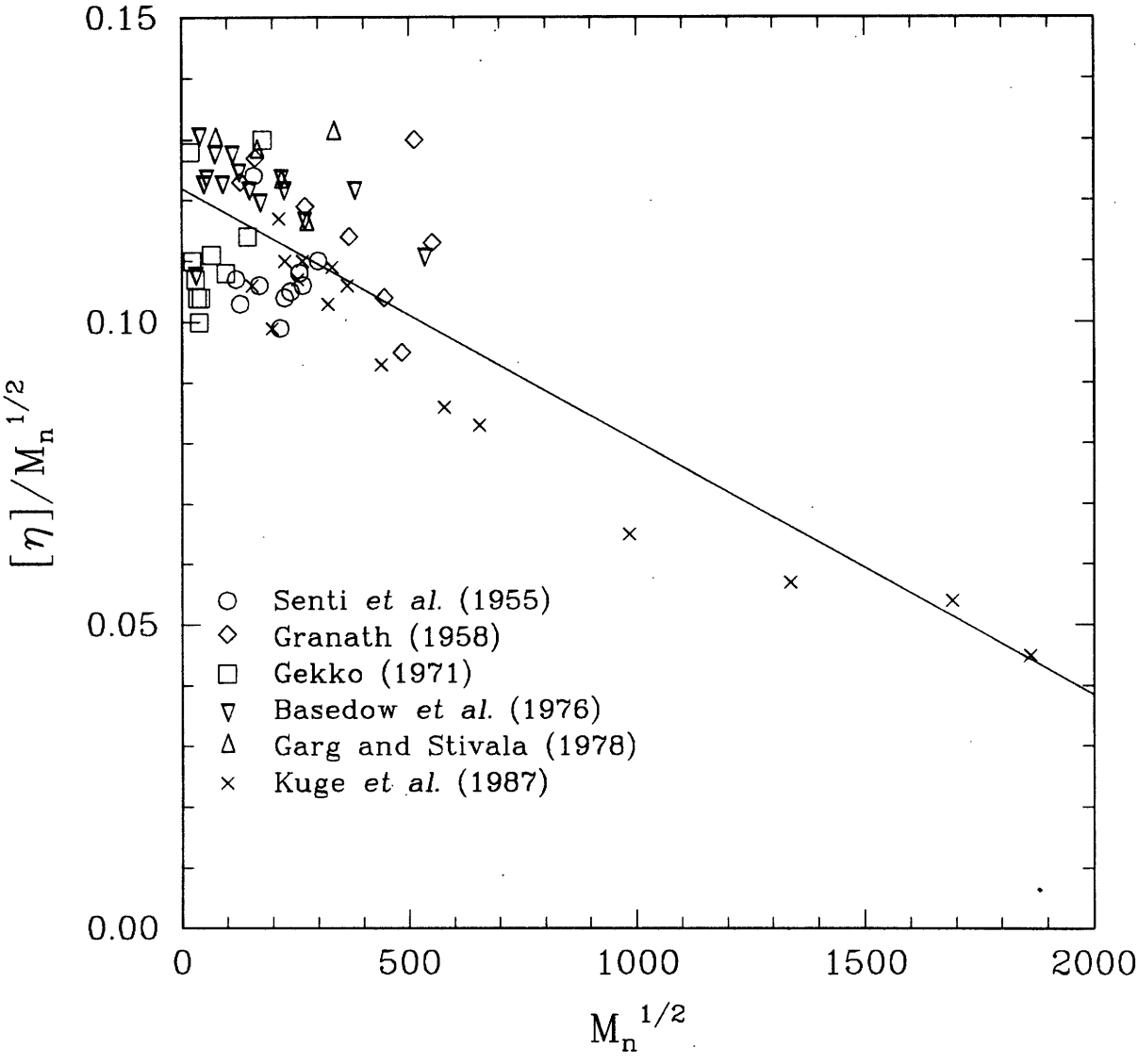

Figure F-4: Stockmayer-Fixman plots for data of Table F.1. Line is best-fit value of $[\eta]/\sqrt{M_n} = 0.122 - 4.17 \times 10^{-5}\sqrt{M_N}$.

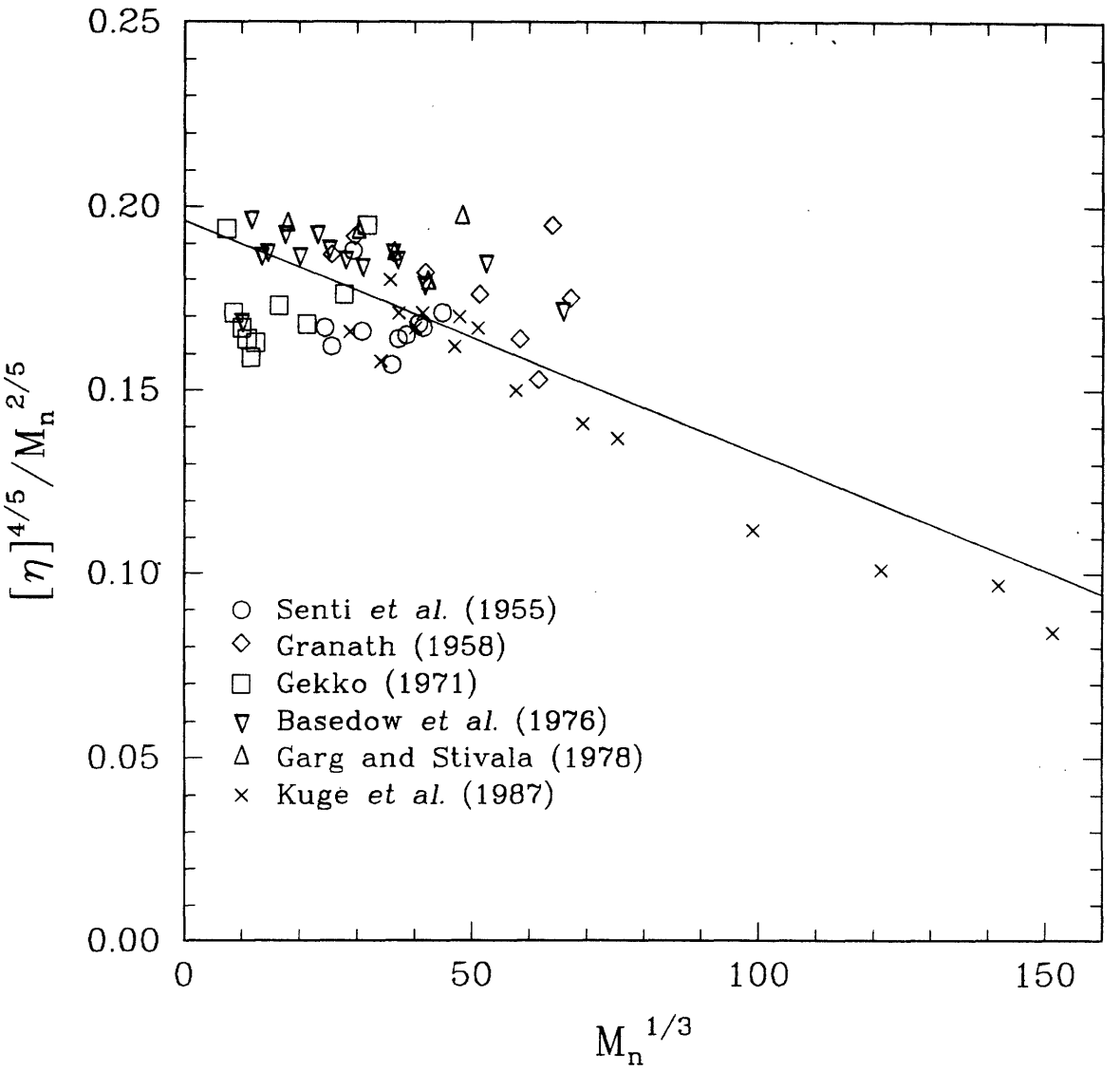

Figure F-5: Inagaki-Ptitsyn plots for data of Table F.1. Line is best-fit value of $[\eta]^{4/5}/M_n^{2/5} = 0.196 - 6.35 \times 10^{-4} M_n^{1/3}$.

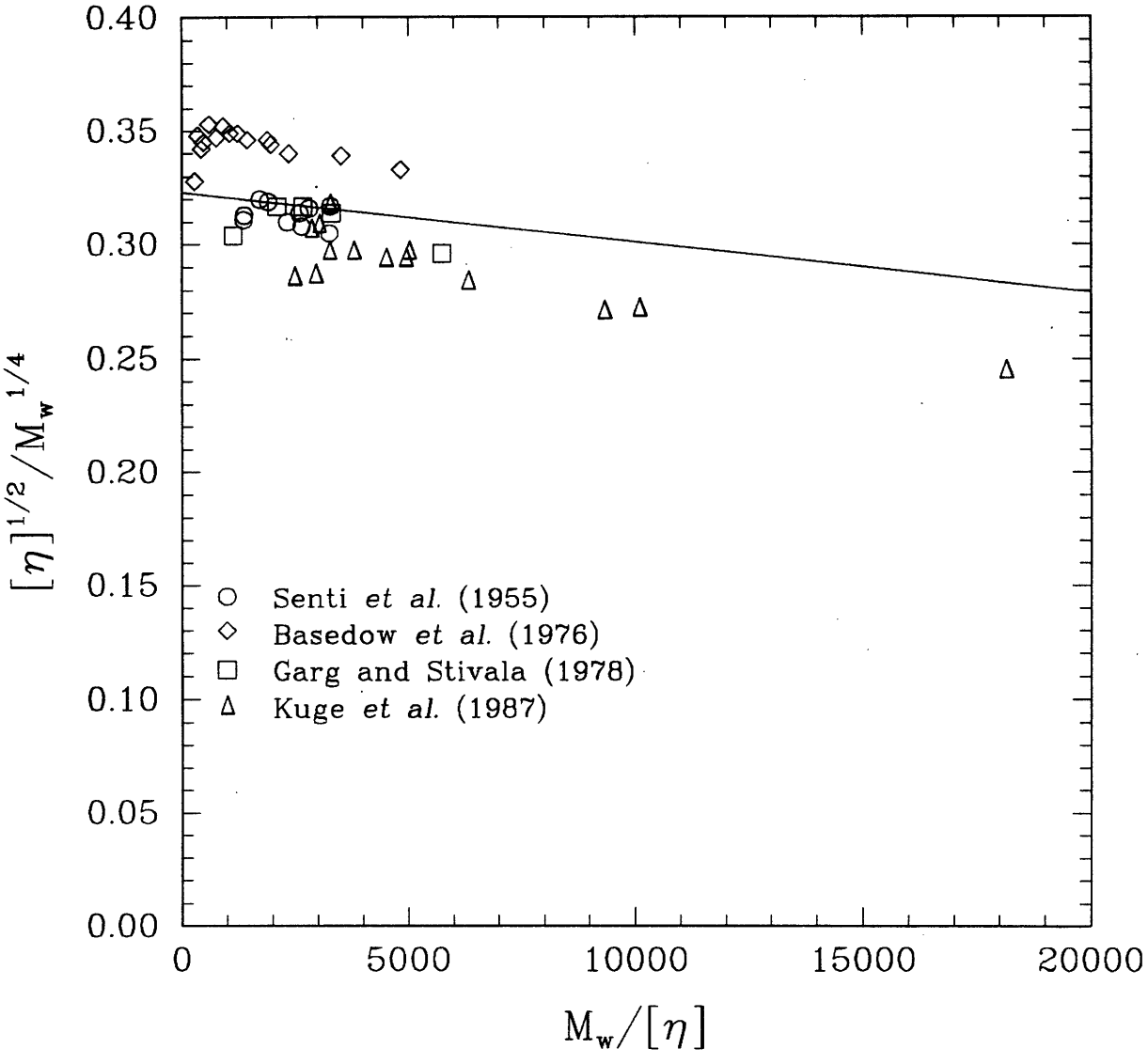

Figure F-6: Berry plots for data of Table F.1. Line is best-fit value of $[\eta]^{1/2}/M_w^{1/4} = 0.323 - 2.18 \times 10^{-6}\ M_w\ /\ [\eta]$.

values are somewhat higher than those calculated from the Stockmayer-Fixman equation (Eq. F.7a) by Wales *et al.*[251] (0.092 cm^3-$g^{-3/2}$-$mol^{1/2}$), Gekko[113] (0.091 cm^3-$g^{-3/2}$-$mol^{1/2}$), and Garg and Stivala[109] (0.087 cm^3-$g^{-3/2}$-$mol^{1/2}$).

If the Stockmayer-Fixman plot (except for the data of Gekko, where M_w/M_n is not known) is replotted according to Eq. F.11a, the correction for polydispersity, then the intercept $q_2\kappa_0 = 0.110$. If an averaged M_w/M_n value of 1.38 is assumed, then from Eq. F.11b, $q_2 = 0.966$. The corrected value for κ_0 is then 0.114.

Thus, $\kappa_0 = 0.113$ cm^3-$g^{-3/2}$-$mol^{1/2}$ is a justified estimate based on the average of these methods, and from this $A_0 = 0.769$ Å-$g^{-1/2}$-$mol^{1/2}$, which compares well to values of 0.717 obtained from the Wales *et al.*[251] result, 0.714 obtained from Gekko,[113] and 0.703 obtained from Garg and Stivala.[109]

F.4.2 Expansion Factor from Intrinsic Viscosity

Figure F-7 shows the intrinsic viscosity data plotted as $\alpha_\eta^3 = [\eta]/\kappa_0 M_n^{1/2}$ versus molecular weight, with $\kappa_0 = 0.113 cm^3$-$g^{-3/2}$-$mol^{1/2}$. If only the data for $M_n < 10^6$ are considered, then a nearly constant value of $\alpha_\eta^3 = 0.983$ is indicated, consistent with theta conditions. This implies that $\alpha_S \approx 1$. Also, since the maximum value of α_η^3 is less than 1.2, the use of Eq. F.7a for the Stockmayer-Fixman plot is justified.[27]

Yamakawa[259] notes that graphical extrapolation methods provide consistent values of unperturbed dimensions, but excluded volume parameters derived from them are often not accurate. Therefore, the alternative methods described previously will be employed in the next two sections.

F.4.3 Expansion Factor from Radius of Gyration

A value for the expansion factor can be calculated by combining Eqs. F.16 and F.27:

$$\alpha_S = 2.59 M^{-0.062} \tag{F.28}$$

which over the range $M = 1000$ to 100,000 gives $\alpha_S = 1.69$ to 1.27. These values are a slight departure from the theta-condition behavior ($\alpha_S \approx 1$) indicated by the flatness of the Stockmayer-Fixman, Inagaki-Ptitsyn, and Berry plots, which imply that . This method is obviously dependent on the quality of the radius of gyration correlation used.

F.4.4 Expansion Factor from Second Virial Coefficient

Calculation of α_S^2 from Eq. F.18 and the data of Kuge *et al.*[152] is shown in Figure F-8. These results indicate that the excluded volume effects are negligible ($\alpha_S \approx 1$) at least for M_n up to 100,000, in agreement with the intrinsic viscosity results.

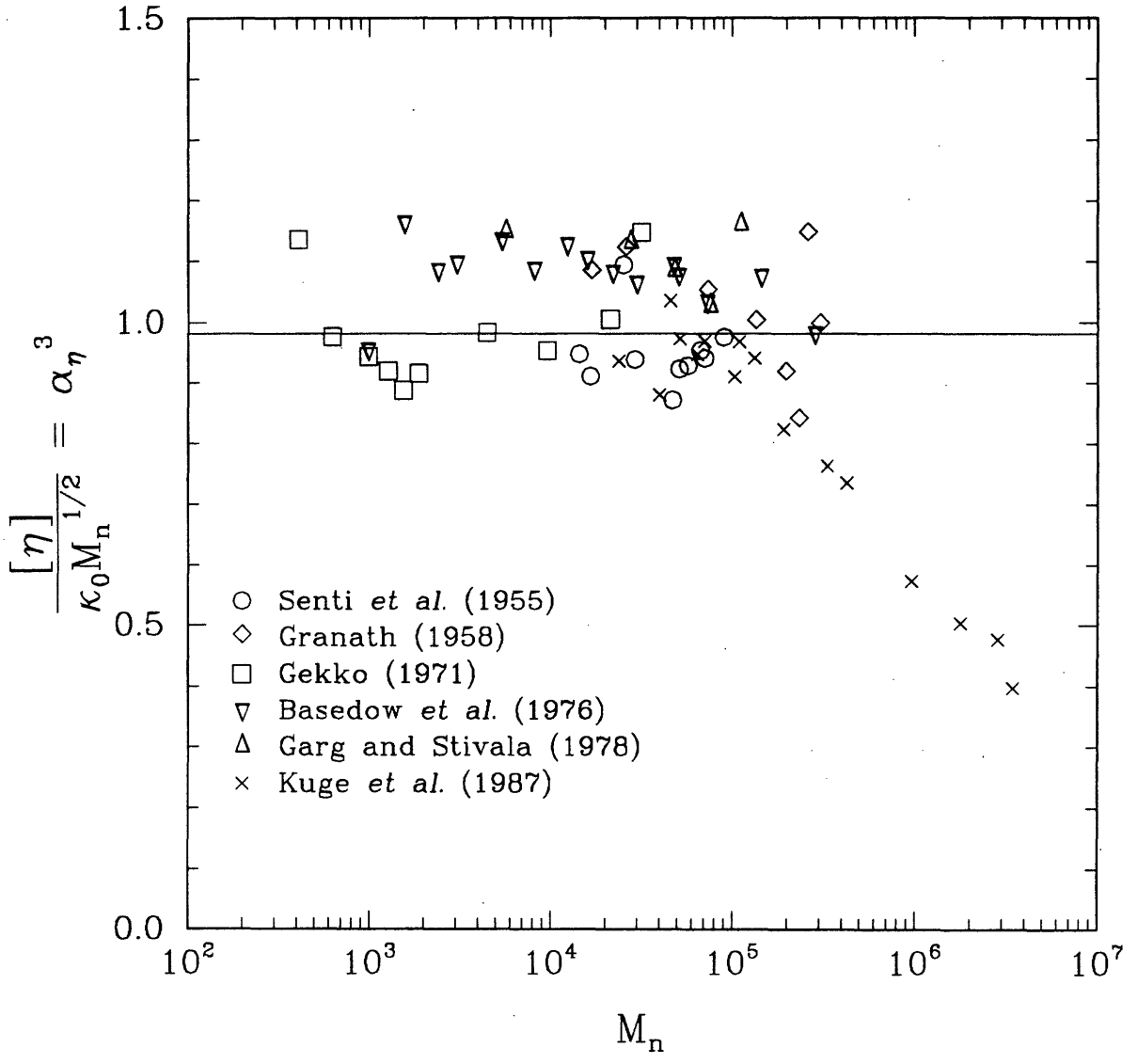

Figure F-7: Values of the cubed hydrodynamic radius expansion coefficient (α_η^3) from data of Table F.1. Line is a constant value of $\alpha_\eta^3 = 0.983$.

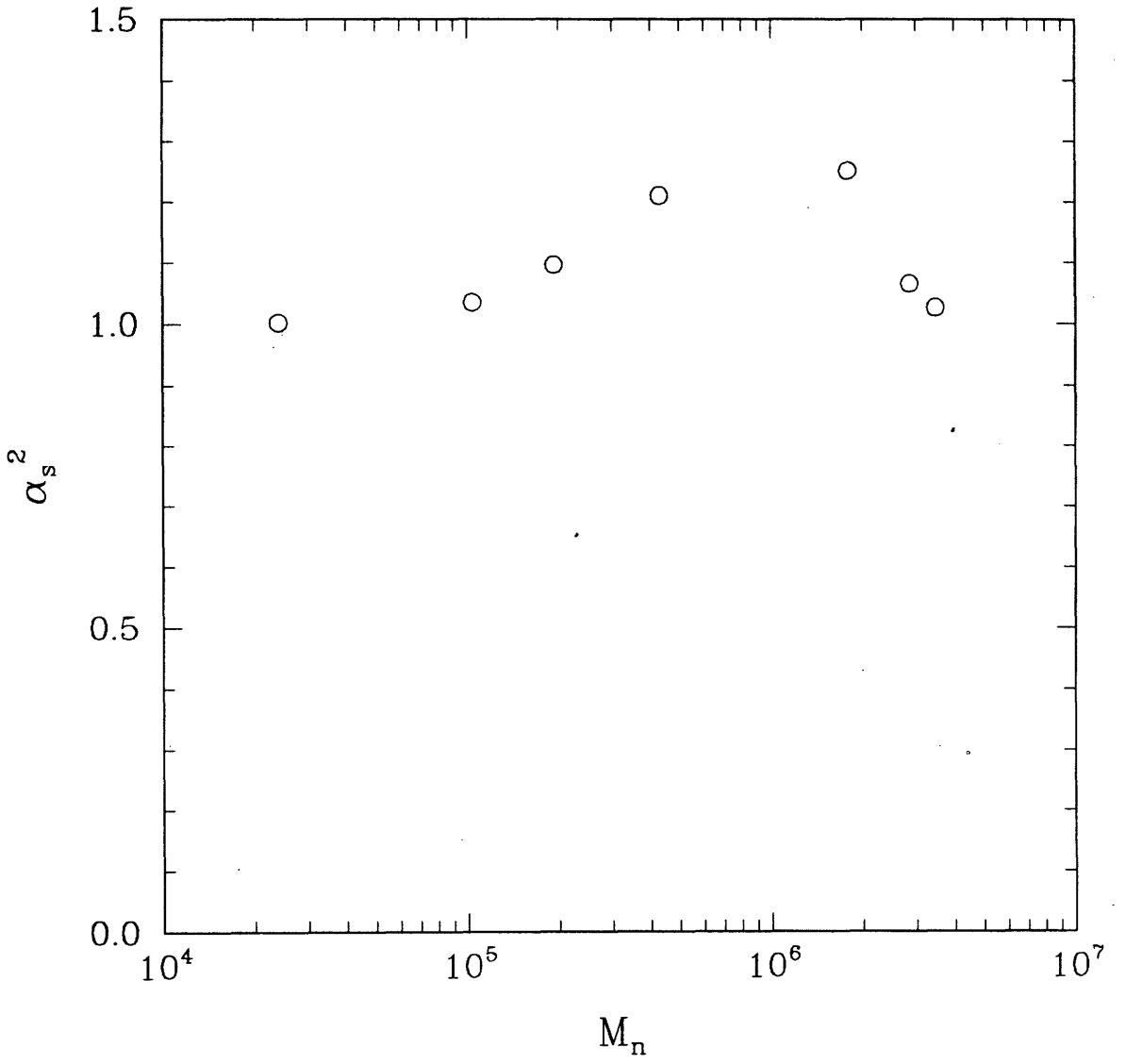

Figure F-8: Values of the radius of gyration expansion coefficient (α_S^2) calculated from second virial coefficient. Data is that of Kuge *et al.*.[152]

F.4.5 Skeletal Factor

Having calculated the unperturbed value $A_0 = 0.769$ as described in Section F.4.1, the skeletal factor is then given by

$$s = \left(\frac{A_0}{A_{00}}\right)^2. \tag{F.29a}$$

(F.29b)

Values for A_{00} are available from the calculations of Cleland[68] (Section F.2.5). Using $A_{00} = 0.394$, $s = 3.81$, and using $A_{00} = 0.424$, $s = 3.29$. This compares favorably with estimates of $s \approx 2.89$ to 3.24 by Gekko.[113]

F.4.6 Equivalent Bond Dimensions N and L

Intrinsic viscosity and second-virial coefficient data indicate that $\alpha_S \approx 1$, while the radius of gyration data indicated that $\alpha_S \approx 4$. The value of α_S from the radius of gyration correlation seems unrealistically high. Using a value for $s = 3.6$, an estimate of $g/g_0 = 1.2$, and $\alpha_S \approx 1$,

$$L = s\alpha_S^2 \frac{g}{g_0} l \approx 4.32l = 4.32 \cdot 5.2\text{Å} = 22.5\text{Å} \tag{F.30a}$$

$$N = n/(s\alpha_S^2 \frac{g}{g_0}) = n/4.32 \tag{F.30b}$$

$$M_{\text{seg}} = 4.32 M_{\text{mon}} \approx 700 \text{ daltons} \tag{F.30c}$$

Thus an effective segment length is calculated to be equal to 4–5 monomer lengths. Alternatively, Garg and Stivala[109] report values for a^* ranging from 20 to 28 Å over $M_n = 5700$ to 112,500. L is thus estimated to be around 45–50 Å (8.7l to 9.6l) by this method.[109] These results are about a factor of two larger than those from intrinsic viscosity plots.

F.4.7 Discussion

All previously published calculations using the random coil model with dextran have assumed a segment size corresponding to a glucose monomer. The rationale for doing so is based on excess thermodynamic measurements that indicate that dextran begins to exhibit the properties of a random-flight coil in solution at molecular weights of around 2000.[114] The results presented here indicate that $N = 2.86$ segments at 2000 daltons, which seems an unrealistically small number of effective segments for random coil behavior. N is even smaller if the persistence length result is used. Davidson[70] justified using $N = n$ in order to maintain compatibility with the idea of a random coil at low molecular weights.

Both short-range steric interaction represented by s and branching effects denoted by g/g_0 appear

to have an effect on the molecular dimensions of dextran. Dextran/water at 20-25 °C is not strictly a theta system because the second virial coefficient is nonzero, but it appears that there is an effect of chain branching which leads to a reduction of the molecular dimensions compared to an equivalent linear molecule. The result is a branched molecule with the solution properties of a lighter linear molecule in a theta solvent.

The effective contraction of the molecular dimensions resulting from chain branching, which is more significant than would be predicted by theory, is fortuitously counterbalanced by excluded volume effects resulting from the expansion of dextran in water. Thus, though it is not strictly a theta system, dextran/water at 20-25 °C exhibits the behavior of a linear molecule with no excluded volume. The effective segment size of dextran is estimated to be about 4.3 glucose monomers, 28% of that factor resulting from excluded volume, 72% from impedance to internal rotations, and essentially negligible bond angle restriction.

The theta-state radius of gyration is seen to be considerably smaller than would have been predicted based on what is surmised about its chemical structure. Specifically, it would be expected that dextran's short branches would result in minimal deviation from straight chain behavior, but instead its radius of gyration is about 70% of an equivalently-sized linear molecule at molecular weights around 50,000. Whatever physical characteristic of dextran is responsible for this behavior will probably also influence its hindered transport in pores. It is not clear to what extent this is of a concern for sieving calculations, but it could be potentially significant for application of results from the Monte Carlo simulations.

4750 - 36